THE UNIVERSITY OF MANITOBA

LIBRARY

AUTHOR ..... BAYOUMI, Mohamed R. .....

TITLE ..... STUDY OF THE RELATION BETWEEN FRACTURE TOUGHNESS AND DUCTILITY .....

.....

.....

THESIS ..... Ph.D., 1984 .....

I, the undersigned, agree to refrain from producing, or reproducing, the above-named work, or any part thereof, in any material form, without the written consent of the author:

.....

.....

.....

.....

.....

.....

.....

.....

.....

.....

.....

.....

.....

.....

.....

.....

.....

.....

THE UNIVERSITY OF MANITOBA

STUDY OF THE RELATION BETWEEN FRACTURE TOUGHNESS AND DUCTILITY

BY

MOHAMED R. BAYOUMI

A Thesis

Submitted to the Faculty of Graduate Studies in

Partial Fulfillment of the Requirements

for the Degree of

Doctor of Philiosphy

Department of Mechanical Engineering

Winnipeg, Manitoba

January 1984

THE UNIVERSITY OF MANITOBA

FACULTY OF GRADUATE STUDIES

The undersigned certify that they have read, and recommend to the Faculty of Graduate Studies for acceptance, a Ph.D. thesis entitled: Study of the Relation Between Fracture Toughness and Ductility

submitted by Mohamed R. Bayoumi

in partial fulfilment of the requirements for the Ph.D. degree.

Advisor

Dr. J. Matthews
External Examiner
Defence Research Establishment Atlantic
Dartmouth, Nova Scotia

Date of oral examination: February 20th, 1984.

The student has satisfactorily completed and passed the Ph.D. oral examination.

Advisor

Chairman of Ph.D. Oral*

(*The signature of the Chairman does not necessarily signify that the Chairman has read the complete thesis.)

STUDY OF THE RELATION BETWEEN FRACTURE TOUGHNESS AND DUCTILITY

by

Mohamed R. Bayoumi

A thesis submitted to the Faculty of Graduate Studies of the University of Manitoba in partial fulfillment of the requirements of the degree of

DOCTOR OF PHILOSOPHY

To my parents and the spirit of my brother

ABSTRACT

Correlation between ductility and fracture toughness of engineering materials, as a function of material parameters and testing conditions, is a major objective in fracture research. A study of the variation of the fracture toughness parameter J_{IC} and ductility, measured under both tensile loading and biaxial plane strain (bulge) loading of AISI 1045 steel in the annealed condition, in the transition temperature range of -60 to 25°C was carried out. This temperature range delineates the changes in behavior from linear elastic to elastic-plastic behavior for this steel as determined from Charpy tests. It was found that the variation of J_{IC} with temperature shows a transition of about -20°C while the bulge ductility only has a marked transition below -40°C. These trends were explained in terms of the effect of material properties, namely the flow stress, on crack blunting, while the bulge ductility is correlated with the total strain to cause significant crack growth to take place. In the elastic-plastic region, a linear relationship between J_{IC} and bulge ductility was found to occur.

A theoretical model relating fracture toughness expressed as J_{IC} and bulge ductility $\bar{\varepsilon}_{F,\alpha=1,\beta=0}$ for a material exhibiting linear elastic behavior at low temperatures and elastic-plastic behavior at high temperatures is proposed. This model shows a variation of J_{IC} with $\bar{\varepsilon}^{-2}_{F,\alpha=1,\beta=0}$ for

linear elastic behavior and J_{IC} with $\bar{\varepsilon}_{F,\alpha=1,\beta=0}$ for elastic-plastic behavior. The model contains three constants to be determined experimentally, for a given material, specimen geometry and testing conditions. A case study on 1045 steel in the temperature range -60 to 25°C confirms the validity of the model. The experimental results help in determining the size of the fracture zone ahead of the crack as well as the mechanisms for crack blunting and crack growth.

Stretch zone width measurements of the fractured specimens were performed as a function of temperature in the transition region of AISI 1045 steel. The results show the existence of a transition in the variation of fracture toughness and stretch zone width with temperature. Such a transition is indicative of the blunting process at the crack tip.

The temperature dependence of ductility, strength and fracture toughness for BCC materials undergoing predominantly linear elastic behavior at low temperatures and elastic-plastic behavior at high temperatures was examined. A model, based on ductile fracture mechanisms involving void nucleation followed by cavity growth and void coalescence, is developed to relate the fracture toughness parameter J_{IC} with temperature. Application of this model to experimental data obtained on 1045 steel show that J_{IC} varies with T^2 at low temperatures and with T at high temperatures, thus defining a transition temperature.

The variation of fracture toughness of AISI 1045 steel with loading rates ranging from quasi-static to dynamic conditions was studied. A wedge loaded compact tension (WLCT) specimen geometry was used in both testing conditions. The onset of crack propagation was detected using a strain gage mounted near the crack tip. The fracture toughness testing in the dynamic range was achieved by the longitudinal stress wave loading using the Split Hopkinson Pressure Bar technique. The fracture toughness parameter J_{IC} decreased significantly under high loading rates. The measured values of J_{IC} using WLCT specimens were confirmed from stretch zone measurements using scanning electron microscopy of the fracture surface of the WLCT specimens.

Strain rate $\dot{\varepsilon}$ dependence of ductility, strength and fracture toughness for materials with high strain sensitivity such as steels and aluminium alloys was examined. Cracked specimens of these materials usually undergo predominantly linear elastic behavior at high strain rates and elastic-plastic behavior at low strain rates. Based on ductile fracture mechanisms, a model is developed to relate the fracture toughness parameter J_{IC} with strain rate $\dot{\varepsilon}$. Two general equations describing the variation of J_{IC} with strain rate $\dot{\varepsilon}$ are obtained. Application of this model to experimental data obtained on a carbon steel show that J_{IC} varies with $\log (\dot{\varepsilon}/10^{-3})$ at low strain rates and with $\log [(\dot{\varepsilon}/10^{-3})]^2$ at higher strain rates.

The effect of microstructure on fracture toughness and ductility in the transition temperature range was investigated. The transition in behavior from linear elastic to elastic-plastic, in the relation between fracture toughness J_{IC} and temperature from one hand and in the relation between J_{IC} and bulge ductility from the other hand for the tempered martensitic microstructure of AISI 1045 steel was shown to be similar to that obtained for pearlitic microstructure of AISI 1045 steel, as long as the flow stress as a function of temperature for both microstructures exhibit similar behavior.

ACKNOWLEDGEMENTS

The author would like to express his sincere appreciation to his advisor Dr. M.N. Bassim for the suggestion of the problem and for his invaluable advice, guidance, discussions and criticism throughout this work.

Thanks are due to Professor J.R. Klepaczko and Professor T.R. Hsu for their valuable help and discussions in using the Split Hopkinson pressure bar system. Special thanks are due to Mr. D. Mardis, Mr. J. Van Dorp and Mr. R. Hartle in the metallurgical sciences laboratory and to Mr. L. Wilkins and Mr. J. Shewchuk in the machine shop for their excellent technical help and for their warmth and friendship.

The author wishes to express his gratitude to Professor J.R. Cahoon, Head of the Mechanical Engineering Department for his kindness, discussions and encouragement and for the opportunity to work in the department.

Thanks are also due to Professor K. Tangri and Professor M.C. Chatruvedi for their kind interactions which the author enjoyed during his work in the Metallurgical Sciences Laboratory.

Special thanks is due to Mrs. V. Lee for her cheerfulness and immense patience in typing of this manuscript.

Finally, the author wishes to express his deepest gratitude to his wife and his son. They have endured with him the hardships of long hours and night work necessary for completing this thesis.

TABLE OF CONTENTS

LIST OF TABLES

LIST OF FIGURES

NOMENCLATURE

All notations are specifically defined where they are first introduced. The symbols in this thesis are however listed below:

a	Crack length
Δa	Crack extension
Δa_{cr}	Critical crack extension
A	Cracked area
b	Length of the ligament
B	Specimen thickness
C_o	Elastic wave speed = $(E/\rho)^{1/2}$
COD	Crack opening displacement
Δc	Change in compliance
dJ/da	Slope of the crack advance line
dS	Differential element of an arch length along contour path
D_1, D_E	The diameter of the striker bar and the diameter of the Hopkinson bars respectively
E	Young's modulus
F	Opening force for WLCT specimen
$g(a/w)$	Compliance function of geometry of the specimen
G_c	Work required to form a unit crack extension
J	Path independent contour integral defined by Rice [21].
J_{IC}	Fracture toughness parameter
K	Stress intensity factor
K_I, K_{II}, K_{III}	Stress intensity factor for Mode I, Mode II and Mode III respectively
K_c, K_{IC}	Plane stress and plane strain fracture toughness respectively
$\dot{K}_I$	Loading rate defined as K_{IC}/t_c
K_R	Crack growth resistance
L_e^*, L_p^*	Microstructure characteristic distances
LEFM	Linear elastic fracture mechanics

m	Constraint factor
m_1	Strain rate sensitivity = ∂ Log σ / ∂ log $\dot{\varepsilon}$
n	Strain hardening exponent
n_j	Direction cosines of a unit vector $\bar{n}$
$\bar{n}$	Unit vector
P	Applied force
$\bar{P}$	Average applied force
r_y	Plastic zone radius
R	Crack growth resistance curve
s	Specimen span length
S	Shape factor characterizing the geometry of the plastic zone
T	Temperature
T_i	Surface traction vector
T_R	Tearing modulus = $\frac{dJ}{da} \cdot \frac{E}{\sigma_y^2}$
t_c	The critical time interval from the start of loading to the point when the critical state of the crack is achieved
u_i	Displacement vector
U	Potential energy
$U_{i,i+1}$	Area under the load versus load line displacement between lines of constant displacement at points i and i + 1
V_o	Impact velocity
V_f	Volume fraction of voids
w	Specimen width
W_{szc}	Stretch zone width
Y	The flow stress in the region of an inclusion
X,Y,Z and r,θ	Coordinate system
α	Stress state ratio = σ_2/σ_1
β	Stress state ratio = σ_3/σ_1
γ_p	The plastic work
γ_s	The work needed to create a new surface (surface or elastic energy)

δ	Load line displacement
δ_1	Crack tip opening displacement
δ_1^*	Crack tip opening displacement at initiation of fracture
δ_{cr}	Critical load line displacement
$\bar{\varepsilon}$	Effective strain
ε_y	Yield strain
$\varepsilon_I, \varepsilon_R, \varepsilon_T$	The incident, reflected and transmitted elastic strain waves
$\bar{\varepsilon}^p$	Mean plastic strain
$\bar{\varepsilon}_{F,\alpha,\beta}$	Fracture strain under stress state $\alpha = \sigma_2/\sigma_1$ and $\beta = \sigma_3/\sigma_1$
$\bar{\varepsilon}_{i,\alpha,\beta}$	Nucleation strain under stress state $\alpha = \sigma_3/\sigma_1$
$\bar{\varepsilon}_{c,\alpha,\beta}$	Coalescence strain under stress state $\alpha = \sigma_2/\sigma_1$ and $\beta = \sigma_3/\sigma_1$
$\bar{\varepsilon}_{F,\alpha=1,\beta=0}$	Equibiaxial bulge ductility
$\dot{\bar{\varepsilon}}$	Strain rate
μ	Coefficient of friction
ρ	Density of material
ρ^*	Neuber's microsupport effect constant = 0.025 mm.
Γ	Contour path in J-integral evaluation
σ_{ij}	Stress tensor
$\sigma_1, \sigma_2, \sigma_3$	Principal stress components
$\bar{\sigma}$	Effective stress
σ_y	Yield strength of material
σ_F	Fracture stress
σ_m	Mean stress = $(\sigma_1 + \sigma_2 + \sigma_3)/3$
σ_o	Flow stress
σ_{fc}	Cleavage fracture stress
σ_{rr}	Interface stress
σ_u	Ultimate tensile strength of material
ν	Poisson's ratio
ϕ	Tilting angle

CHAPTER 1

INTRODUCTION

For most metallic materials, the dominant mechanism resisting fracture and hence increasing toughness is the occurrence of plastic deformation. Therefore, fracture toughness, in addition to its dependence on material properties such as Young's modulus, flow stress and strain hardening exponent, should also be dependent on the effective ductility in the region ahead of the crack.

The dominant microstructural events that control ductility, and therefore fracture toughness, are void nucleation, void growth and void coalescence. Void nucleation at an inclusion-matrix interface or grain boundary is governed by the value of the difference between interface strength and the flow stress and is consequently, temperature and strain rate sensitive.

The relation between ductility and fracture toughness in the transition temperature range, for materials which show change in behavior from predominantly linear elastic behavior to elastic plastic behavior with large plastic zone size at the crack tip has not been quantitatively studied. The use of the J-integral as a fracture criterion for those materials is strongly dependent on their ductility and a study relating fracture toughness J_{IC} with inherent ductility is hence of great importance. Because a quantitative assessment of the relationship between fracture toughness, ductility,

temperature, loading rate and microstructure is lacking, this present study attempts to address this fundamental problem both experimentally and theoretically.

Experimental procedures, described in Chapter 3, were adopted to obtain the experimental data for ductility and fracture toughness under different conditions of test temperature and loading rate. Bulge ductility equipment was designed and constructed to measure the material ductility, while the J_{IC} criterion, using standard three-point bending specimens were used to characterize the material fracture toughness. Wedge loaded compact tension specimens were used to obtain the fracture toughness data over a wide range of loading rates. Fracture in the dynamic range was achieved by the Split Hopkinson Bar technique. The measurement of the stretch zone width with the scanning electron microscopy was used as an alternative method to determine the fracture toughness parameter J_{IC}. Two microstructures were tested, namely a pearlitic and a tempered martensitic microstructure.

Experimental results for the pearlitic microstructure of AISI 1045 steel are presented in Chapter 4. These results include the variation of fracture toughness and ductility in the transition temperature range, quasi-static and dynamic fracture toughness results and stretch zone measurements results.

A model relating the fracture toughness J_{IC} and the bulge ductility for predominantly linear elastic behavior and elastic-plastic behavior is presented in Chapter 5.

Temperature dependence of fracture toughness, strength and ductility in the transition region for BCC materials is described in Chapter 6.

A model relating fracture toughness J_{IC} and ductility for predominantly linear elastic behavior at high strain rates and mostly elastic-plastic behavior at low strain rates, is described in Chapter 7.

Fracture toughness J_{IC} and ductility studies, in the transition temperature range for tempered martensitic AISI 1045 steel, are presented and discussed through Chapter 8.

A general discussion as well as the main conclusions of the entire study are given in Chapter 9.

This study casts some new light on the correlation between fracture toughness and ductility as a function of material parameters and testing conditions. A better understanding of the mechanisms of crack initiation and propagation in the transition region for temperature and strain rate sensitive materials will hopefully result therefrom.

CHAPTER 2

LITERATURE REVIEW

The fracture mechanisms which may be encountered in engineering materials and structures can be classified into two general groups. The first category is termed brittle fracture and occurs in brittle materials such as glass, or in mild steel at very low temperatures. Brittle fracture may also occur in most other engineering materials under very high loading rates. This type of fracture is associated with relatively low fracture toughness (i.e. low input energy required to propagate the crack) and small plastic deformation prior to and during unstable crack extension. The second type of fracture falls into the general category of ductile fracture which corresponds to a high fracture toughness, and usually occurs in non brittle materials. For example structures composed of materials with high ductility would be expected to undergo large plastic deformation prior to and during the rupture process.

Research in the field of fracture mechanics was initially concerned with investigating brittle fracture problems, since these types of failures are of more disastrous consequences and are easier to analyze than the ductile fracture cases. In this chapter, the concept of linear elastic fracture mechanics is briefly described, and the current level of knowledge in elastic-plastic fracture is discussed. Also, a review of the literature on ductile

fracture mechanisms, including the effect of temperature and loading rate on fracture toughness, as well as the relationship between fracture toughness and ductility is presented.

2.1 Linear Elastic Fracture Mechanics

Linear-elastic fracture mechanics (LEFM) is based on an analytical procedure that relates the stress field magnitude and distribution in the vicinity of a crack tip to the nominal stress applied to the structure, to the size, shape and orientation of the crack and to the material properties. The fracture modes, shown in Fig. 2.1 are denoted as the opening mode, the edge sliding mode and the tearing mode [1,2].

- The opening mode (mode I) is associated with local displacement in which the crack surfaces move apart in a direction perpendicular to these surfaces (symmetric with respect to the X-Y and Z-X planes).
- The edge sliding mode (mode II) is characterized by displacements in which the crack surfaces slide over one another and remain perpendicular to the leading edge of the crack. (Symmetric with respect to the X-Y plane and skew-symmetric with respect to Z-X plane).
- The tearing mode (mode III) is defined by the crack surfaces sliding with respect to one another parallel to the leading edge of the crack. (skew-symmetric with respect to the X-Y and X-Z planes).

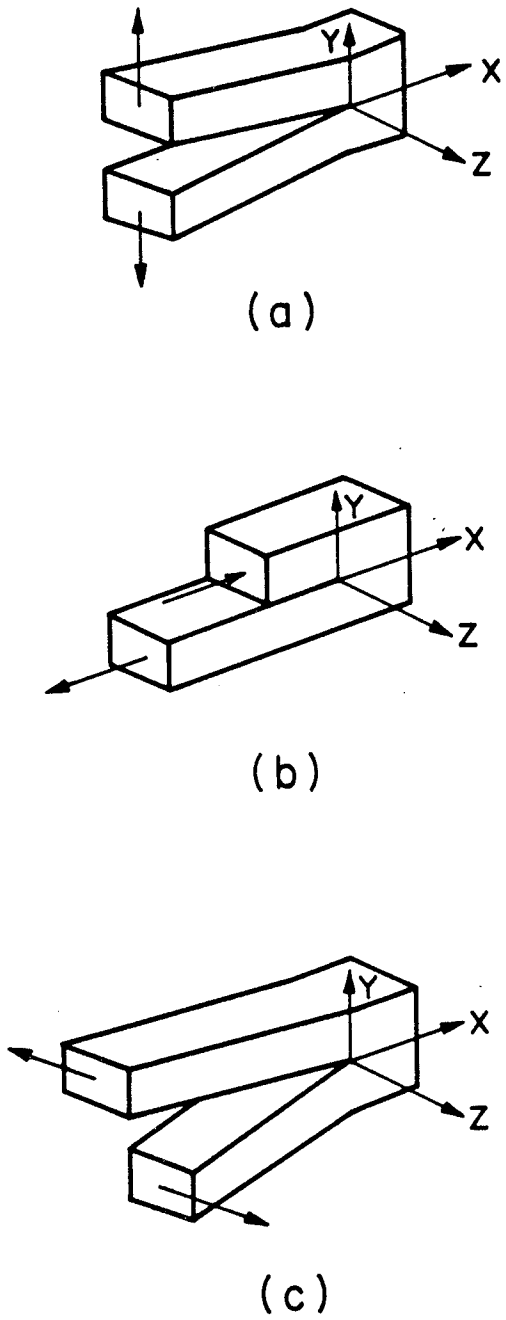

Figure 2.1 The three modes of fracture (After Ref. 1)
(a) Mode I, (b) Mode II and (c) Mode III

Griffith theory [3] was based on the assumption that incipient fracture in ideally brittle materials occurs when the magnitude of the elastic energy supplied to the crack tip during an incremental increase in crack length exceeds the magnitude of the energy required to create the new crack surface during the same incremental increase in crack length. This strain energy release rate G, or the elastic energy made available per unit extension of the crack area is:

$$G = - \frac{dU}{dA} \qquad (2.1)$$

where U is the potential energy of the structure and A is the cracked area.

Irwin [4] developed the analytical basis of the elastic crack tip stress field theory, which in turn was the starting point of modern fracture mechanics. In his theory, the stress intensity factor K (K_I, K_{II} and K_{III} are defined as mode I, mode II and mode III stress intensity factors, respectively), is extracted from the solutions for stresses and displacements near the crack tip and is a combination of applied load P, crack length a and specimen configuration

$$K = p.\ f\ (a,\ \text{geometry}) \qquad (2.2)$$

K is said to be the controlling parameter of a crack tip field, because stresses and displacements are proportional to this factor. In general, the stress and displacement fields can be expressed mathematically as follows:

$$\sigma_{ij} = \frac{K}{\sqrt{2\pi r}}\ f_{ij}\ (\theta) + \ldots\ldots \qquad (2.3a)$$

$$\frac{K}{G_1}\left[\frac{r}{2\pi}\right]^{1/2} g_1(\theta) + \ldots\ldots \qquad (2.3.b)$$

where (r, θ) is a polar coordinate system at the crack tip as shown in Fig. 2.2 and G_1 is the shear modulus. The truncated terms of equation (2.3) are the terms with higher order in r. For small values of r (i.e. very close to the crack tip), only the first term is significant. Crack extension will occur when the intensity of the stress field in the close vicinity of the crack tip reaches a critical value. This means that fracture must be expected to occur when K reaches a critical value K_c.

Irwin et al [5] also showed that there is a unique relationship between K and G as follows:

$$G = \frac{K^2}{E_o} \qquad (2.4)$$

in which $E_o = E$ plane stress

$= E/(1 - \nu^2)$ plane strain

where E is a Young's modulus and ν is Poisson's ratio. The consistency of the two approaches of Griffith and of Irwin is thus apparent.

Kobayashi et al [6] and Chan et al [7] used the finite element method to calculate the stress intensity factor. Once the numerical values of the nodal displacements and the element stresses near the crack tip are obtained, the K value can be calculated using equation (2.3) at several points. The K value at the crack tip is evaluated by extrapolating these values to the crack tip and by disregarding the first few points very close to the crack tip.

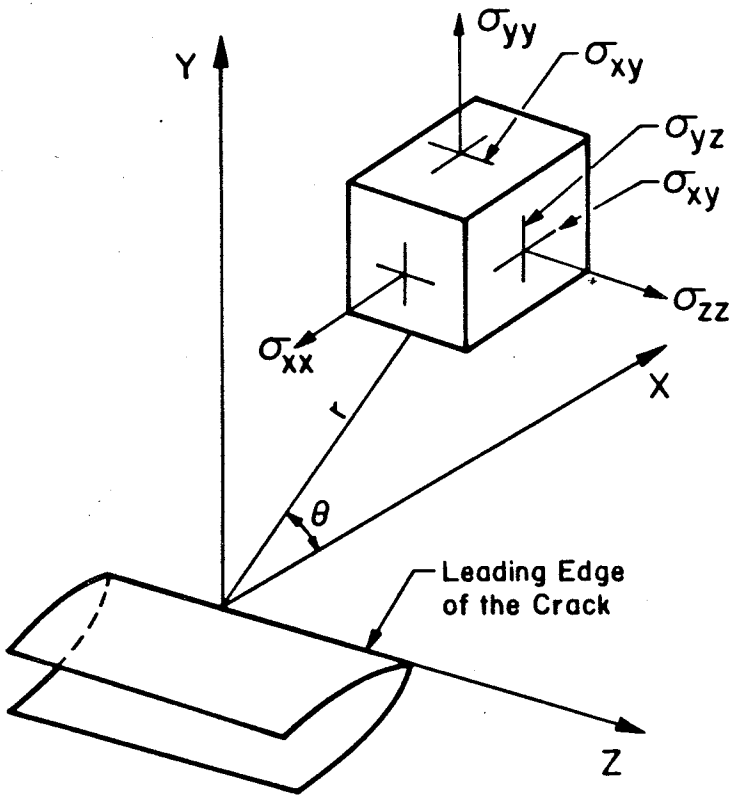

Fracture Mode	Stress Components
Mode I	$\sigma_{xx} = \frac{K_I}{(2\pi r)^{1/2}} \cos\frac{\theta}{2}\left[1 - \sin\frac{\theta}{2}\sin\frac{3\theta}{2}\right]$
	$\sigma_{yy} = \frac{K_I}{(2\pi r)^{1/2}} \cos\frac{\theta}{2}\left[1 + \sin\frac{\theta}{2}\sin\frac{3\theta}{2}\right]$
	$\sigma_{xy} = \frac{K_I}{(2\pi r)^{1/2}} \sin\frac{\theta}{2}\cos\frac{\theta}{2}\cos\frac{3\theta}{2}\right]$
	$\sigma_{zz} = \nu(\sigma_{xx} + \sigma_{yy})$, $\sigma_{xy} = \sigma_{yz} = 0$
	$U = \frac{K_I}{G}\left[\frac{r}{2\pi}\right]^{1/2} \cos\frac{\theta}{2}\left[1 - 2\nu + \sin^2\frac{\theta}{2}\right]$
	$V = \frac{K_I}{G}\left[\frac{r}{2\pi}\right]^{1/2} \sin\frac{\theta}{2}\left[2 - 2\nu - \cos^2\frac{\theta}{2}\right]$, $W = 0$
Mode II	$\sigma_{xx} = \frac{K_{II}}{(2\pi r)^{1/2}} \sin\frac{\theta}{2}\left[2 + \cos\frac{\theta}{2}\cos\frac{3\theta}{2}\right]$
	$\sigma_{yy} = \frac{K_{II}}{(2\pi r)^{1/2}} \sin\frac{\theta}{2}\cos\frac{\theta}{2}\cos\frac{3\theta}{2}\right]$
	$\sigma_{xy} = \frac{K_{II}}{(2\pi r)^{1/2}} \cos\frac{\theta}{2}\left[1 - \sin\frac{\theta}{2}\sin\frac{3\theta}{2}\right]$
	$\sigma_{zz} = \nu(\sigma_{xx} + \sigma_{yy})$, $\sigma_{xz} = \sigma_{yz} = 0$
	$U = \frac{K_{II}}{G}\left[\frac{r}{2\pi}\right]^{1/2} \sin\frac{\theta}{2}\left[2 - 2\nu + \cos^2\frac{\theta}{2}\right]$
	$V = \frac{K_{II}}{G}\left[\frac{r}{2\pi}\right]^{1/2} \cos\frac{\theta}{2}\left[-1 + 2\nu + \sin^2\frac{\theta}{2}\right]$, $W = 0$
Mode III	$\sigma_{xz} = \frac{K_{III}}{(2\pi r)^{1/2}} \sin\frac{\theta}{2}$, $\sigma_{yz} = \frac{K_{III}}{(2\pi r)^{1/2}} \cos\frac{\theta}{2}$
	$\sigma_{xx} = \sigma_{yy} = \sigma_{zz} = \sigma_{xy} = 0$
	$W = \frac{K_{III}}{G}\left[\frac{2r}{\pi}\right]^{1/2} \sin\frac{\theta}{2}$, $u = v = 0$

Figure 2.2 Coordinate system and stress components ahead of the crack tip.

Watwood [8] calculated the K value by computing the strain energy release rate G. In the finite element method for calculation of K, a number of special singular elements (Wilson [9], Byskov [10], Hilton and Sih [11], and Tracey [12]) have been presented to accommodate the singularity at the crack tip. These elements are the result of incorporating both the eigen-function expansions for the crack tip field conditions and the finite element method. The theoretical background of this approach is based on the mathematical properties of the two numerical technique employed, i.e. the asymptotic expansion becomes increasingly more accurate as one approaches the crack tip, while the finite element method is very accurate everywhere except near the crack tip. Another class of special singular elements is the quarter point element, used in conjunction with the standard isoparametric element. The Jacobian transformation from physical to isoparametric coordinates will produce spatial derivatives (i.e. strains) which are singular at the crack tip, if nodal points along the sides of the element are positioned in a certain way. Henshell [13] and Barsoum [14,15] perceived that by moving the middle nodal point of a quadratic isoparametric element to the quarter point closest to the crack tip, the strain singularity is achieved.

Due to the singular nature of equation (2.3a), a plastic zone is always formed at the crack tip where the

stress field exceeds the yield strength of the material. Since equation (2.3) is based on the theory of elasticity, K has significance only when the geometry of the crack or the remaining ligament exceeds the plastic zone size by a factor of about 50 [1], a criterion which is met in the plane strain condition. In order to use an experimentally determined plane strain fracture toughness K_{IC} value as a fracture criterion, the American Society for testing and Materials (ASTM) specifies the following thickness requirement

$$B > 2.5 \frac{K_{IC}^2}{\sigma_{ys}^2} \qquad (2.5)$$

where B is the thickness of the specimen and σ_{ys} is the yield strength of the material.

2.2 Elastic-Plastic Fracture Mechanics

Most of the large complex engineering structures such as airplane frames, ships, pipelines, etc. have small wall thickness and are usually made of ductile materials. Thus, for many structural applications, the linear elastic analysis used to calculate the stress intensity factor K, is invalidated by the formation of large plastic zones around the crack tip. Currently, much effort is being devoted to the development of elastic-plastic fracture mechanics analyses as an extension of LEFM [1,2]. Among the various techniques the following approaches are most popular:

(1) Plastic zone corrections

(2) Crack opening displacement (COD)

(3) Crack growth resistance curve or R-curve

(4) J-integral

The above techniques hold considerable promise for appraising structural integrity in terms of an allowable loading or crack size. The significance of each technique is reviewed in the following sections.

2.2.1 Plastic Zone Corrections

The first attempt in extending fracture mechanics beyond the LEFM limits involved a correction to the crack length to account for the effect of the plastic zone while continuing to use the LEFM approach. This procedure, proposed by Irwin [5], consists of moving the crack tip to the center of the plastic zone by a distance r_y or

$$a \rightarrow a + r_y \tag{2.6}$$

The distance r_y is evaluated as:

$$\begin{aligned} r_y &= \frac{1}{2\pi} \frac{K_c^2}{\sigma_{ys}^2} \quad \text{(plane stress)} \\ &= \frac{1}{6\pi} \frac{K_{IC}^2}{\sigma_{ys}^2} \quad \text{(plane strain)} \end{aligned} \tag{2.7}$$

Although Irwin's plastic zone correction gives consistent results for small scale yielding or plasticity at the crack tip, the limits of its applicability to larger plastic zone sizes are uncertain.

A more rigorous correction for plastic zone size was proposed by Dugdale [16]. He assumed that yielding occurs in a thin strip-like zone at the crack tip, extending the

crack by a distance c - a (Fig. 2.3). The stresses in this yielding zone are considered to be a continuous distribution of point loads, which act to restrain the crack from opening. An expression for the restraining stress intensity factor can then be obtained by integrating from a to c with the appropriate Westergaard stress function [1] as:

$$K = 2\sigma_{ys}\left(\frac{c}{\pi}\right)^{1/2}\cos^{-1}\left(\frac{a}{c}\right) \qquad (2.8)$$

The size of the plastic zone is obtained by equating the restraining stress intensity factor (2.8) with the K value for the opening of the crack, $K = \sigma\sqrt{\pi c}$. Thus;

$$r_y = \frac{\pi}{16}\frac{K^2}{\sigma_{ys}^2} \qquad (2.9)$$

The plastic zone size calculated by equation (2.9) is about 20% larger than that calculated by equation (2.7) for the plane stress case.

2.2.2 Crack Opening Displacement

Wells [17] proposed that the fracture behavior in the vicinity of a crack could be characterized by the opening of the crack faces namely the crack opening displacement (COD), as shown in Fig. 2.3. Furthermore, he showed that the COD value could be related to the plane-strain fracture toughness K_{IC}. Since COD measurement can be made when there is considerable plastic flow around the crack tip, this technique gives useful information for elastic-plastic fracture analysis.

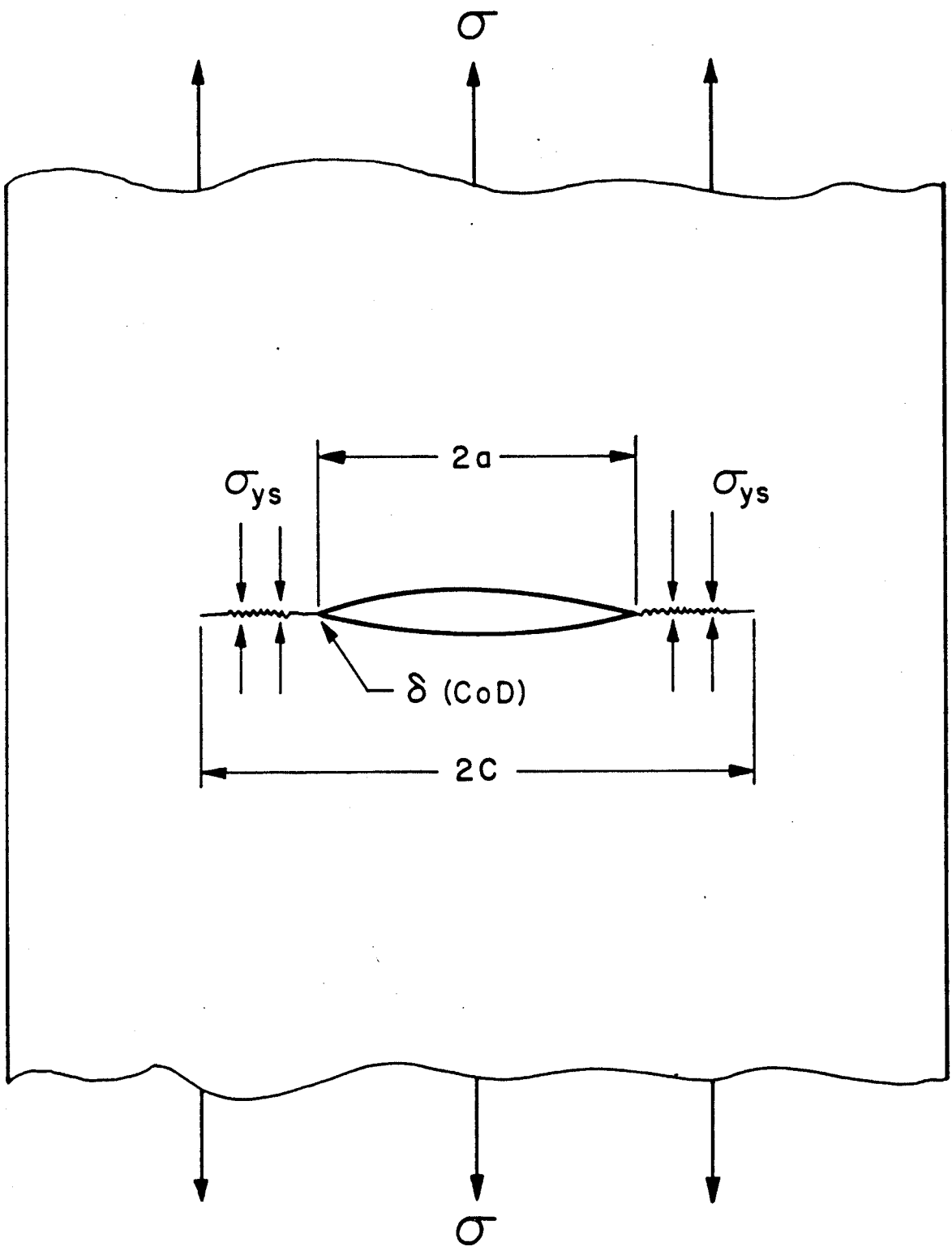

$$\frac{a}{c} = \cos\frac{\pi\sigma}{2\sigma_{ys}}$$

Figure 2.3 Dugdale model for a central crack specimen loaded in Mode I.

An extension of the Dugdale analysis yields an expression for the crack opening displacement normal to the crack plane at the crack tip, δ

$$\delta = \frac{8}{\pi} \frac{\sigma_{ys}}{E} a \ln \left[\sec \frac{\pi}{2} \frac{\sigma}{\sigma_{ys}} \right] \tag{2.10}$$

which for $\sigma/\sigma_{ys} << 1$ reduces to

$$\delta = \frac{K_I^2}{E\sigma_{ys}} \tag{2.11}$$

Equation (2.11) implies that at the onset of crack instability, where K_I reaches K_{IC}, the COD value reaches a critical value δ_c. Under plane strain conditions, unstable fracture will occur upon crack initiation, and thus $\delta_i = \delta_c$. Like K_{IC}, a δ_c value under plane strain conditions is a material property.

2.2.3 Crack Growth Resistance or R-Curve

Since the plane stress fracture toughness K_c is generally 2 - 10 times larger than K_{IC} and varies with specimen thickness, representation of the fracture toughness of thin sheet materials by a resistance curve has been attempted by a number of scientists [18-20], and is still under development. The concept of the crack growth resistance R-curve is based on the observation that during the fracture process of most sheet materials, the unstable fracture is always preceded by a certain amount of stable crack growth under a monotonically rising load.

Fig. 2.4 illustrates a typical R-curve with the crack length as the abscissa and the crack growth resistance as

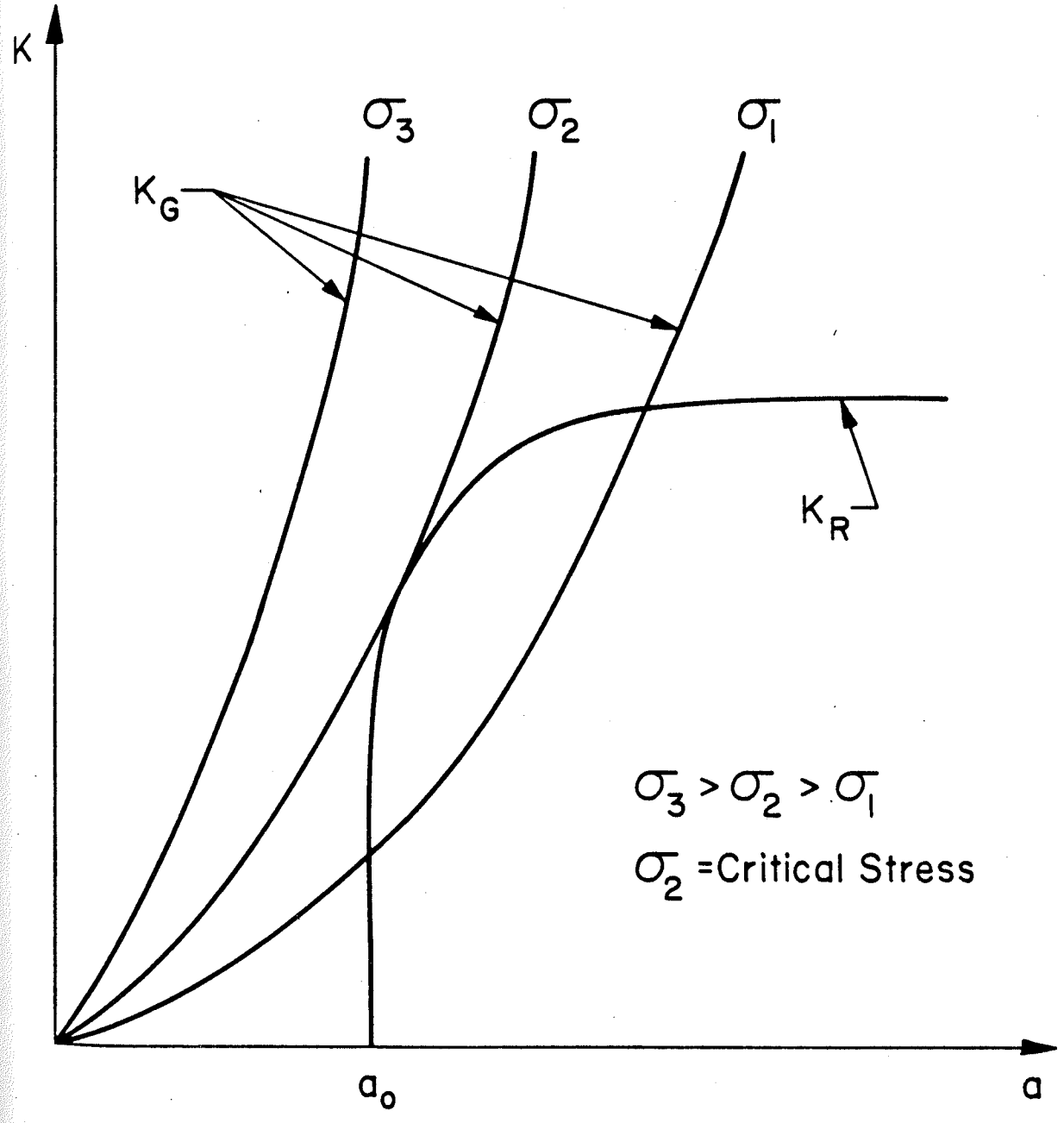

Figure 2.4 R-Curve approach.

the ordinate. The curve labelled K_R is the R-curve, determined from experiment, with the stress intensity factor K_R at any crack length a being that required to propagate the crack from length a_o to a.

2.2.4 J-Integral

Rice [21] proposed a path-independent contour integral, the J-integral, for a two dimensional deformation field, evaluated over the contour Γ in a counter-clockwise direction, as illustrated in Fig. 2.5:

$$J = \int_{\Gamma} \left(W dy - T_i \frac{\partial u_i}{\partial X} ds \right) \tag{2.12}$$

where w is the strain energy density, T_i is the surface traction vector ($= \sigma_{ij} n_j$), u_i is the displacement vector, ds is a differential element of an arc length along Γ and n_j are the direction cosines of a unit vector $\bar{n}$. The J-integral has been increasingly used for characterization of the fracture of materials exhibiting elastic-plastic behavior at the crack tip and undergoing general yielding in the uncracked ligament before fracture. Since the early work of Begley and Landes [22] who measured the J-integral using the definition

$$J = \frac{1}{B} \frac{\delta U}{\delta a} \tag{2.13}$$

where B is the specimen thickness, U is the potential energy to fracture, and a is the crack length, several methods for determination of the J-integral have been proposed. These methods have evolved considerably in the past decade. Among

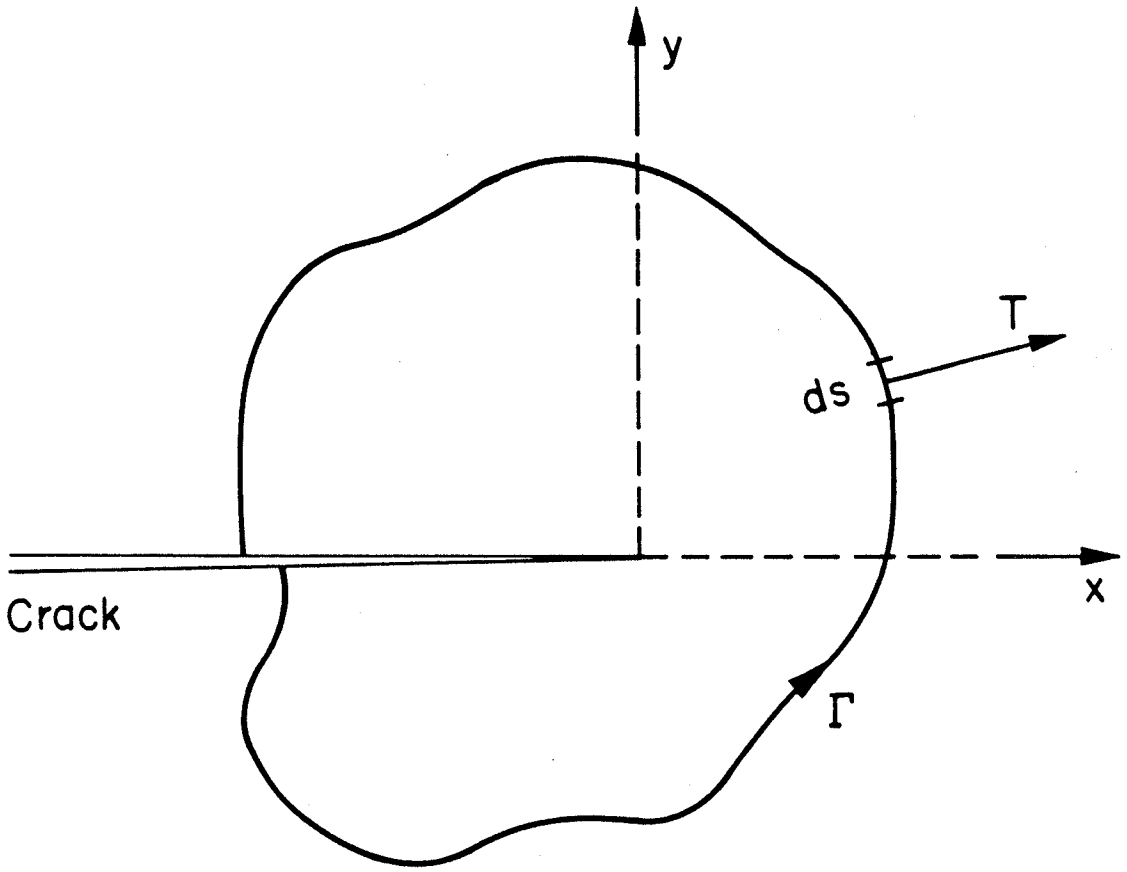

Figure 2.5 J-Integral.

the various methods for its measurement are the analysis of Rice et al [23] for determination of J using the equation:

$$J = \frac{2U}{Bb} \tag{2.14}$$

where U is the area under the load load-point displacement curve at the point of J evaluation and b is the length of the ligament, this equation allows measurement of J using a single specimen provided that the crack length is large enough to create bending loading on the remaining ligament. Equation (2.14) was modified by Merkle and Corten [24] to:

$$J = \frac{2U(1 + \alpha)}{Bb(1 + \alpha^2)} \tag{2.15}$$

where α is the Merkle and Corten correction factor for the tension component of stress in the compact tension specimen. Other studies on determination of the J-integral include that of Lanteigne et al [25] where J was determined under prescribed loading using a plastic zone correction at the crack tip, the A-C potential drop technique developed by Marandet and Sanz [26] and used by Nguyen-Duy and Philippeau [27] among others to detect the point of stable crack growth in steels.

Presently the most common method for evaluation of the J-integral is based on the J-resistance curve. The critical J-integral value J_{IC} is determined from the intersection of the crack blunting line whose slope is given by $2\sigma_o$ where σ_o is the flow stress, taken as the average between the yield strength and the ultimate tensile strength of the material tested, and the crack advance line, where the

J vs Δa is determined from equations (2.14) or (2.15) using partial unloading steps and measuring the change in the compliance of the specimen due to propagation of the crack. In this case, the change in compliance is related to the crack advance by

$$\Delta a = \frac{b}{2} \frac{\Delta c}{c} \cdot g\ (a/w) \qquad (2.16)$$

where c is the compliance, Δc is the change in compliance and g (a/w) is a function of geometry of the specimen. Such procedure allows determination of the J-integral from a single specimen using a data analysis procedure [28] which can be automated using a minicomputer or a microprocessor unit to produce plots of J-resistance curve. Presently, a standard test method for evaluation of the J-integral is available as an ASTM E813-81 specification. Illustration and diagramatic details for J-integral R curve technique are shown in Fig. 2.6.

The effect of material and geometrical variables on the J-integral criterion has been investigated. Namely, Munz [29] has studied the effect of thickness while Penelon et al [30] have studied the effect of specimen size, loading condition (prescribed load vs prescribed displacement) and alloy content on the J-integral in welded HSLA steels. The effect of prior deformation on J-integral has been studied by Amouzouvi and Bassim [31]. Generally, it was found that such parameters have a marked effect on the measured value of J_{IC}.

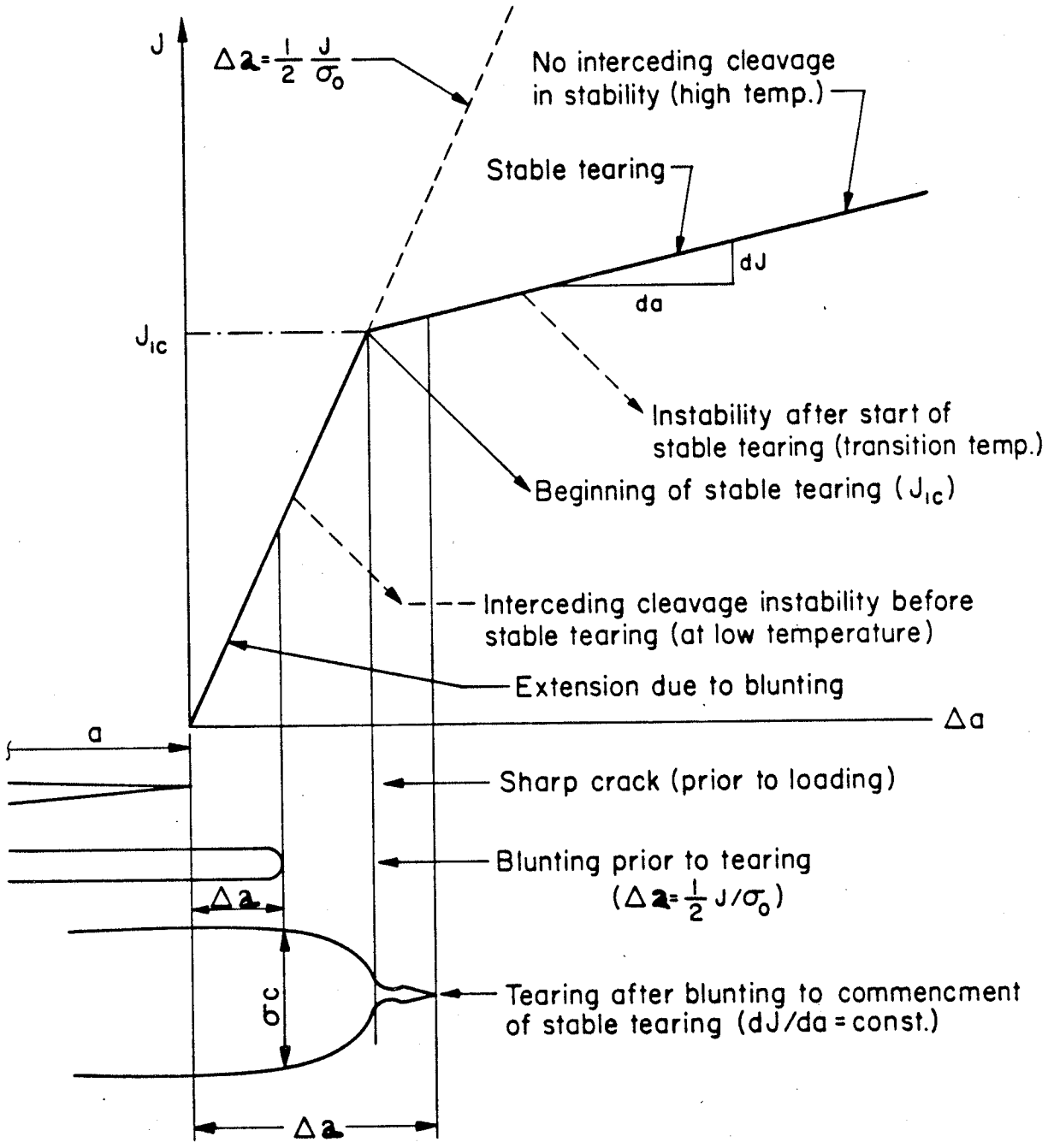

Figure 2.6 Illustration and diagramatic details for J-integral R curve technique.

2.3 Ductile Fracture Mechanisms:

Fibrous fracture is the most frequently observed ductile failure mode. In an overwhelming number of publications, cup and cone fracture is analyzed with void initiation, void growth and void coalescence. In these phenomena, second phase particles play a dominant role and almost all microstructural analysis of ductile fracture have been in defining this role. Most efforts were aimed at (i) the immediate processes leading to void initiation and (ii) an understanding of void growth and void coalescence which results in final separation.

2.3.1 Void Nucleation

The study of void initiation has received considerable attention during the past decade. An overview by Goods and Brown [32] in 1979 covers some of the earlier material, including the nucleation of voids at grain boundaries. From the reviewed results, it can be concluded that, in the case of rather large, widely spread inclusions, a continuum mechanics approach can be used to estimate the stresses and strains inside the inclusions and in the neighboring matrix when the material is plastically deformed. It is generally assumed that the initiation of cavities from inclusions takes place when either the inclusion or the matrix-inclusion interface is subjected to a critical normal stress. The determination of the local stresses and strains as a

function of the macroscopic stresses and strains applied on the material follows the model of Eshelby [33] which has been used by Tanaka et al [34]. This theory, which is based on an elastic analysis, is strictly valid only when the applied strains are not too large. In the case where cavity initiation takes place after large plastic strains, Argon et al [35] have found that the interface stress normal to the inclusion matrix interface σ_{rr} is given by

$$\sigma_{rr} = Y\left(\bar{\varepsilon}^{p}\right) + \sigma_{m} \qquad (2.17)$$

where $Y\left(\bar{\varepsilon}^{p}\right)$ is the flow stress in the region of the inclusion, σ_{m} is the mean stress for void nucleation and $\bar{\varepsilon}^{p}$ is the mean plastic strain.

Experimental determination of σ_{rr} at room temperature [36] yields a value for Fe_3C particles in spherodized 1045 steel $\left(Y \simeq 860 \text{ Mpa } (125 \text{ ksi})\right)$ of σ_{rr} equal to 1670 MPa (242 ksi). Generally, the value of σ_{rr} for different materials range between 0.008 and 0.009E.

A model based on careful measurements of void nucleation in spheroidized steels was developed by Fisher and Gurland [37,38]. Their approach includes a detailed assessment of the energy stability of the particle-void system followed by a calculation of the debonding stress. Recently, LeRoy et al [39] attempted to take into account the reasonable expectation that the void nucleation and void growth are not sequential processes but, after the first

voids had been nucleated, void nucleation and void growth would take place simultaneously. The non-sequential nature of void nucleation and void growth is not limited to steels but certainly is a general phenomenon. This point has been made recently by Neumann [40] who indicated that the deformation of an internally necked-down ligament between voids could produce additional voids.

It is worth noting that the strain necessary to nucleate cavities is small as compared with the strain at failure, since nucleation strain represents less than 15% of the fracture ductility even in a conventional tensile test [41].

2.3.2 Void Growth and Coalescence

Next to void initiation, research on fibrous fracture has largely been concerned with void growth. Approaches from a microstructural viewpoint have been reviewed by Rosenfield [42]. Extensive treatments in those years came from continuum theory through the work of McClintock [43] and of Rice and Tracey [44]. In addition, Thomason [45] studied the internal necking process between cavities in a rigid-plastic non-hardening matrix, while Berg [46] published the results of an investigation on the growth of cylindrical voids in a viscous material which was extended by McClintock et al [47] for hole growth in shear bands. Work-hardening and interaction effects were taken into account by Tracey [48] whose results show that void interactions lead to a

significant acceleration of growth and that cylindrical voids lying transverse to the stress axis in a bar will have larger growth rates than voids with their long dimension parallel to the axis. Agreement exists also for the conclusion of Tracey regarding the effect of work hardening and those of Rice and Rosengren [49], namely that stress triaxiality rises with increasing work hardening exponent and that the flow stress will be increased together with the stress state.

Microstructural investigations on void growth and coalescence have been less frequent than the continuum mechanics calculations. For the two dimensional void growth model, McClintock [50] obtained an equation for void coalescence strain of the form:

$$\bar{\varepsilon}_{c,\alpha,\beta=o} = \frac{(1 - n)\ell n\ v_f^{-1/3}}{\sinh[(1 - n)(\sigma_1 + \sigma_2)/2\sigma_o/(3)^{1/2}]} \qquad (2.18)$$

where v_f is the volume fraction of the voids, σ_1, σ_2 are the applied stresses, n is the strain hardening exponent, and σ_o is the flow stress.

Examination of equation (2.18) shows that, for a given material and constant stress state, the principal influence on $\bar{\varepsilon}_{c,\alpha,\beta}$ is the void density v_f. For a typical BCC material, a coalescence strain between 0.01 and 0.5 depending on the stress state ahead of the crack, is expected [51].

2.4 Effect of Temperature and Loading Rate on Fracture Toughness

For materials with strong temperature and strain rate dependence, the fracture toughness usually decreases with decreasing temperature and increasing loading rates. Thus, it is desirable, from a practical point of view, to evaluate experimentally the fracture toughness in the regions where it may show its minimal value.

2.4.1 Temperature Effect

Considerable effort has been undertaken in recent years for characterization, both from macroscopic and microstructural aspects, of the fracture toughness of metallic materials. Particularly, research has recently aimed at development of criteria for these materials which accurately describe their behavior as a function of testing temperatures [52,53]. Because of the strong dependence of the mechanical properties of BCC metals with temperature, their fracture toughness will be greatly influenced by variation in temperature, particularly in the transition region where the behavior changes from brittle (cleavage) fracture to ductile fracture. The temperature effect on toughness is currently obtained from impact testing methods using Charpy and other tests. Empirical correlations between K_{IC} and temperature are given in Ref. [54] while other analytical equations relating K_{IC} and temperature are summarized in Table 2.1.

TABLE 2.1

Methods for the estimation of the temperature dependence of K_{IC}

Method and Reference	Equation
1. Krafft and Sullivan [58]	$K_{IC} = M\,\sigma_y^{-1.5}$
2. Krafft [59]	$K_{IC} = E\,n\,(2\pi d_T)^{1/2}$
3. Irwin et al [60]	$K_{IC} = \frac{\sigma_y(T_o)}{\sigma_y} \cdot K_{IC}(T_o)$
4. Hahn and Rosenfield [61]	$K_{IC} = (\frac{2}{3} E\,\sigma_y n^2 \varepsilon_{ft})^{1/2}$
5. Hahn et al [62]	$\frac{\sigma_{fc}}{\sigma_y} = \alpha^* (\frac{K_{IC}}{\sigma_y})^{\beta^*}$
6. Malkin and Tetelman [63]	$K_{IC}(\rho) = 2.89\,\sigma_y[\exp(\sigma_{fc}/\sigma_y - 1) - 1]^{1/2} \cdot \rho^{1/2}$
7. Sailors and Corten [64]	$K_{IC} = 2C\,H\sigma_y[n\varepsilon_{ft}]^{1/2}$
8. Schwalbe [65]	$K_{IC} = \frac{\sigma_y}{1-2\nu}\,[\pi(1+n)2\lambda_c\varepsilon_{ps}(\frac{E}{\sigma_y})^{1+n}]^{1/2}$
9. Weiss and Sengupta [66]	$K_{IC} = 0.34\,[S\rho^*]^{1/2} \cdot \bar{\varepsilon}_{d,\alpha=1,\beta=0}$
10. Hahn and Rosenfield [67]	$K_{IC} = [2\sigma_y E(\frac{\pi}{6})^{1/3} D_i]^{1/2} \cdot f_c^{1/6}$
11. Kotilainen [54]	$K_{IC} = K_o + K\,\frac{[\sigma_u + [\sigma_y(o) - \sigma_u]\,e^{-mT}]}{\sigma_\theta}$

Where:

M = constant
σ_y = yield strength
E = modulus of elasticity
n = strain hardening exponent
d_T = process zone
T_o = critical temperature
ε_{ft} = tensile fracture ductility
α^*, β^* = empirical constant
$\alpha = \sigma_2/\sigma_1$
$\beta = \sigma_3/\sigma_1$
$\bar{\varepsilon}_{f,\alpha\beta}$ = effective fracture strain for complex stress state
K, K_o = constant
σ_u = temperature independent part of the yield strength
σ_{fc} = cleavage fracture strength
ρ = the notched root radius
C, H = modification parameters
λ_c = spacing of cracked particles
ε_{ps} = plane-strain ductility
$S\rho^*$ = Neuber particle parameter
D_i = initial particle size
f_c = fraction of cracked particles
$\sigma_y(o)$ = yield strength at 0°K
m = constant
T = absolute temperature
σ_θ = Temperature dependent part of yield strength
ν = Poisson's ratio

In cleavage fracture, the starting point in the analysis of the effect of temperature is the plastic zone at the crack tip. Using the stress concentration inside the plastic zone, it has been possible to calculate a microstructural length X_o over which the stress has to exceed the critical cleavage fracture strength σ_{fc} needed to fracture the material [55]. Cleavage fracture is estimated by assuming that the cleavage fracture stress σ_{fc} is equal to the yield stress at T = 0, namely σ_y (0) [54]. The specimen breaks when the maximum stress σ_{yy}^{max} at the tip of the crack has reached the cleavage fracture stress, or $\sigma_{fc} = \sigma_y(0) = \sigma_{yy}^{max}$.

For elastic-plastic fracture behavior, the predominant parameter for its characterization is presently the J-integral [56]. Its temperature dependence has been investigated. Generally, it was found that J_{IC} increases as a function of temperature. The shape of the J_{IC}-temperature curve seems, however, to vary depending on the procedure for determination of J_{IC}. Thus, Bassim and Mikhail [57] found that, if J_{IC} was determined at the point of maximum load in deep cracked specimens, the variation of J_{IC} with temperature can be described by the intersection of two straight lines defining a transition between completely linear elastic behavior and elastic-plastic behavior. Also, such transition depends on the rate of application of the

load (quasi-static versus impact). Other investigators report different tendencies where J_{IC} reaches a maximum at a certain temperature followed by a plateau of J_{IC} as temperature is further increased [68]. Such curves still define, to a lesser degree, this transition temperature described earlier. Other investigators have determined J_{IC} under quasi-static as well as dynamic loading conditions as a function of temperature in Charpy-size specimens for the purpose of development of an inexpensive and simple approach for measurement of J_{IC} in engineering materials [26,69].

2.4.2 Loading Rate Effect

Recently, the analysis of dynamic fracture and crack propagation problems under high loading rates has become of significant importance in materials research.

Although the recognition of dynamic effects in the fracture process dates back over 100 years [70,71], in comparison to fracture propagation under quasi-static loads, the behavior of cracks under dynamic loading conditions has received much less attention. A measure of comparison may be obtained by comparing the number of pages devoted to dynamic fracture and to fracture in quasi-static situations in the seven volume comprehensive treatise on fracture [72]. The discussions on quasi-static fracture outdo those on dynamic problems by a ratio of about 4600:120 based on page count. There are several reasons for this uneven distribution of effort, foremost among which is that there are of course many more structures designed to support quasi-static loads than dynamic ones. But beyond this, a convincing deterrent is the analytical complexity adhering to most dynamic crack analyses. The experimental aspects of the problem are also burdened by complications. Studies of dynamic crack propagation require both loading and measuring techniques which are not readily achievable with commercially available facilities. Moreover, the requisite experimental apparatus is complex and its development constitutes usually a heavy investment of time before experiments can begin.

An important earlier contribution to the field of dynamic loading is that due to Krafft [59] who through his testing of mild, medium and high strength steels over a range of temperatures and loading rates, was able to obtain a correlation between the stain hardening exponent and the plane strain fracture toughness K_{IC}.

When the fracture process can be described as linear elastic event, it is possible to define a $\dot{K}_I$ parameter, which is frequently used to characterize how fast the crack tip region is loaded. $\dot{K}_I$ is given as:

$$\dot{K}_I = K_{IC}/t_c \qquad (2.19)$$

where K_{IC} is the critical stress intensity factor in mode I (plane strain fracture toughness), and t_c is the time interval from the start of loading to the point when the critical state of the crack is achieved, that is, when the crack starts to propagate. It is obvious that the loading rate parameter $\dot{K}_I$ may be changed over several orders of magnitude mainly due to changes in loading time t_c. Consequently, the $\dot{K}_I$ spectrum can be constructed. It is assumed that the value of $\dot{K}_I^o$ = 1 MPa$\sqrt{\text{m}}$ s^{-1} constitutes the static value [73]. Accordingly the following ranges of $\dot{K}_I$ are recognized.

(a) 1 MPa $\sqrt{\text{m}}$ s^{-1} $\leq \dot{K}_I \leq$ 10^3 MPa $\sqrt{\text{m}}$ s^{-1}; quasi-static loading with a closed-loop static-dynamic testing machine.

(b) 10^4 MPa $\sqrt{\text{m}}$ s^{-1} $\leq \dot{K}_I \leq$ 10^5 MPa $\sqrt{\text{m}}$ s^{-1}, instrumented hammers as, for example, instrumented Charpy.

(c) 10^6 MPa $\sqrt{m}\ s^{-1} < \dot{K}_I < 10^9$ MPa $\sqrt{m}\ s^{-1}$, stress wave loading.

In the early experimental studies [58,74], it was shown that about an order of magnitude increase in loading rate $\dot{K}_I$ is required to decrease K_{IC} by 10%. It may be mentioned that the newer, instrumented pre-cracked Charpy test provides more accurate results for K_{IC} over the range of loading rates 10^4 MPa $\sqrt{m}\ s^{-1} < \dot{K}_I < 10^5$ MPa $\sqrt{m}\ s^{-1}$. However, the major difficulty with this technique is the method of measurement for determining the critical fracture load. Due to the lack of a detailed understanding of the inertia forces, together with the wave mechanics in the Charpy specimen, the test leads to difficulties in interpreting the resulting oscillograms. Even if such difficulties could be overcome, there is a limitation on the loading rate parameter $\dot{K}_I$. In addition, the conditions of plane strain are not usually present in the prefatigued Charpy specimen.

Recently an experimental method has been employed [75-77] to obtain fracture toughness data with loading rates in excess of 10^6 MPa $\sqrt{m}\ s^{-1}$. In those experiments, the notched and pre-fatigued section of a long bar specimen is loaded to failure by the rising portion of an incident tensile wave, resulting from the detonation of an explosive charge placed at a properly shaped loading end of a bar. Essentially, this technique is an adoption of the Split

Hopkinson pressure bar [78]. An experimental method was described for measuring the fracture properties of metals and alloys over a wide range of loading rates [79], which can cover over six orders of magnitude in $\dot{K}_I$. Wedge loaded compact tension specimen (WLCT) was used [79,80] for quasi-static testing and dynamic testing using a special arrangement of the Split Hopkinson pressure bar. Experiments performed on some aluminum alloys enabled K_{IC} to be plotted as a function of $\dot{K}_I$ over a wide range of loading rates. In general, a substantial decrease in fracture toughness K_{IC} was observed under impact loading for the strain rate sensitive alloys [79-81].

2.5 Dependence of Fracture Toughness on Ductility

Considerable effort has been made to correlate a material fracture toughness with its uniaxial tensile properties. The key ingredients to most of these approaches are a critical crack tip strain and a length parameter. The former is related to the fracture ductility, usually obtained on smooth tension specimens [61]. Although some of these approaches give useful correlations, the use of the uniaxial tensile fracture ductility must be questioned for several reasons; due to plastic instability the stress state in a tension test changes as a function of strain [82]; tensile fracture ductility itself depends on the section size, and the stress state near the crack tip is multiaxial [83].

In order to avoid this complexity some researchers have employed a "plane-strain tension specimen" as proposed by Clausing [84]. However, even there, necking may occur under certain experimental conditions [85,86], thereby altering the stress state in the course of a test. Based on these considerations, Weiss proposed the use of equibiaxial fracture ductility or bulge ductility, for correlation with fracture toughness based on LEFM [87]. The bulge ductility is considered to offer the most promising measure of the material ductility to correlate with its fracture toughness. The reason for this is that for most materials of medium and high strength, fracture in the bulge test occurs prior to the onset of necking or instability. Bulge testing is relatively simple. A variety of bulge test configurations are illustrated in Fig. 2.7. These are the hydraulic bulge tests Fig. 2.7a, the bulge test on a specimen geometry suggested by Azrin and Backofen [88], Fig. 2.7b, and a further modification of the Azrin-Backofen geometry Fig. 2.7c. The effective fracture strain is determined from measurement of the change in thickness during the test and is given by:

$$\bar{\varepsilon}_{F,\alpha=1,\ \beta=0} = \ln t_o/t_f \qquad (2.20)$$

where $\alpha = \sigma_2/\sigma_1$ and $\beta = \sigma_3/\sigma_1$ where σ_1, σ_2 and σ_3 are the principal stress components.

The experimental results obtained for high strength steels show a linear relationship between effective bulge

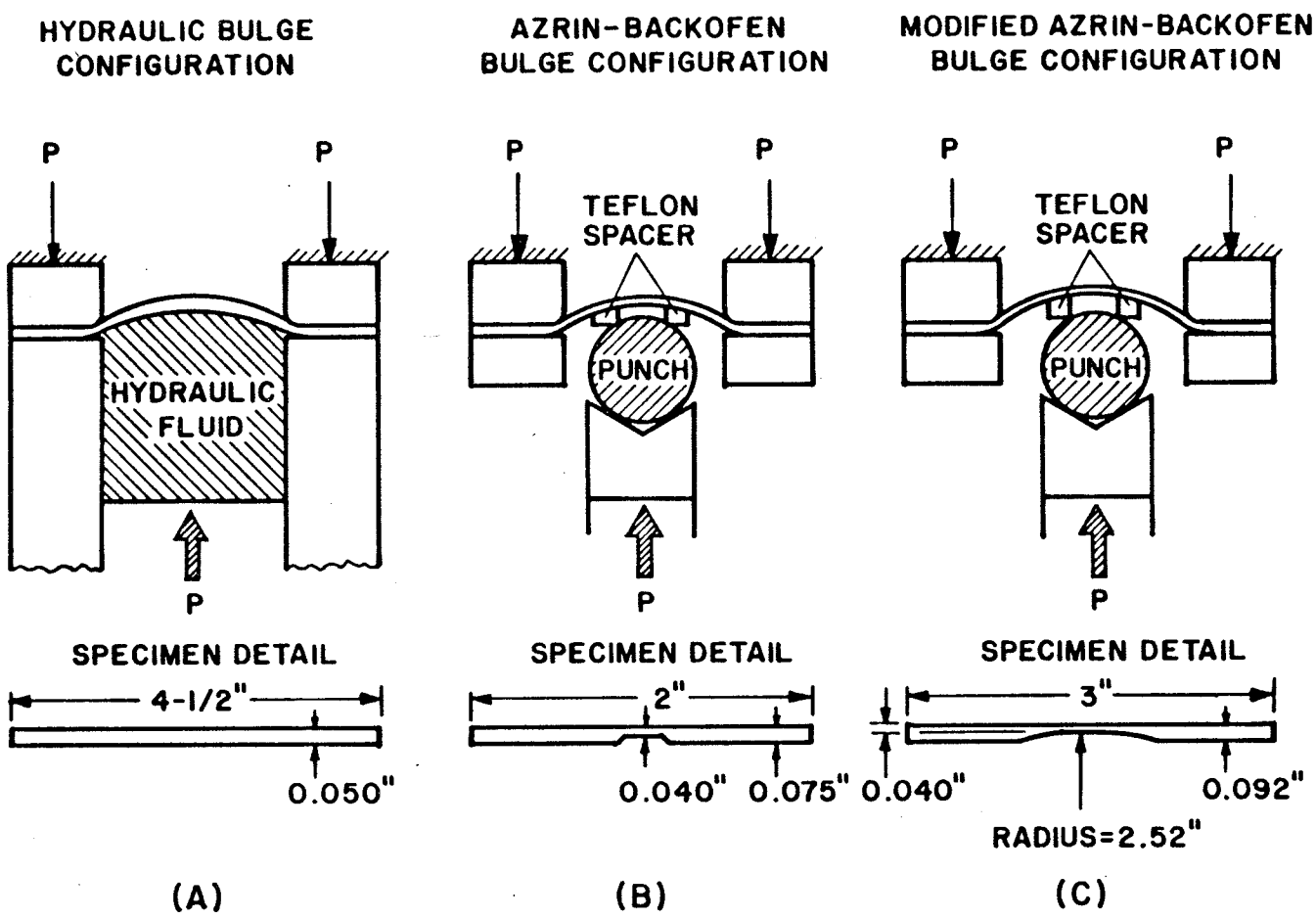

Figure 2.7 Bulge fixtures for equibiaxial ductility test.

ductility and plane strain fracture toughness K_{IC} with a scatter of about 30% [51]. The bulge ductility was correlated analytically with K_{IC} and G_{IC} using an equation of the form:

$$G_{IC} = S\rho^* \, (0.279)^{2/n} \, \bar{\varepsilon}_{f,\alpha=1,\ \beta=0} \cdot f(E,K,n,\bar{\varepsilon}_y) \qquad (2.21)$$

where S is the shape factor characterizing the geometry of the plastic zone, taken as equal to 1.0, ρ^* is Neuber's microsupport effect constant $\cong$ 0.025 mm (0.001"), $\alpha = \frac{\sigma_2}{\sigma_1} = 0.81$ and $\beta = \frac{\sigma_3}{\sigma_1} = 0.61$ for plane strain, n is the strain hardening exponent, E is the modulus of elasticity and $\bar{\varepsilon}_y$ is the yield strain = σ_y/E.

The relation between ductility and toughness in materials which show elastic-plastic behavior at the crack tip and hence has a large plastic zone size has not been quantitatively studied. The use of the J-integral as a fracture criterion for those materials is strongly dependent on their ductility and a study relating J with inherent ductility is hence of great importance.

2.6 Summary

The contents of this chapter review some of the major developments in the field of fracture mechanics. Initially, linear elastic fracture mechanics, based on Griffith analysis, has led to a definition of a single parameter for

describing the stress state at the crack tip, namely the critical stress intensity factor K_{IC}. Several criteria have been suggested for elastic-plastic behavior, the most important of those is the J-integral. The mechanisms of ductile failure in terms of void nucleation, void growth and void coalescence have been reviewed and the relation between fracture toughness and temperature, on one hand, and between fracture toughness and ductility, on the other hand, have been presented. It is shown that a quantitative assessment of the relationship between fracture toughness, ductility, temperature and loading rate is lacking. This present study attempts to address this problem both experimentally and theoretically.

CHAPTER 3

EXPERIMENTAL PROCEDURES

3.1 Material

An AISI 1045 steel plate, with 12.5 mm in thickness, 75mm in width and 4 m in length was used. The chemical composition of the steel is given in Table 3.1. The heat treatment of the plate after cutting it into short pieces was to anneal at 790°C for 30 min. at temperature. The resulting hardness of the material was R_C 15. As shown in Fig. 3.1, the material had a lamelar pearlite structure surrounded by a network of ferrite.

3.2 Charpy Impact Testing

Standard Charpy impact (CVN) test specimens were machined from the annealed plate with the notch in the Longitudinal-Transverse (L-T) orientation. Tests were performed at temperatures from -100°C to 100°C in accordance with recommended practice ASTM E23-72. The transition temperature region was determined from this test and was found to be between -60°C and 25°C.

3.3 Tensile and Bulge Ductility Testing

Tensile tests were performed on flat tensile specimens with the tensile axis along the rolling direction and having a width of 6.5 mm and a thickness of 3 mm according to ASTM specification E-8. The crosshead speed during the tensile

TABLE 3.1

Chemical composition of 1045 steel. (Weight percent)

C	Mn	P(max)	S(max)	Fe
0.43 - 0.5	0.6 - 0.9	0.04	0.05	balance

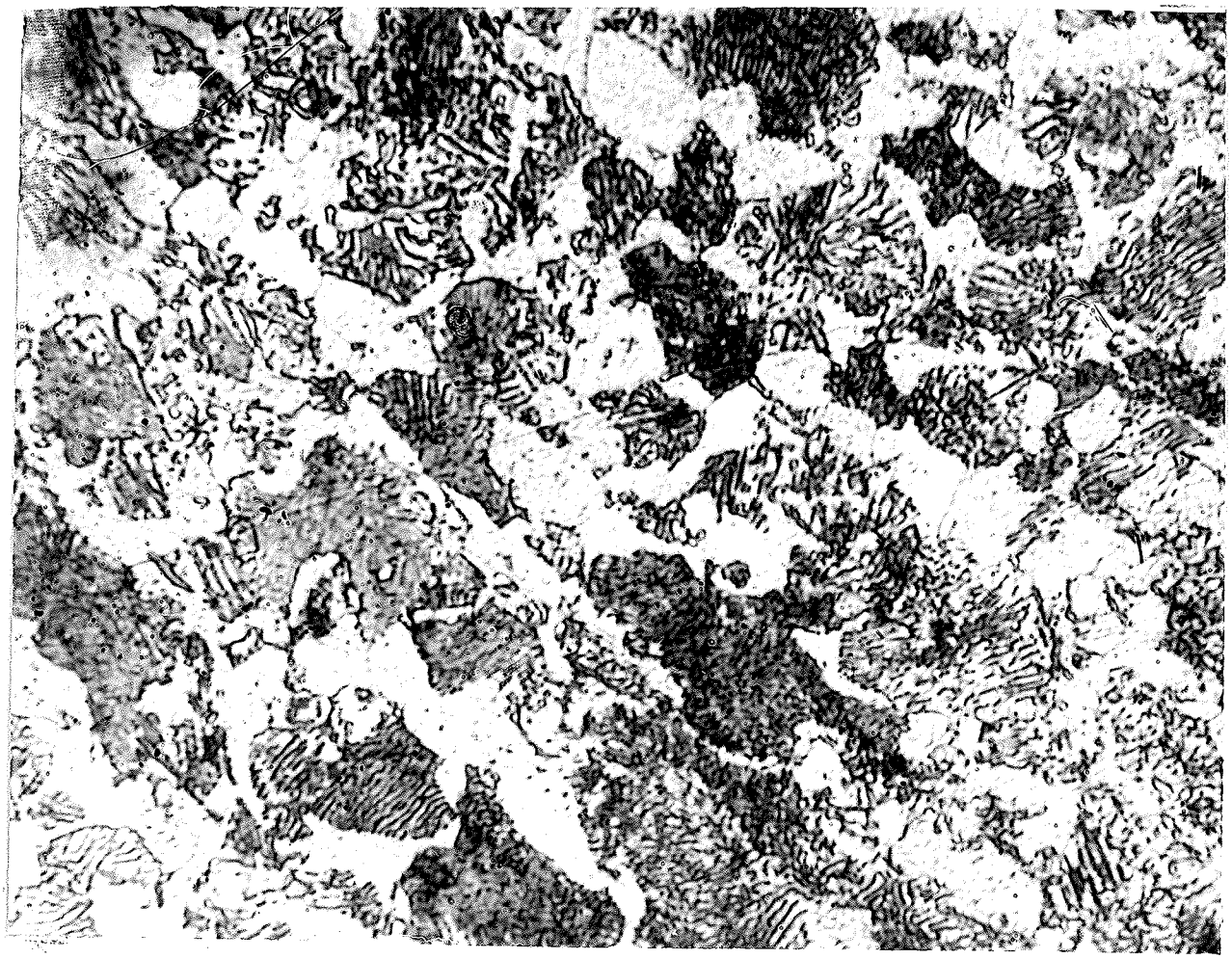

Figure 3.1 Microstructure of 1045 steel in the annealed condition (1040 X)

testing was 0.5 mm/min for all tests. Tests were performed over the transition temperature range. The yield stress at 0.2% offset σ_y and the ultimate tensile strength σ_u were determined and the flow stress σ_o was calculated. The strain-hardening exponent n, the percentage elongation and reduction in area at fracture were also determined from these tests.

A bulge ductility set-up similar to that of Azrin and Backofen [88] was designed and constructed. Such a set-up for the test is described in Fig. 3.2. Bulge ductility specimens with the dimensions shown in Fig. 3.3 were machined from 12.5 mm thick plate using multipass hot rolling processes to obtain 1.9 mm (0.075") thickness and then followed by normalizing and annealing to obtain a Rockwell-C hardness of 15 (the same hardness as the other specimens for simple tension, CVN, and fracture tests). A specially made template was used to drill the holes in the specimen and a jig was used to machine the reduced area.

The bulge ductility tests were performed over the transition temperature range. The required temperature was obtained by immersing all the equipment in a mixture of alcohol and liquid nitrogen and the temperature was adjusted using a thermocouple located on the specimen. The bulge ductility equibiaxial fracture strain defined as $\ln t_o/t_f$ was determined, where t_o is the initial thickness and t_f is the thickness at fracture provided that necking does not take

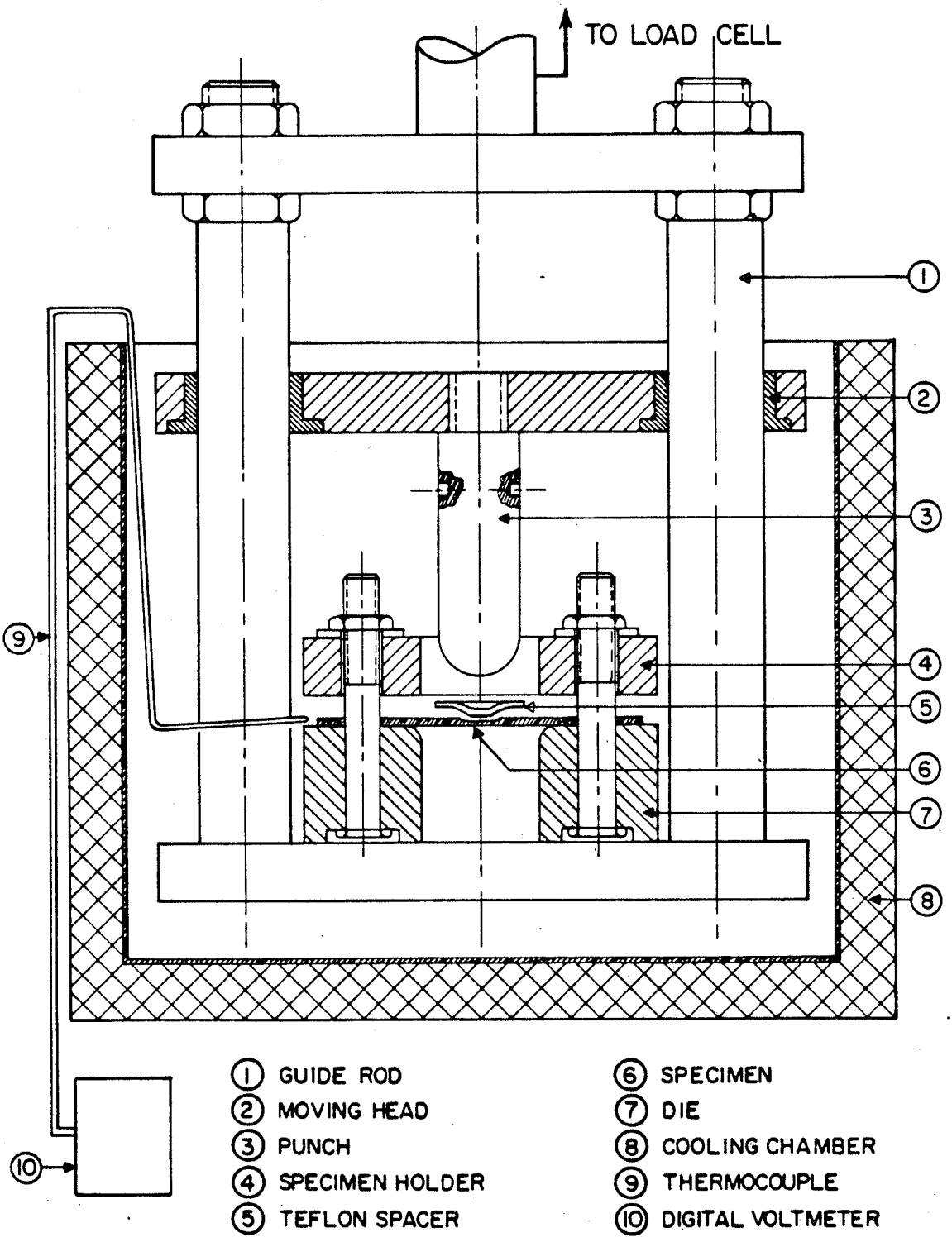

Figure 3.2(a) Experimental set-up for bulge ductility.

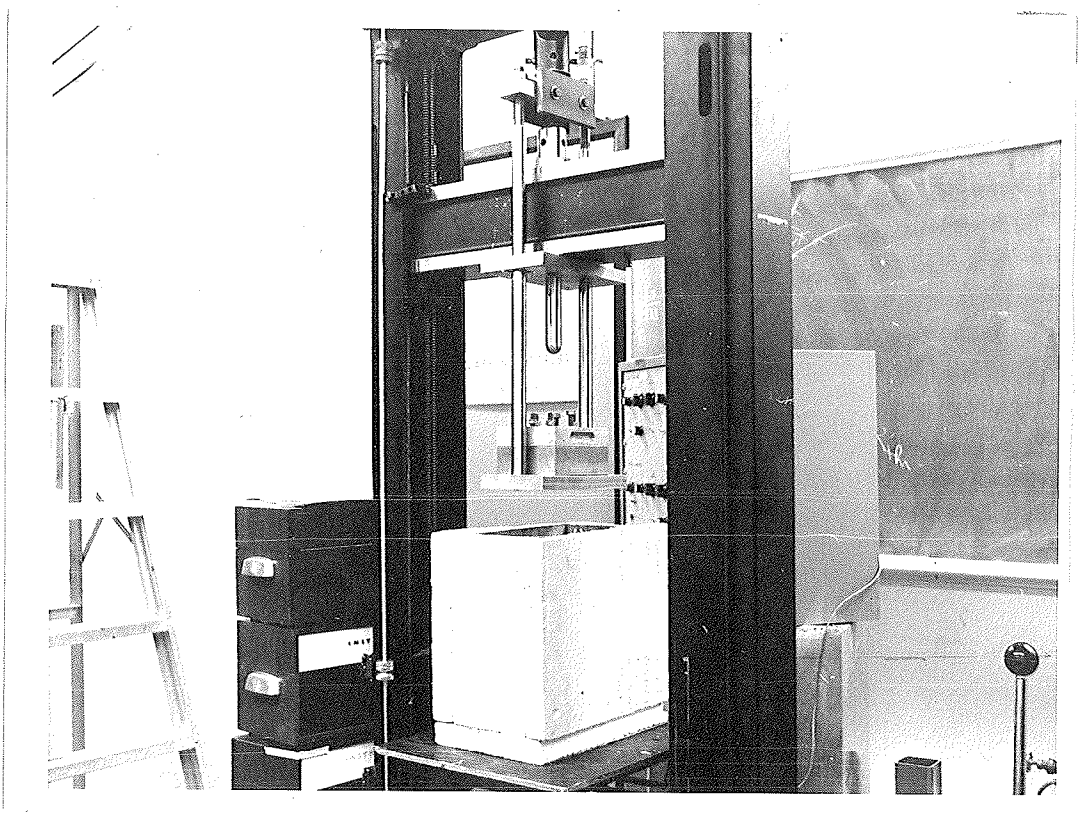

Figure 3.2(b) A photograph for the bulge ductility set-up.

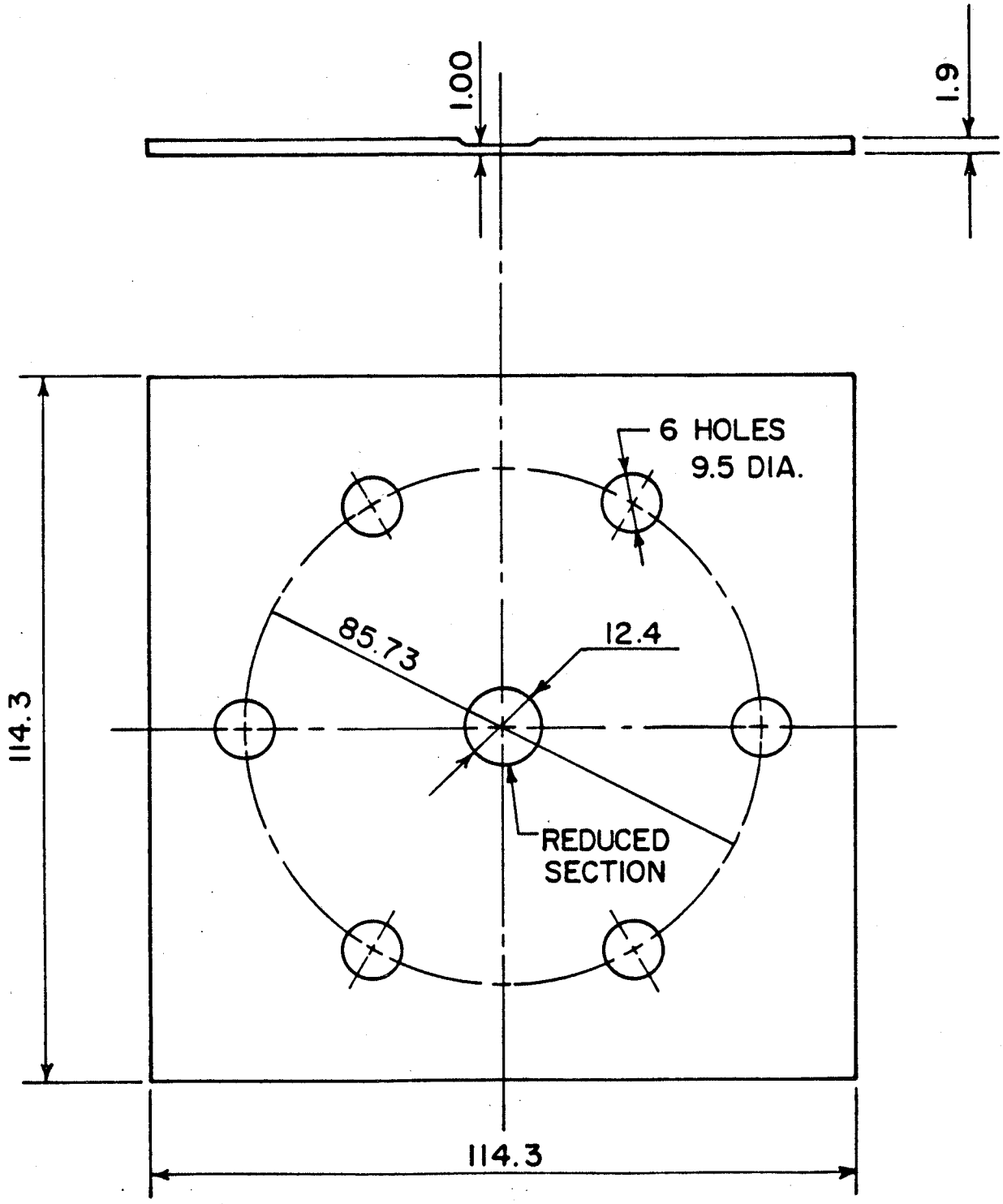

Figure 3.3 Geometry and dimensions of bulge ductility specimen (dimensions are in mm).

place before fracture. All the tests were carried out at a cross-head speed of 0.5 mm/min.

3.4 Fracture Toughness Testing

Standard 3-point bend specimens, 12.4 mm thick, were produced from the annealed pieces. A notch was machined in the longitudinal-transverse (L - T) orientation. All the 3-point bend specimens prepared had the same thickness (12.4 mm). The specimens were fatigue precracked, at room temperature, according to the ASTM specification for Plane-Strain Fracture Toughness of Metallic Materials (E399 -78) to crack length $\frac{a}{w} = 0.57$. For the last 50% of fatigue precrack extension, the K_{max} (maximum stress intensity factor) was kept below 15 MPa $m^{1/2}$. Fracture tests were carried out in the same range of temperature as for tensile and bulge ductility tests. The required temperature was attained by controlling the liquid nitrogen spray in a cooling chamber around the specimen. The detection of specimen temperature was obtained using a thermocouple located on the specimen and connected with a digital voltmeter. The temperature was maintained within ± 2.0°C during each test.

All fracture tests were performed with a hydraulic Instron (Model 1320) testing machine, according to the plane-strain J_I-resistance curve test procedure [89]. For purposes of J_I computation, the load line displacement was measured

remotely using the actuator transducer while for Δa computation, the displacement gage used was an E-399 standard COD gage attached to razor blade-knife edges fixed at the front face of the notch to measure the crack mouth opening displacement.

The errors which may be introduced in the load-load line displacement curves due to elastic compression of the jig with increased load as well as the indentation of the test specimen at the load application points were corrected by performing the same type of tests on unnotched specimens. All fracture tests were performed at controlled displacement with a constant testing speed of 0.25 mm/min. The load - COD displacement and load line displacement were recorded on a 3-channel X-Y plotter. Fig. 3.4 shows a photograph of the set-up for fracture testing.

The J-integral was determined by the single specimen unloading compliance method, where a series of 10 percent unloadings are performed to cause the crack extension Δa during the fracture test. The changes in the slope of the linear portion of the load-displacement curve (i.e. the change in compliance) gives a measure of any change in crack length. An autographic method was used in the compliance measurements. The crack extension was calculated by using the relation developed by Joyce et al [90]:

$$\frac{a}{w} = 0.998265 - 3.81662\ U_x - 1.80596\ U_x^5 + 32.314\ U_x^3 - 44.1566\ U_x^4 - 52.6788\ U_x^5 \qquad (3.1)$$

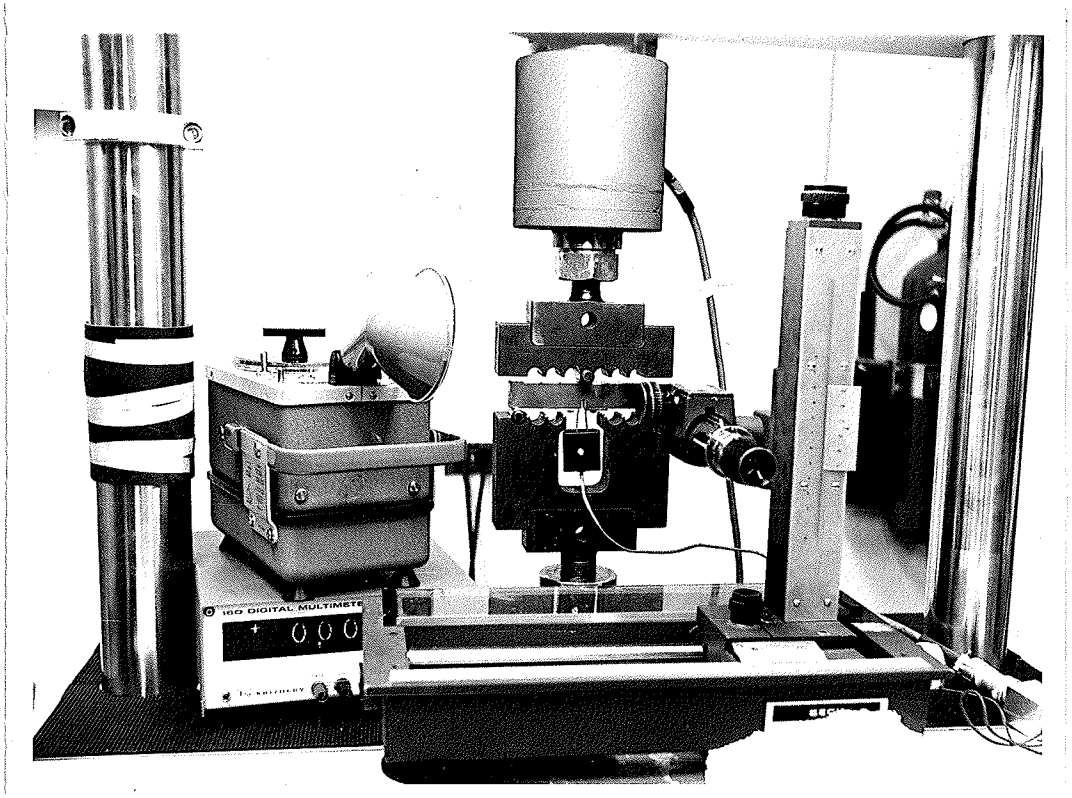

(a) Fatigue precracking set-up

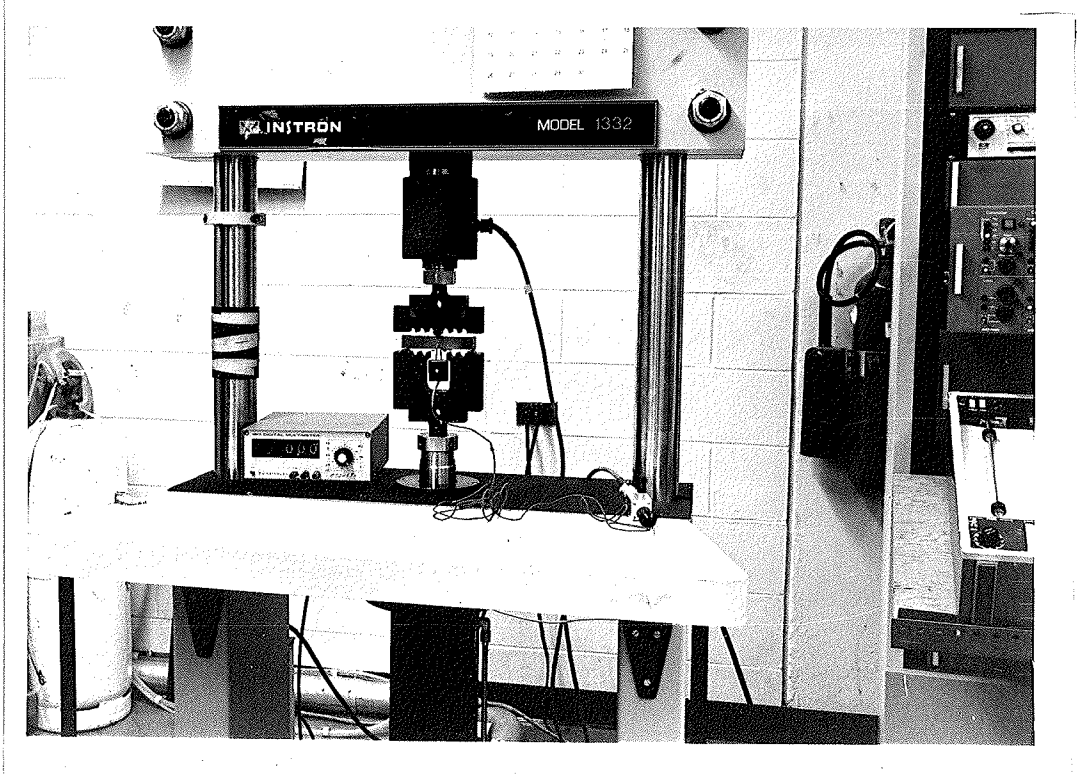

(b) Fracture Testing set-up

Figure 3.4 Photographs for fatigue precracking and fracture testing set-ups using standard three point bending specimens.

where

$$U_x = \frac{1}{\left[\frac{BWE\ \delta_x}{PS/4}\right]^{1/2} + 1}$$

$\frac{\delta_x}{p}$ is the specimen elastic compliance during unloading

δ_x is the crack opening displacement at the notched edge

B is the specimen thickness

E is the specimen elastic modulus

W is the specimen width

S is the specimen span length

The J-integral is given by:

$$J_{(i+1)} = \left[J_i + \left(\frac{\eta}{b}\right)_i \frac{U_{i,i+1}}{B}\right]\left[1 - \left(\frac{\gamma}{b}\right)_i (a_{i+1} - a_i)\right] \qquad (3.2)$$

where $\eta = 2$ for 3-point load specimens

$\gamma = 1 + (0.76)b/w$

$a_{i+1} - a_i$ = crack extension

$U_{i,i+1}$ = area under the load versus load line displacement between lines of constant displacement at points i and i+1.

The area under the load versus load-line displacement record was measured with a planimeter. J_i in equation (3.2) was calculated using equation (2.14).

A plot of J-integral versus crack extension Δa is constructed to obtain the crack advance line. The critical J-integral value J_{IC} is obtained at the intersection of the

experimentally constructed crack advance line and the blunting line defined by the relationship:

$$J = 2 \sigma_o \cdot \Delta a \qquad (3.3)$$

where σ_o is an arithmetic average of the yield stress and the ultimate tensile strength of the material.

The J_{IC} values at low temperatures where valid elastic K_{IC} region was obtained, were calculated using the equation:

$$J_{IC} = \frac{(1 - \nu^2) K_{IC}^2}{E} \qquad (3.4)$$

For each experimental point, at least two fracture tests were performed and an average was taken on the values obtained.

3.5 Quasi-Static and Dynamic Fracture Testing

3.5.1 Specimens and Wedges

The wedge loaded compact tension specimens configuration was used to study the effect of loading rate on fracture toughness parameter J_{IC}. It was tested both under quasi-static and dynamic loading conditions. The dimensions of this specimen are shown in Fig. 3.5. Wedges with an angle of 50° were machined from Atlas cold work steel type NN and used for fatigue precracking while wedges made of a titanium alloy (Ti-6Aℓ-4V) with an angle of 60° were used for both static and dynamic tests. Fig. 3.6 shows the force distribution for a WLCT specimen.

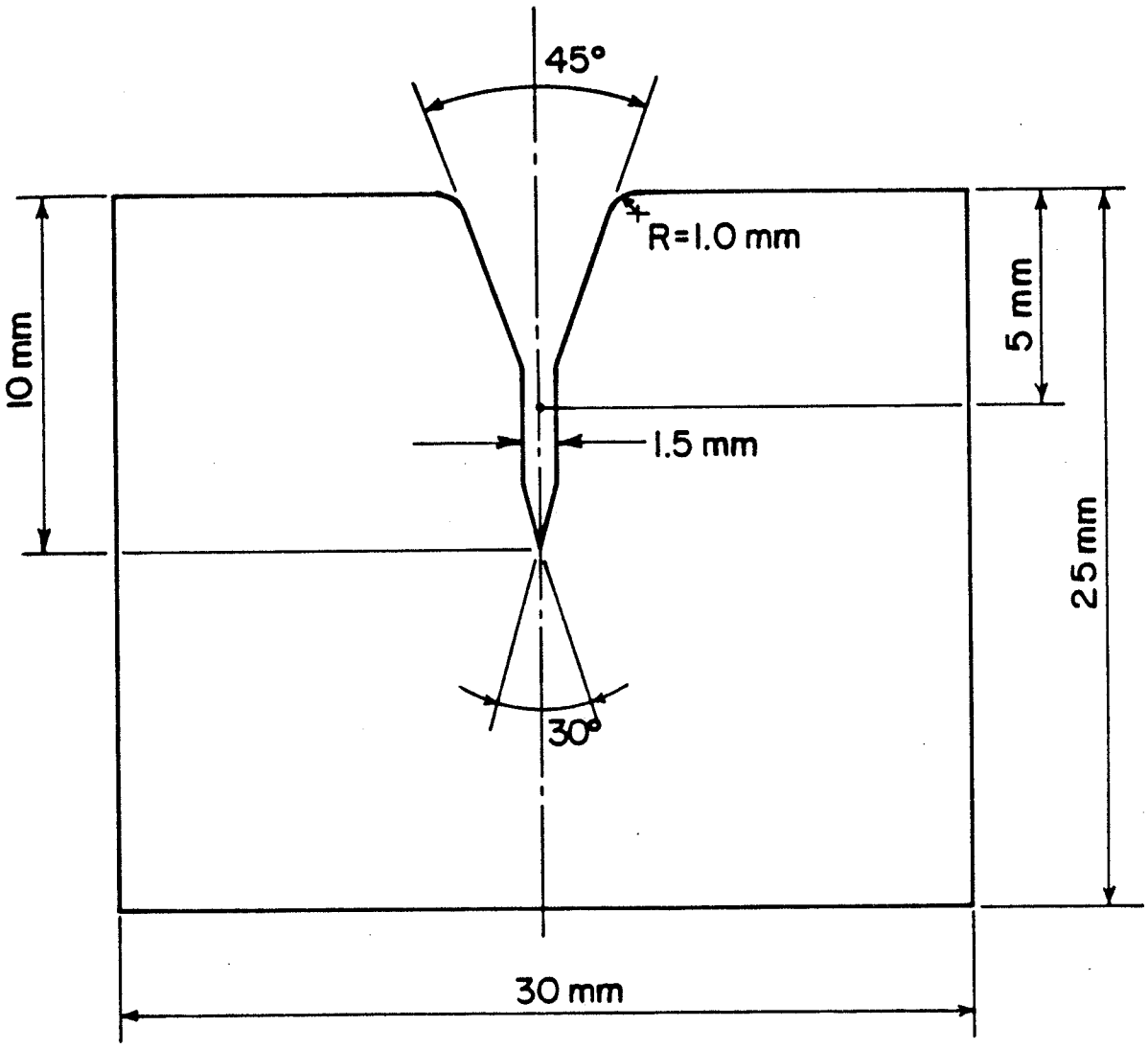

Figure 3.5 Geometry and dimensions of wedge loaded compact tension (WLCT) specimen.

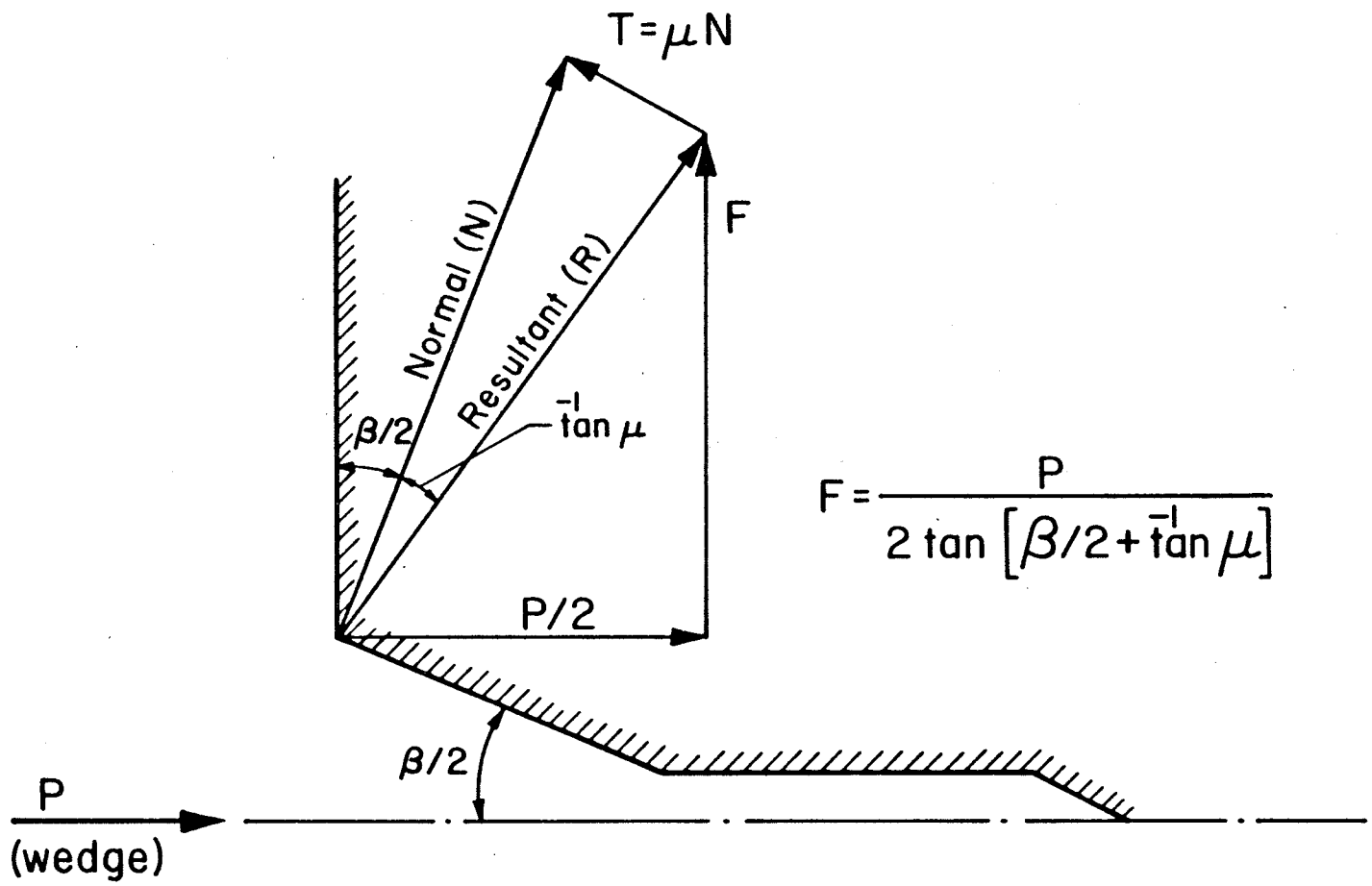

Figure 3.6 Force distribution for a wedge loaded compact tension (WLCT) specimen.

The experimental set-up shown in Fig. 3.7 was built to fit a standard closed loop testing machine. This set-up was used for fatigue precracking such that the load ratio R_s = 0.1, the frequency f = 40 HZ, and the fatigue crack length Δa = 3 mm.

3.5.2. Quasi-Static Experimental Testing

Fig 3.8 shows a schematic drawing of the quasi-static experimental arrangement while Fig. 3.9 shows a photograph of this set-up. The WLCT specimen is positioned on the support which is installed on the lower platten. The wedge is attached to the upper platten and the platten itself is fixed to the load cell. The load P versus linear displacement δ of the wedge is measured by two high resolution tranducers (DCDT) held by the lower platten. Calibration of the DCDT is obtained using fillers. This configuration allows for exact measurements of the movement of the lower platten with respect to the wedge. The lower platten is supported on the loading ram by a one-ball bearing to avoid any non-axial loading.

The specimen, its geometry, configuration and way of loading is based on the WLCT method proposed in [79] and [80]. The point of onset of crack propagation is determined by using a strain gage attached on the WLCT specimens very close to the front of the fatigue crack and connected to a bridge, a DC amplifier and X-Y-Y recorder. To minimize the friction effect, the wedge surfaces and the angular incision

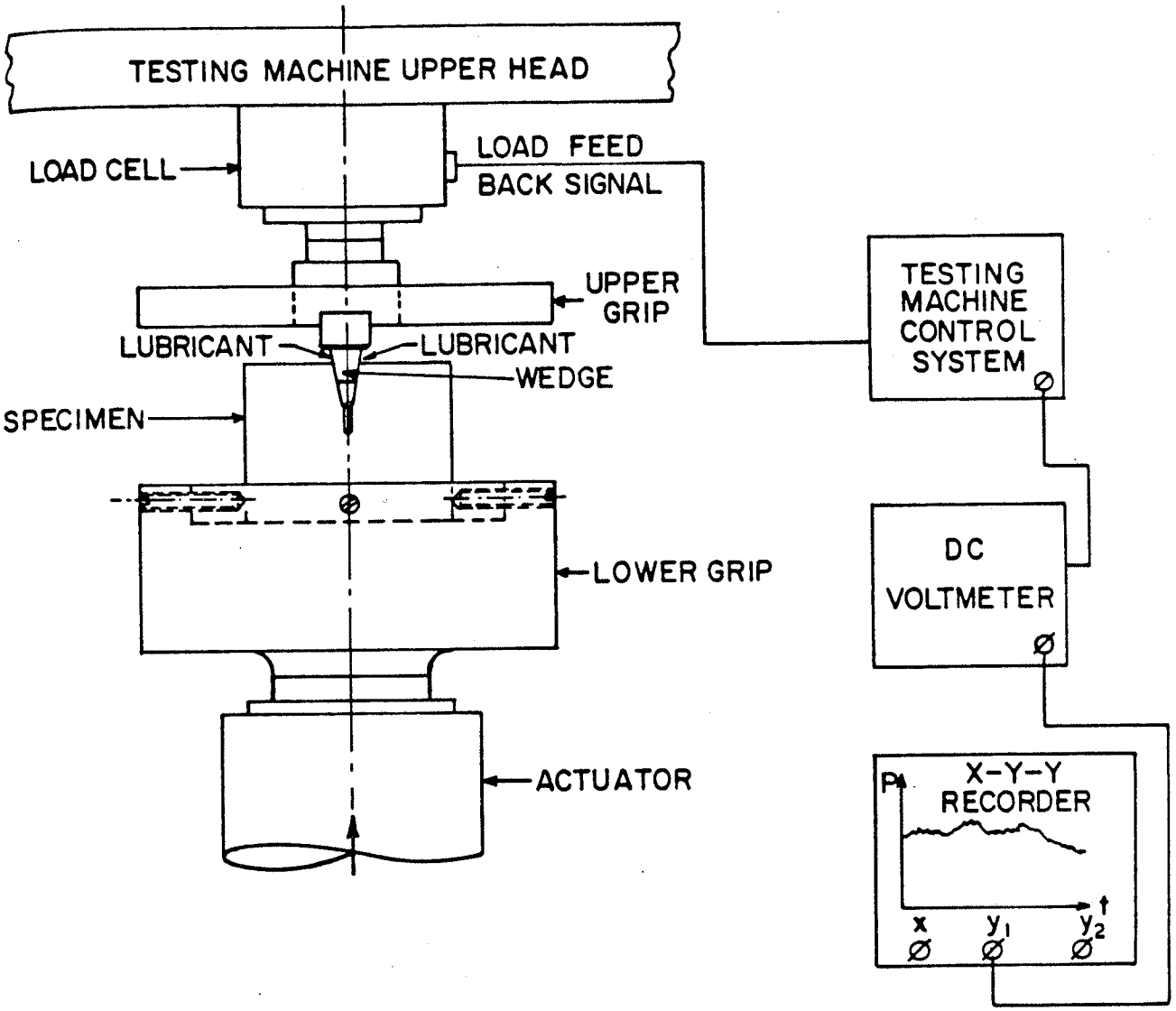

Figure 3.7 Experimental set-up for fatigue precracking of WLCT specimens.

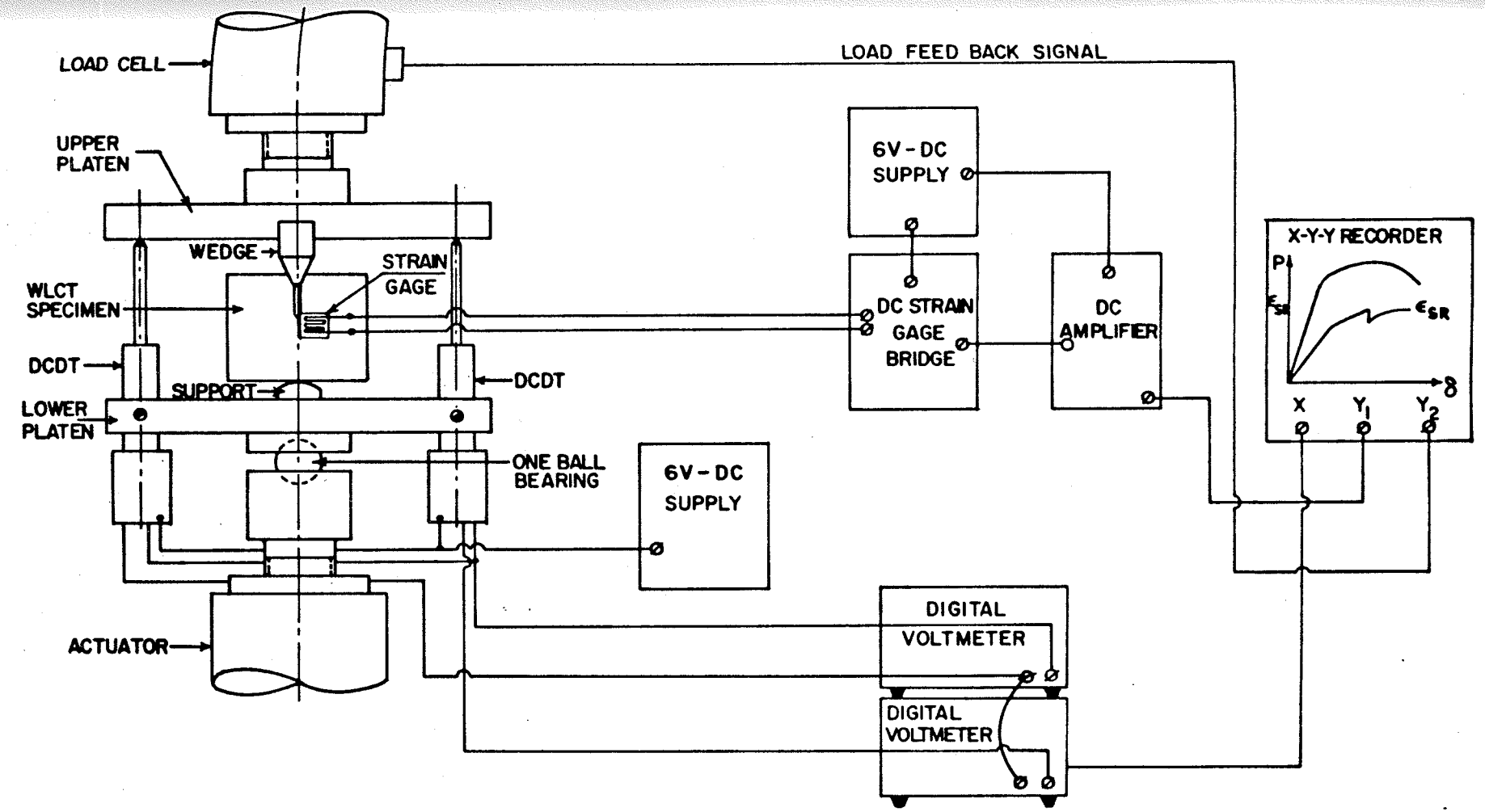

Figure 3.8 Experimental set-up for the quasi-static tests of WLCT specimens.

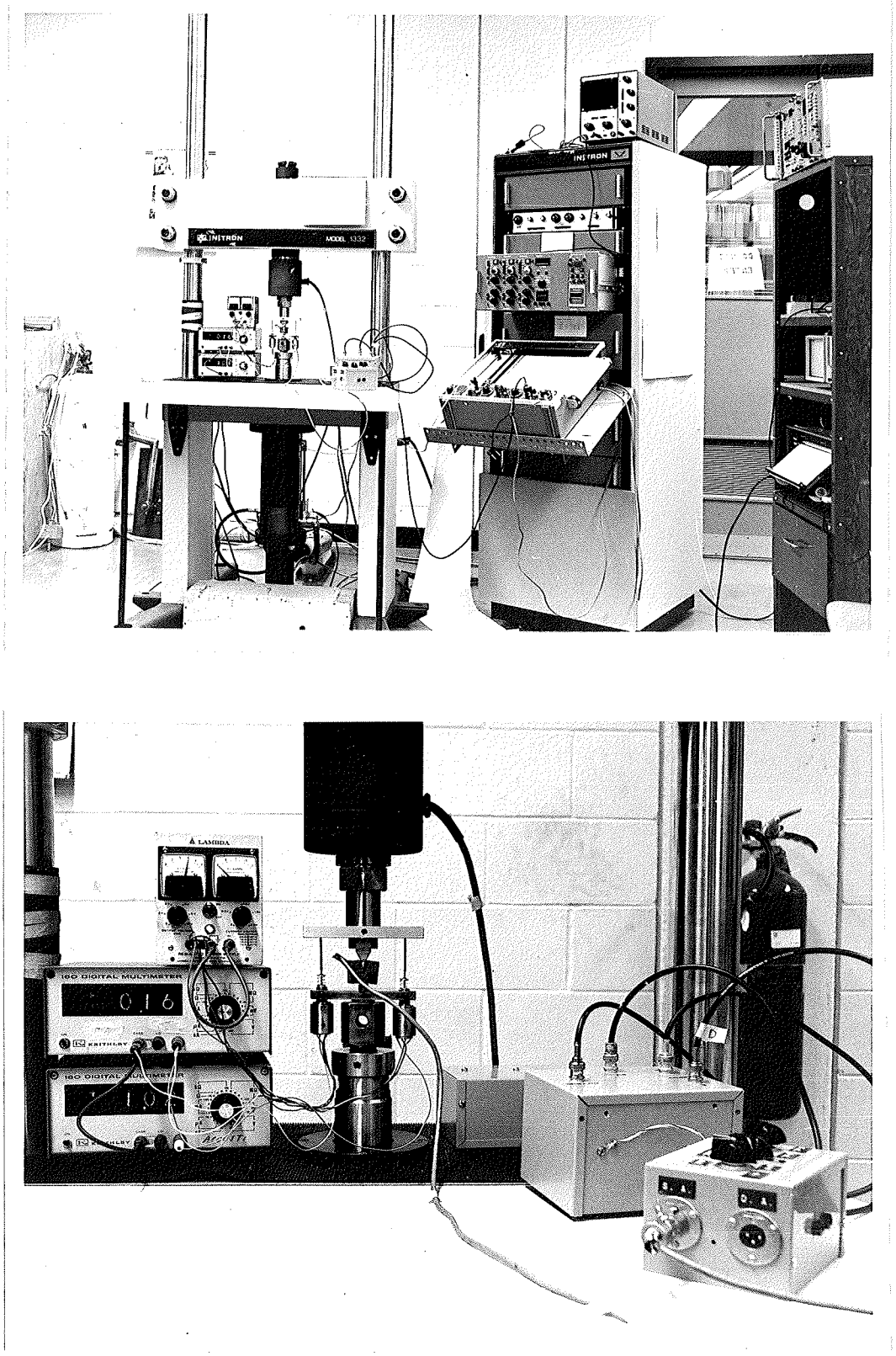

Figure 3.9 A photograph for the equipment used during quasi-static testing for WLCT.

surfaces of the WLCT specimen were lubricated using an MoS_2 base lubricant. Thus, the axial load P and the wedge displacement δ as well as the strain gage signal could be recorded using the X-Y-Y recorder.

The following force distribution formula (see Fig. 3.6) can be used to calculate the opening force F:

$$F = \frac{P}{2 \tan[\beta/2 + \tan^{-1}(\mu)]} \tag{3.5}$$

where P is the axial force acting on the wedge

β is the angle of the specimen incision, and

μ is the friction coefficient between the wedge and the specimen.

The fracture toughness parameter $\frac{U}{Bb}$ was determined from each load-displacement curve up to the point of crack propagation as determined from the output of the strain gage.

3.5.3 Impact Loading by Longitudinal Waves, Split Hopkinson Pressure Bar Technique

The fundamentals of stress wave loading are shown in Fig. 3.10. The box diagram of the experimental set-up is shown in Fig. 3.11. The system consists of a gas gun (not shown in Fig. 3.11), two properly instrumented Hopkinson bars and measuring and recording equipment. Photograph of the experimental installations is shown in Fig. 3.12. A wedge loaded compact tension speicimen (WLCT) of the same geometry as that used in quasi-static tests is placed between the

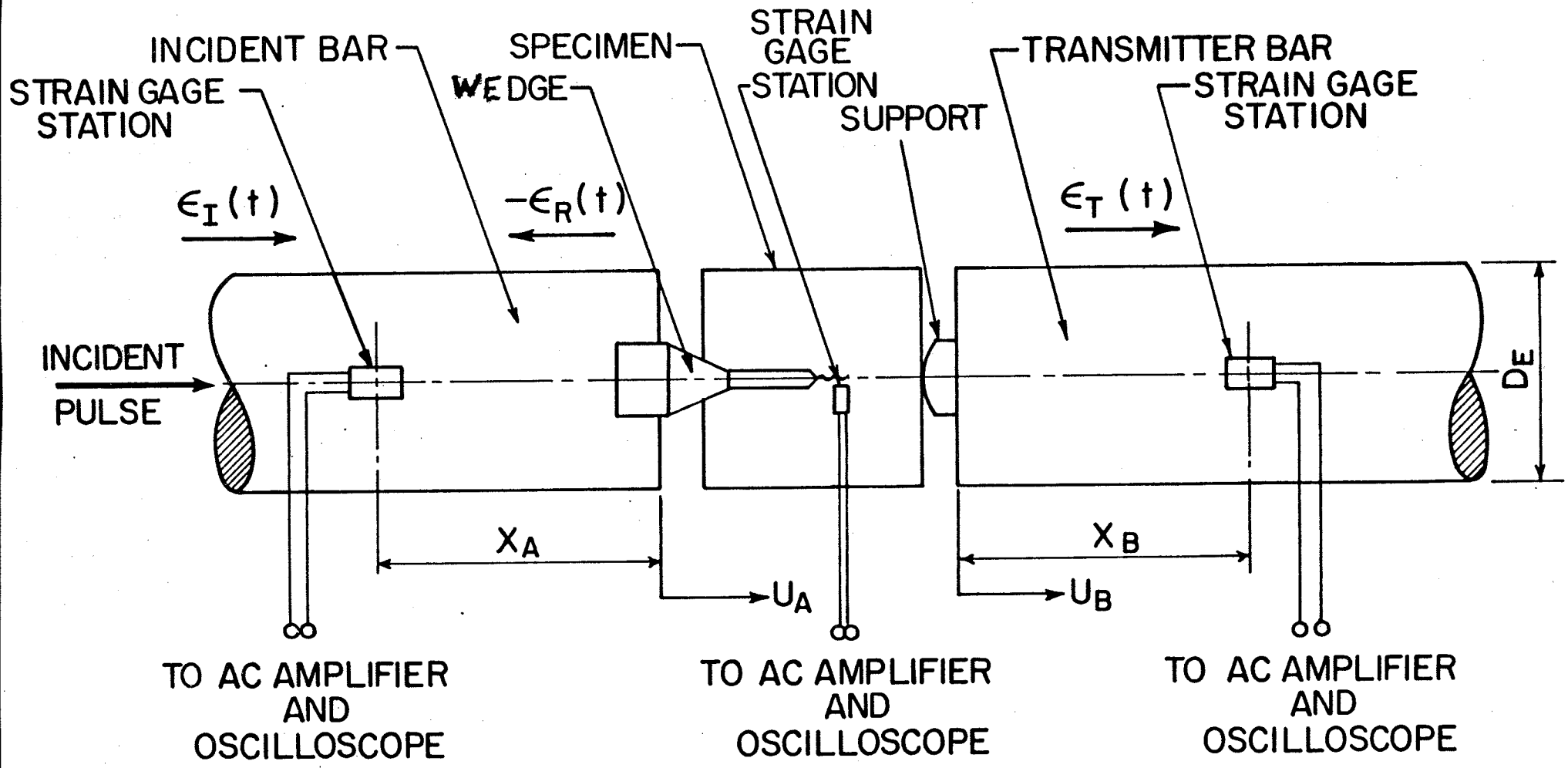

Figure 3.10 Wave dynamics and instrumentation on Split Hopkinson bar for dynamic fracture test.

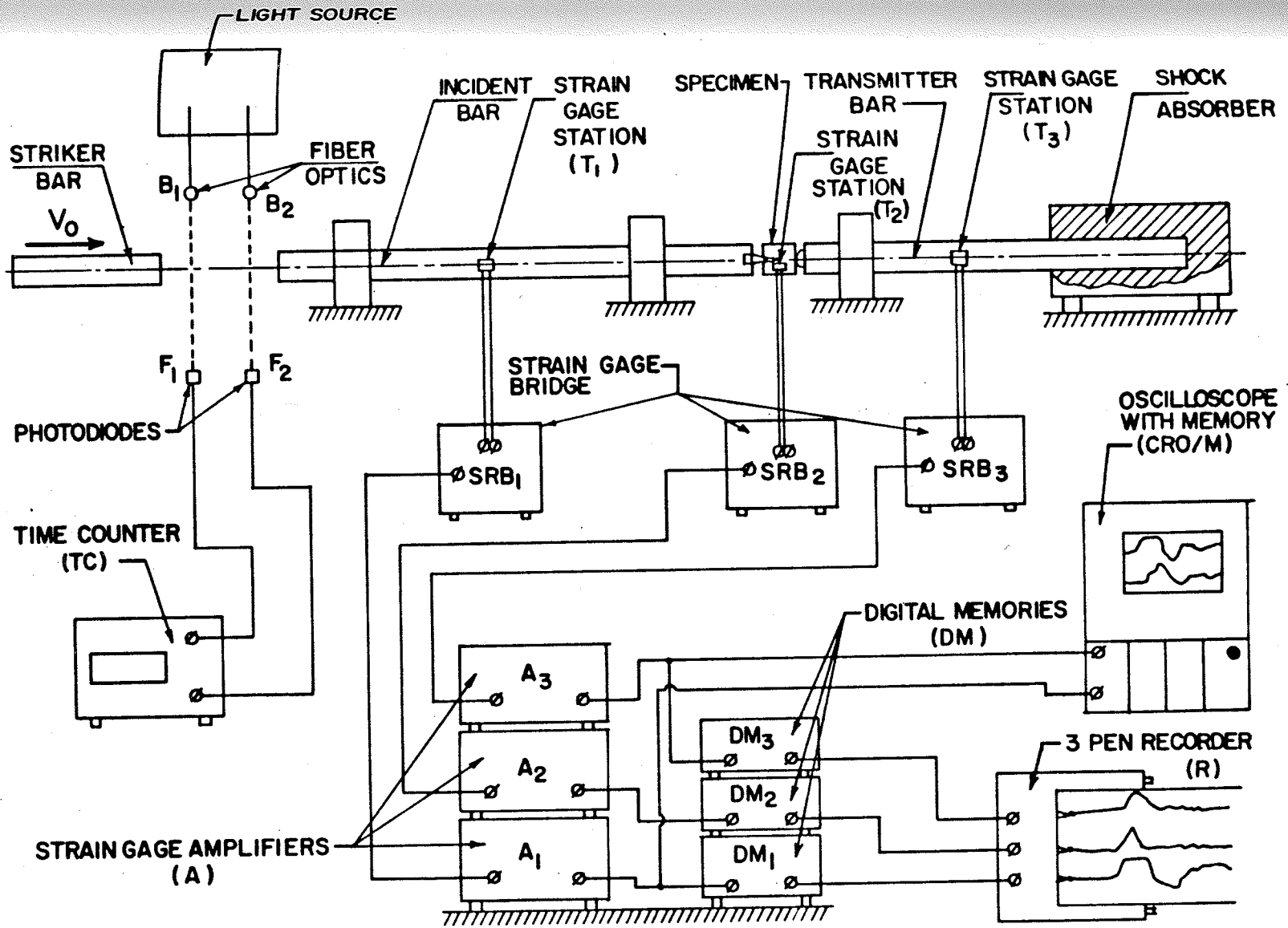

Figure 3.11 Experimental set-up drawing of impact testing using Split Hopkinson bar system.

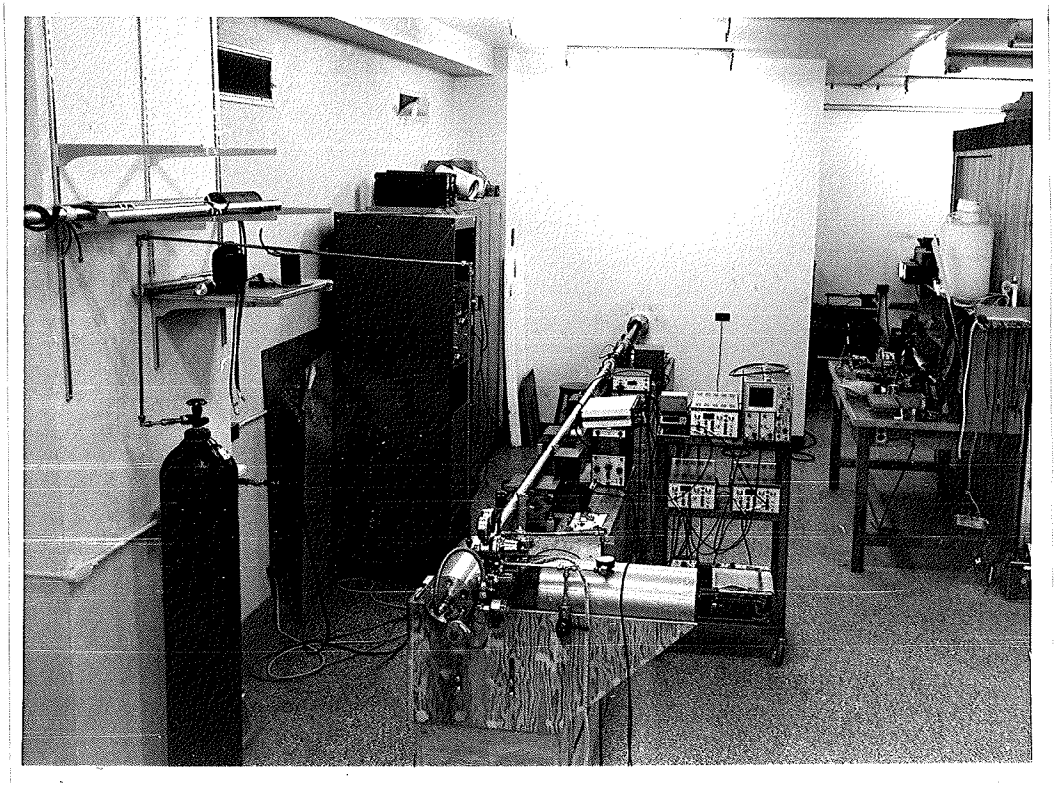

Figure 3.12 Photographs for equipment used in impact testing of the WLCT specimens.

incident bar and the transmitter bar. Since the wedge is attached to the incident bar, the specimen is loaded in exactly the same manner as for the quasi-static configuration. The diameter of all bars was 38 mm and the aluminum alloy 2024-T3 was used for making these bars to obtain the best performance (low mechanical impedance ρC_o, where ρ is the density of the bar and C_o is the longitudinal elastic wave speed)[91].

The use of the system to test fracture toughness K_{IC} have been described earlier [79]. Namely, a striker bar is launched from a gas gun at a prescribed velocity V_o. The impact of the striker bar into the face of the incident bar develops the longitudinal compressive wave $\varepsilon_I(t)$ which propagates along this bar. The incident wave $\varepsilon_I(t)$ is measured by the strain gage station (T_1), with the aid of the strain gage bridge (SRB_1), strain amplifier (A_1), the digital memory (DM_1) and the oscilloscope with memory (CRO/M) as shown in Fig. 3.11 where ε denotes elastic longitudinal strain and t is time. At the instant when the incident wave $\varepsilon_I(t)$ reaches the notch the WLCT specimen starts to be loaded. Since the striker bar must be at least ten times longer than the total length of the WLCT specimen, the process of its loading by the incident wave through the wedge may be assumed to be similar to the quasi-static case [78-80]. Next, part of the compressive incident wave $\varepsilon_I(t)$ is reflected at the wedge end

of the incident bar as a tensile pulse, $-\varepsilon_R(t)$, and part is transmitted into the transmitter bar as a compressive pulse $\varepsilon_T(t)$. The transmitted compressive wave $\varepsilon_T(t)$ is measured by the strain gage station (T_3) and recorded with the aid of strain gage bridge (SRB_3), amplifier (A_3), digital memory (DM_3) and oscilloscope with memory (CRO/M). The point of crack initiation is detected through the strain gage (T_2) and the signal is measured and recorded with the aid of strain gage bridge (SRB_2), amplifier (A_2), digital mamory (DM_2) and time recorder (R). Thus, incident $\varepsilon_I(t)$ and reflected $-\varepsilon_R(t)$ elastic waves are measured by the strain gage station (T_1) whereas the transmitted elastic wave $\varepsilon_T(t)$ and the specimen strain gage signal are measured by the strain gage stations (T_3) and (T_2) respectively. All four pulses provide the information concerning specimen loading and fracturing. The proper distance X_A and X_B, between the strain gage station (T_1) and (T_2), see Fig. 3.10, make it possible to separate in time the $\varepsilon_I(t)$ and $-\varepsilon_R(t)$ waves.

The following quantitative analysis of the three waves to describe the dynamic fracturing of a specimen is similar to that introduced by Kolsky [78] and discussed in [79,80]. The solution for long elastic waves (without any dispersion) will be employed. The displacement of the wedge, as a rigid body denoted by U_A in Fig. 3.10 may be written as follows:

$$U_A(t) = C_o \int_o^t [\varepsilon_I(t) - \varepsilon_R(t)]dt \qquad (3.6)$$

and the displacement of the transmitter bar face which is backing the specimen, denoted by $U_B(t)$ is written analogously as:

$$U_B(t) = C_o \int_o^t \varepsilon_T(t)\, dt \tag{3.7}$$

where C_o is the elastic wave speed in the Hopkinson bars which is given by

$$C_o = (E/\rho)^{1/2} \tag{3.8}$$

where E and ρ are the Young's modulus and density of the Hopkinson bars respectively.

The net displacement of the wedge δ can be written as a function of time as:

$$\delta(t) = U_A(t) - U_B(t) \tag{3.9}$$

Introducing equations (3.6) and (3.7), the displacement $\delta(t)$ as a function of time can be directly related to the measured quantities

$$\delta(t) = C_o \int_o^t [\varepsilon_I(t) - \varepsilon_R(t) - \varepsilon_T(t)]dt \tag{3.10}$$

It may be remembered that the reflected wave $\varepsilon_R(t)$ has a negative value.

If an equilibrium of forces on face A and face B is attained, which usually takes place within a few micro-seconds, the following simplified formula can be used to calculate the net displacement

$$\delta(t) = -2\, C_o \int_o^t \varepsilon_R(t)dt \tag{3.11}$$

The condition for equilibrium is:

$$\varepsilon_I(t) + \varepsilon_R(t) = \varepsilon_T(t) \tag{3.12}$$

Also, axial forces acting on the specimen from both sides A and B (from side A through the wedge) can be calculated. For this purpose, Hooke's law is used, thus:

$$P_A(t) = E\ A_E\ [\varepsilon_I(t) + \varepsilon_R(t)] \tag{3.13}$$

and the force acting on the contact surface between the transmitter bar and specimen (face B) is:

$$P_B(t) = E\ A_E \varepsilon_T(t) \tag{3.14}$$

where, E and A_E are Young's modulus and cross section area of the Hopkinson bars respectively. The average force $\bar{P}$ in the loading system is

$$\bar{P}(t) = \frac{1}{2}\ [P_A(t) + P_B(t)] \tag{3.15}$$

After introducing equations (3.13) and (3.14), the average force $\bar{P}$ can be also related to the measured quantities

$$\bar{P}(t) = \frac{1}{2}\ EA_E\ [\varepsilon_I(t) + \varepsilon_R(t) + \varepsilon_T(t)] \tag{3.16}$$

When the difference of forces P_A and P_B is not large (equilibrium condition is satisfied), the relation in equation (3.16) reduces to

$$\bar{P}(t) = E\ A_E \varepsilon_T(t) \tag{3.17}$$

It is concluded from the above equations that equation (3.9) enables the calculation of wedge displacement as a function of time, and equation (3.15) permits the calculation of the average force as a function of time. The simplified relation in equation (3.17) predicts that the average force $\bar{P}$ is proportional to the transmitted pulse.

Eliminating the time in $\bar{P}(t)$ and $\delta(t)$ plots, it is possible to obtain a P - δ plot. The area under the P - δ

curve can be calculated up to the point of crack initiation as determined from the strain gage attached on the specimen. This area is ultimately an indication of the material fracture toughness J_{IC}.

It must be mentioned that great advantage of the three-bar system is the dynamic calibration of the elastic strains measured by the strain gage stations at each experiment. Application of Hooke's law $\sigma = E\ \varepsilon_{gage}$, together with the elastic wave solution $\sigma = \rho\ C_o V$, where V is the mass velocity, enables the following calibration formula to be derived:

$$\varepsilon_I^* = \frac{1}{2}\left(D_1/D_E\right)^2 \cdot V_o/C_o \qquad (3.18)$$

where ε_I^* is the maximum amplitude of the incident pulse, V_o is the impact velocity as measured with the photodiodes (F_1, F_2) and time counter (TC) as shown in Fg. 3.11, D_1 is the diameter of the striker bar and D_E denotes the diameter of the Hopkinson bars.

To calibrate the amplifications of gages (T_1) and (T_3), see Fig. 3.11, a longitudinal pulse is sent through the system of bars with the wedge and specimen removed. Different desired loading rates can be achieved by different initial velocities of the striker bar.

In the wedge loaded specimen method, the effect of friction must be taken into account since the loading tensile force is influenced by the friction coefficient μ. With lubrication using MoS_2, an average value of μ about 0.1 is considered. This value is assumed to be identical in both dynamic and quasi-static conditions [92,93].

3.6 Stretch Zone Width Measurements

An alternative method to determine the fracture toughness J_{IC} is the measurement of the stretch zone width [94-97]. The stretch zone is the transition between the end of the fatigue pre-crack and the stable crack growth. It is characterized by an extensive plastic deformation prior to crack initiation. This zone can be distinguished from the fatigue pre-crack region and the stable crack growth region on scanning electron micrographs of the fracture surface. Assuming that deformation prior to crack initiation takes place along 45° slip lines, the critical stretch zone width (WSZC) can be measured by tilting a fractured specimen an angle of 45° and examining it in the scanning electron microscope. This measurement is shown schematically in Fig. 3.13.

Considering a symmetric blunt crack, Nguyen-Duy [95] has derived an equation relating the stretch zone width (WSZC) to the crack opening displacement (COD). If AB in Fig. 3.13 is the critical stretch zone width, it can be shown that the stretch zone width and the critical crack opening displacement are given by [95]:

$$WSZC = \frac{d}{\cos(\theta - \psi)} \cdot \frac{1}{G} \tag{3.19}$$

and

$$(COD)_C = \frac{2d}{\cos\psi - \sin\psi} \cdot \frac{1}{G} \tag{3.20}$$

where d is the measured length of the stretch zone on the micrographs, ψ is the incident angle of the beam (tilt-

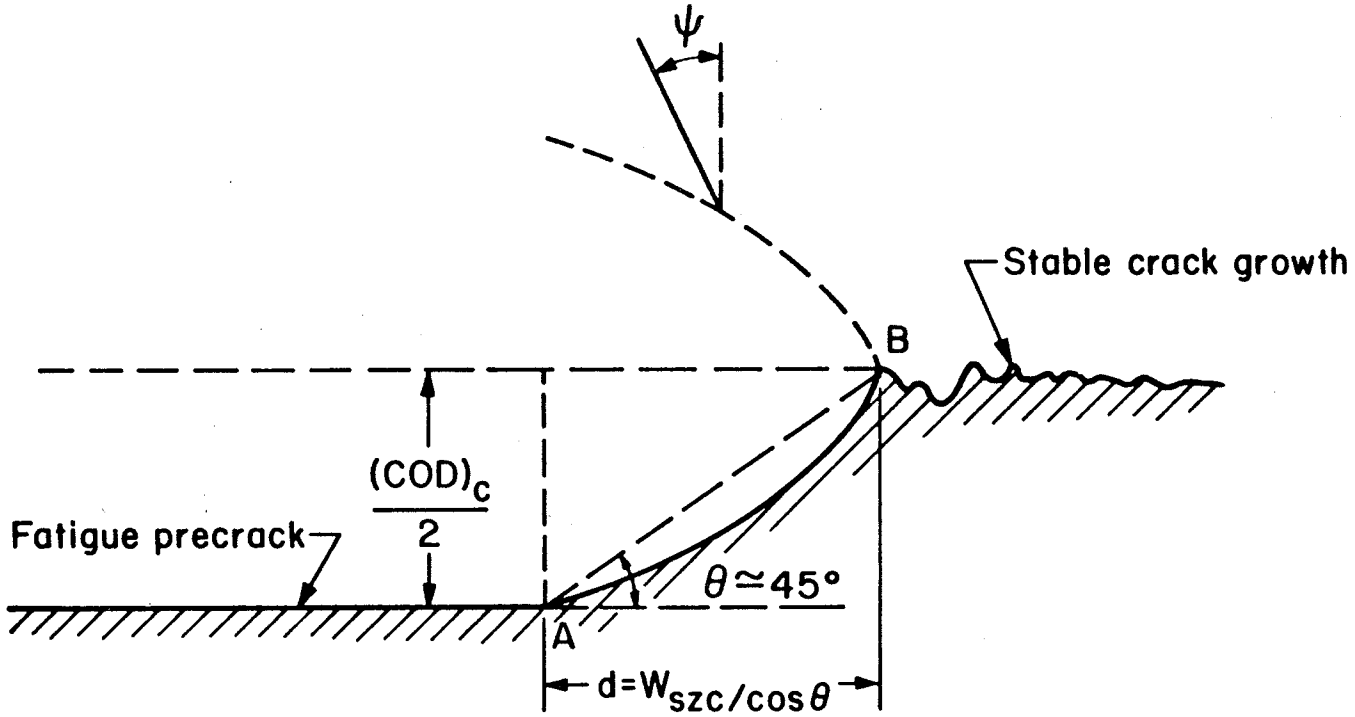

Figure 3.13 Illustration of the stretch zone of broken specimen half (After 95)

angle), $\theta = 45°$, and G is the magnification. Under plane-strain conditions, the critical value of J-integral (J_{IC}) is related to the $(COD)_C$ by [98,99]:

$$J_{IC} = m\ \sigma_o (COD)_C \qquad (3.21)$$

where σ_o is the flow stress and m is a constraint factor due to plane strain loading. It is usually taken approximately to be equal to 2.0. Substituting equation (3.20) into equation (3.21), with m equal to 2, equation (3.21) becomes:

$$J_{IC} = \frac{4\ \sigma_o d}{\cos\psi + \sin\psi} \cdot \frac{1}{G} \qquad (3.22)$$

Halves of broken 3-point bend and WLCT specimens were examined by a scanning electron microscope (Super Mini-SEM ISI) using mostly a tilt angle $\psi = 30°$ and a magnification about 100 to 300. The length of the stretch zone d was measured at different points along the crack front and the results were averaged. The value of J_{IC} was calculated using equation (3.22).

3.7 Heat Treatment

A different microstructure corresponding to tempered martensite was obtained through a heat treatment process. Specimens of different shapes and geometries including Charpy, tensile, bulge ductility and three point bending specimens machined from 1045 steel were water quenched from 810°C and then tempered at a temperature of 540°C for 1.5 hours. The resulting hardness of the material R_C 23. As

shown in Fig. 3.14 the material had a tempered martensitic structure. The relationship between fracture toughness, ductility and temperature was also investigated for this microstructure.

3.8 Summary

This chapter has described the different procedures to obtain the experimental data for ductility and fracture toughness under different conditions of test temperature and loading rate. Tensile and bulge ductility were adopted to measure the material ductility while the J_{IC} criterion, using standard three point bending specimens was adopted to characterize the material fracture toughness. A wedge loaded compact tension specimen (WLCT) was used to obtain the fracture toughness data over a wide range of loading rates. Fracture in the dynamic range was achieved by the Split Hopkinson bar technique. The measurement of the stretch zone width with the scanning electron microscopy, was used as an alternative method to determine the fracture toughness J_{IC}, and to confirm those results of fracture toughness J_{IC} obtained from the standard three point bending and wedge loaded compact tension testing. Two microstructures were tested, namely a pearlitic and a tempered martensitic structure. The experimental results are described in the next chapter.

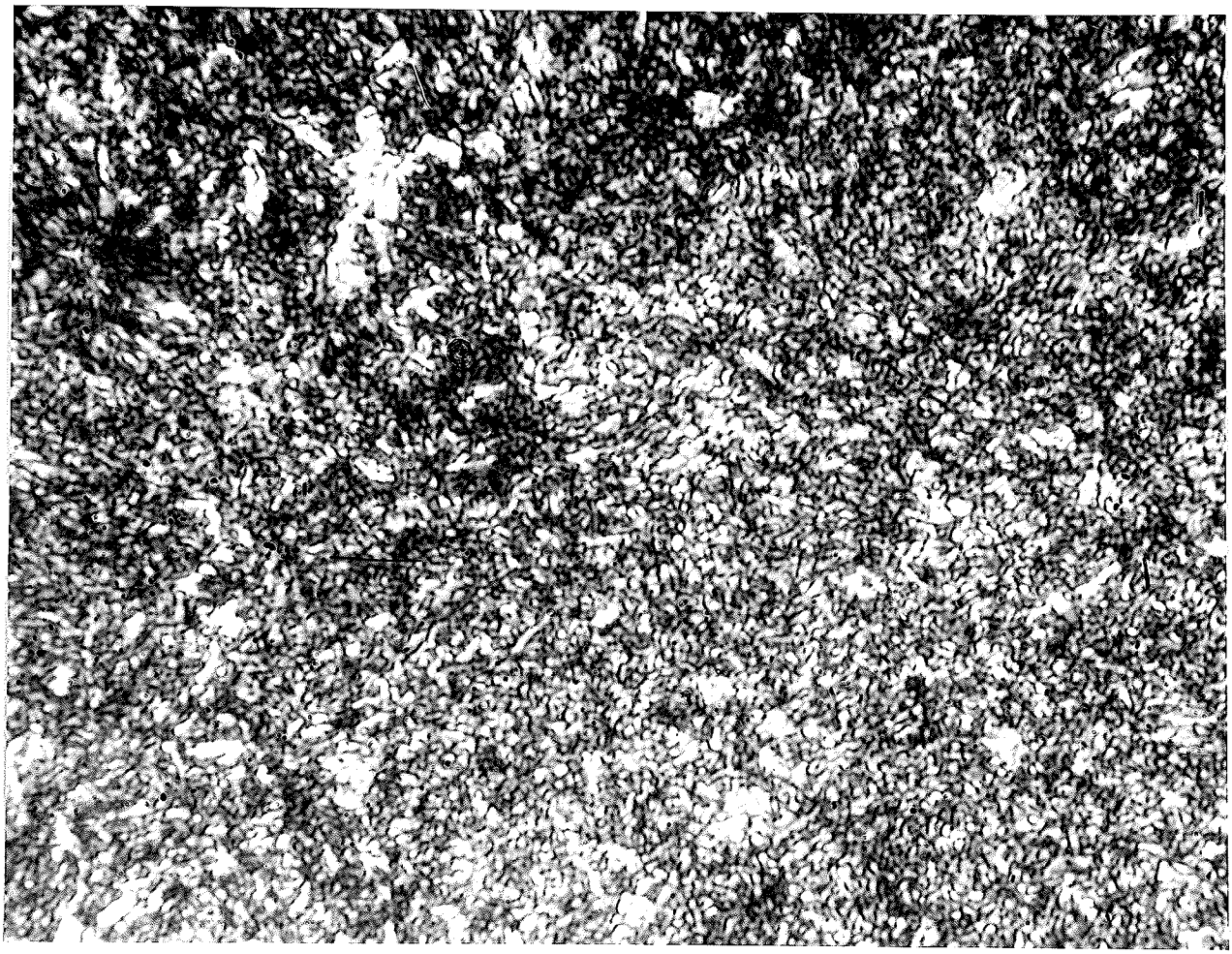

Figure 3.14 Microstructure of tempered martensitic 1045 steel. (1040 X)

CHAPTER 4

EXPERIMENTAL RESULTS

4.1 Charpy Impact Toughness

The variation of Charpy V-notch toughness with temperature for the annealed 1045 steel is shown in Fig. 4.1. A ductility transition temperature corresponding to a Charpy energy of 15 ft-lb occurs at about 0°C. Upper shelf was obtained at temperatures above 60°C while lower shelf was obtained at temperatures below - 40°C.

4.2 Tensile Properties

Results for the tensile test as function of temperature of the annealed 1045 steel are shown in Figs. 4.2, 4.3 and 4.4. Figure 4.2 shows the variation of the yield stress σ_y, the flow stress (equal to $(\sigma_u + \sigma_y)/2$) and the ultimate tensile strength σ_u, as a function of temperature. Figure 4.3 shows the temperature dependence of tensile ductility, in percent elongation and percent reduction in area. The variation of the strain hardening exponent n with temperature is given in Fig. 4.4. As expected, there is a significant temperature dependence of the yield stress, ultimate tensile strength and consequently the flow stress. The tensile ductility shows also a temperature dependence. Decreasing the temperature, as expected, decreases the tensile ductility and increases the yield stress and flow stress.

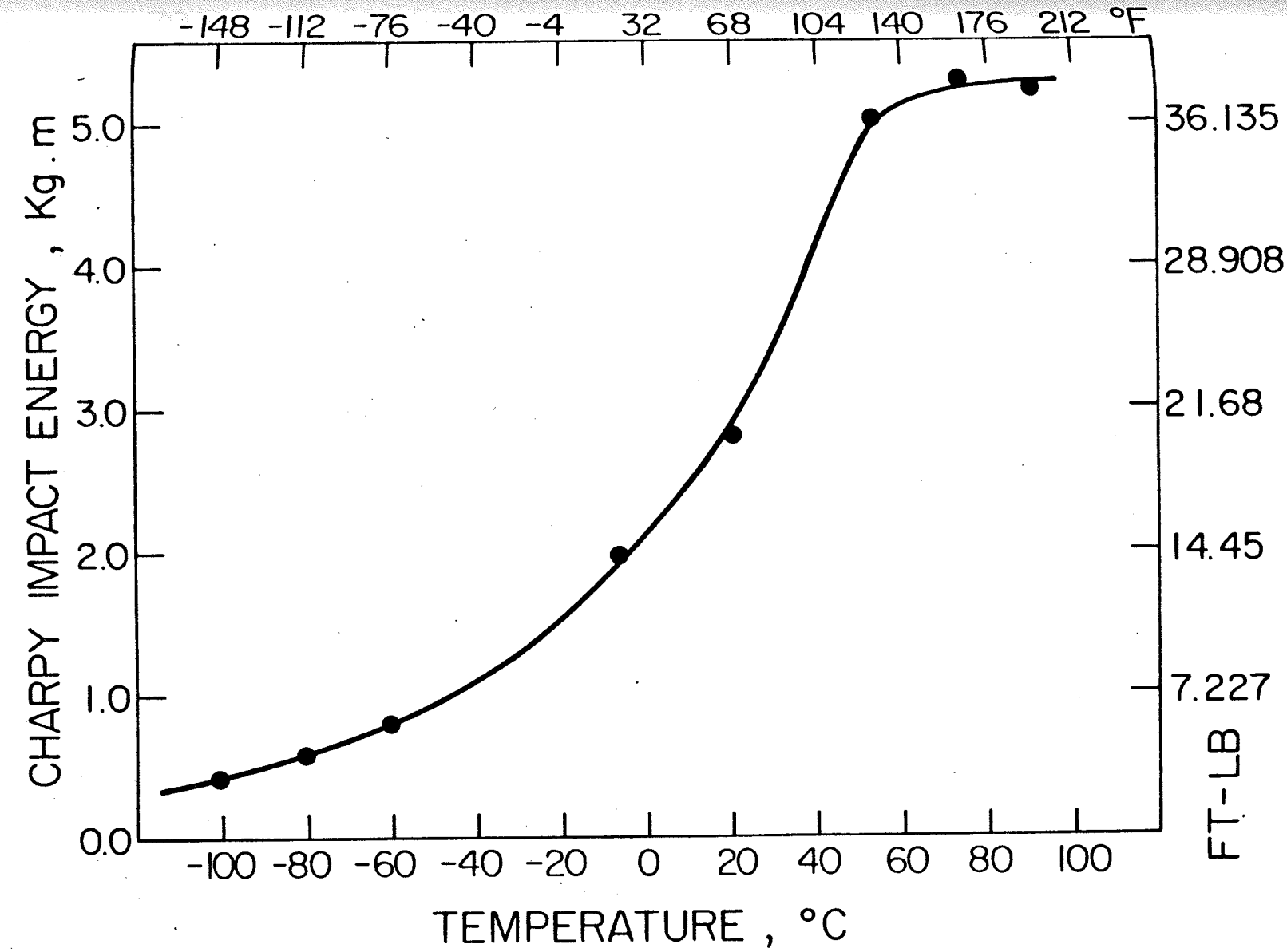

Figure 4.1 Variation of Charpy V-notch toughness with temperature for the annealed AISI 1045 steel.

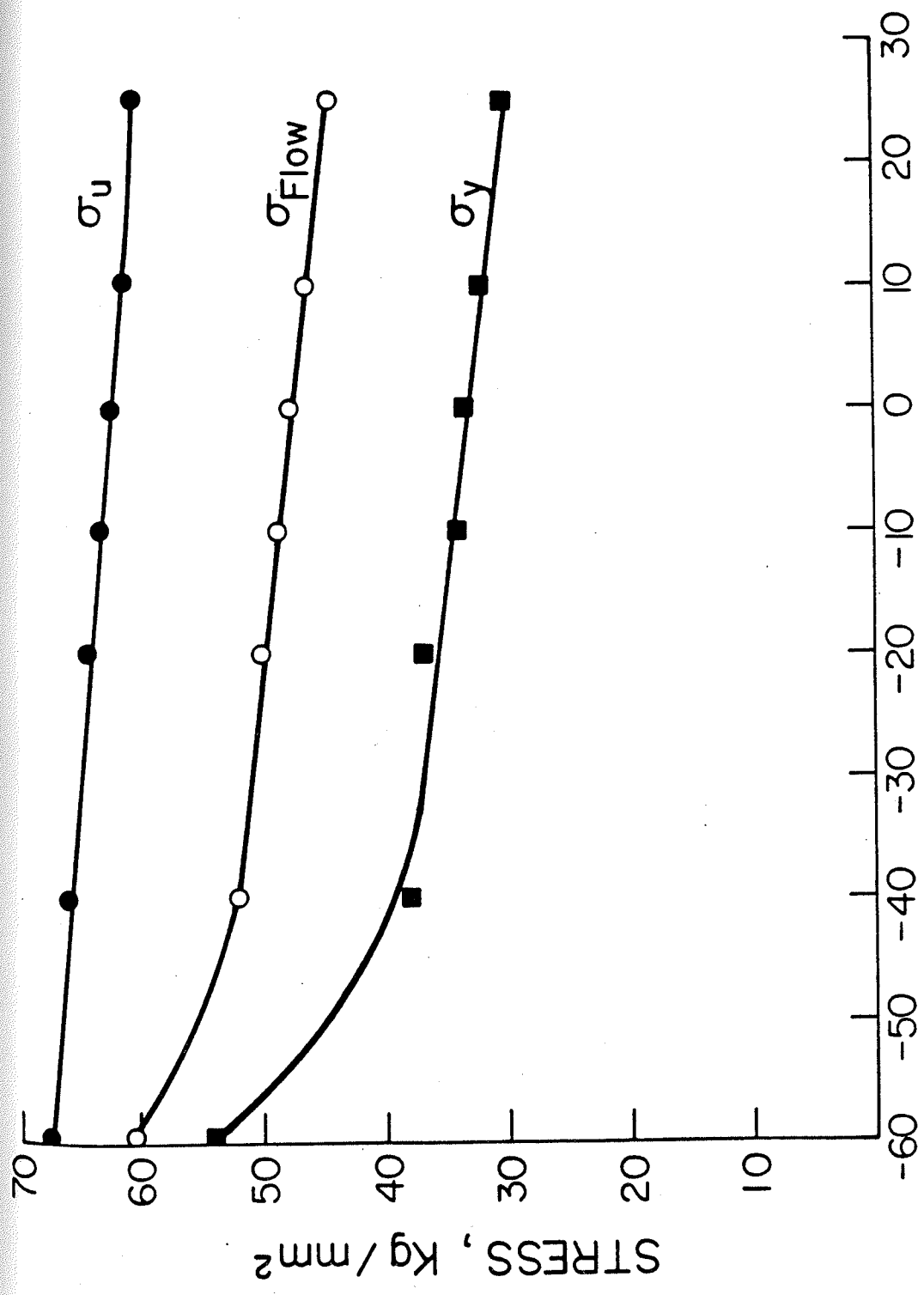

Figure 4.2 Variation of tensile properties of the annealed 1045 steel with temperature.

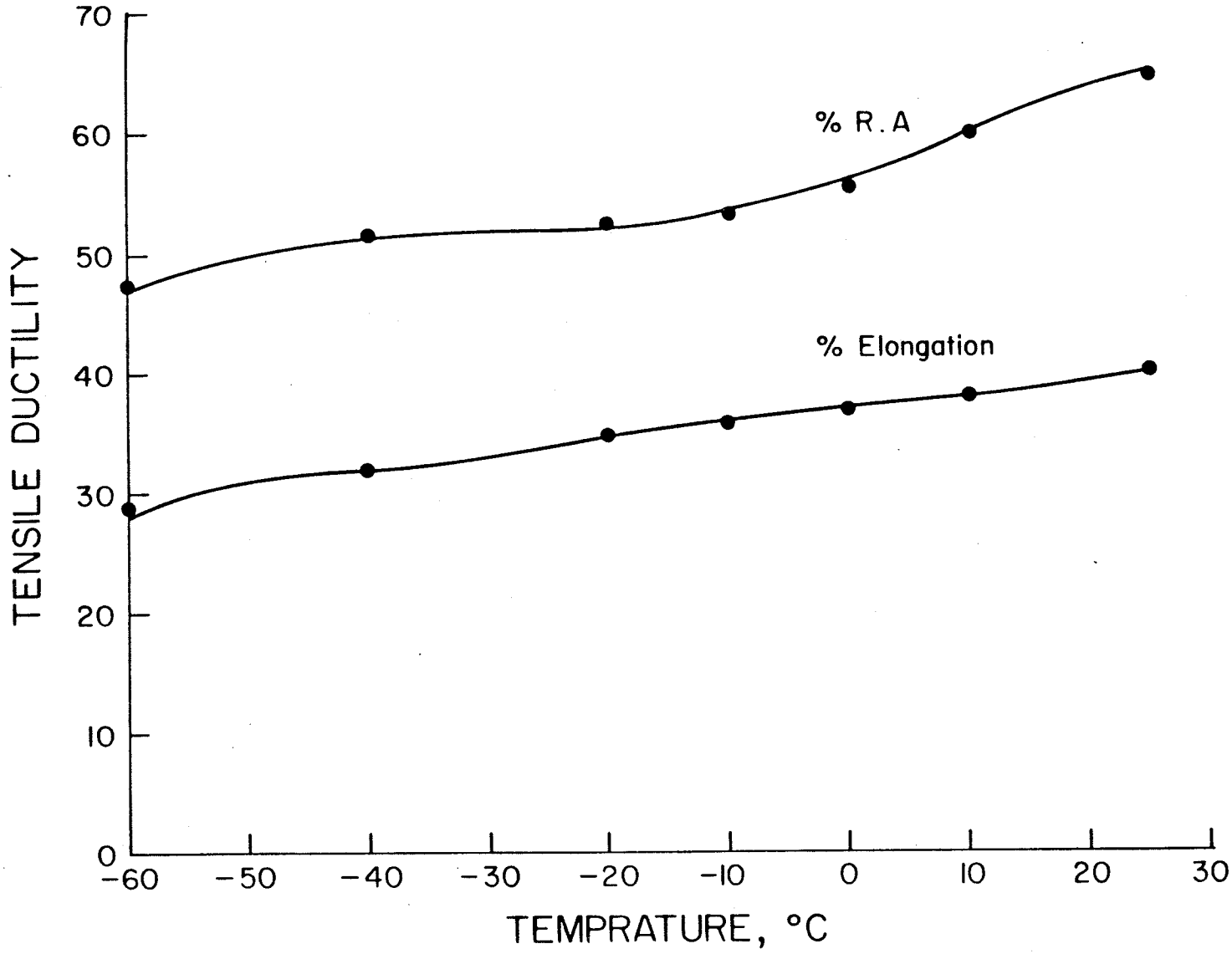

Figure 4.3 Variation of tensile ductility with temperature for 1045 steel in the annealed condition.

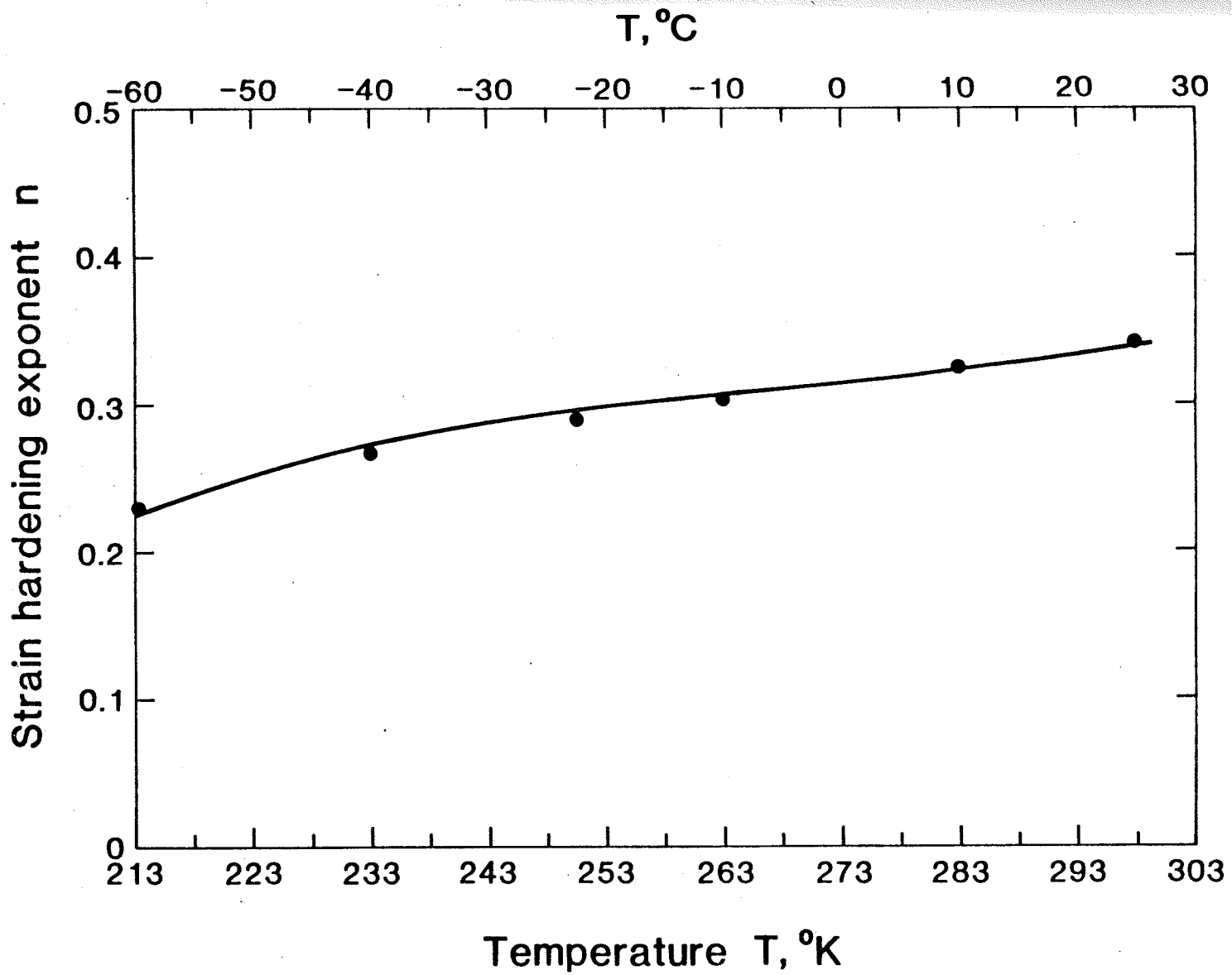

Figure 4.4 Variation of the strain hardening exponent n with temperature for AISI 1045 steel in the annealed condition.

4.3 Bulge Ductility

The variation of the bulge ductility with temperature for AISI 1045 steel in the annealed condition, is presented in Fig. 4.5. It is shown that as the temperature decreases, bulge ductility also decreases. There is a significant drop in ductility observed at - 60°C. The bulge ductility at 25°C reaches a value of 0.55 while it is 0.16 at - 60°C. The marked drop in bulge ductility seems to take place below -40°C.

4.4 Fracture Toughesss (J_{IC}) Results from the Compliance Method

J-resistance curves, which are plots of J versus Δa for the different testing temperatures, were obtained. They are shown in Figs. 4.6 (a) to 4.6 (f) for temperatures 25, 10, 0, -10, -20 and -40°C respectively. The intersection of the blunting line and the crack advance line gives the J_{IC} values as shown. The values of J_{IC} obtained for all the specimens tested meet the size requirement

$$B,\ b > \alpha \frac{J_{IC}}{\sigma_o} \qquad (4.1)$$

where α is a nondimensional constant taken to be equal to 25. Thus all the J_{IC} values determined can be considered as valid values of toughness of the material based on ASTM specification E813-81.

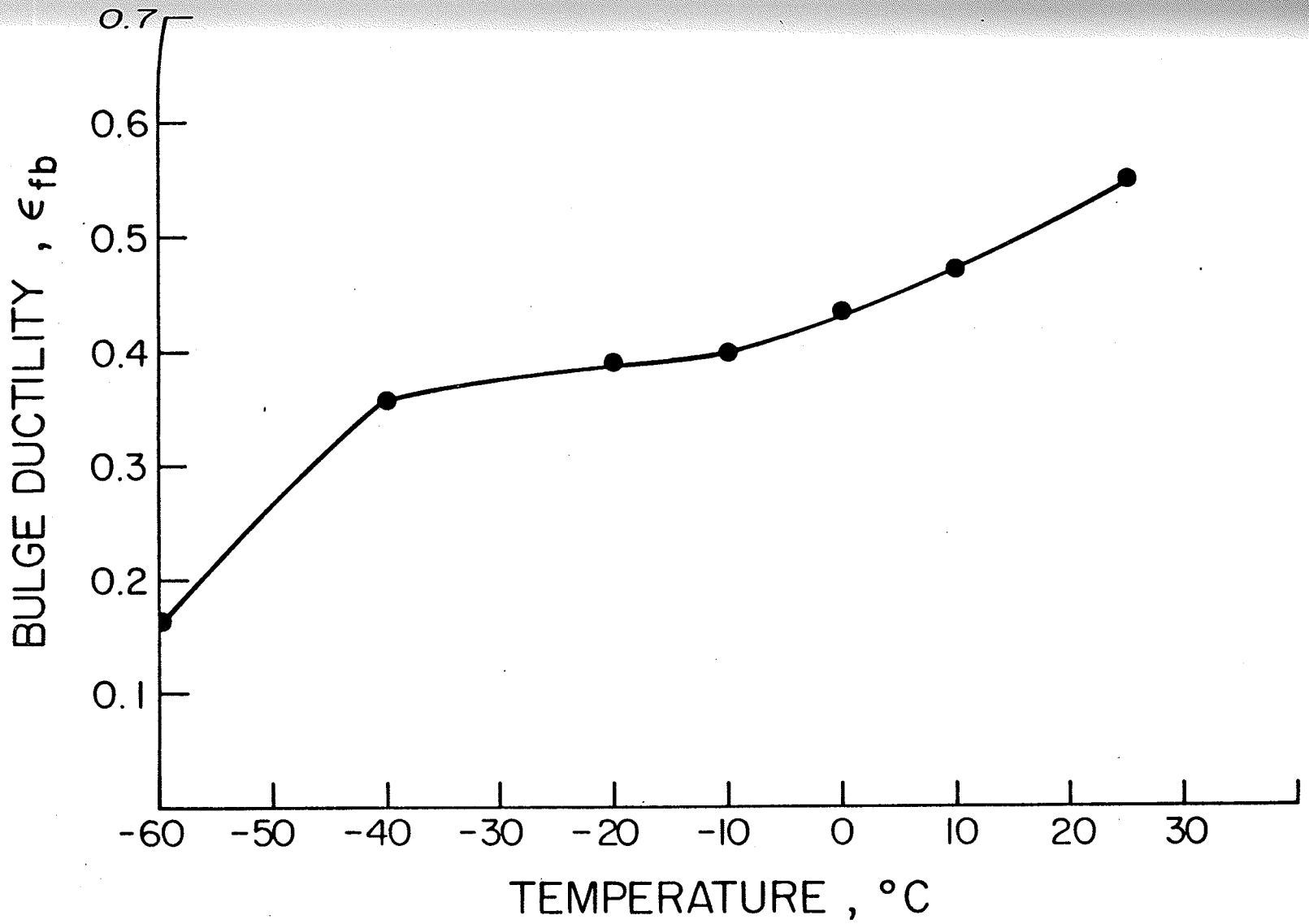

Figure 4.5 Variation of the bulge ductility with temperature for AISI 1045 steel in the annealed condition.

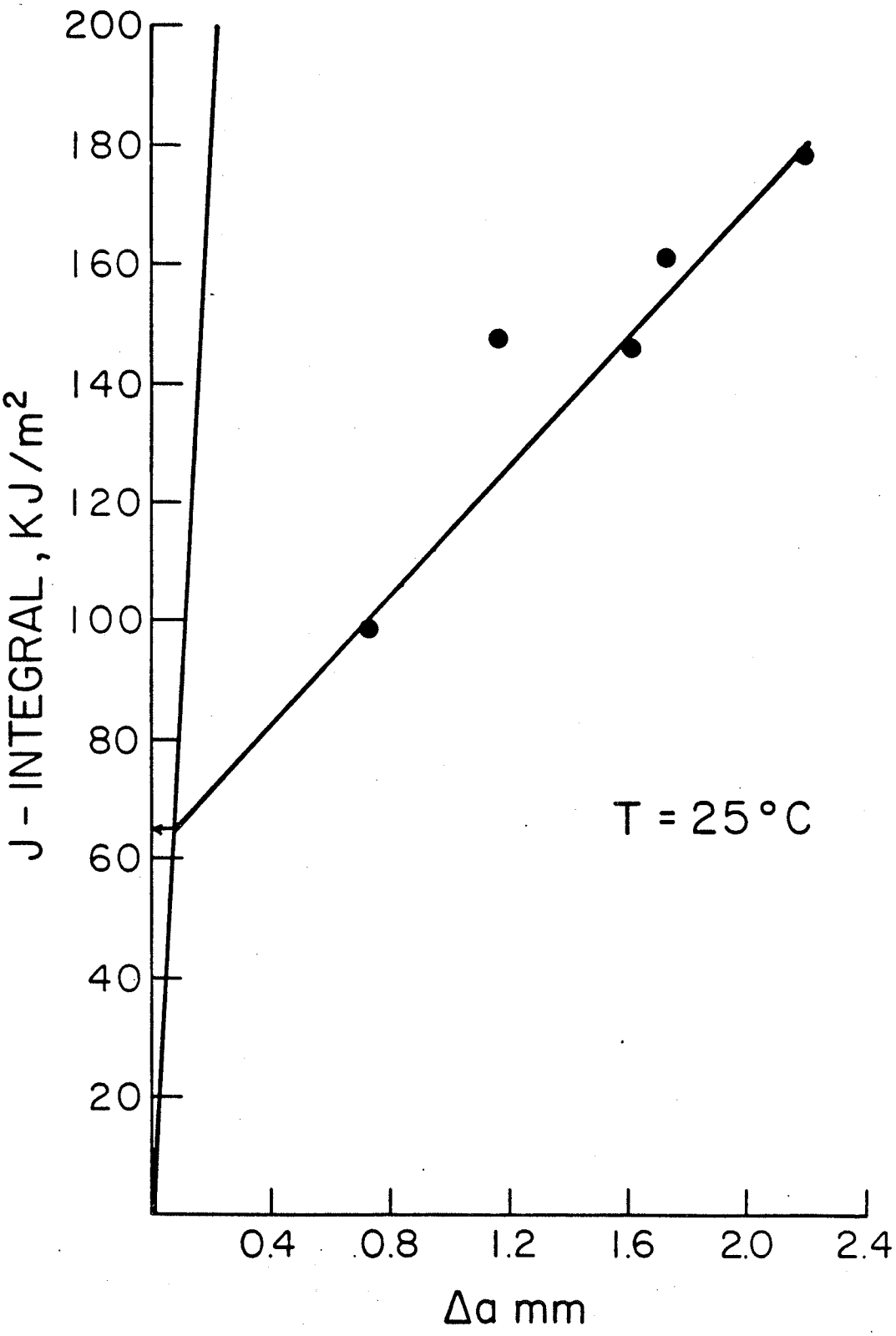

Figure 4.6(a) J-resistance curves for the different testing temperature for AISI 1045 steel in the annealed condition.

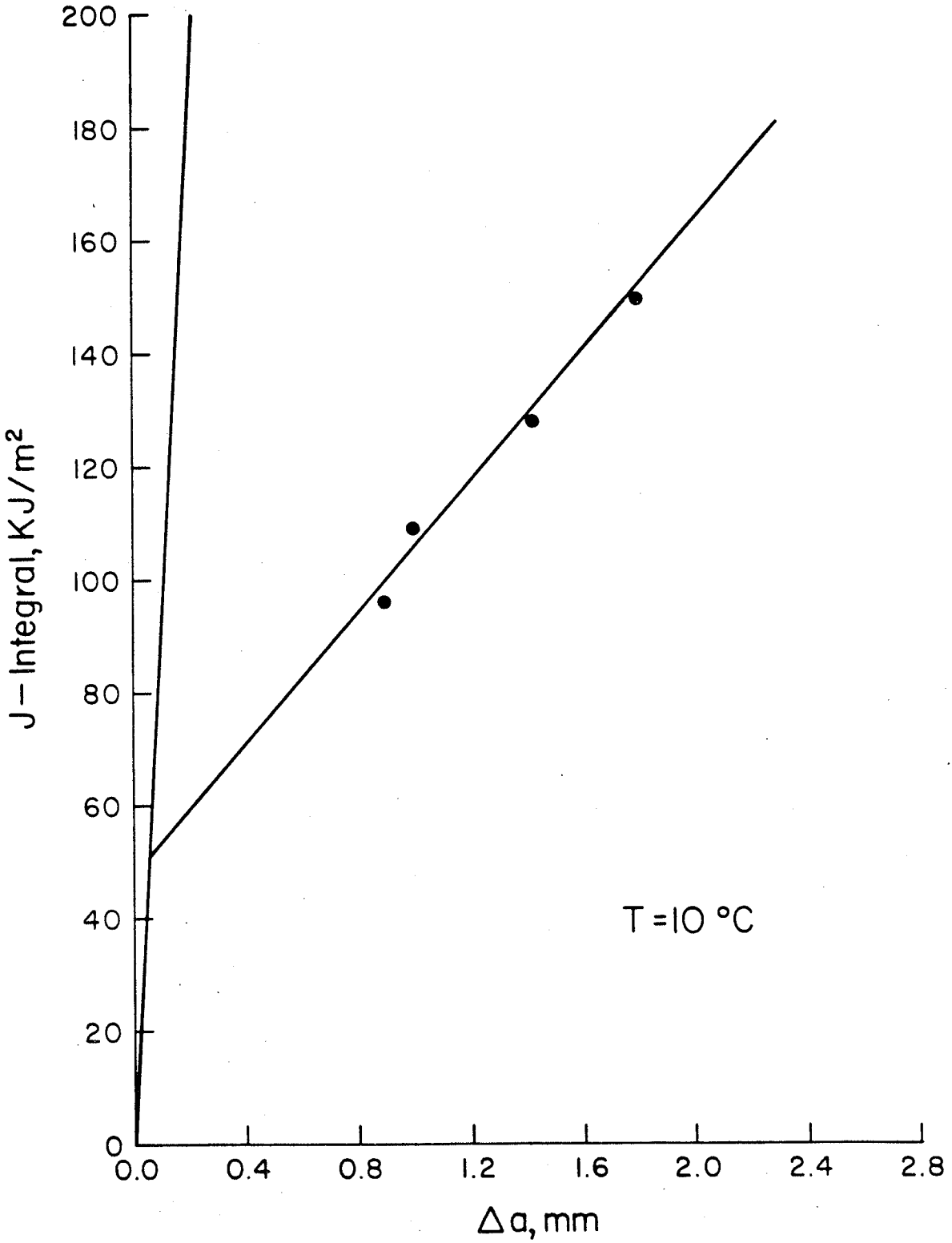

Figure 4.6(b) J-resistance curves for the different testing temperature for AISI 1045 steel in the annealed condition.

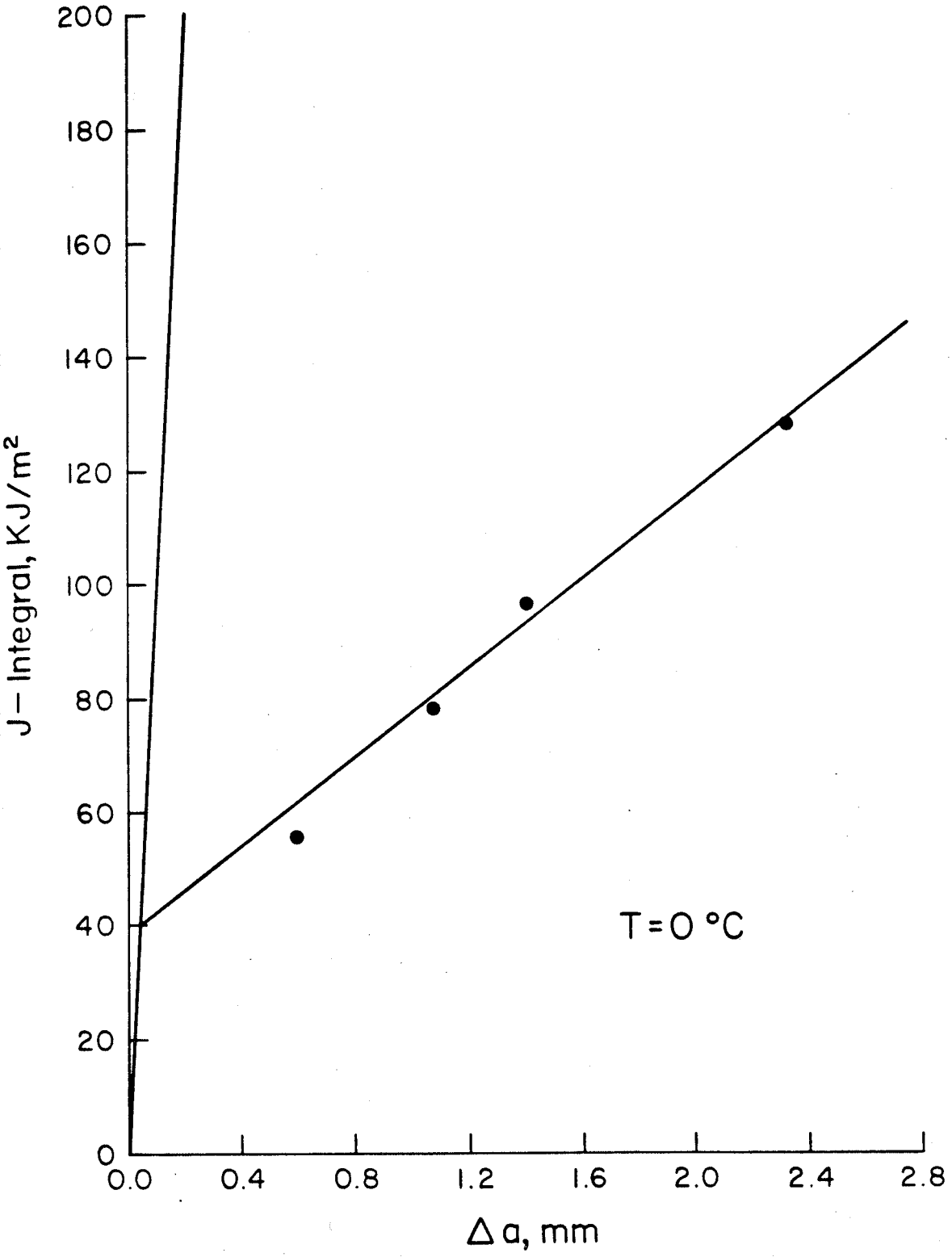

Figure 4.6(c) J-resistance curves for the different testing temperatures for AISI 1045 steel in the annealed condition.

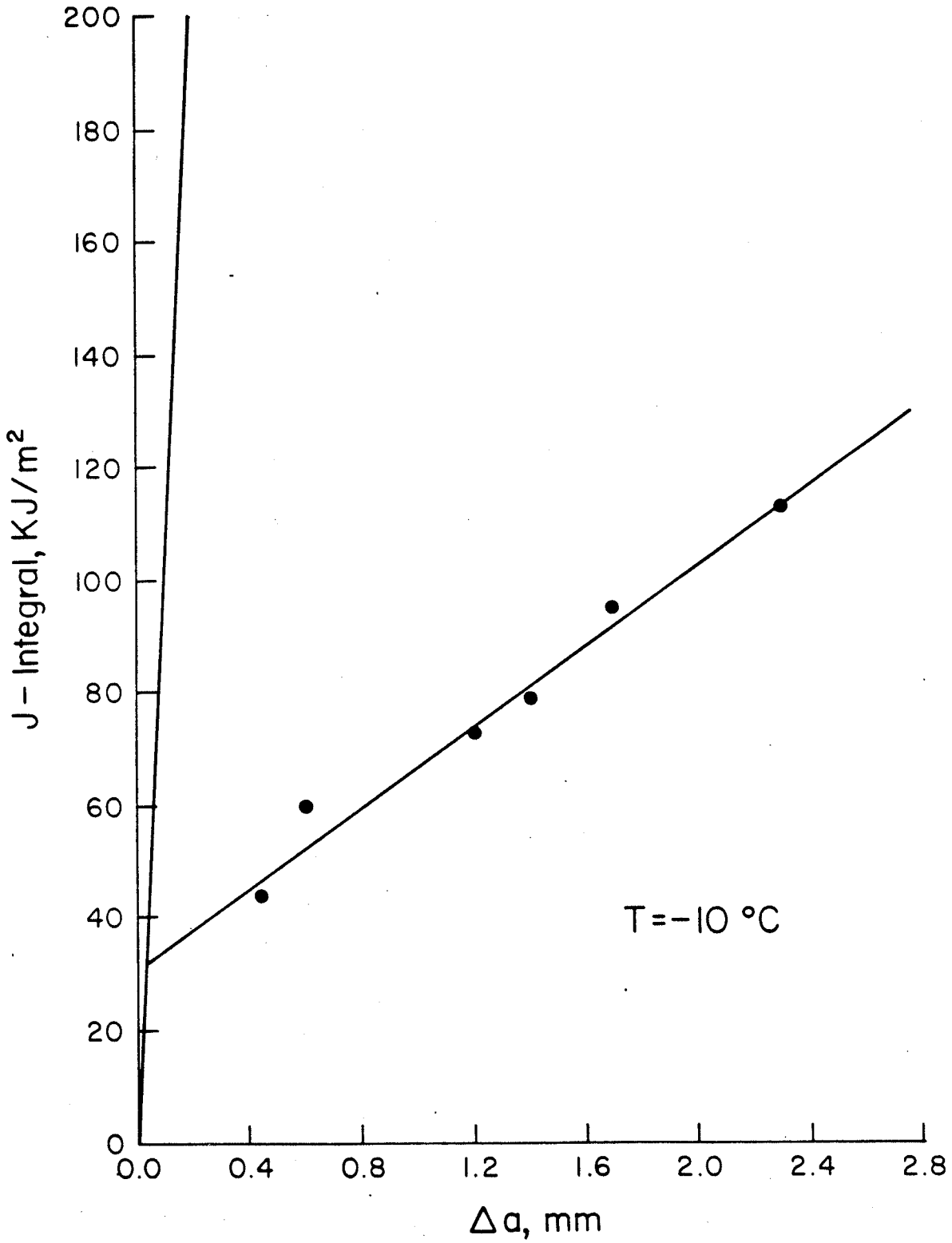

Figure 4.6(d) J-resistance curves for the different testing temperatures for AISI 1045 steel in the annealed condition.

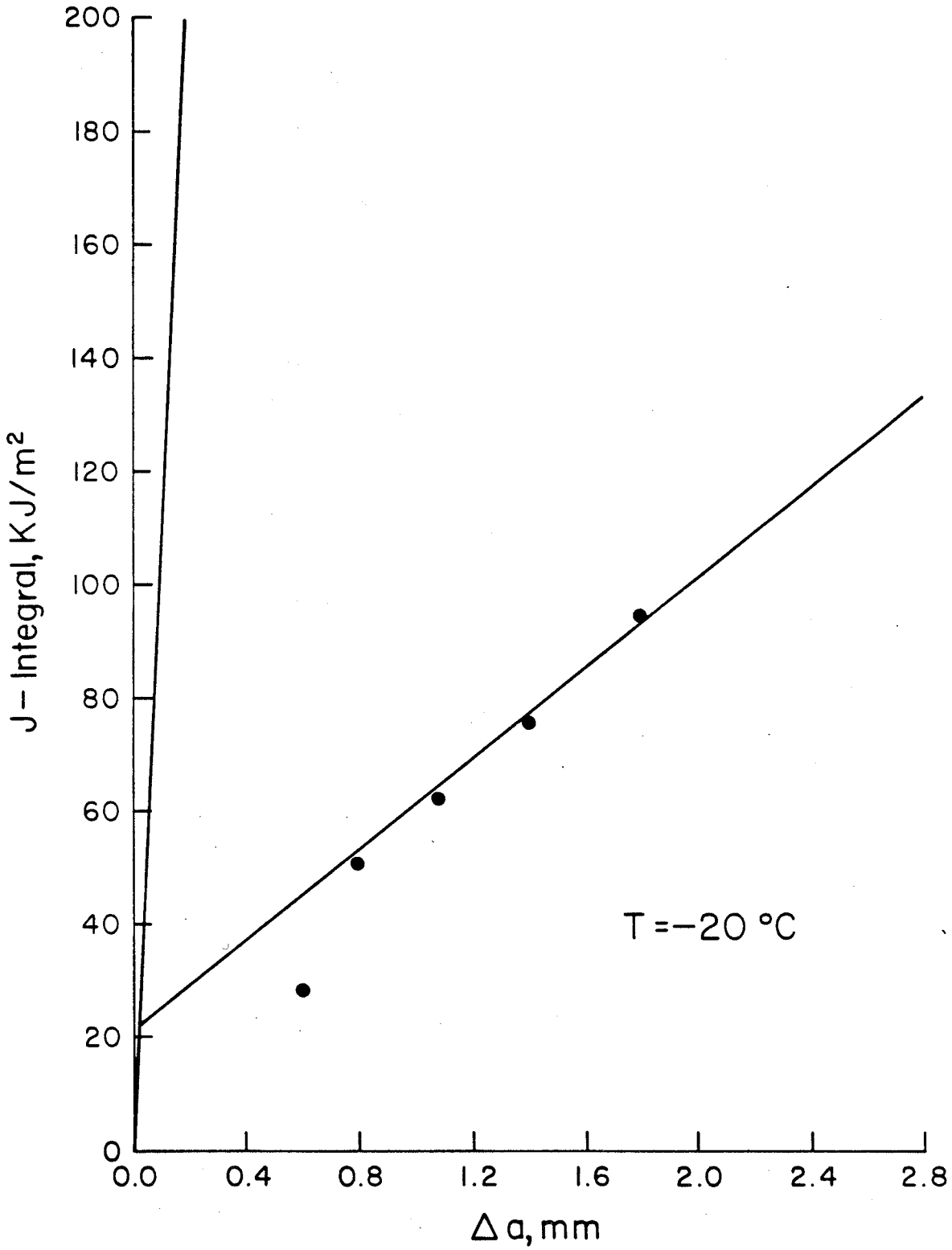

Figure 4.6(e) J-resistance curves for the different testing temperatures for AISI 1045 steel in the annealed condition.

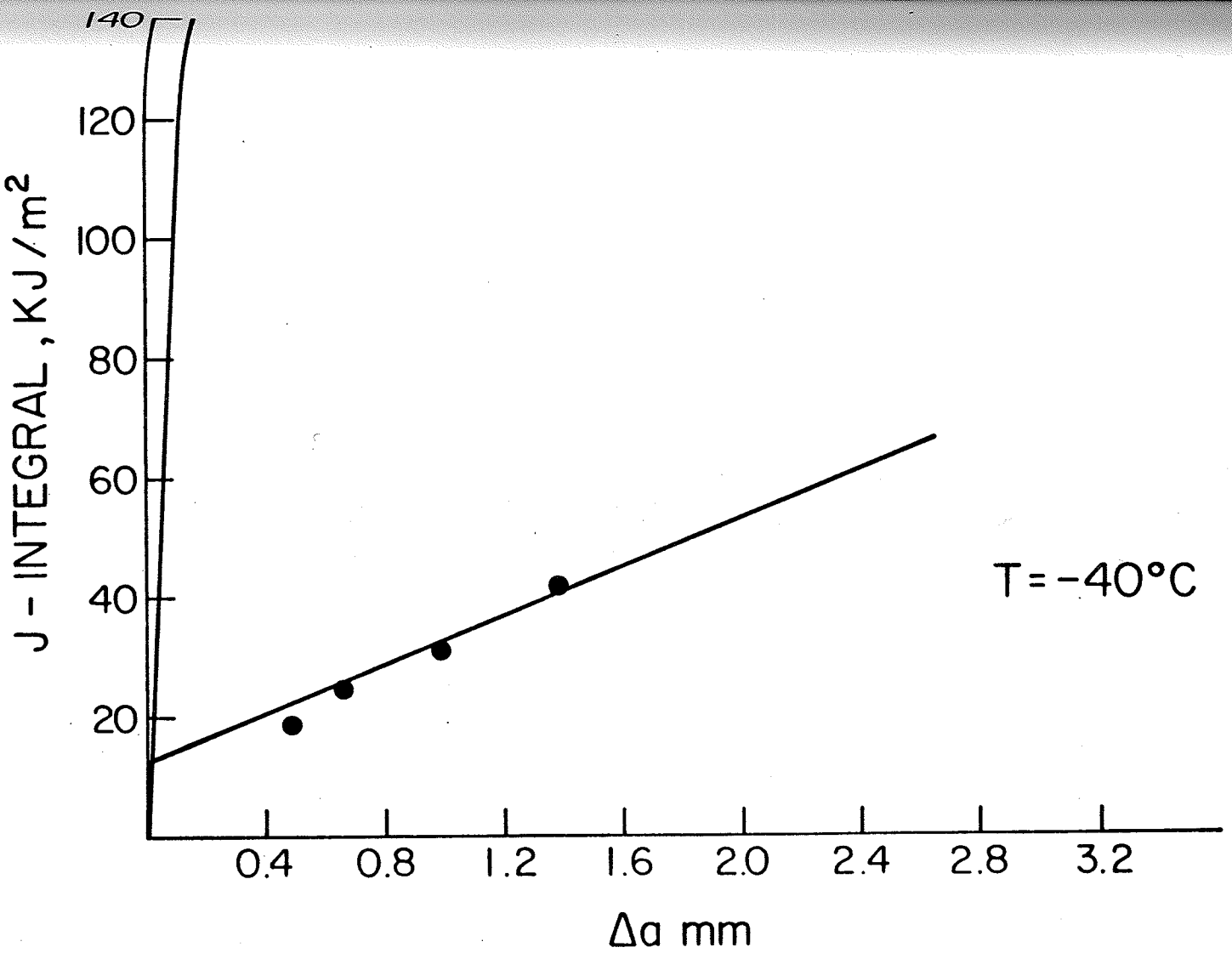

Figure 4.6(f) J-resistance curves for the different testing temperatures for AISI 1045 steel in the annealed condition.

The variation of J_{IC} with temperature is presented in Fig. 4.7. J_{IC} decreases from a value of 70 KJ/m^2 at 25°C to a value of 9 KJ/m^2 at -60°C. The relation between J_{IC} and temperature appears to be characterized by the presence of two regions. Namely, from -60°C to about -20°C, the slope of the curve of J_{IC} with temperature is much lower than in the region from -20°C to 25°C. While it can be initially postulated that this transition defines the change between linear elastic and elastic-plastic behavior, further analysis is required to determine the reason for this transition in terms of the two processes of crack blunting followed by stable crack growth.

The slope of the crack advance line, as well as the tearing modulus T_R defined by Paris et al [100] as:

$$T_R = \frac{dJ}{da} \cdot \frac{E}{\sigma_y^2} \qquad (4.2)$$

as a function of temperature are shown in Figs. 4.8 and 4.9 respectively. Both Figures show an almost linear relation of these parameters as a function of temperature in the region from 25°C to -40°C. It should be pointed out that at -60°C, the behavior of the material is entirely elastic and no stable crack growth is observed. Because the slope of the crack advance line and T_R vary linearly with temperature down to -40°C, it can be deduced that the same mechanisms of stable crack growth are present as long as stable crack propagation takes place, in the range of -40°C to 25°C.

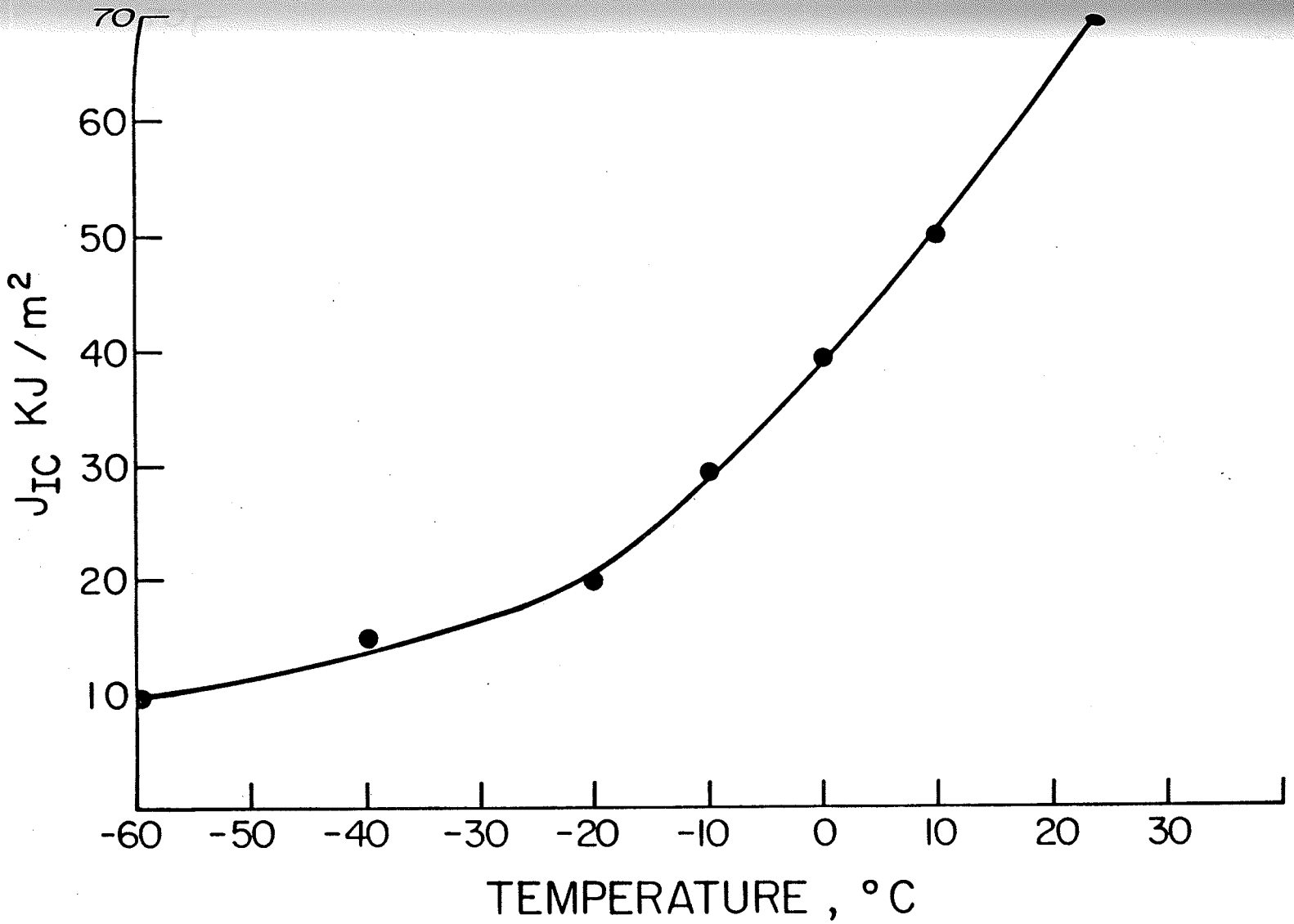

Figure 4.7 J_{IC} versus temperature for AISI 1045 steel in the annealed condition.

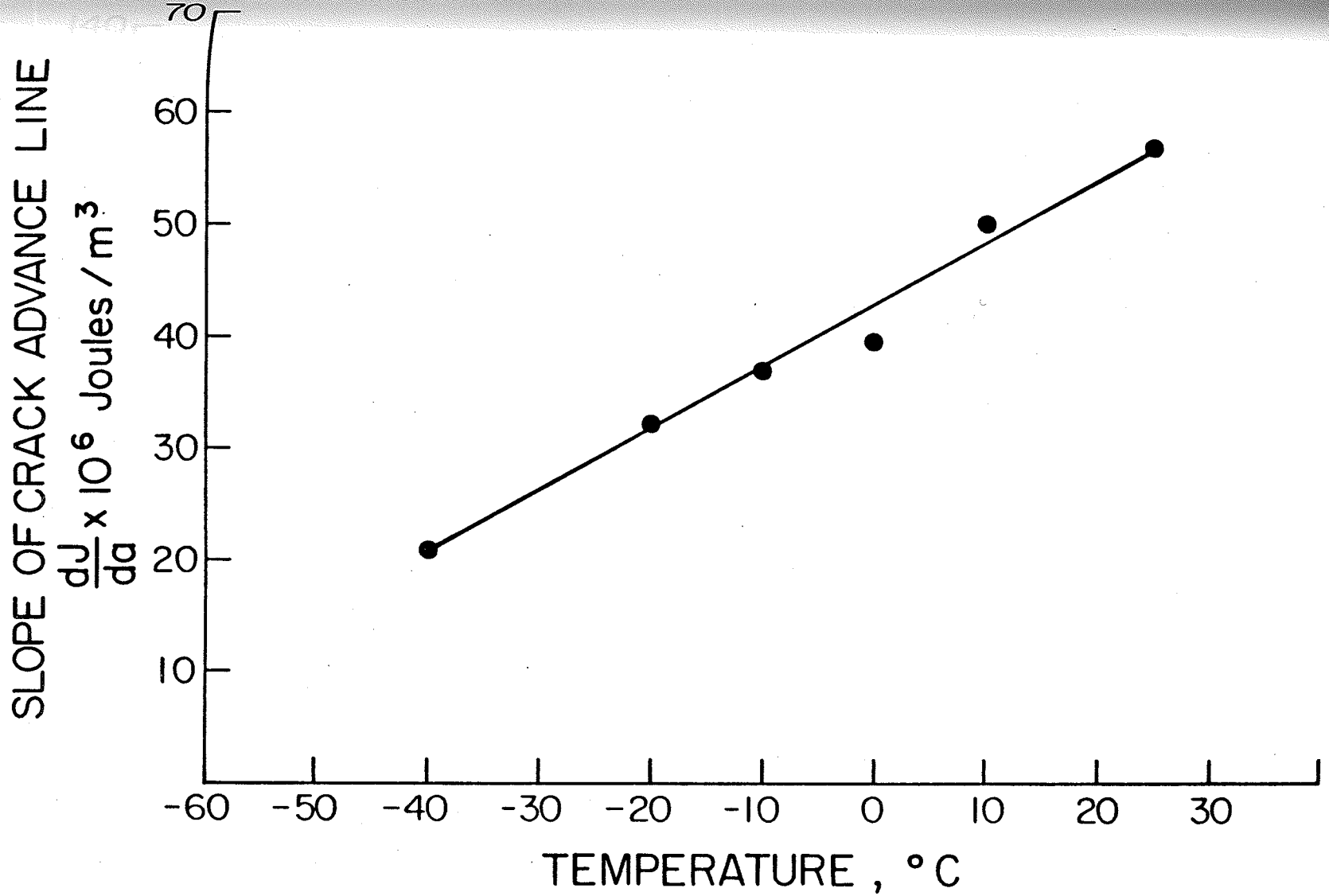

Figure 4.8 Variation of the slope of the crack advance line with temperature for annealed 1045 steel.

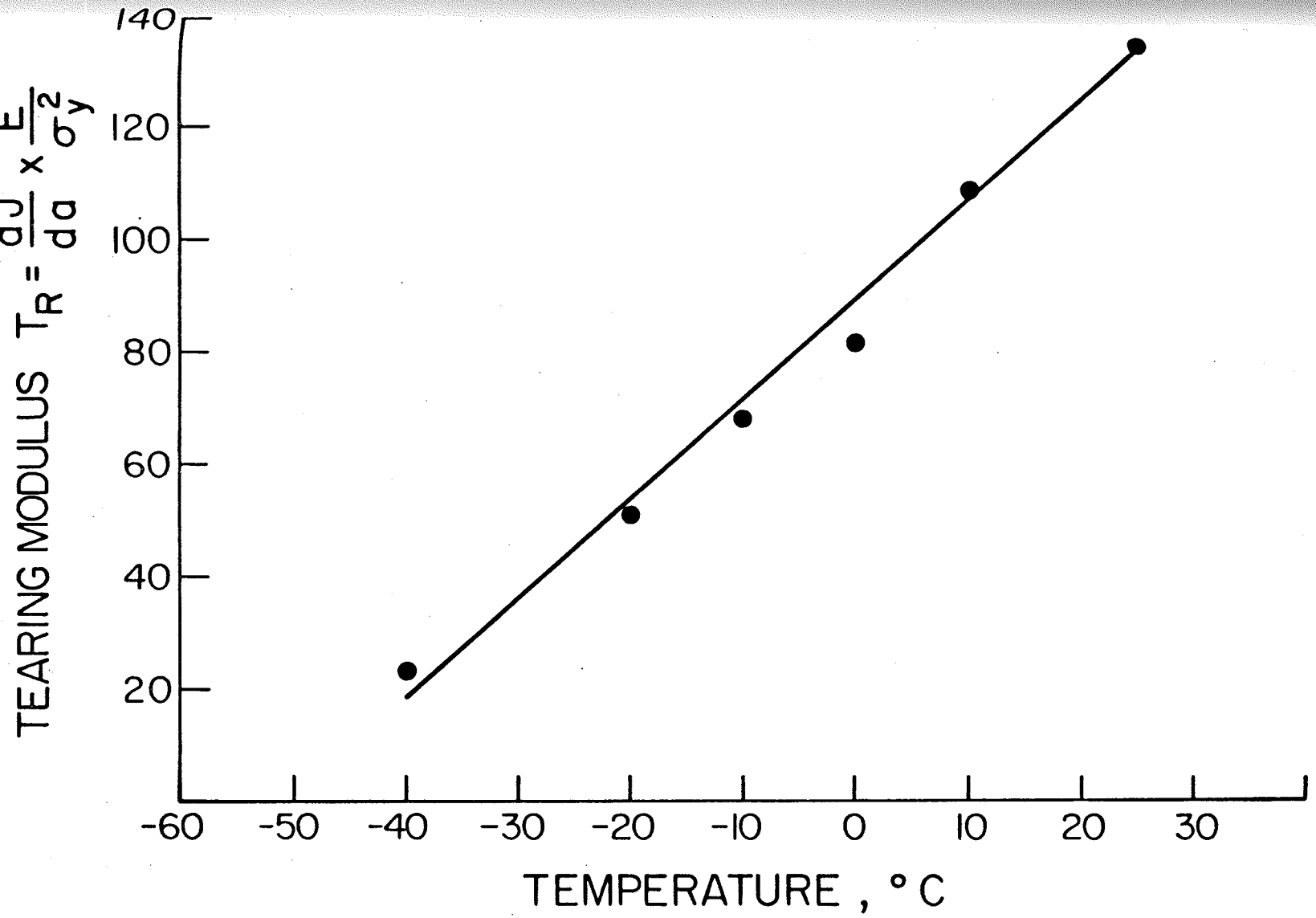

Figure 4.9 Variation of the tearing modulus (T_R) with temperature for annealed 1045 steel.

The variation of the parameter Δa_{cr} (critical crack extension) with temperature is shown in Fig. 4.10. Also Fig. 4.11 gives the effect of temperature on the critical load line displacement δ_{cr}. Both of these parameters show a transition at about -20°C.

The variation of tensile ductility ε_{ft} and bulge ductility ε_{fb} or $\varepsilon_{f,\alpha=1,\ \beta=0}$ with temperature show the same type of behavior. Actually, the relationship between ε_{ft} and ε_{fb} is linear in all the temperature range studied as shown in Fig. 4.12.

The relationship between the fracture toughness J_{IC} and the bulge ductility is given in Fig. 4.13. A linear relationship is obtained in the range from -40°C to 25°C. A quantitative analysis of the variation of J_{IC} with bulge ductility will be presented in the next chapter.

4.5 Quasi-Static and Dynamic Fracture Toughness (J_{IC}) Results

4.5.1 Quasi-static Tests

Three wedge loaded pre-fatigued tension specimens with the notch machined in the longitudinal-transverse (LT) orientation were fractured. A typical load-displacement curve as well as the signal of the strain gage which was attached to the specimen to detect the point of onset crack propagation, are shown in Fig. 4.14.

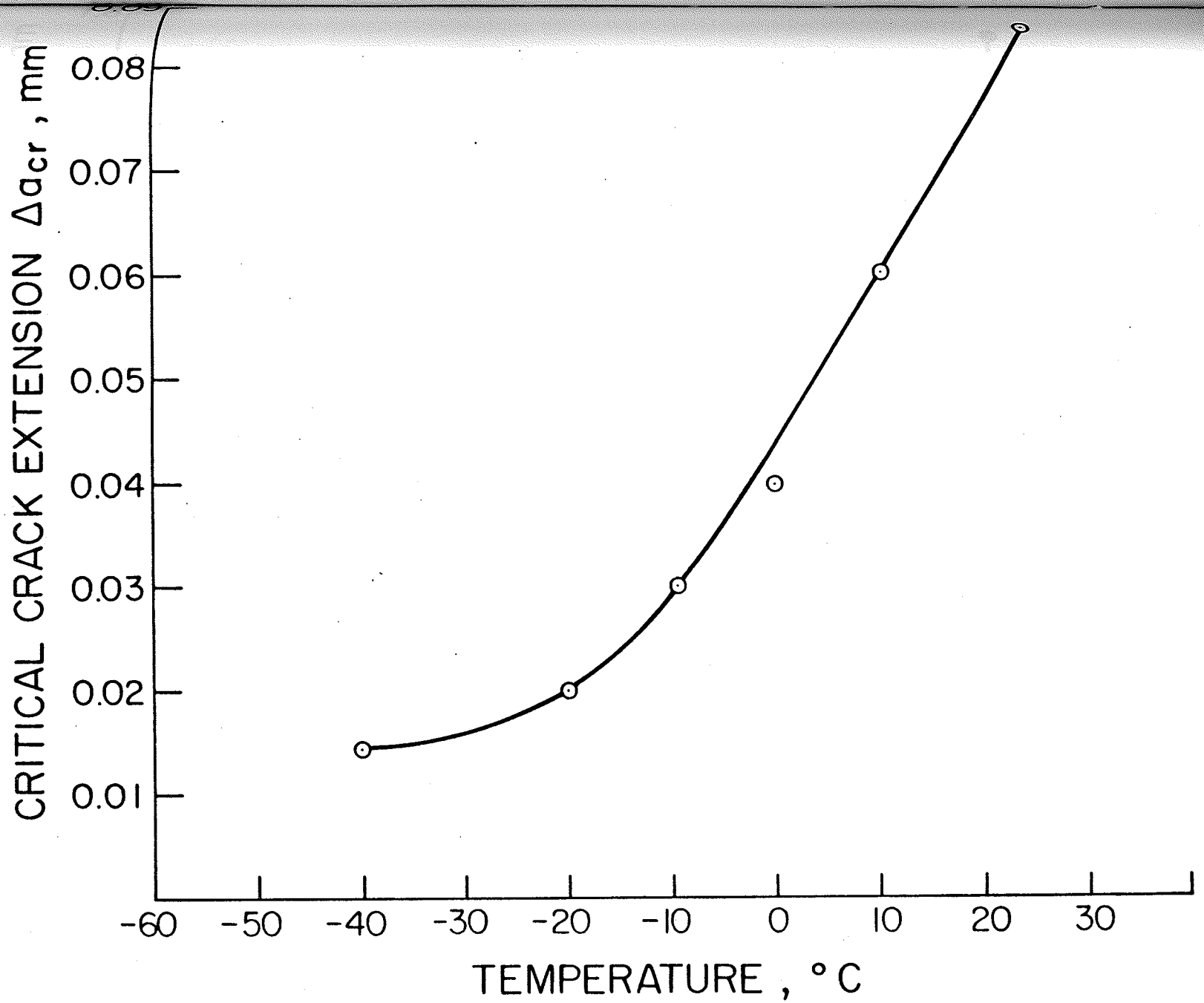

Figure 4.10 Variation of the critical crack extension (Δa_{cr}) with temperature for annealed 1045 steel.

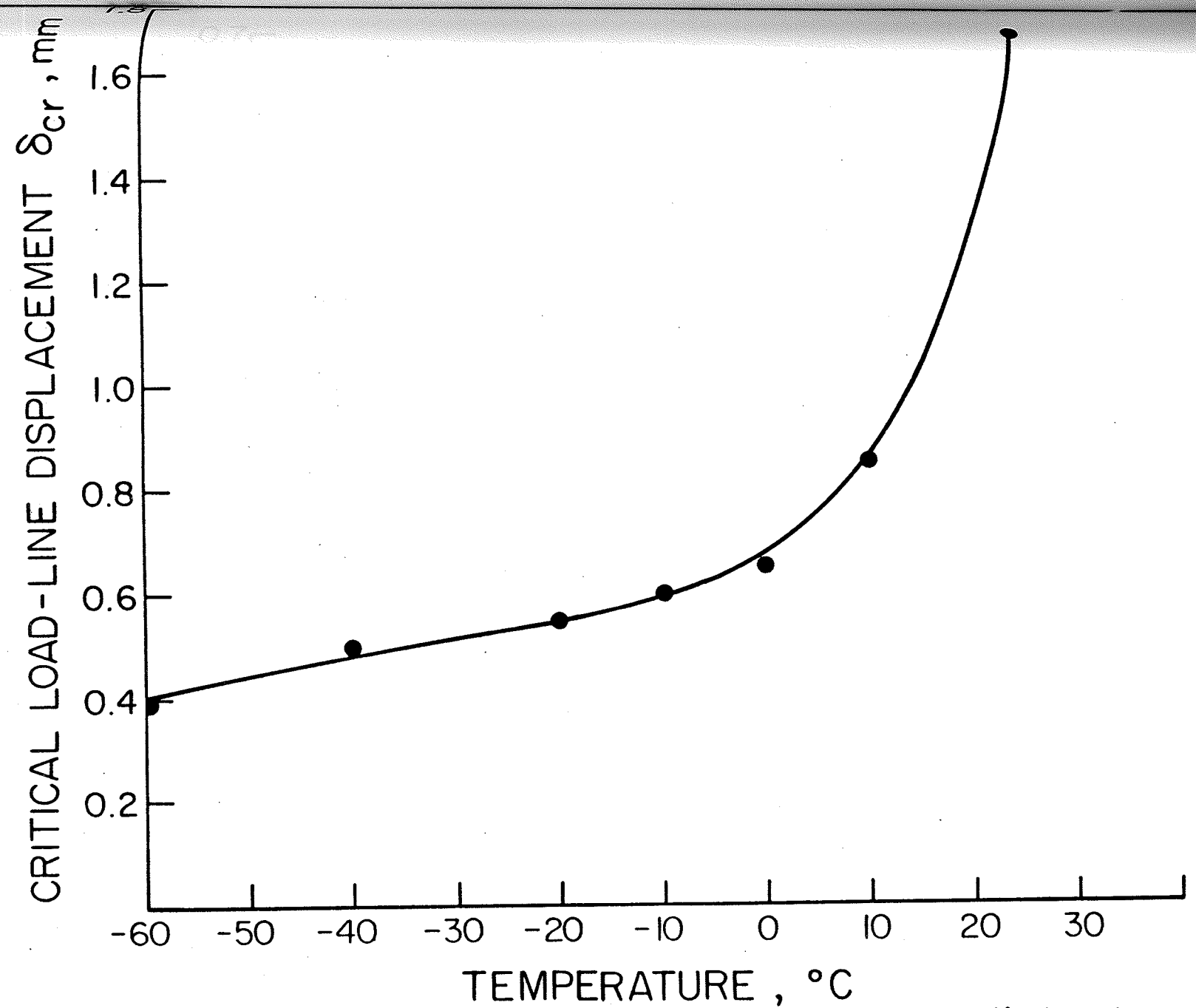

Figure 4.11 Variation of the critical load line displacement (δ_{cr}) with temperature for annealed 1045 steel.

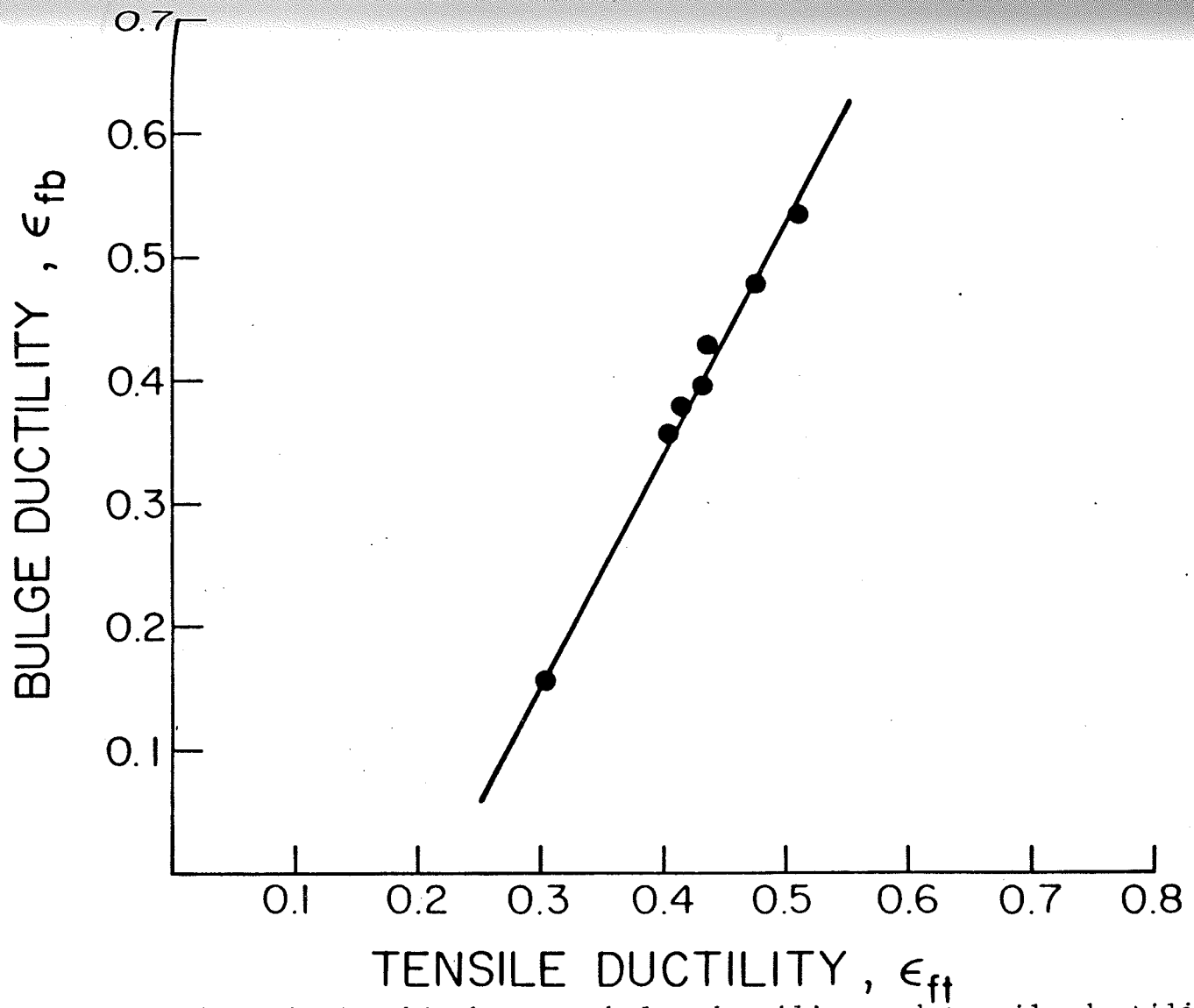

Figure 4.12 The relationship between bulge ductility and tensile ductility for annealed 1045 steel.

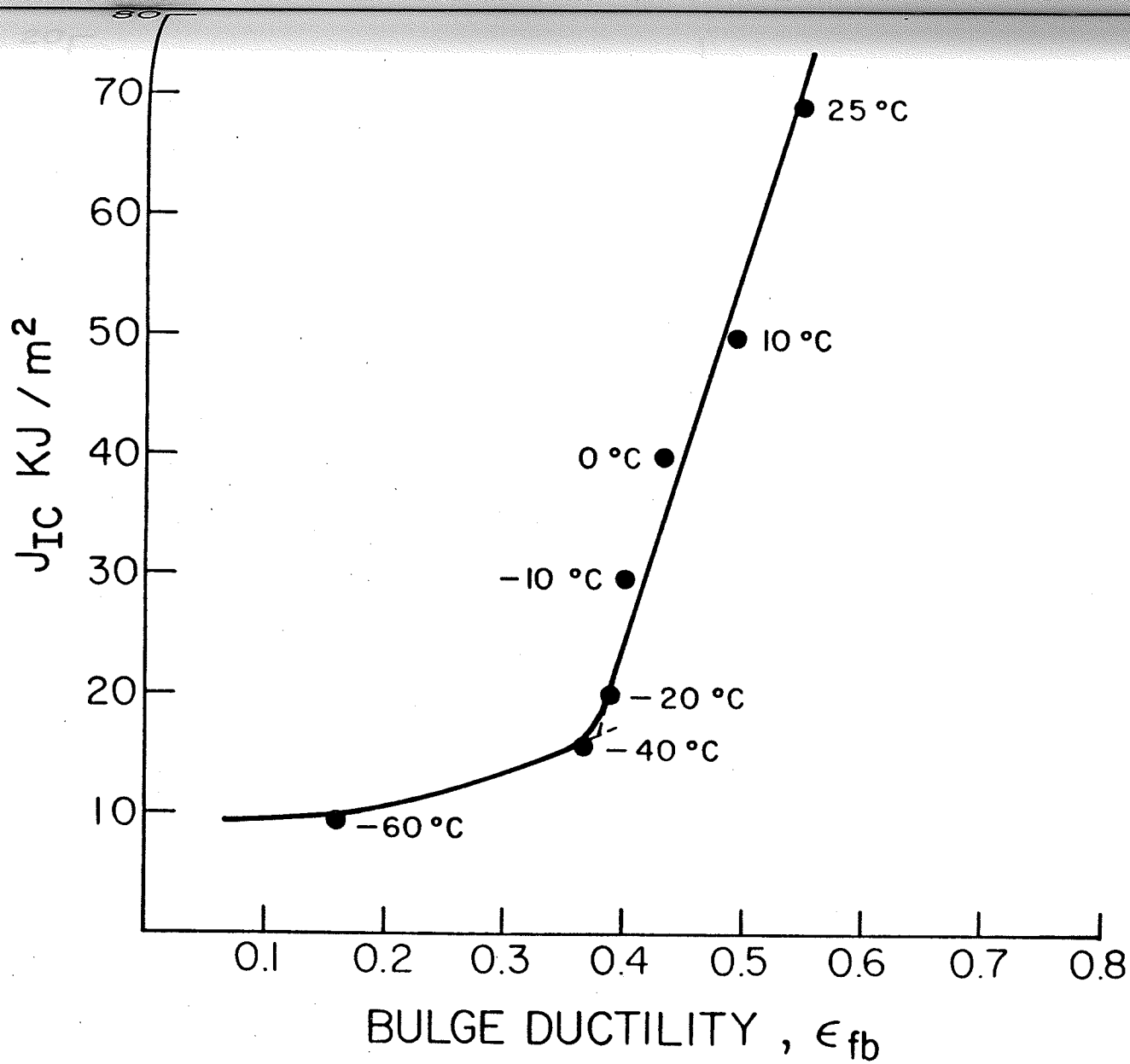

Figure 4.13 The relationship between J_{IC} and bulge ductility for annealed 1045 steel.

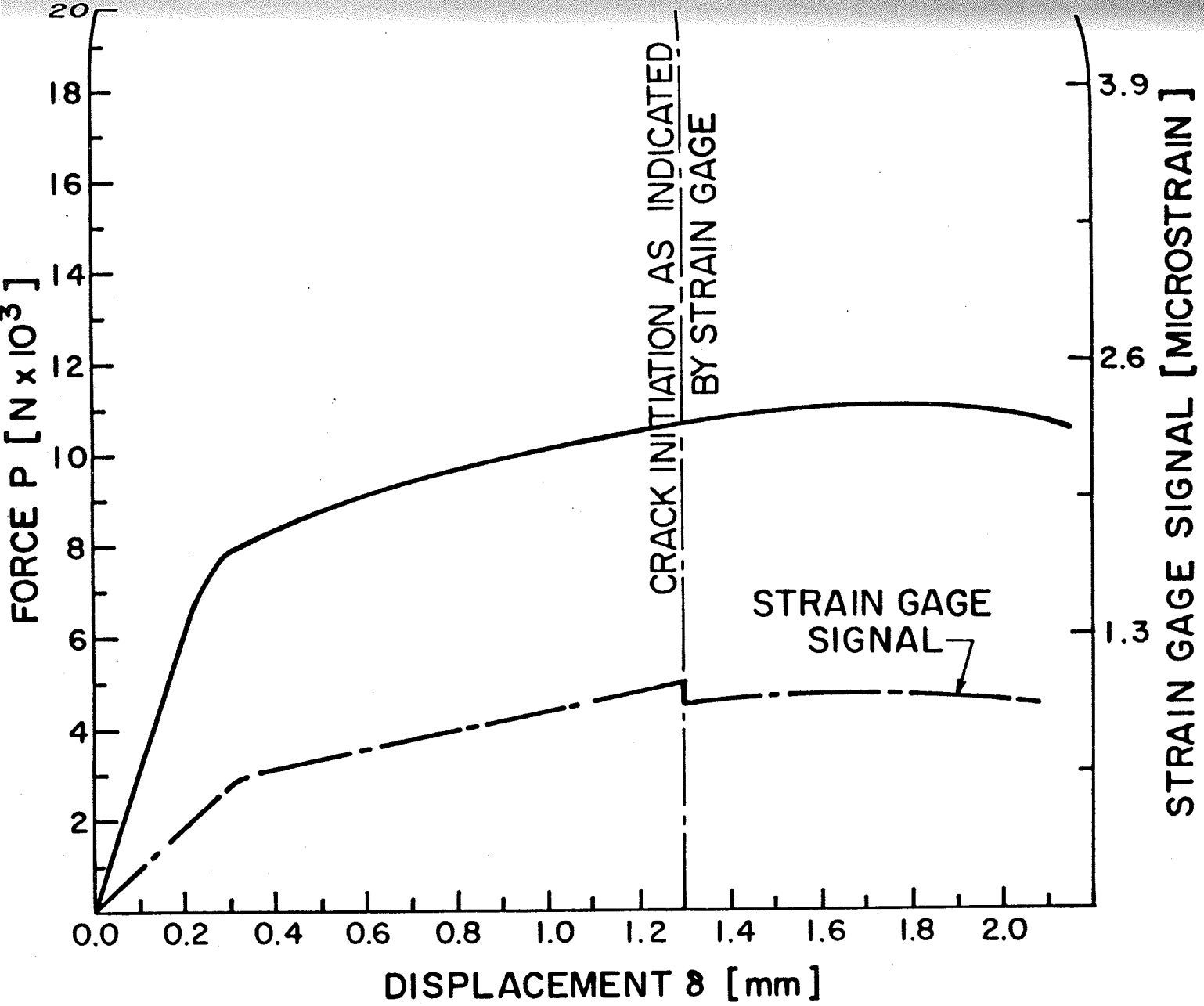

Figure 4.14 Typical load-displacement curve and strain gage output during quais-static tests of WLCT specimens.

For each load-displacement curve up to the point of onset of crack propagation, as determined from the output of the strain gage, the parameter $\frac{U}{bB}$ was calculated. The values of this parameter are given in Table 4.1. An average value for $\frac{U}{bB}$ of 69 KJ/m^2 was obtained. Comparing the fracture toughness values of WLCT specimens with those obtained from standardized three-point bending specimens indicates that if

$$J = \frac{kU}{bB} \tag{4.3}$$

then k has a value of 2 for the three point bending specimens while it is around 1 for the WLCT specimen. This an empirical calibration and thus k should be identified as one for the WLCT specimen. The value of k equal one may be attributed to the higher stiffness of the WLCT specimen compared to the three point bending specimen as shown in Fig. 4.15. It will be further assumed that k has a value of 1 for the dynamic tests and thus the parameter $\frac{U}{bB}$ will be equal to J_{IC} for all tests on the WLCT specimens.

4.5.2 Dynamic Tests

Seven wedge loaded compact tension specimens (WLCT) were tested using the Split Hopkinson pressure bar. They all showed similar behavior, and typical signals comprising the incident wave $\varepsilon_I(t)$, the reflected wave $\varepsilon_R(t)$, the transmitted wave $\varepsilon_T(t)$, and the specimen strain gage signal ε_{SR} are shown in Fig. 4.16. Load and displacement as a function of time were plotted. A typical example is shown in Fig. 4.17. Eliminating time from these plots results in

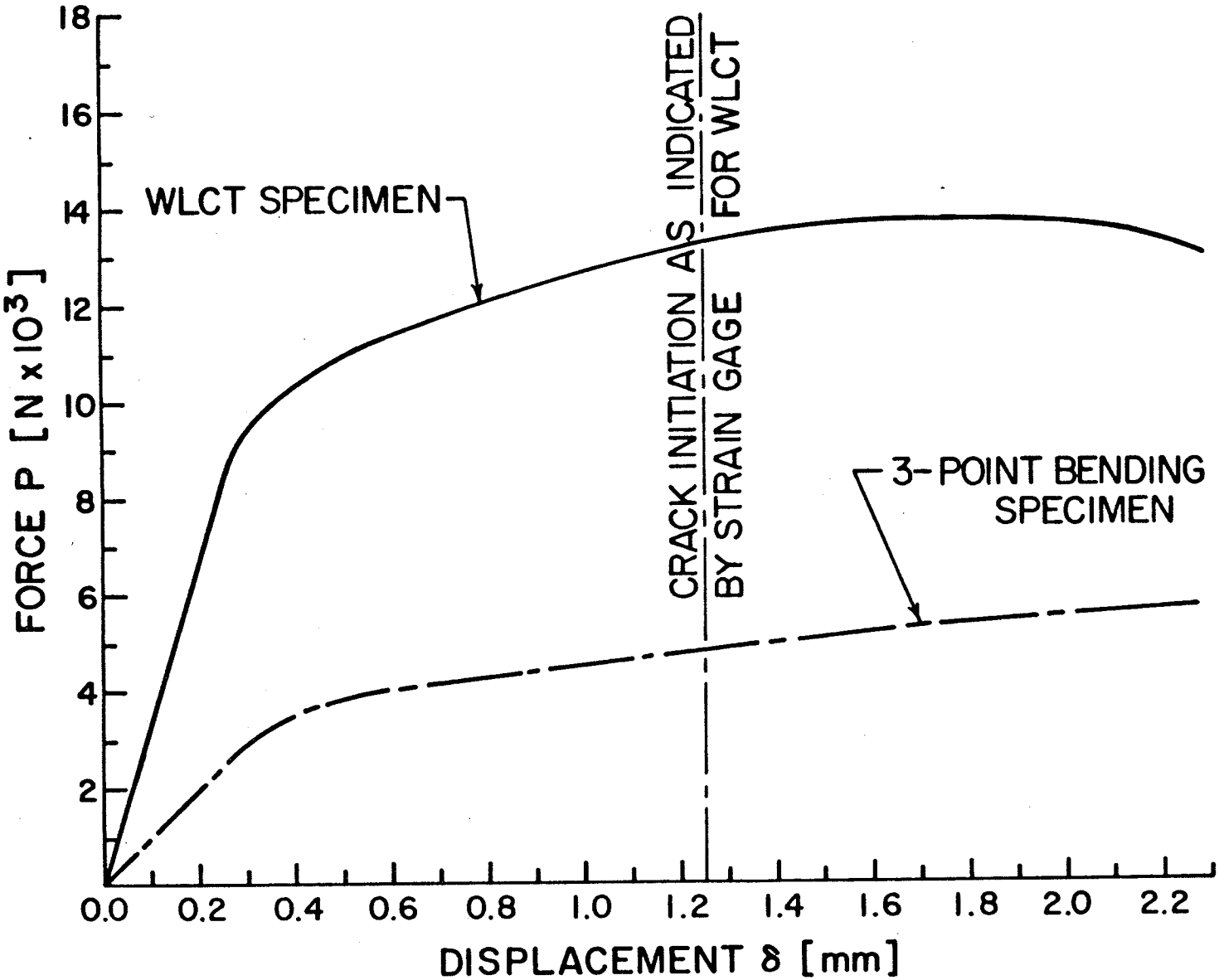

Figure 4.15 Comparison between a typical load-displacement curve for a WLCT specimen and a three-point bending specimen in quasi-static tests.

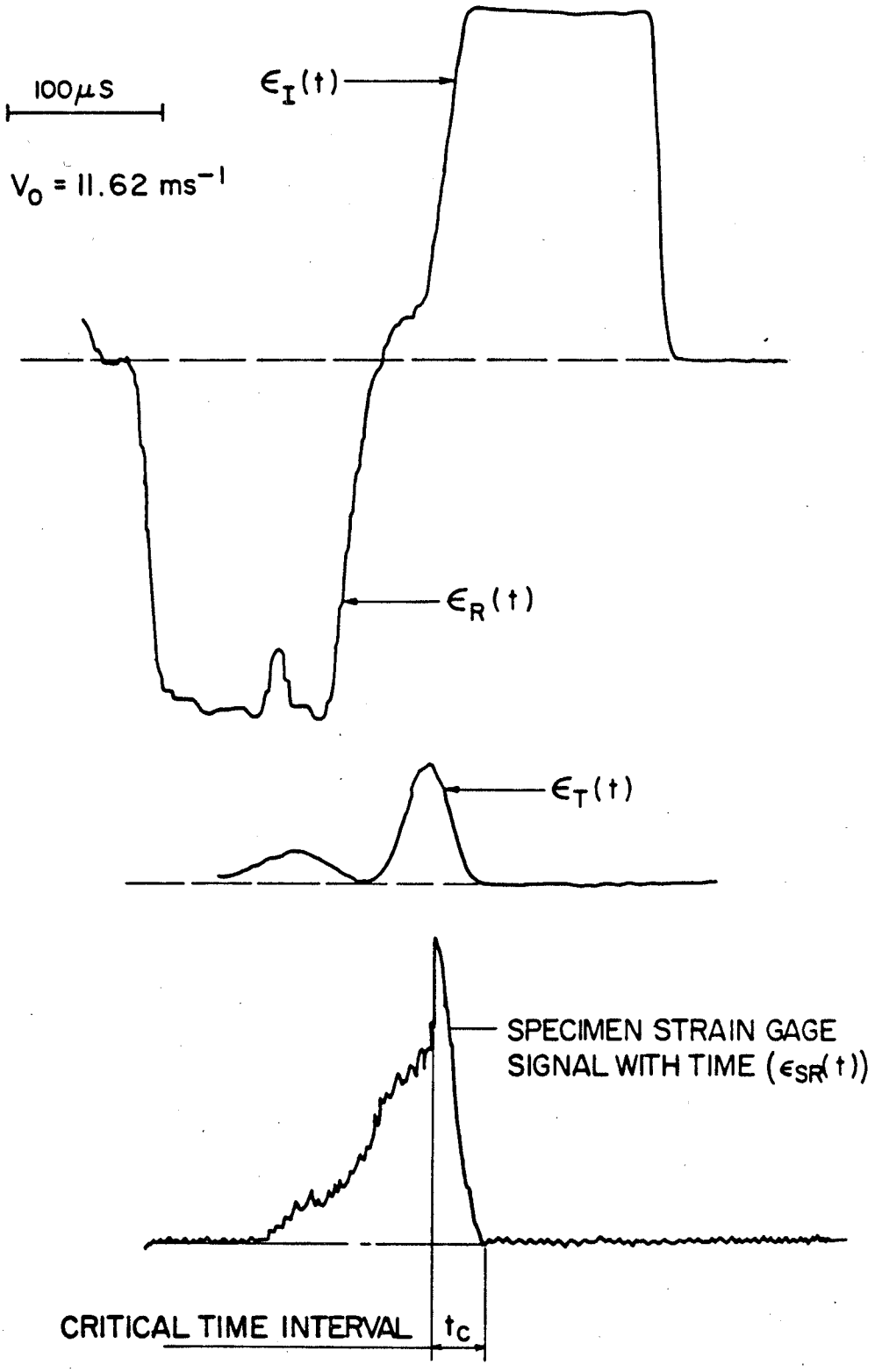

Figure 4.16 Typical $\varepsilon_I(t)$, transmitted $\varepsilon_T(t)$ and reflected $\varepsilon_R(t)$ elastic strains during impact tests. Also shown is the output of the strain gage mounted on the specimen.

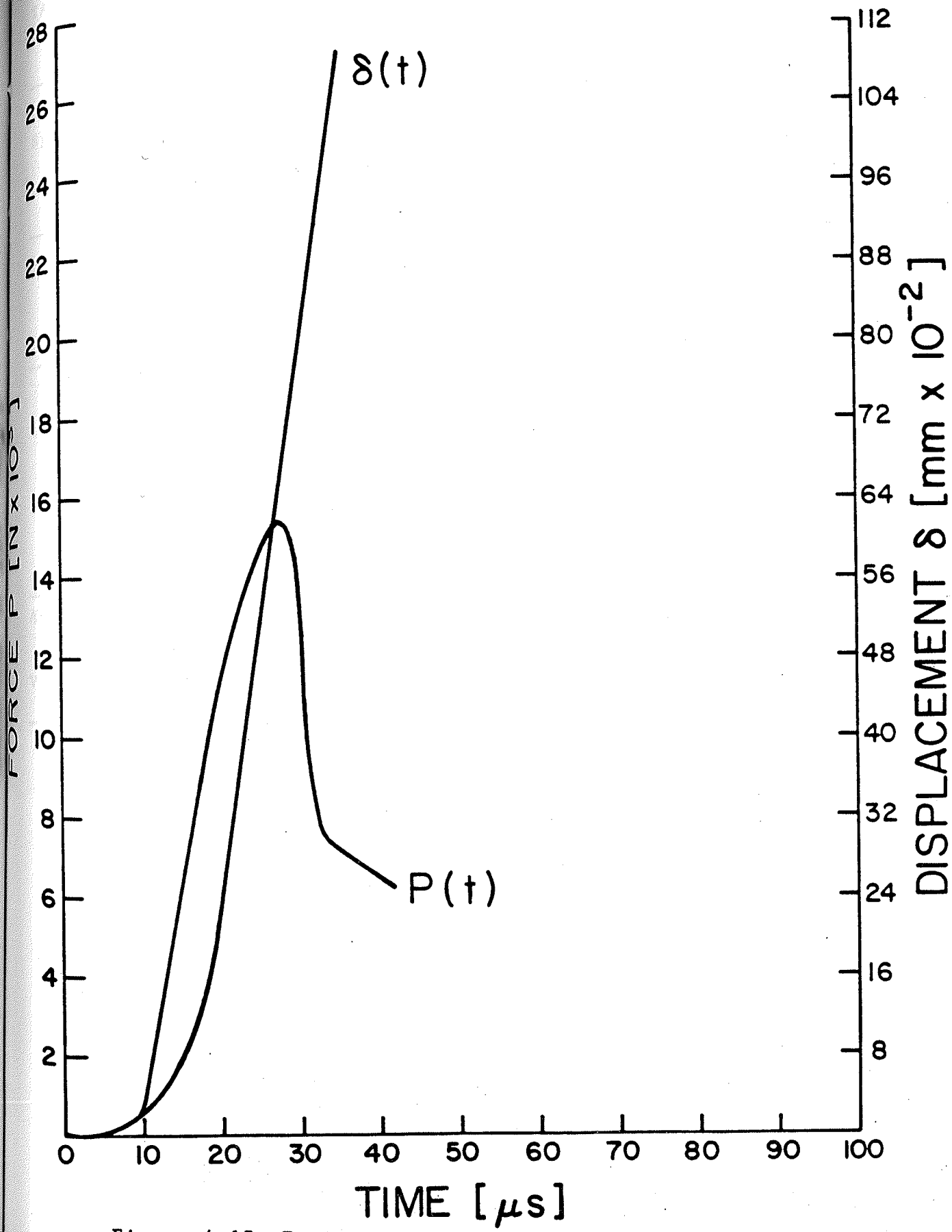

Figure 4.17 Typical load-time and displacement-time curve during impact loading.

TABLE 4.1 Results of WLCT specimens under quasi-static and dynamic testing

Specimen No	Type of Testing	$\frac{U}{bB}$ KJ/m^2	$J_{IC} = \frac{U}{bB}$ Average value	Equivalent K_{IC} MPa$\sqrt{m}$	Critical Time t_c μs	$K_I = \frac{\dot{K}_{IC}}{t_c}$ MPa$\sqrt{m}$ S^{-1}
X1	Quasi-Static	65.7		119.4	3.12×10^8	0.38
X2	Quasi-Static	77.5	68.5	140.8	3×10^8	0.4
X3	Quasi-Static	62.1		112.9	2×10^8	0.6
X4	Dynamic	28.1		46	30	1.5×10^6
X5	Dynamic	22.5		36.9	30	1.33×10^6
X6	Dynamic	30.1		49.1	27	1.8×10^6
X7	Dynamic	31.6	27.8	51.6	20	2.5×10^6
X8	Dynamic	33		54	25	2.16×10^6
X9	Dynamic	38		62.2	25	1.32×10^6
Average	Quasi-Static Testing		68.5	124.5	2.66×10^8	0.5
Value	Dynamic Testing		27.8	50	26	3.1×10^6

load-displacement P (δ) curves such as that shown in Fig. 4.18. The time interval up to the onset of crack propagation as indicated by the specimen strain gage signal, was used to define the critical time t_c.

The value of $\frac{U}{bB}$ for all specimens is also listed in Table 4.1, with an average equal to 27.8 KJ/m^2.

4.6 Stretch Zone Width Measurements

4.6.1 Three Point Bending Specimens Tested at Different Temperatures

Scanning electron micrographs of the fractured surfaces of the three point bending specimens tested in the temperature range from -60°C to 25°C are shown in Fig. 4.19. The stretch zone width as well as the size of stable crack growth are identified. It is evident that these parameters increase as a function of temperature. This is shown in Figs. 4.20 and 4.21 for the stretch zone width and the stable crack growth respectively. While there is a marked transition in the variation of the stretch zone width with temperature occurring at about -20°C, a change in behavior of the stable crack growth with temperature occurs at a lower temperature, around -40°C.

The width of the stretch zone obtained was used to calculate the variation of fracture toughness J_{IC} with temperature. This is shown in Fig. 4.22. There is a

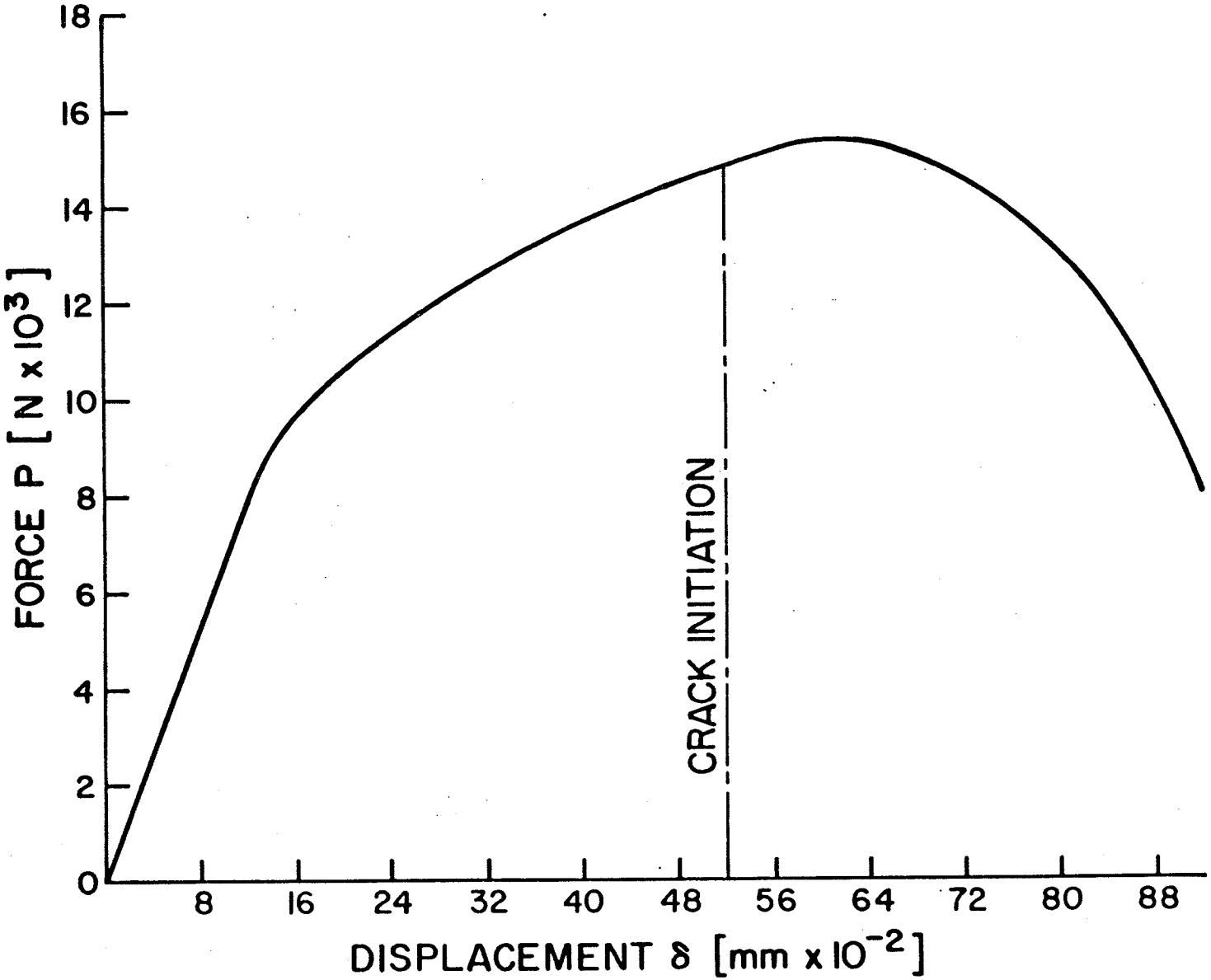

Figure 4.18 Constructed load-displacement curve during impact loading.

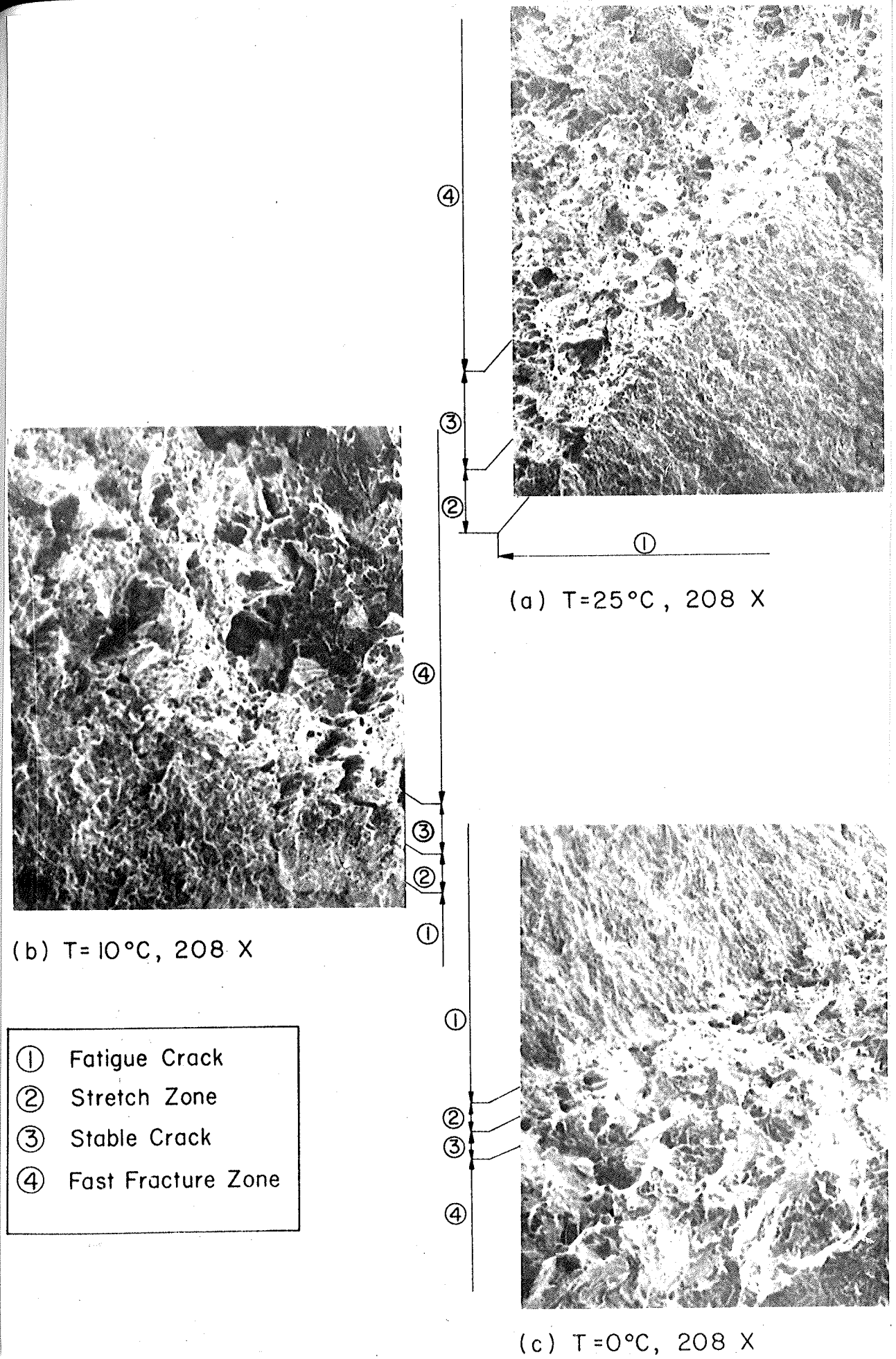

Figure 4.19 Scanning electron micrographs of the fractured three-point bending specimens at different temperatures.

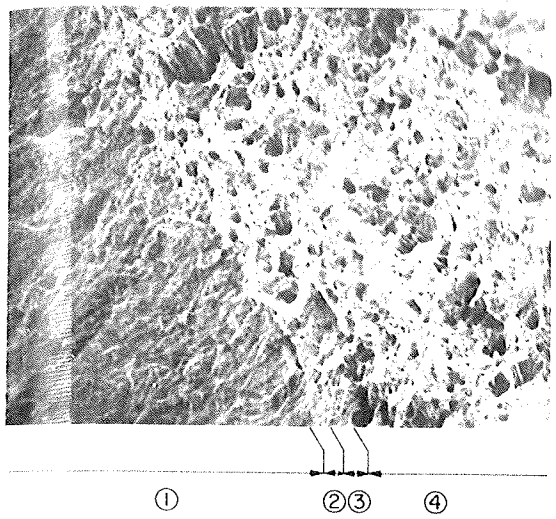

(d) T=−10°C, 208 X

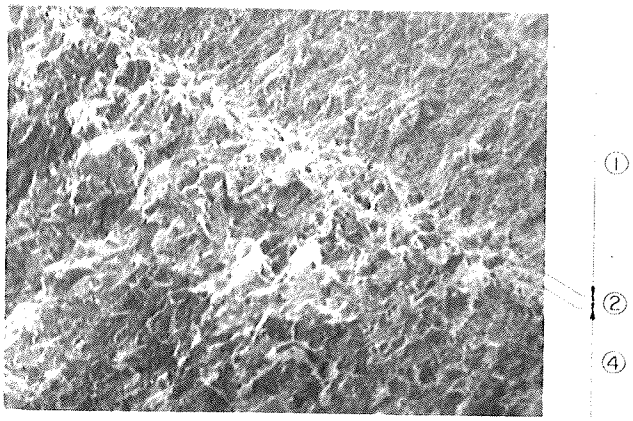

(f) T=−40°C, 182 X

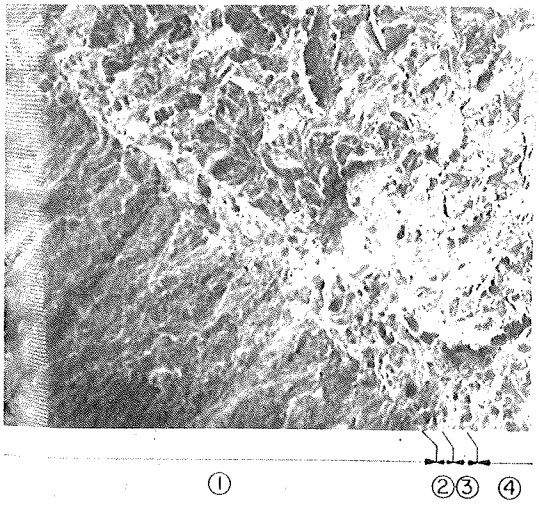

(e) T=−20°C, 182 X

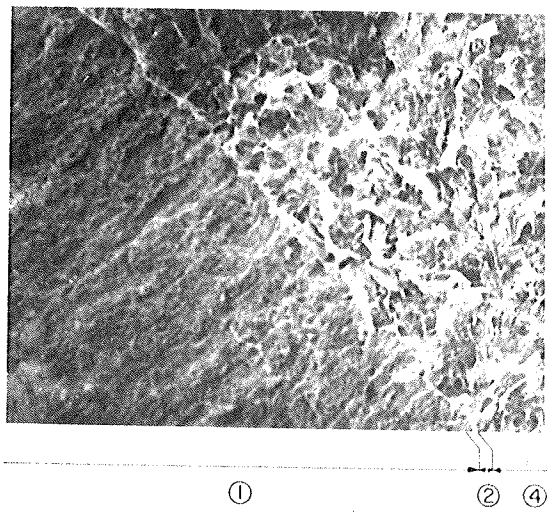

(g) T=−60°C, 182 X

Fig. 4.19 (Continue) Scanning electron micrographs of the fractured three-point bending specimens at different temperatures.

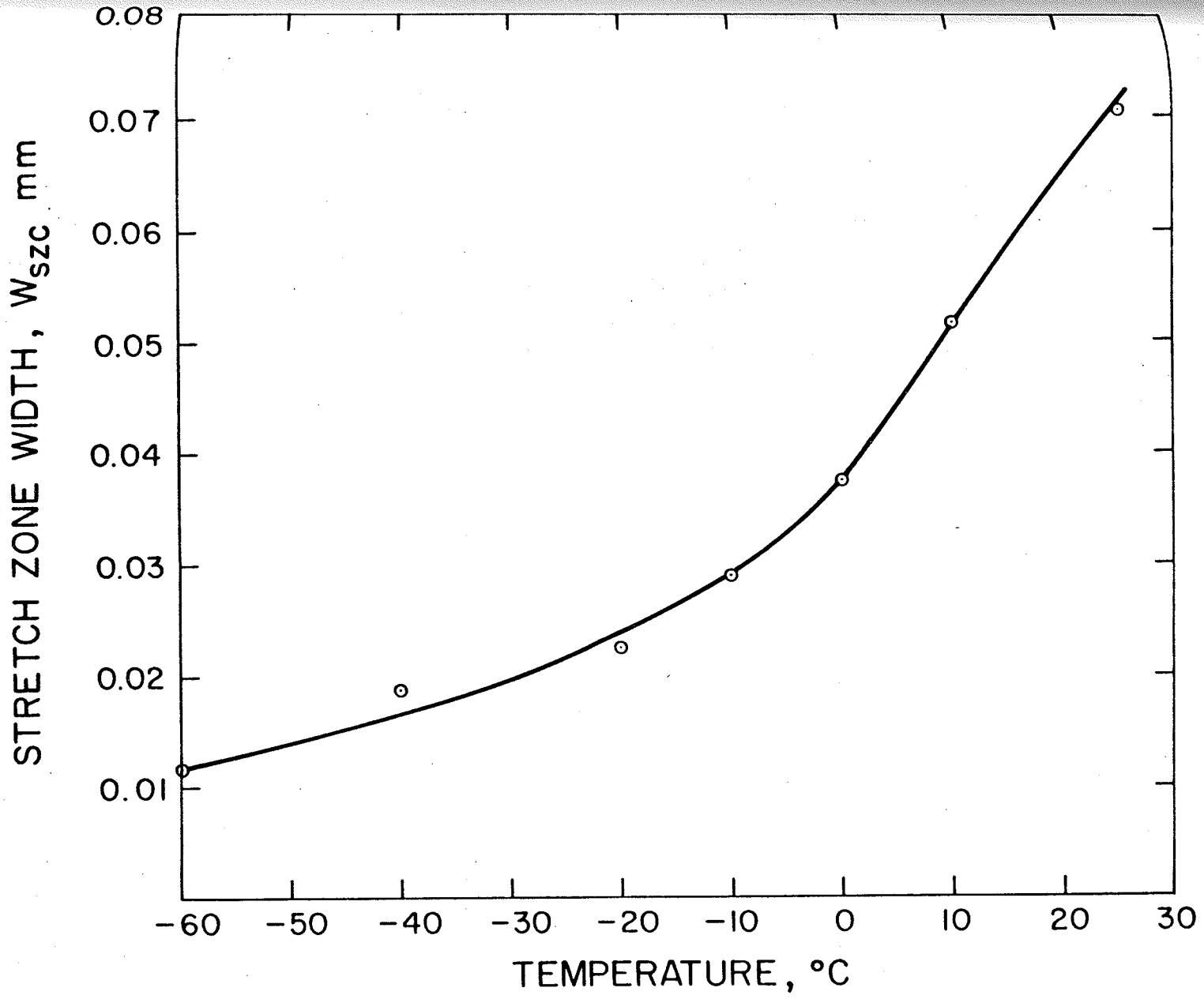

Figure 4.20 Stretch zone width as a function of temperature.

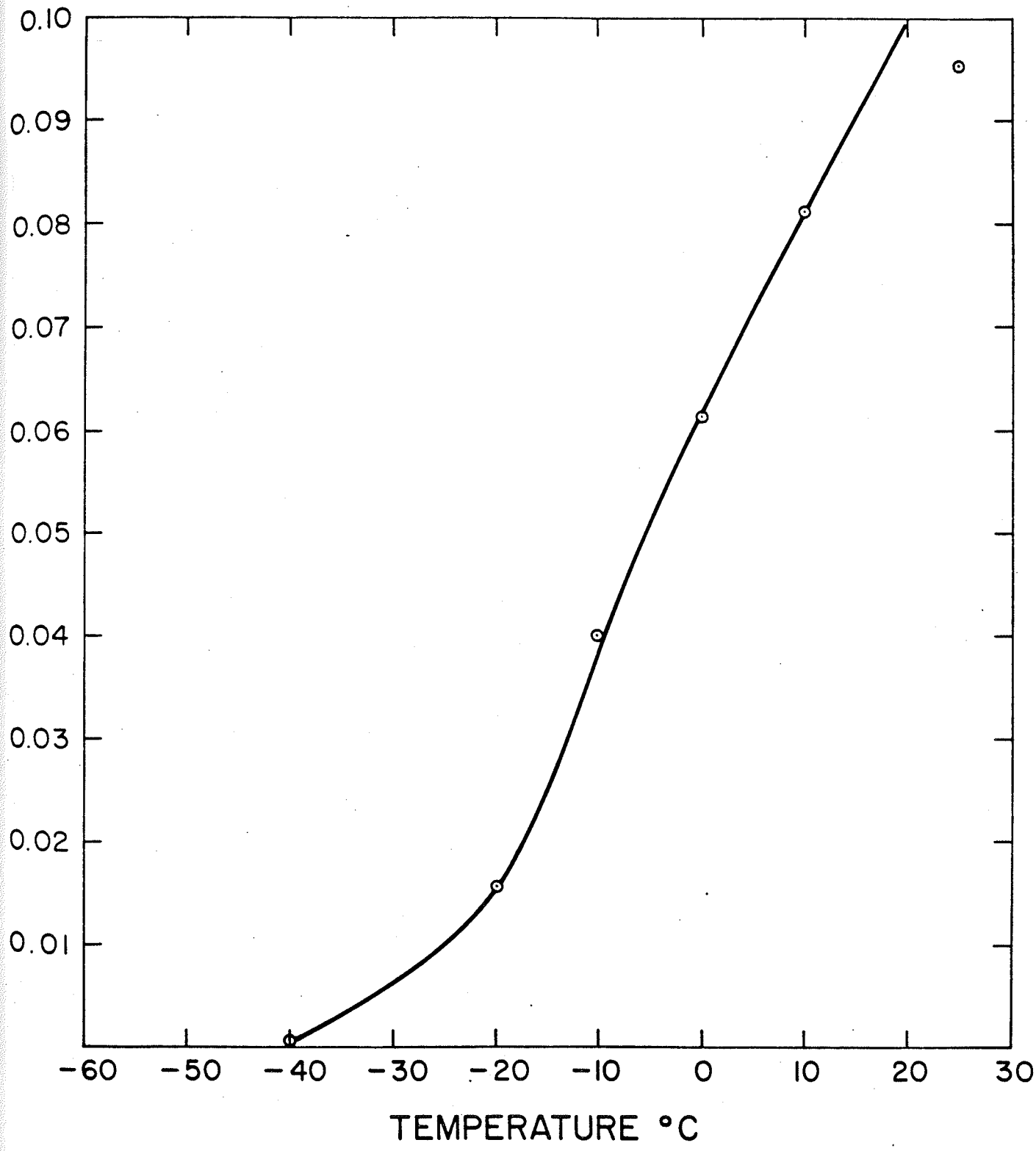

Figure 4.21 Stable crack growth as a function of temperature.

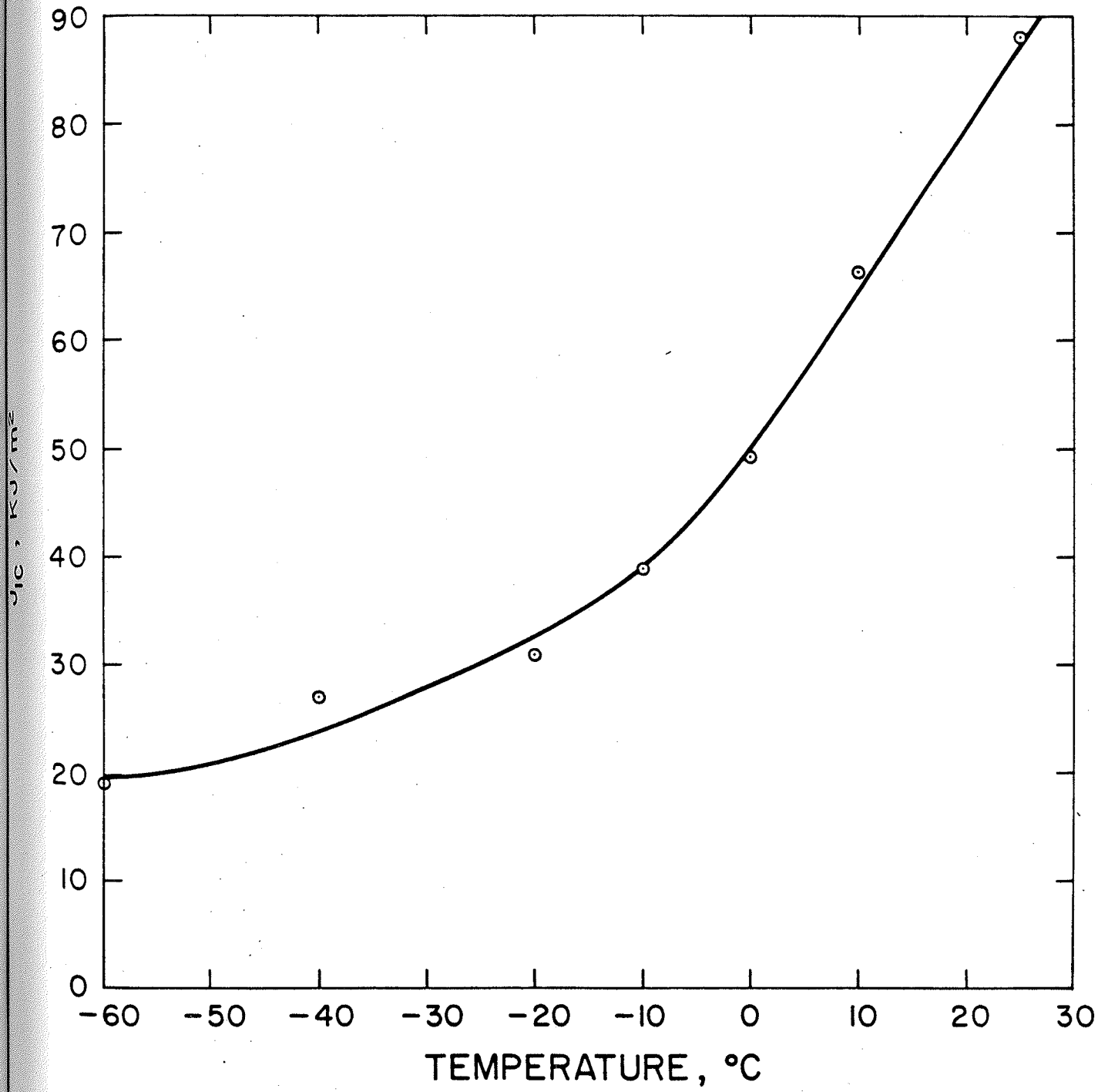

Figure 4.22 The variation of J_{IC}, calculated from stretch zone width measurements, with temperature.

transition from mostly linear elastic to elastic-plastic behavior taking place at -20°C. The presence of such a transition is in agreement with that reported from direct measurements of J_{IC} using the partial unloading method Fig. 4.7. However, the value of J_{IC} from stretch zone measurements are generally higher by about 25% to 40% depending on the temperature. This increase in J_{IC} is explained in terms of using a value of 2 for the constraint factor m in equation 3.21. However if such a parameter is adjusted for the variation in temperature, m was found to vary from 1.02 to 1.6 as shown in Fig. 4.23, where J_{IC} is taken from J-resistance curves obtained from partial unloading and COD is evaluated from stretch zone width measurements.

The relationship between bulge ductility and stretch zone width as well as stable crack growth are shown in Fig. 4.24. From -40°C to 25°C, the variation of bulge ductility with stable crack growth is linear, while the variation of bulge ductility with stretch zone width indicates a transition occuring at -20°C. It is noted that at the low temperature of -60°C, the material exhibits an entirely elastic behavior with unstable crack growth.

4.6.2 Wedge Loaded Compact Tension Specimens Tested under Quasi-Static and Dynamic Loading Conditions

Halves of broken wedge loaded compact tension

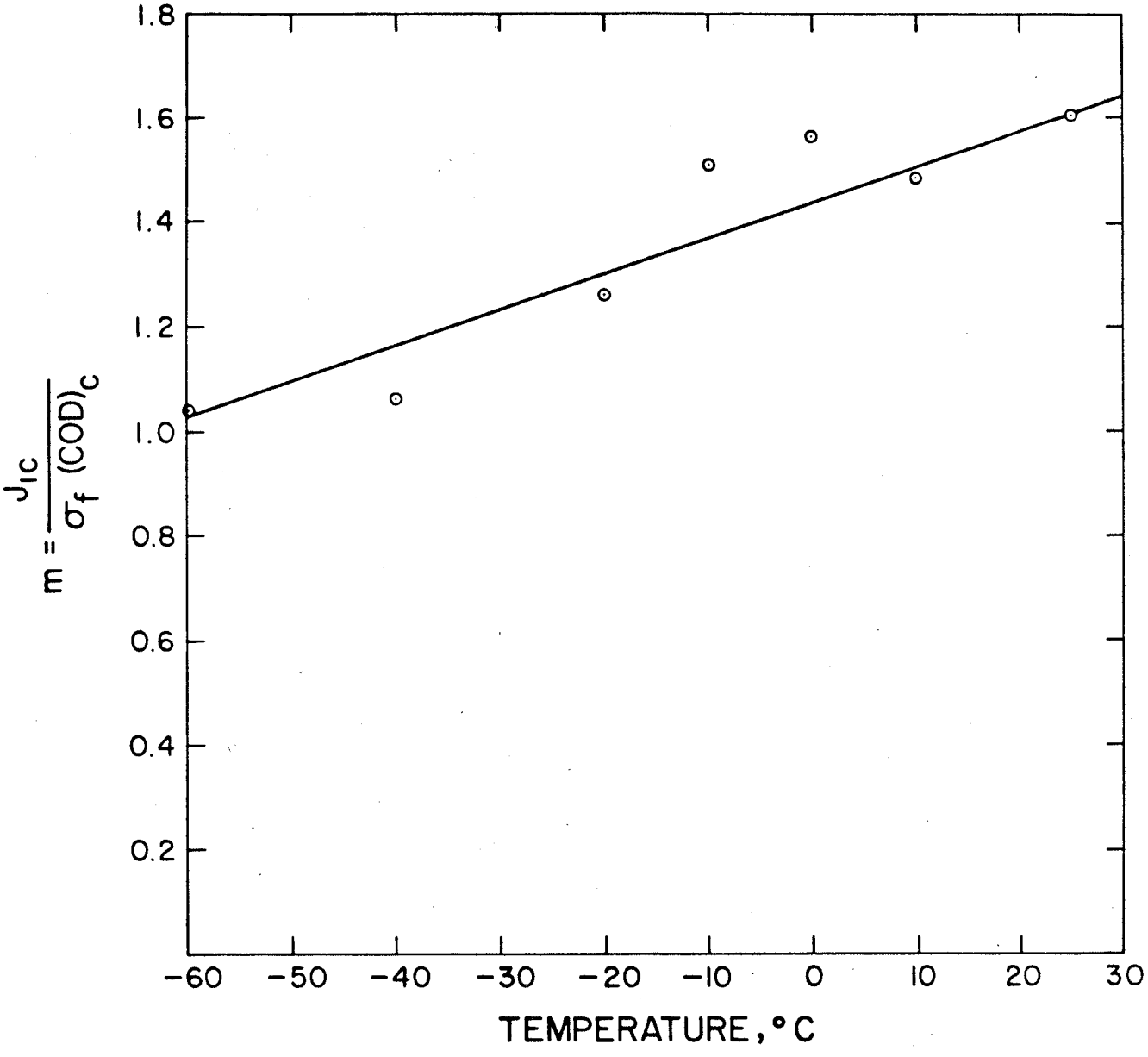

Figure 4.23 Dependence of constraint factor m on temperature.

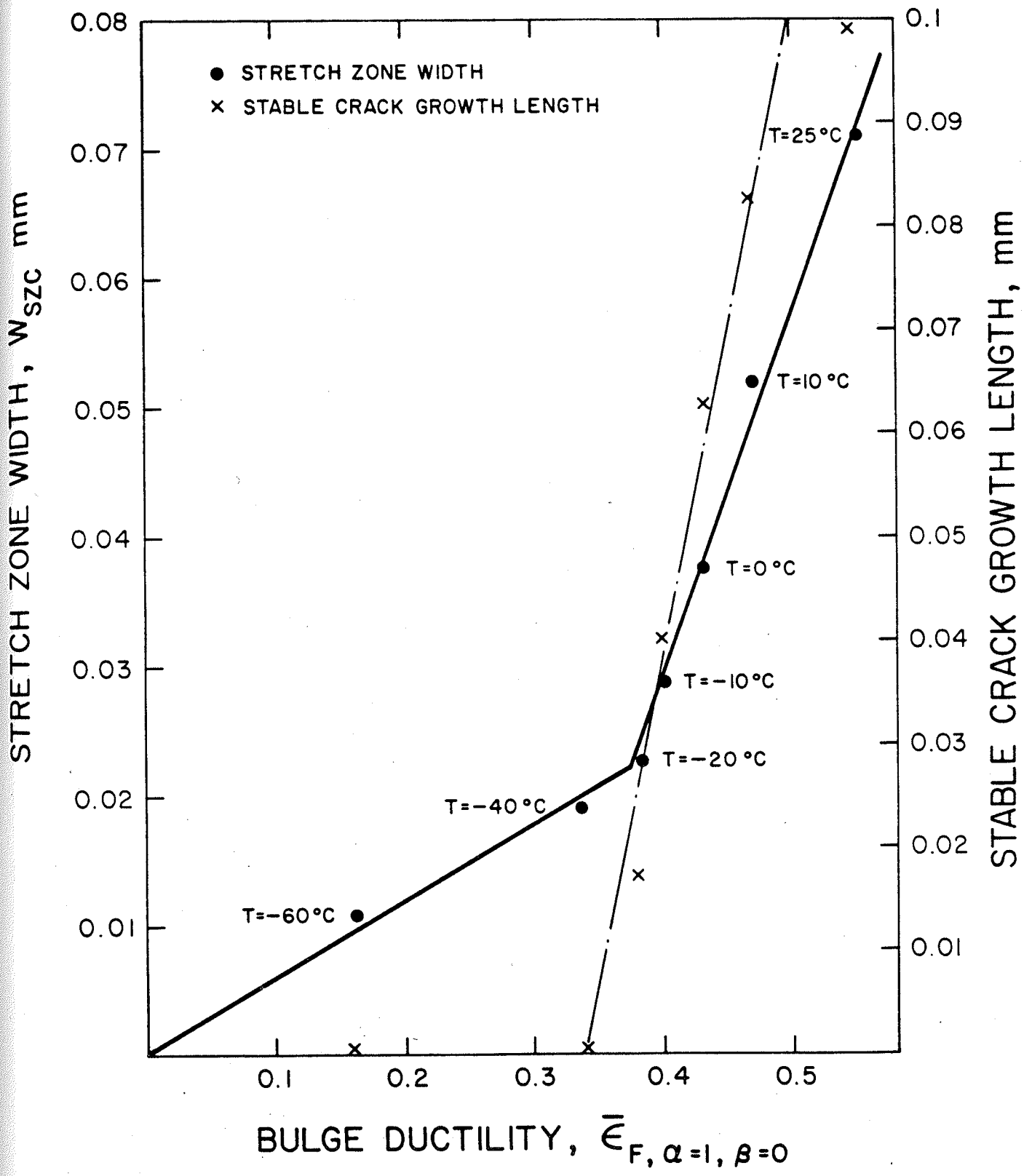

Figure 4.24 Stretch zone width, stable crack growth versus bulge ductility.

specimens were examined in the scanning electron microscope, using mostly a tilt angle $\psi = 30°$ and magnification of about 100. The length of the stretch zone was measured at different points along the crack front and the results were averaged. The values of J_{IC} under quasi-static and dynamic testing was calculated using equation (3.22). To calculate σ_o in equation (3.22), the variation of the flow stress σ_o is jssumed to be similar to the variation of yield strength with strain rates [101], namely:

$$\sigma_o(\dot{\varepsilon}) = (\sigma_o)_{static} \cdot \left(\frac{\dot{\varepsilon}}{\dot{\varepsilon}_{static}}\right)^{m_1}_{\text{Temperature, structure}} \qquad (4.4)$$

where $(\sigma_o)_{static}$ is the quasi-static flow stress, taken as 450 MPa for AISI annealed 1045 steel at room temperature, $\dot{\varepsilon}_{static}$ is the quasi-static strain rate taken as $10^{-3}s^{-1}$, and m_1 is the strain rate sensitivity which is defined as

$$m_1 = \left(\frac{\partial \log \sigma}{\partial \log \dot{\varepsilon}}\right)_{\text{Temperature, structure}} \qquad (4.5)$$

Examples of the scanning electron micrographs showing the stretch zones of quasi-static and dynamic tested WLCT specimens are shown in Figures 4.25 and 4.26 respectively. These micrographs indicate that the fracture behavior is almost brittle at high loading rates.

The average value of J_{IC} determined from stretch zone width for quasi-static tests was found to be 74 KJ/m^2, while for dynamic tests the average value was 30.5 KJ/m^2.

4.7 Summary

This chapter has described the experimental results of the variation of fracture toughness J_{IC} and ductility

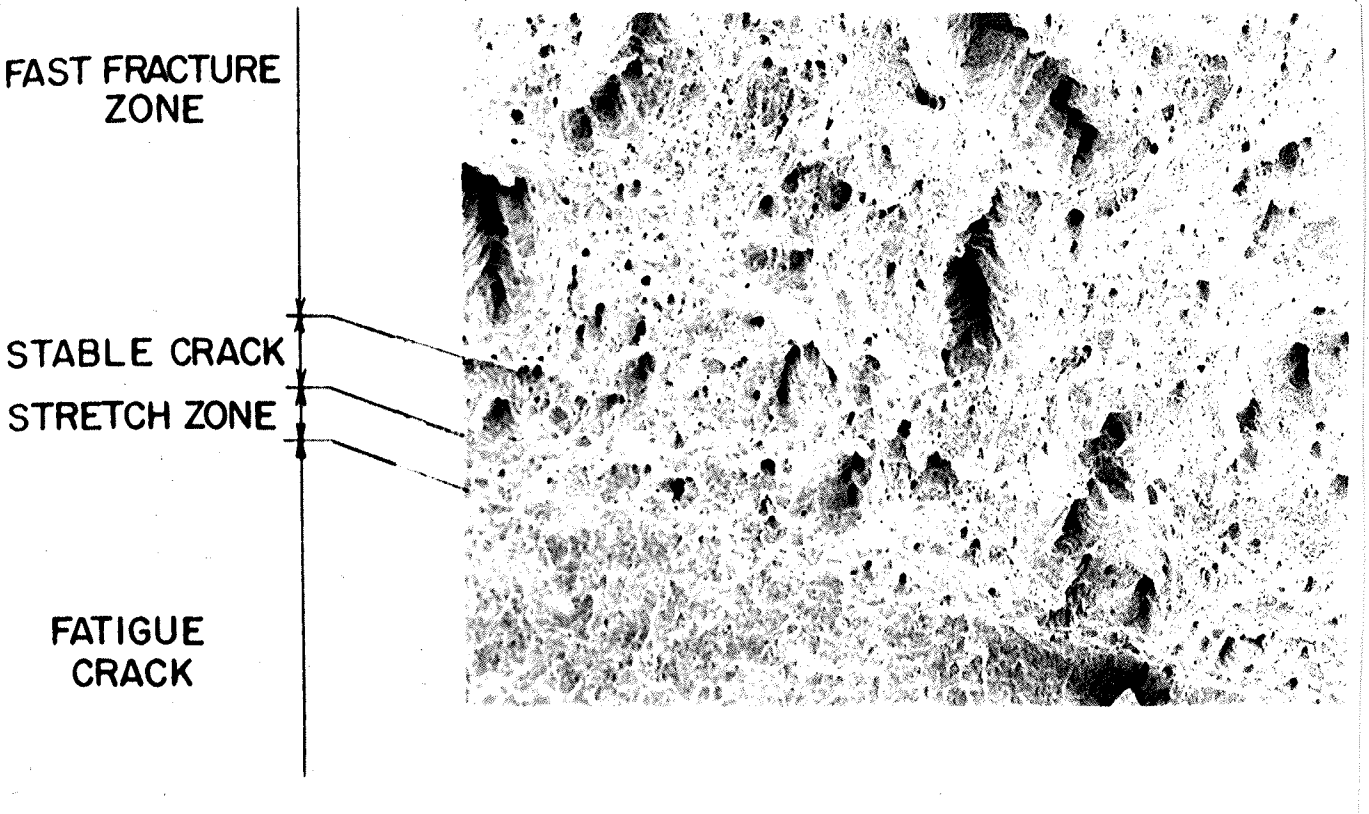

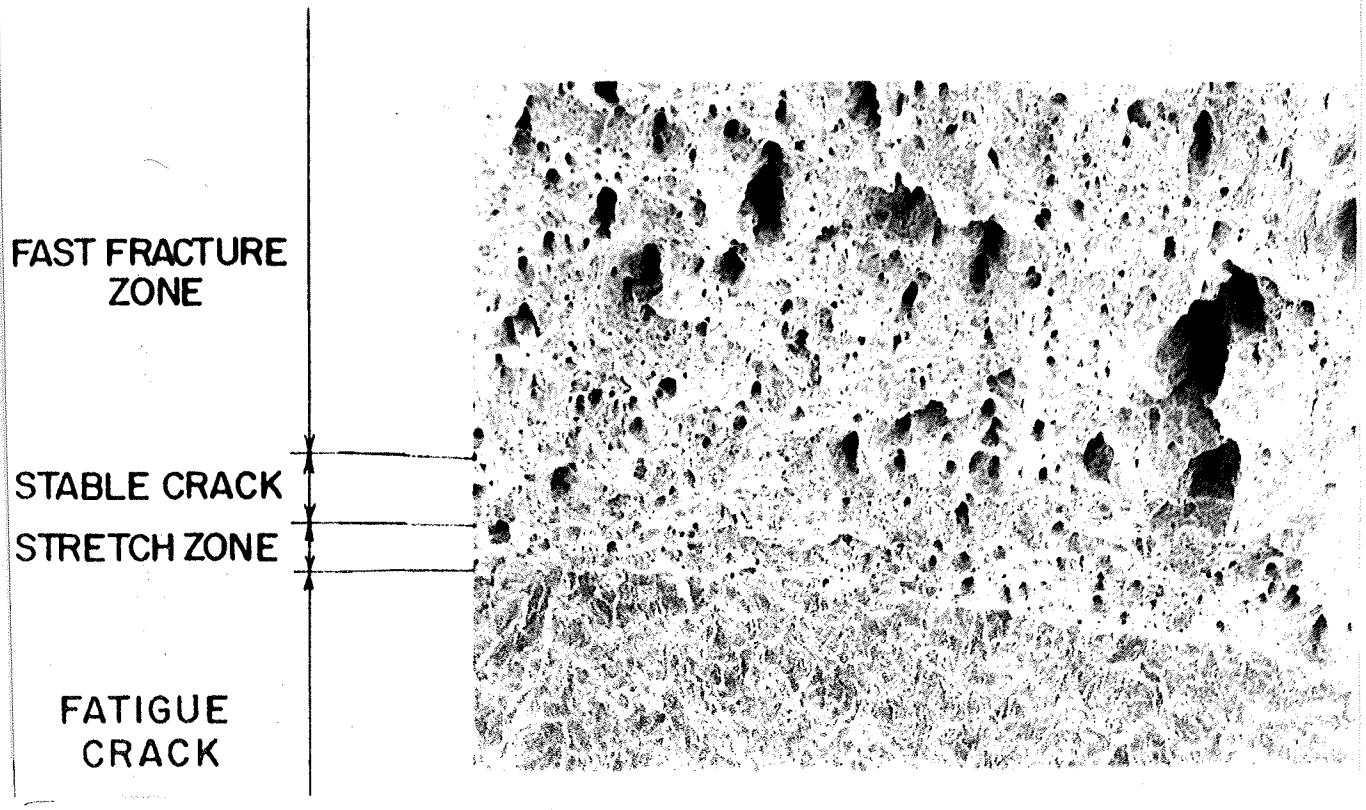

Figure 4.25 Scanning electron micrographs from two WLCT specimens showing the stretch zone and stable crack growth during quasi-static tests. (100 X)

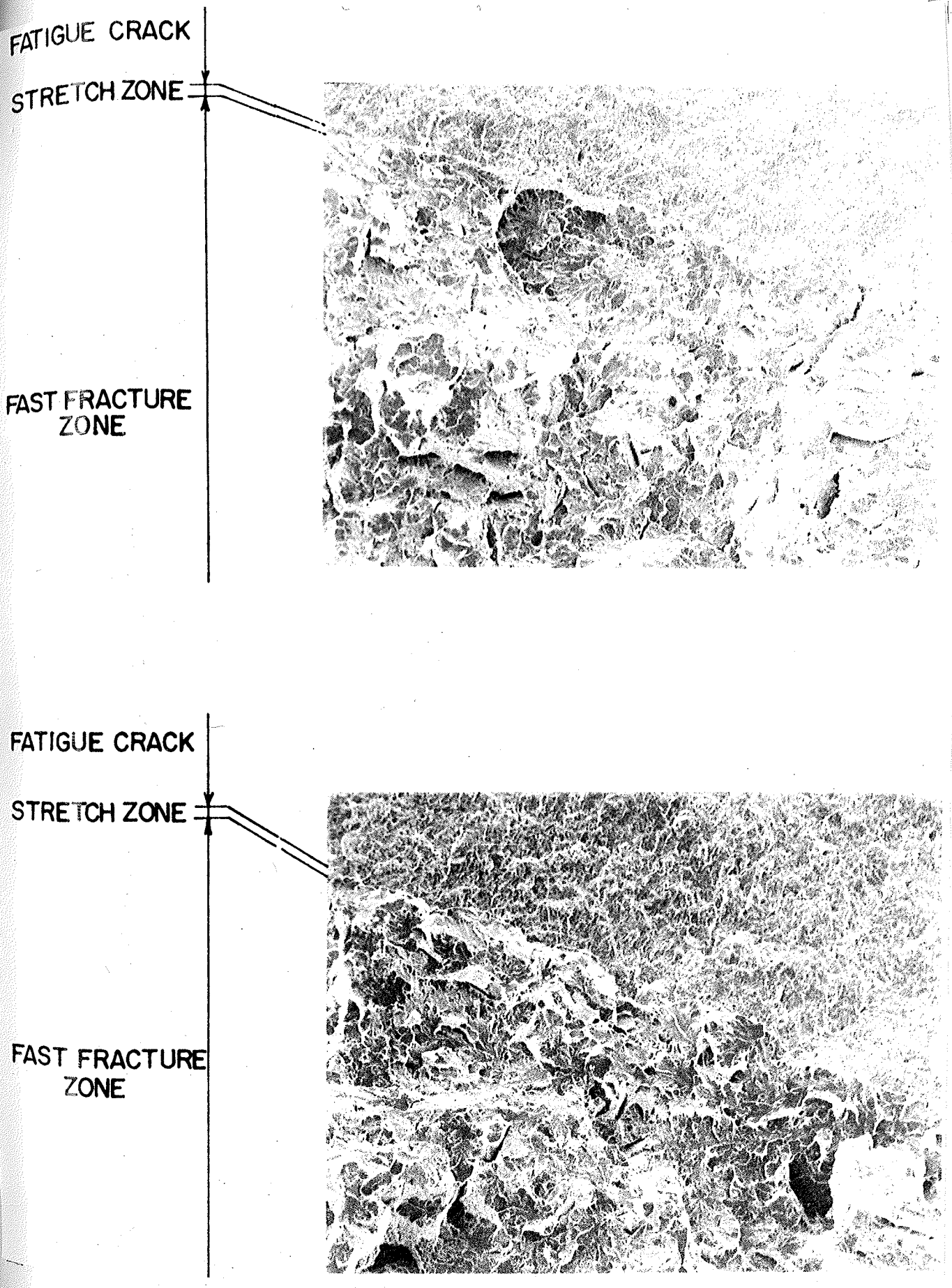

Figure 4.26 Scanning electron micrographs from two WLCT specimens showing the stretch zone during impact tests. (100 X)

measured under both tensile loading and biaxial plane strain (bulge) loading in the transition temperature range for annealed 1045 steel. In this temperature range there are changes in behavior from primarily linear elastic to elastic-plastic. Wedge loaded compact tension specimens (WLCT) were adopted for quasi-static and dynamic fracture toughnes, the analysis of the results was based on the determination of the parameter $\frac{U}{bB}$.

Scanning electron microscope results for both three point bending specimens tested at different temperatures, and wedge loaded compact tension specimens tested at different strain rates, showed also the same trend of behavior, namely, mostly linear elastic behavior at low temperatures or high loading rates, and elastic-plastic behavior at high temperatures or low loading rates. An analytical model to characterize the relationship between the fracture toughness J_{IC} and ductility for the linear elastic behavior and the elastic-plastic behavior will be treated in the next chapter.

CHAPTER 5

MODEL RELATING FRACTURE TOUGHNESS (J_{IC}) AND DUCTILITY

Quantitative correlation between ductility and fracture toughness of engineering materials has been a major objective in fracture research. While these two properties are intimately related, in the sense that generally high ductility corresponds to high fracture toughness and vice versa, the analytical approach for establishing relationships between these properties has been rather difficult. As reported in the previous chapter, the correlation between the fracture toughness parameter J_{IC} and bulge ductility for AISI 1045 steel in the annealed condition in the transition region was experimentally determined. These two parameters were measured as a function of temperature in the range -60°C to 25°C. By varying the temperature, a transition from plane strain linear elastic behavior to elastic-plastic behavior is obtained. The objective of this chapter is to develop an analytical model to characterize the relationship between J_{IC} and bulge ductility in this temperature range.

5.1 J_{IC} - Ductility Relationship

5.1.1 Linear Elastic Behavior

In the linear elastic region, a similar analysis to that leading to equation (2.21) will be used. However, as it will be demonstrated, a second term in equation (2.21) is necessary to account for the fact that, as bulge ductility approaches zero, the material still has a measurable value of fracture toughness.

The fracture toughness G_c is defined as the work required to form a unit crack extension

$$G_c = \frac{\partial W}{\partial A} \tag{5.1}$$

∂W consists of two parts: the plastic work ∂W_p and the work required to create a new surface ∂W_s. For plane strain fracture toughness:

$$J_{IC} = G_{IC} = \gamma_p + \gamma_s \tag{5.2}$$

where γ_s is the work to create a new surface (surface or elastic energy) and γ_p is the plastic work.

Using Griffith analysis [3], γ_s can be written as:

$$\gamma_s = 2\ \sigma_F^2\ \pi\ L_e^*\ (1 - \nu^2)/E \tag{5.3}$$

where σ_F is the fracture stress which can be estimated as equal to $3\sigma_o$ (σ_o is the flow stress) using Prandtl slip line field as reported by Rice [102], L_e^* is a characteristic distance which depends on the microstructure of the material, ν is the Poisson's ratio and E is the modulus of elasticity.

For plane strain condition, with very small plasticity at the crack tip, the plastic work ΔW_p accompanying unit crack extension is the plastic work required to advance the plastic zone by Δa, as schematically illustrated in Fig. 5.1. In polar coordinates (see Fig. 5.1), this work increment is:

$$dWp = \bar{\sigma}\ x\ d\bar{\varepsilon}\ x\ rd\theta dr \tag{5.4}$$

where $\bar{\sigma}$ amd $\bar{\varepsilon}$ are the effective stress and effective strain

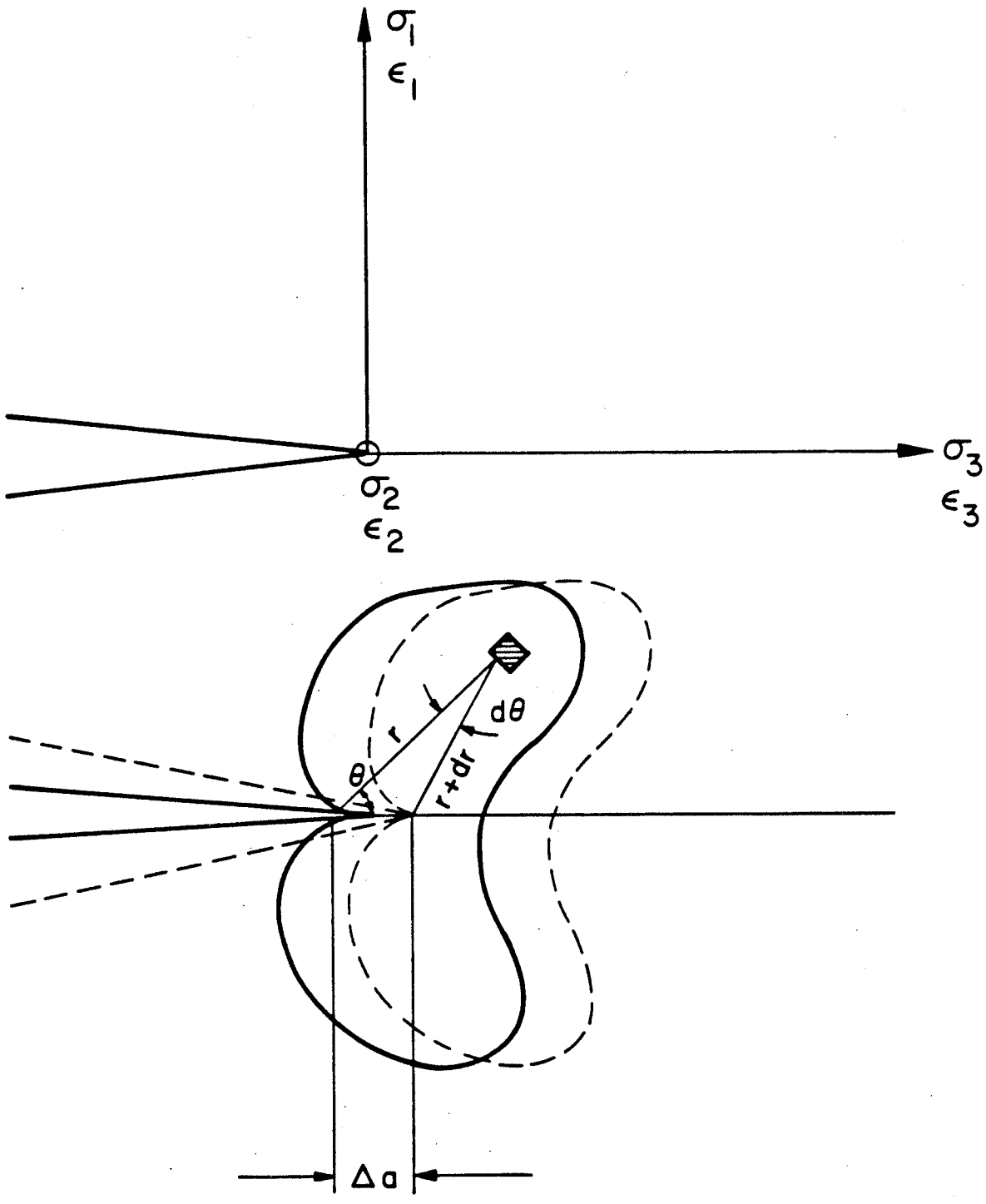

Figure 5.1 Crack tip coordinate system and schematic for the determination of $\gamma_p = \partial W_p / \partial A$.

respectively, ΔW_p is given by

$$\Delta W_p = 2 \int_o^{rp} \int_o^{\pi} dWp = 2 \int_o^{rp} \int_o^{\pi} \bar{\sigma}\, d\bar{\varepsilon}\, r d\theta dr$$

$$= \Delta a \times KS' \times \bar{\varepsilon}^{n+1}_{F,\alpha,\beta} \int_o^{rp} \left[\frac{\rho^*}{\rho^* + 2r}\right]^{(n+1)/2} dr \qquad (5.5)$$

where

$$S' = \int_o^{\pi} g(\theta) \times [f_{ij}(\theta)]^{n+1} \qquad (5.6)$$

Equation (5.5) applies to a power law strain hardening material $\bar{\sigma} = K \bar{\varepsilon}^n$, and a strain distribution characterized by the $r^{-1/2}$ singularity. Thus at the onset of fracture the stress and strain distributions are given by

$$\bar{\varepsilon}(r,\theta) = \bar{\varepsilon}_{F,\alpha.\beta} \left[\frac{\rho^*}{\rho^* + 2r}\right] f_{ij}(\theta) \qquad (5.7)$$

$$\bar{\sigma}(r,\theta) = K \bar{\varepsilon}^n_{F,\alpha,\beta} \left[\frac{\rho^*}{\rho^* + 2r}\right]^{n/2} [f_{ij}(\theta)]^n \qquad (5.8)$$

where ρ^* is Neuber's microsupport effect constant equal to 0.025 mm (0.001"), $\alpha = \frac{\sigma_2}{\sigma_1}$, $\beta = \frac{\sigma_3}{\sigma_1}$, and σ_1, σ_2 and σ_3 are the principal stress components. For plane strain condition α and β are equal to 0.81 and 0.61 respectively [103].

The effective strain can be separated into a radial and an angular component [50] as

$$\bar{\varepsilon}(r,\theta) = \bar{\varepsilon}(r) \Big|_{\theta=0^\circ} \times f_{ij}(\theta) \qquad (5.9)$$

The radial part of dW_p equation (5.4) can be integrated and yields

$$(dW_p)_{radial} = \frac{\rho^*}{a - n} \left[\left(\frac{\rho^* + 2r_p}{\rho^*}\right)^{(1-n)/2} - 1\right] \text{ for } n \neq 1 \qquad (5.10)$$

$$\text{and } (dW_p)_{radial} = \frac{\rho^*}{2} \ell_n \left(\frac{\rho^* + 2r_p}{\rho^*}\right) \qquad \text{for } n=1 \qquad (5.11)$$

Substituting the plastic zone length [65]

$$r_p = \frac{\rho^*}{2}\left[\left(\frac{\bar{\varepsilon}_{F,\alpha,\beta}}{\bar{\varepsilon}_y}\right)^2 - 1\right] \qquad (5.12)$$

in equation (5.5), thus γ_p which is equal to $\partial W_p/\partial A$ can be written as:

(1) For a material which follows a linear strain hardening law $\bar{\sigma} = K\bar{\varepsilon}$

$$\gamma_p = K\, S'\, \rho^*\, \bar{\varepsilon}^2_{F,\alpha,\beta}\, \ell n \left(\frac{\bar{\varepsilon}_{F,\alpha,\beta}}{\varepsilon_y}\right) \qquad (5.13)$$

(2) For a material which follows a power strain hardening $\bar{\sigma} = K\,\bar{\varepsilon}^n$

$$\gamma_p = \frac{K\, S'\, \rho^*}{1-n}\, \bar{\varepsilon}^{n+1}_{F,\alpha,\beta}\left[\left(\frac{\bar{\varepsilon}_{F,\alpha,\beta}}{\bar{\varepsilon}_y}\right)^{1-n} - 1\right] \qquad (5.14)$$

(3) For a material which has a rigid linear strain hardening $\bar{\sigma} = \bar{\sigma}_o + K\bar{\varepsilon}$

$$\gamma_p = \rho^*\, \bar{\varepsilon}_{F,\alpha,\beta}\left[S\,\bar{\sigma}_o\left(\frac{\bar{\varepsilon}_{F,\alpha,\beta}}{\bar{\varepsilon}_y} - 1\right) + K\, S'\, \bar{\varepsilon}_{F,\alpha,\beta}\, \ell n \left(\frac{\bar{\varepsilon}_{F,\alpha,\beta}}{\bar{\varepsilon}_y}\right)\right] \qquad (5.15)$$

(4) For a material which follows a rigid power strain hardening law $\bar{\sigma} = \bar{\sigma}_o + K\,\bar{\varepsilon}^n$

$$\gamma_p = \rho^*\, \bar{\varepsilon}_{F,\alpha,\beta}\left[S\,\bar{\sigma}_o\left(\frac{\bar{\varepsilon}_{F,\alpha,\beta}}{\bar{\varepsilon}_y} - 1\right) + \frac{K\, S'}{1-n}\, \bar{\varepsilon}^n_{F,\alpha,\beta}\left\{\left(\frac{\bar{\varepsilon}_{F,\alpha,\beta}}{\bar{\varepsilon}_y}\right)^{1-n} - 1\right\}\right] \qquad (5.16)$$

(5) Finally, for a rigid plastic material

$$\gamma_p = S\rho^* \bar{\sigma}_o \frac{\bar{\varepsilon}_{F,\alpha.\beta}}{\bar{\varepsilon}_y} \tag{5.17}$$

In these equations, the parameters ρ^*, S, α, β, S' and $\bar{\varepsilon}_y$ have their usual meaning defined earlier, $\bar{\varepsilon}_{F,\alpha,\beta}$ is the effective fracture strain near the crack tip under a stress state corresponding to a plane strain condition.

All the above expressions for γ_p are of the form

$$\gamma_p = S\rho^* \bar{\varepsilon}^{-2}_{F,\alpha,\beta} \cdot f(E, K, n, \bar{\varepsilon}_y) \tag{5.18}$$

In equation (5.18) γ_p is proportional to $\bar{\varepsilon}^{-2}_{F,\alpha,\beta}$. Substituting equation (5.3) and equation (5.18) into equation (5.2) gives

$$J_{IC} = S\rho^* \bar{\varepsilon}^{-2}_{F,\alpha,\beta} f(E,K,n,\bar{\varepsilon}_y) + 2\sigma_F \pi L_e^* (1 - \nu^2)/E \tag{5.19}$$

Equation (5.19) contains a second term in the right hand side which gives a value for fracture toughness as $\bar{\varepsilon}_{F,\alpha,\beta}$ approaches zero. $\bar{\varepsilon}_{F,\alpha,\beta}$ is evaluated from extrapolation from the experimentally determined bulge ductility $\bar{\varepsilon}_{F,\alpha=1,\beta=0}$ by the following procedure:

If $$\bar{\sigma} = \left\{\frac{1}{2}\left[(\sigma_1 - \sigma_2)^2 + (\sigma_2 - \sigma_3)^2 + (\sigma_3 - \sigma_1)^2\right]\right\}^{1/2} \tag{5.20}$$

$$\sigma_{mean} = (\sigma_1 + \sigma_2 + \sigma_3)/3 \tag{5.21}$$

and $d\bar{\varepsilon}_p$ = increment of effective plastic strain

$$= \left\{\frac{2}{9}\left[(d\varepsilon_1^p - d\varepsilon_2^p) + (d\varepsilon_2^p - d\varepsilon_3^p)^2 + (d\varepsilon_3^p - d\varepsilon_1^p)^2\right]\right\}^{1/2} \tag{5.22}$$

with

$$d\varepsilon_1^p + d\varepsilon_2^p + d\varepsilon_3^p = 0$$

The fracture strain for a given stress state characterized by $\alpha = \sigma_2/\sigma_1$ and $\beta = \sigma_3/\sigma_1$ for a material following $\bar{\sigma}$

$= K \bar{\varepsilon}^n$ is given by

$$\bar{\varepsilon}_{F,\alpha,\beta} = (H\,M)^{1/n} \cdot \varepsilon_{ft} \tag{5.23}$$

where ε_{ft} is the fracture ductility in tension, $H = 1/(1+\alpha+\beta)$ and $M = \left[(1+\alpha+\beta)^2 - 3(\alpha+\beta+\alpha\beta)\right]^{1/2}$.

Using the bulge ductility $\bar{\varepsilon}_{F,\alpha=1,\beta=0}$ the relationship in equation (5.23) becomes

$$\bar{\varepsilon}_{F,\alpha,\beta} = (2\,H\,M)^{1/n} \cdot \bar{\varepsilon}_{F,\alpha=1,\beta=0} \tag{5.24}$$

Thus, the relationship between $\bar{\varepsilon}_{F,\alpha=1,\beta=0}$ and $\bar{\varepsilon}_{F,\alpha=0.81,\beta=0.61}$ is:

$$\bar{\varepsilon}_{F,\alpha=0.81,\beta=0.61} = (0.279)^{1/n}\, \bar{\varepsilon}_{F,\alpha=1,\beta=0} \tag{5.25}$$

Substituting equation (5.25) into equation (5.19) gives

$$J_{IC} = S\rho^* (0.279)^{2/n} \cdot \bar{\varepsilon}^2_{F,\alpha=1,\beta=0} \cdot f(E,K,n,\bar{\varepsilon}_y) + 2\,\sigma_F^2\,\pi\,L_e^*\,(1-\nu^2)/E \tag{5.26}$$

or in general form

$$J_{IC} = C_1\,\bar{\varepsilon}^2_{F,\alpha=1,\beta=0} + C_2 \tag{5.27}$$

5.1.2 Elastic-Plastic Behavior

In the elastic-plastic region, Rice and Johnson [103] have described a region of intense strain at the crack tip. For semi-circular blunting, this region extends ahead of the cracks to approximately twice the value of the crack opening displacement. Within the region of intense strain, an approximate r^{-1} strain singularity exists. Crack tip blunt-

ing occurs under a condition of biaxial stress and is observed on the fracture surface as a stretch zone.

In this analysis, the biaxial stress state which exists at the blunted crack tip is assumed to be analogous to that obtained macroscopically in the bulge ductility specimen. Using the model described earlier [104], the distribution of the plastic strain $\bar{\varepsilon}_p$ and the stress state $(\sigma_m/\bar{\sigma})$ ahead of the crack tip as a function of distance ahead of the crack x normalized with respect to crack tip opening displacement δ_1 is shown in Fig. 5.2.

The strain distribution $\bar{\varepsilon}_p$ is related to δ_1/x by:

$$\bar{\varepsilon}_p = C \frac{\delta_1}{x} \tag{5.28}$$

where C is a constant which is determined from Fig. 5.2.

Referring to a typical J-resistance curve [99], at initiation of ductile fracture

$$\delta_1 = \delta_1^* \tag{5.29}$$

and $\bar{\varepsilon}_p = \bar{\varepsilon}_f^*$ which occurs at a distance L_p^* from the crack tip. J_{IC} is also related to the critical crack tip opening displacement δ_1^* by:

$$J_{IC} = m \sigma_o \delta_1^* \tag{5.30}$$

where m is a constraint factor which depends on the material and testing conditions [97]. If it is now assumed that

$$\bar{\varepsilon}_f^* = k \bar{\varepsilon}_{F,\alpha=1,\beta=0} \tag{5.31}$$

which relates the fracture strain $\bar{\varepsilon}_f^*$ to the bulge ductility $\bar{\varepsilon}_{F,\alpha=1,\beta=0}^*$, k is a constant which is usually less than one and which may vary with temperature and material conditions.

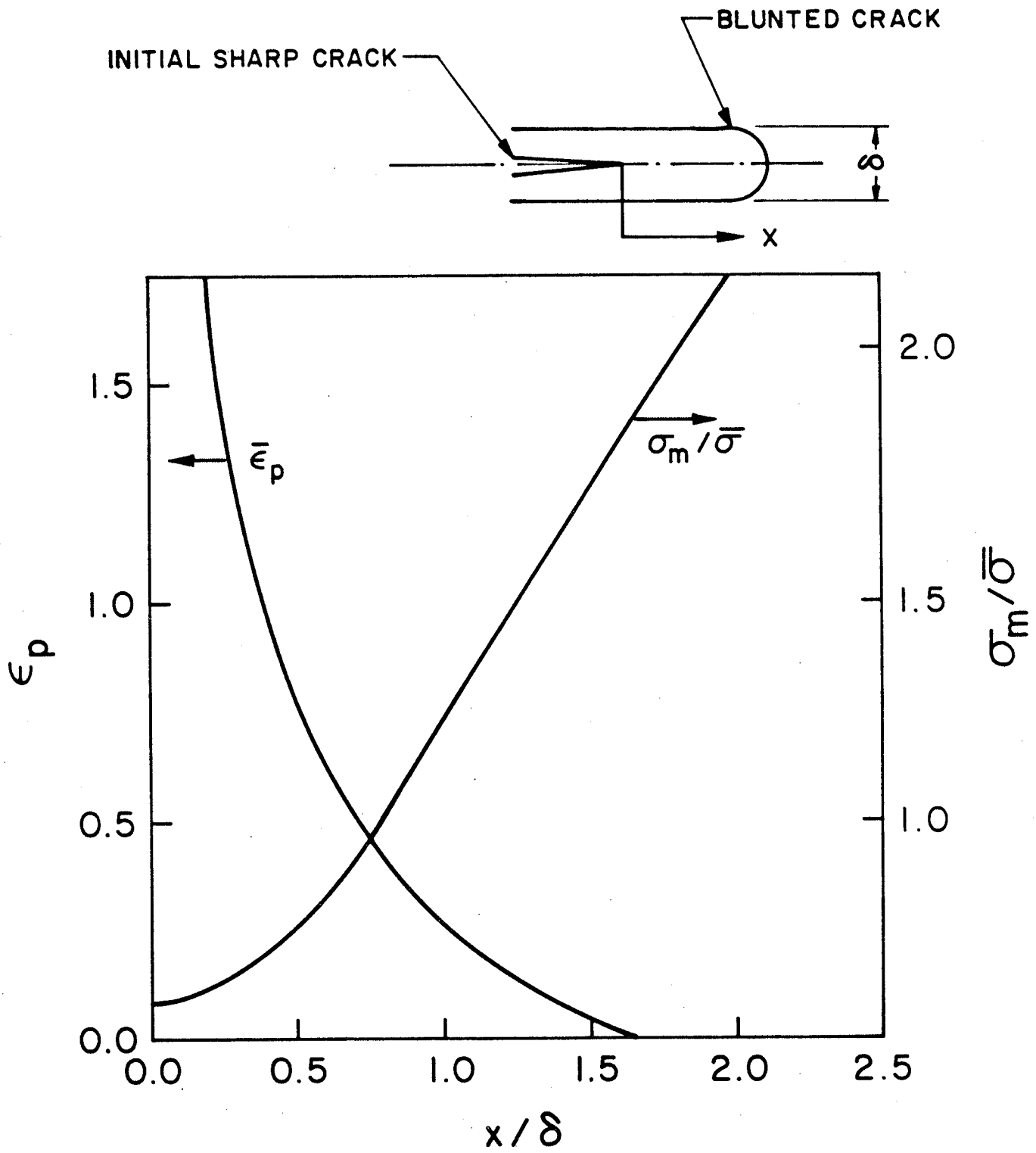

Figure 5.2 Distribution of plastic strain ($\bar{\epsilon}_p$) and stress state ($\sigma_m/\bar{\sigma}$) near crack tip (following Rice et al. [104]).

From equations (5.28), (5.30) and (5.31), it is possible to write the following relationship:

$$J_{IC} = k \frac{m\sigma_o}{C} L_p^* \bar{\varepsilon}_{F,\alpha=1,\beta=0} \tag{5.32}$$

or, in general form

$$J_{IC} = C_p \bar{\varepsilon}_{F,\alpha=1,\beta=0} \tag{5.33}$$

where $C_p = (k\ m\ \sigma_o/C)\ L_p^*$.

Equation (5.33) indicates that the variation of J_{IC} with bulge ductility $\bar{\varepsilon}_{F,\alpha=1,\beta=0}$ is linear in the elastic-plastic region.

Figure 5.3 represents a summary of the model showing the relation between J_{IC} and bulge ductility and defining the transition between linear-elastic and elastic-plastic regimes.

5.2 Application of the Model

As indicated in Fig. 4.13 in Chapter 4, experimental results of the variation of fracture toughness expressed as J_{IC} and bulge ductility were obtained for AISI 1045 steel in the annealed conditions as a function of temperature. The range of temperature was -60°C to 25°C and includes both the linear elastic and elastic-plastic regions for this steel.

These experimental results were used to evaluate the constants C_1 and C_2 in equation (5.27) and C_p in equation (5.33). The values of these constants are given in Table 5.1, which also shows the calculated values of L_e^* and

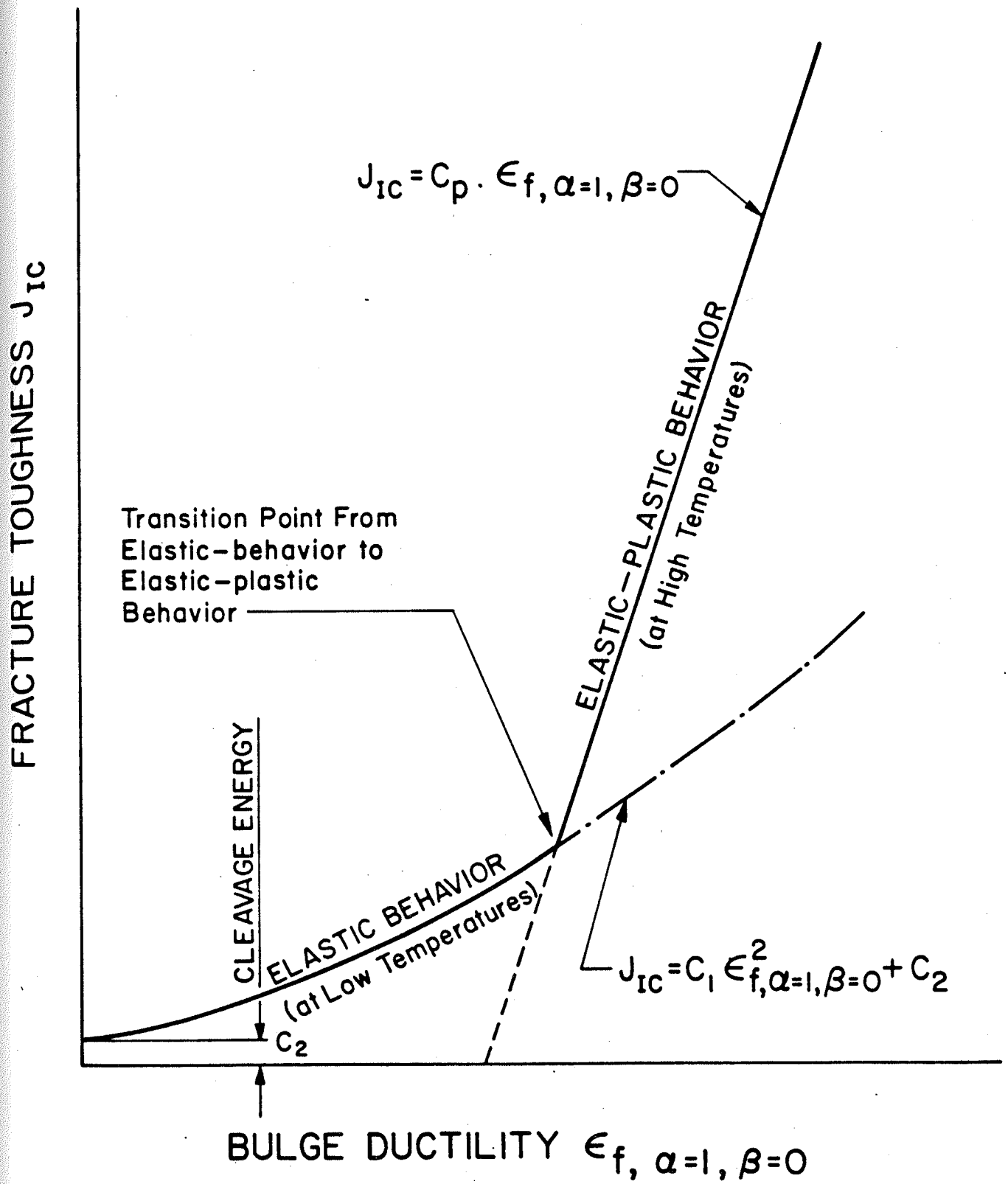

Figure 5.3 Diagramatic representation for the proposed model to correlate J_{IC} and bulge ductility $\bar{\epsilon}_{F,\alpha=1,\beta=0}$ in the transition region.

TABLE 5.1 Values of constants in Eqns. (5.27) and (5.33) for annealed 1045 steel

Constant	Value	
C_1 in Eq. (5.27)	49	kJ/m^2
C_2 in Eq. (5.27)	8.6	kJ/m^2
$C_p = \frac{\Delta J_{IC}}{\Delta \varepsilon_{f,\alpha=1,\beta=0}}$ in Eq. (5.33)	310	kJ/m^2
$\bar{d}$ = pearlite colony diameter	50	μm
L_e^* om Eq. (5.26)	75	μm
kL_p^* in Eq. (5.32)	178	μm (evaluated at 25°C)

kL_p^* (evaluated at 25°C). The determined values of L_e^* and L_p^* should be compared with the size of the pearlite colony dimension $\bar{d}$, for this steel which was found to be about 50μm.

The value of L_e^* of 75 μm compares favorably with $\bar{d}$ while kL_p^* = 178 μm (at 25°C) indicates that plasticity ahead of the crack will extend from three to four times the size of the pearlite colony before ductile tearing takes place.

5.3 Summary

In this chapter, a model relating the fracture toughness J_{IC} and the bulge ductility $\bar{\varepsilon}_{F,\alpha=1,\beta=0}$ is proposed. It is based on the isotropic behavior of the material. This model showed that in the linear-elastic region, J_{IC} varies with $\varepsilon_{F,\alpha=1,\beta=0}^{-2}$ while in the elastic-plastic region, J_{IC} varies linearly with $\bar{\varepsilon}_{F,\alpha=1,\beta=0}$. The two equations developed for the linear elastic and elastic-plastic region contain constants which are evaluated experimentally for a given material, specimen geometry and testing conditions. From these constants, it is possible to evaluate a characteristic length (L_e^* or kL_p^*) which is related to the microstructure of the material and which describes the fracture process at the crack tip.

In the next chapter the temperature dependence of ductility, strength and fracture toughness J_{IC} for a material undergoing predominantly linear elastic behavior at low temperatures and elastic plastic behavior at higher temperatures will be examined.

CHAPTER 6

TEMPERATURE DEPENDENCE OF FRACTURE TOUGHNESS (J_{IC}) AND DUCTILITY

Because of the strong dependence of the mechanical properties of BCC metals on temperature, their fracture toughness will be greatly influenced by variation in temperature, particularly in the transition region where the bahavior changes from brittle to ductile fracture. While in the previous chapter a model relating the fracture toughness J_{IC} and ductility $\bar{\varepsilon}_{F,\alpha,\beta}$, for a material exhibiting a transition from linear elastic to elastic-plastic behavior was developed, the present chapter will examine a model relating fracture toughness J_{IC} with temperature. Such a model is applicable to BCC metals, particularly steels, which show a strong variation in mechanical properties as well as fracture behavior with temperature.

6.1 J_{IC} and Ductility-Temperature Relationship

Because of the strong dependence of fracture toughness on ductility, particularly in the elastic-plastic regime, the approach for determination of the temperature dependence of J_{IC} relies on the examination of the microstructural events which control ductile fracture. Previous investigations have shown that ductile fracture involves two successive damage processes, namely the nucleation of cavities at inclusions and grain boundaries followed by cavity growth and void coalescence.

As reported in Chapter 2, in the case where cavity initiation takes place after large plastic strains, Argon et al [35] have found that the interface stress normal to the inclusion matrix interface σ_{rr} is given by:

$$\sigma_{rr} = Y(\bar{\varepsilon}^p) + \sigma_m \tag{6.1}$$

where $Y(\bar{\varepsilon}^p)$ is the flow stress in the region of the inclusion, σ_m is the mean stress for void nucleation and $\bar{\varepsilon}^p$ is the mean plastic strain.

Because $Y(\bar{\varepsilon}^p)$ has a strong temperature dependence, equation (6.1) indicates that the critical mean stress required for void nucleation varies with temperature as

$$\sigma_m(T) = \sigma_{rr}(T) - Y(\bar{\varepsilon}^p, T) \tag{6.2}$$

This equation assumes that σ_{rr} varies only moderately with decreasing temperature (like Young's modulus), much less than the flow stress (or yield strength).

For a material obeying the equation

$$\bar{\sigma} = K\,\bar{\varepsilon}^n = 3\,\sigma_m \cdot f(\alpha,\beta) \tag{6.3}$$

where $\bar{\sigma}$ is the effective stress, $\bar{\varepsilon}$ is the effective strain, n is the strain hardening exponent, K is the strength coefficient, and $f(\alpha,\beta)$ is the function of stress state, the strain for void nucleation $\bar{\varepsilon}_{i,\alpha,\beta}$ which is obtained by equating $\bar{\varepsilon} = \bar{\varepsilon}_{i,\alpha,\beta}$ in equation (6.3) becomes a function of σ_m only if the stress state (α,β) remains the same. It is worth noting that the strain necessary to nucleate cavities $\bar{\varepsilon}_{i,\alpha,\beta,}$ is small as compared with the strain at failure.

The growth of cavities in a material which is plastically deformed has been analyzed and reviewed in chapter two. Among these analyses, McClintock [50] and Rice and Tracey [44] are the most widely used. For the two dimensional void growth model, McClintock [50] obtained an equation for void coalescence of the form

$$\bar{\varepsilon}_{c,\alpha,\beta=0} = \frac{(1-n)\,\ln v_f^{-1/3}}{\sinh\left[(1-n)(\sigma_1+\sigma_2)/2\sigma_o/(3)^{1/2}\right]} \qquad (6.4)$$

where v_f is the volume fraction of voids. Examination of equation (6.4) shows that, for given material and constant stress state, the strain required for void coalescence $\bar{\varepsilon}_{c,\alpha,\beta}$ is independent of temperature. The principal influence on $\varepsilon_{c,\alpha,\beta}$ is the void density v_f. For a typical BCC material, a coalescence strain $\bar{\varepsilon}_{c,\alpha,\beta}$ between 0.01 and 0.5, depending on the stress state ahead of the crack, is expected [51].

Since the two main components of the fracture strain $\bar{\varepsilon}_{F,\alpha,\beta}$ are the nucleation strain $\bar{\varepsilon}_{i,\alpha,\beta}$ and the coalescence strain $\bar{\varepsilon}_{c,\alpha,\beta}$, these two strains are additive, thus

$$\bar{\varepsilon}_{F,\alpha,\beta} = \bar{\varepsilon}_{i,\alpha,\beta} + \bar{\varepsilon}_{c,\alpha,\beta} \qquad (6.5)$$

Using the equations (6.2), (6.3) and (6.4), equation (6.5) can be written in the form

$$\bar{\varepsilon}_{F,\alpha,\beta}(T) = \bar{\varepsilon}_{i,\alpha,\beta}\left[\sigma_{rr}(T) - Y(T,n)\right] + \bar{\varepsilon}_{c,\alpha,\beta}[v_f,n] \qquad (6.6)$$

where $\bar{\varepsilon}_{F,\alpha,\beta}(T)$ is the fracture strain as a function of temperature, $Y(T,n)$ is the flow stress as a function of temperature, and $\sigma_{rr}(T)$ is the interface stress normal to the inclusion-matrix interface as a function of temperature,

$\sigma_{rr}(T)$ is assumed to vary with temperature similar to Young's modulus. The temperature dependence of σ_{rr} can be written as

$$\sigma_{rr}(T) = \sigma_{rr}(0) - \alpha_o T \tag{6.7}$$

where $\sigma_{rr}(0)$ is the interface stress at 0°K, T is the absolute temperature, and α_o is a constant.

In equation (6.6), it is evident that the dependence of the fracture strain on temperature is similar to that of the strain for void nucleation since the cavity coalescence strain is only dependent on the volume fraction of the voids as well as the stress state. Thus a plot of $\bar{\varepsilon}_{F,\alpha,\beta}$ versus temperature should be parallel to that of $\bar{\varepsilon}_{i,\alpha,\beta}$ versus temperature, displaced upwards by an amount corresponding to $\bar{\varepsilon}_{c,\alpha,\beta}$.

It is next assumed that the relation between the fracture strain $\bar{\varepsilon}_{F,\alpha,\beta}$ for the stress state ahead of the crack is proportional to the bulge as well as the tensile ductility described previously in the last two chapters. Namely, this relationship is of the form

$$\bar{\varepsilon}_{F,\alpha,\beta} = k\, \bar{\varepsilon}_{F,\alpha=1,\beta=0} \tag{6.8}$$

where $\bar{\varepsilon}_{F,\alpha=1,\beta=0}$ is the bulge ductility and k is a constant having a value less than unity. The assumption in equation (6.8) is justified if one considers the bulge ductility as

representing the strain corresponding to the total fracture process while $\bar{\varepsilon}_{F,\alpha,\beta}$ corresponds to the fracture strain associated with a single stable crack growth event.

As reported in chapter five, the relationship between fracture toughness J_{IC} and bulge ductility $\bar{\varepsilon}_{F,\alpha=1,\beta=0}$ is:

(a) For low temperatures

$$J_{IC} = S\rho^{*}(0.279)^{1/n} \cdot \bar{\varepsilon}^{-2}_{F,\alpha=1,\beta=0} \cdot f(E,K,n,\bar{\varepsilon}_y) + 2\,\sigma_f\,\pi\,L_e^{*}(1-\nu^2)/E \qquad (6.9)$$

and

(b) For high temperatures

$$J_{IC} = k\,\frac{m\sigma_o}{C}\,L_p^{*}\,\bar{\varepsilon}_{F,\alpha=1,\beta=0} \qquad (6.10)$$

where S, ρ^*, m, σ_o, C, k, L_p^*, L_e^*, n, $\bar{\varepsilon}_y$, ν, E, α and β have been defined earlier.

Substituting equations (6.7) and (6.8) into equations (6.9) and (6.10) gives the temperature dependence of J_{IC}, namely

(a) For low temperatures

$$J_{IC}(T) = \frac{S\rho^{*}}{k^2}(0.279)^{2/n}\left[\bar{\varepsilon}_{i,\alpha,\beta}[\sigma_{rr}(T) - Y(T,n)] + \varepsilon_{c,\alpha,\beta}(v_f,n)\right]^2 \cdot f(E,K,n,\bar{\varepsilon}_y) + 2\,\sigma_f\pi L_e^{*}(1-\nu^2)/E \qquad (6.11)$$

and

(b) For high temperatures

$$J_{IC}(T) = \frac{km\sigma_o}{kc}\,L_p^{*}\left[\bar{\varepsilon}_{i,\alpha,\beta}[\sigma_{rr}(T) - Y(T,n)] + \bar{\varepsilon}_{c,\alpha,\beta}(v_f,n)\right] \qquad (6.12)$$

In equations (6.11) and (6.12), it can be observed that the dependence of J_{IC} on temperature follows that of the void nucleation step in the fracture process. Thus, it is necessary to determine experimentally the variation of the flow stress $Y(T,n)$ and the interface stress $\sigma_{rr}(T)$ with temperature in order to obtain relationships of the variation of J_{IC} with temperature in both linear elastic (at low temperatures) and elastic-plastic (at high temperatures) regimes for a given material and stress state.

6.2 Application of the Model to Fracture of AISI 1045 Steel

The experimental study carried out on AISI 1045 steel in the annealed condition to determine its mechanical properties as a function of temperature and described in Cahpter 4 was used to verify the proposed model. Thus Figure 4.2 shows the variation of σ_y and $Y(= \sigma_{flow})$ as a function of temperature while Figure 4.4 gives the variation of the strain hardening exponent n with temperature for this steel.

In equations (6.11) and (6.12), each of the terms in the right-hand side will be considered separately. First, the variation of σ_{rr} with temperature T is obtained from equation (6.7). It is assumed that σ_{rr} varies with temperature similar to Young's modulus [51]; namely that $[\sigma_{rr}(T = 298°K)]/[\sigma_{rr}(T = 0°K)] \cong 0.8$. For 1045 steel in the

annealed conditions $\sigma_{rr}(T = 0°K)$ is estimated to be equal to 1082 MPa. It is possible to determine α_o in equation (6.7) which then becomes:

$$\sigma_{rr}(T) = 1082 - 0.72\ T \quad MPa \tag{6.13}$$

Using equation (6.13), as well as the data for Y(T) and n(T) in Figs. 4.2 and 4.4, the ratio $[\bar{\varepsilon}_{i,\alpha,\beta}(T)]/[\bar{\varepsilon}_{i,\alpha,\beta}(T = 298°K)]$ is calculated as a function of temperature. This is shown in Fig. 6.1. It is noticed that it consists of two distinct regions which intersect at a temperature T ≈ 250°K (-23°C). This is in agreement with the previous experimental results on the temperature dependence of J_{IC} for this material as reported in chapter four.

The coalescence strain $\bar{\varepsilon}_{c,\alpha,\beta}$ is almost independent of temperature. Thus, the total fracture strain $\bar{\varepsilon}_{F,\alpha,\beta}$ will vary with T in the same way as $\bar{\varepsilon}_{i,\alpha,\beta}$ except for a shift upwards as also shown in Fig. 6.1.

Next, it is now possible to determine the variation of J_{IC} with T in both linear elastic and elastic-plastic regimes for this material.

(a) At low temperatures

$$J_{IC}(T) = \frac{S\rho^*}{k^2}(0.279)^{2/n} \cdot \eta_1^2 \cdot T^2 \cdot f(E,K,n,\bar{\varepsilon}_y) + 2\,\sigma_f \pi\, L_e^* (1 - \nu^2)/E \tag{6.14}$$

where $\eta_1 = \bar{\varepsilon}_{F,\alpha,\beta}/T$ in the low temperature range (213 -

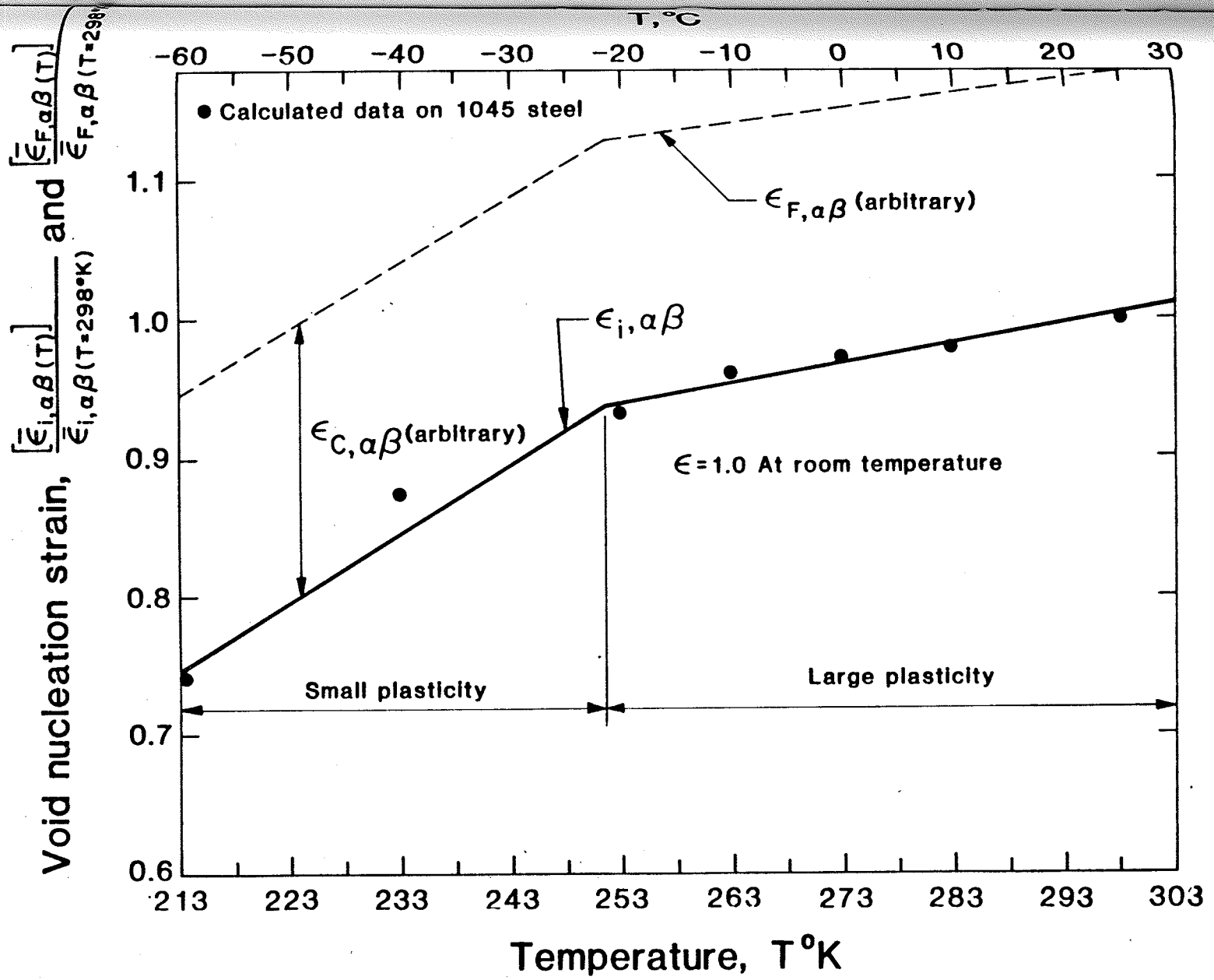

Figure 6.1 Temperature dependence of $\bar{\epsilon}_{i,\alpha,\beta}$ expressed as $\bar{\epsilon}_{i,\alpha,\beta}(T)/\bar{\epsilon}_{i,\alpha,\beta}(T = 298°K)$ and $\bar{\epsilon}_{F,\alpha,\underline{\beta}}$ expressed as $\bar{\epsilon}_{F,\alpha,\beta}(T)/\bar{\epsilon}_{F,\alpha,\beta}(T = 298°K)$ for AISI 1045 steel, $\epsilon_{c,\alpha,\beta}$ denotes an arbitrary value for $\bar{\epsilon}_{F,\alpha,\beta}$.

250°K om Fig. 6.1) or in more general form

$$J_{IC}(T) = J_{IC}(0) + C_e T^2 \qquad (6.15)$$

where $J_{IC}(0)$ is the fracture toughness at T = 0°K

$$J_{IC}(0) \cong 2\sigma_F \pi L_e^* (1 - \nu^2)/E$$

and C_e is a constant which depends on the mechanical properties and microstructure of the steel and is determined experimentally.

(b) At high temperatures

$$J_{IC}(T) = \frac{km\sigma_o}{kC} L_p^* \eta_2 \cdot T \qquad (6.16)$$

where $\eta_2 = \bar{\varepsilon}_{F,\alpha,\beta}/T$ in the high temperature range (250 - 300°K in Fig. 6.1). In more general form

$$J_{IC}(T) = C_{ep} T \qquad (6.17)$$

where C_{ep} is a constant which is determined experimentally. Table 6.1 gives the values of these constants, namely $J_{IC}(0)$, C_e and C_{ep} for this steel.

6.3 Summary

In this chapter, a model for the temperature dependence of J_{IC} in the transition region for BCC materials has been presented. The model suggests that the temperature dependence of ductility and fracture toughness arises in the void nucleation phase of ductile fracture. When the model is applied to the case of a carbon steel in the annealed condition, such as AISI 1045 steel, it is found that J_{IC}

TABLE 6.1 Values of constants in Eqns. (6.15) and (6.17) for annealed 1045 steel

Constant	Value	
$J_{IC}(o)$ in Eq. (6.15)	9.88	KJ/m^2
C_e in Eq. (6.15)	0.0005605	$KJ/m^2/°K^2$
$C_{ep} = \frac{\Delta J_{IC}}{\Delta T}$ in Eq. (6.17)	1.0	$KJ/m^2/°K$

varies with T^2 in the predominantly linear elastic regime while it depends linearly on T in the elastic-plastic regime. A transition temperature, which in the case of annealed AISI 1045 steel has a value of about -20°C, is observed. Above such a transition the material has an elastic-plastic behavior, while below this temperature the behavior is mostly linear elastic, this is shown in Fig. 6.2. Such a transition temperature is also related to the variation of $\bar{\varepsilon}_{i,\alpha,\beta}$ as well as the flow stress Y with temperature for this material and seems to suggest that the controlling factor of fracture toughness is the strength and ductility temperature dependence.

Since the temperature and the loading rate are the main factors affecting strength and ductility of the material, it is important to study the strain rate (loading rate) dependence of fracture toughness and ductility, this will be described in the next chapter.

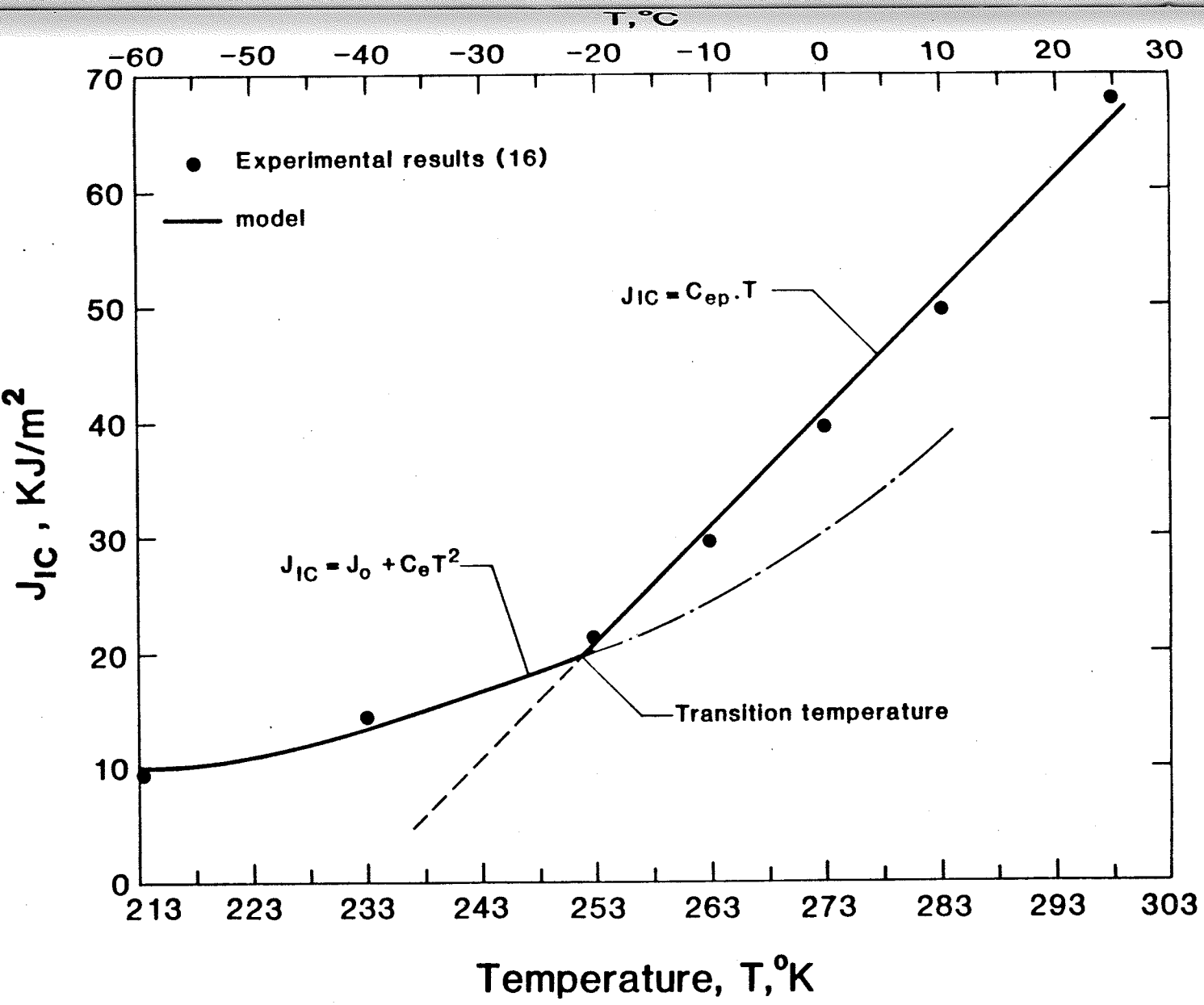

Figure 6.2 Relationship between J_{IC} and temperature.

CHAPTER 7

STRAIN RATE DEPENDENCE OF FRACTURE TOUGHNESS (J_{IC}) AND DUCTILITY

In most cases in engineering practice, fracture initiation in metals and alloys is experimentally determined under slow loading conditions. However, for materials with strong temperature and strain rate dependence, the fracture toughness usually decreases with decreasing temperature and increasing loading rates. It is thus important to obtain a quantitative correlation between ductility and fracture toughness of these materials as a function of temperature and through a wide range of loading rates. Experimental data in these ranges generally reveals a transition region from high to low value of fracture toughness.

In this present chapter, a model relating fracture toughness, expressed as J_{IC}, and ductility with strain rate $\dot{\varepsilon}$ or its equivalent loading rate $\dot{K}_I$ is developed. Such a model is applicable to metals and alloys which show a strong variation in mechanical properties as well as fracture behavior with strain rate.

7.1 The Model

The approach for the determination of the strain rate dependence of fracture toughness J_{IC} relies on examination of the microstructural events which control ductile fracture. Following the same approach as reported in Chapter 6, it is possible to develop a model for fracture toughness J_{IC} and ductility dependence on strain rate, namely, it is assumed that ductile mechanisms such as nucleation of voids at

inclusions or grain boundaries takes place at low strain rates when either the inclusions or the matrix inclusion interface is subjected to critical normal stress σ_{rr}. This stress can be written as

$$\sigma_{rr}(\dot{\bar{\varepsilon}}) = Y(\bar{\varepsilon}^p, \dot{\bar{\varepsilon}}) + \sigma_m(\dot{\bar{\varepsilon}}) \tag{7.1}$$

where σ_{rr}, Y, $\bar{\varepsilon}^p$ and σ_m have the same meaning as defined earlier.

Because $Y(\bar{\varepsilon}^p, \dot{\bar{\varepsilon}})$ has a strong strain rate dependence , equation (7.1) indicates that the critical mean stress required for void nucleation varies with strain rate as:

$$\sigma_m(\dot{\bar{\varepsilon}}) = \sigma_{rr}(\dot{\bar{\varepsilon}}) - Y(\bar{\varepsilon}^p, \dot{\bar{\varepsilon}}) \tag{7.2}$$

This equation assumes that σ_{rr} varies moderately with increasing strain rate.

For a material obeying the equation

$$\bar{\sigma} = K\bar{\varepsilon}^n = 3\,\sigma_m\, f(\alpha,\beta) \tag{7.3}$$

where $\bar{\sigma}$ is the effective stress, $\bar{\varepsilon}$ is the effective strain, n is the strain hardening exponent, K is the strength coefficient and $f(\alpha, \beta)$ is a function of the stress state. The strain for void nucleation $\bar{\varepsilon}_{i,\alpha,\beta}$ which is obtained by equating $\bar{\varepsilon} = \bar{\varepsilon}_{i,\alpha,\beta}$ in equation (7.3) becomes a function of σ_m only if the stress state (α,β) remains the same. The void coalescence strain $\bar{\varepsilon}_{c,\alpha,\beta}$ can be expressed as

$$\bar{\varepsilon}_{c,\alpha,\beta} = \bar{\varepsilon}_{c,\alpha,\beta}(v_f, n) \tag{7.4}$$

Equation (7.4) indicates that, for a given material and

constant stress state, the strain required for void coalescenc is independent of strain rate. The principal influence on $\bar{\varepsilon}_{c,\alpha,\beta}$ is the volume fraction of the voids v_f.

The two main components of the fracture strain $\bar{\varepsilon}_{F,\alpha,\beta}$ are the nucleation strain $\bar{\varepsilon}_{c,\alpha,\beta}$ and the coalescence strain $\bar{\varepsilon}_{c,\alpha,\beta}$. These two strains are additive, thus:

$$\bar{\varepsilon}_{F,\alpha,\beta} = \bar{\varepsilon}_{i,\alpha,\beta} + \bar{\varepsilon}_{c,\alpha,\beta} \tag{7.5}$$

Using equations (7.2), (7.3) and (7.4), the strain rate dependence of the fracture strain $\bar{\varepsilon}_{F,\alpha,\beta}$ can be written as

$$\bar{\varepsilon}_{F,\alpha,\beta}(\dot{\varepsilon}) = \bar{\varepsilon}_{i,\alpha,\beta}\left[\sigma_{rr}(\dot{\varepsilon}) - Y(\dot{\varepsilon},n)\right] + \bar{\varepsilon}_{c,\alpha,\beta}(v_f,n) \tag{7.6}$$

where $\bar{\varepsilon}_{F,\alpha,\beta}(\dot{\varepsilon})$ is the fracture strain as a function of strain rate, $Y(\dot{\varepsilon},n)$ is the flow stress as a function of strain rate which can be expressed as

$$Y(\dot{\varepsilon}) = Y_{static}\left(\frac{\dot{\varepsilon}}{\dot{\varepsilon}_{static}}\right)^{m_1}_{Temperature,\ structure} \tag{7.7}$$

where m_1 is the strain rate sensitivity, defined as

$$m_1 = \frac{\partial\ Log\ \sigma}{\partial\ Log\ \dot{\varepsilon}} \tag{7.8}$$

and ranges from 0.01 - 0.02 for most steels and high strength aluminum alloys, and $\sigma_{rr}(\dot{\varepsilon})$ is the interface stress normal to the inclusion-matrix interface as a function of strain rate. It is assumed that σ_{rr} varies with strain rate as

$$\sigma_{rr}(\dot{\varepsilon}) = (\sigma_{rr})_{static} + \alpha_1\dot{\varepsilon} \tag{7.9}$$

where α_1 is a constant much smaller than one.

Examination of equation (7.6) shows that the dependence of fracture strain on strain rate is similar to the strain for void nucleation since the void coalescence strain is only dependent on the volume fraction of voids as well as the stress state. Thus, a plot of $\bar{\varepsilon}_{F,\alpha,\beta}$ versus strain rate should be parallel to that of $\bar{\varepsilon}_{i,\alpha,\beta}$ versus $\dot{\varepsilon}$ displaced upwards by an amount corresponding to $\bar{\varepsilon}_{c,\alpha,\beta}$.

The relationship between fracture toughness J_{IC} and ductility $\bar{\varepsilon}_{F,\alpha,\beta}$ can be written as:

(a) For low strain rates (elastic-plastic behavior)

$$J_{IC}(\dot{\varepsilon}) = \frac{km\sigma_o}{kC} L_p^* \bar{\varepsilon}_{F,\alpha,\beta}(\dot{\varepsilon}) \tag{7.10}$$

and

(b) For high strain rates (predominantly linear elastic behaviour)

$$J_{IC}(\dot{\varepsilon}) = S\rho^* \bar{\varepsilon}^{-2}_{F,\alpha,\beta}(\dot{\varepsilon}) \cdot f(E,K,n,\bar{\varepsilon}_y) + 2\sigma_F \pi L_e^* (1-\nu^2)/E \tag{7.11}$$

Substituting equation (7.9) into equations (7.13) and (7.14) gives the strain rate dependence of J_{IC}, namely:

(a) For low strain rates

$$J_{IC}(\dot{\varepsilon}) = \frac{km\sigma_o}{kC} L_p^* [\bar{\varepsilon}_{i,\alpha,\beta}[\sigma_{rr}(\dot{\varepsilon}) - Y(\dot{\varepsilon},n)] + \bar{\varepsilon}_{C,\alpha,\beta}(v_f,n)] \tag{7.12}$$

and

(b) For high strain rates

$$J_{IC}(\dot{\varepsilon}) = S\rho^* [\bar{\varepsilon}_{i,\alpha,\beta}[\sigma_{rr}(\dot{\varepsilon}) - Y(\dot{\varepsilon},n)] + \bar{\varepsilon}_{C,\alpha,\beta}(v_f,n)]^2 \cdot f(E,K,n,\bar{\varepsilon}_y) + 2\sigma_F \pi L_e^* (1-\nu^2)/E \tag{7.13}$$

In equations (7.12) and (7.13), it can be observed that the dependence of J_{IC} on strain rate follows that of the void nucleation step in the fracture process. Thus, it is necessary to determine the variation of the flow stress $Y(\dot{\varepsilon},n)$ and the interface stress $\sigma_{rr}(\dot{\varepsilon})$ with strain rate to obtain relationships of the variation of J_{IC} with strain rate in both linear elastic and elastic-plastic regimes for a given material and stress state.

7.2 Application of the Model

The data from the experimental results, which were given in Table 4.1, are used in this section. In equation (7.7) Y_{static} is evaluated to be 450 MPa at strain rate $\dot{\varepsilon}$ corresponding to $10^{-3}\ S^{-1}$ and m_1 is taken 0.018, while in equation (7.9) $(\sigma_{rr})_{static}$ is estimated to be 866 MPa for Fe_3C particles in 105 steel at $\dot{\varepsilon} = 10^{-3}\ s^{-1}$, also α_1 in equation (7.9) is assumed to be 0.002, thus equations (7.7) and (7.9) become:

$$Y(\dot{\varepsilon}) = 450\ \left(\frac{\dot{\varepsilon}}{10^{-3}}\right)^{0.018}\ \text{MPa} \qquad (7.14)$$

and

$$\sigma_{rr}(\dot{\varepsilon}) = 866 + 0.002\ \dot{\varepsilon}\ \text{MPa} \qquad (7.15)$$

Using equations (7.14) and (7.15) it is possible to calculate the ratio of $\bar{\varepsilon}_{i,\alpha,\beta}(\dot{\varepsilon})/\bar{\varepsilon}_{i,\alpha,\beta}(\dot{\varepsilon} = 10^{-3}\ s^{-1})$ as a function of strain rate, Fig. 7.1 shows the variation of this ratio with $\log(\dot{\varepsilon}/10^{-3})$. It is noticed that it consists of two straight lines which intersect at $\log(\dot{\varepsilon}/10^{-3}) \simeq 3.3$.

The coalescence strain $\bar{\varepsilon}_{C,\alpha,\beta}$ is almost independent of strain rate, thus the total fracture strain $\bar{\varepsilon}_{F,\alpha,\beta}$ will vary with $\log(\dot{\varepsilon}/10^{-3})$ in the same way as $\bar{\varepsilon}_{i,\alpha,\beta}$ except for a shift upwards which is also shown in Fig. 7.1.

Next, it is now possible to determine the variation of J_{IC} with $\dot{\varepsilon}$ in both linear elastic and elastic-plastic regimes for 1045 steel in the annealed condition.

(a) For low strain rates

$$J_{IC}(\dot{\varepsilon}) = \frac{km\sigma_o}{kc} L_p^* \cdot \lambda_1 \cdot \eta \qquad (7.16)$$

where $\lambda_1 = \bar{\varepsilon}_{F,\alpha,\beta}/\log(\dot{\varepsilon}/10^{-3})$ in the low strain rates range and $\eta = \log(\dot{\varepsilon}/10^{-3})$. In general form equation (7.16) is:

$$J_{IC}(\dot{\varepsilon}) = K_{ep} \cdot \eta \qquad (7.17)$$

where K_{ep} is a constant which depends on the mechanical properties and microstructure of the steel and is determined experimentally.

(b) For high strain rates

$$J_{IC}(\dot{\varepsilon}) = S\rho^* \lambda_2^2 \cdot \eta^2 \cdot f(E,K,n,\bar{\varepsilon}_y) + 2\sigma_F \pi L_e^* (1 - \nu^2)/E \qquad (7.18)$$

where $\lambda_2 = \bar{\varepsilon}_{F,\alpha,\beta}/\log(\dot{\varepsilon}/10^{-3})$ in the high strain rate range. In general form

$$J_{IC}(\dot{\varepsilon}) = K_o + K_e \eta^2 \qquad (7.19)$$

K_{ep}, K_o and K_e are constants which are determined experimentally using the data in table 4.1. Their values are 1.11, 22.5 and 20.0 KJ/m^2 respectively.

Equations (7.17) and (7.19) are plotted in Fig. 7.2. The intersection of the straight line (equation (7.17)) and the parabola (equation(7.19)) shows a value of $\log(\dot{\varepsilon}/10^{-3})$

where a transition in fracture behavior with strain rate will occur.

7.3 Summary

A quantitative relationship which characterizes the variation of fracture toughness, expressed as J_{IC}, with strain rate is given for low and high loading rates in equations (7.12) and (7.13) respectively. When this model is applied to a specific material such as 1045 steel, it is shown that J_{IC} varies with $\log (\dot{\varepsilon}/10^{-3})$ at low strain rates and with $\left|\log (\dot{\varepsilon}/10^{-3})\right|^2$ at high strain rates.

The relationships between the fracture toughness parameter J_{IC}, bulge ductility, temperature and strain rate are summarized as follows:

- J_{IC} - bulge ductility relationships:

$$J_{IC} = C_1 \bar{\varepsilon}^{-2}_{F,\alpha=1,\beta=0} + C_2 \quad \text{(elastic behavior)}$$

$$J_{IC} = C_p \bar{\varepsilon}_{F,\alpha=1,\beta=0} \quad \text{(elastic-plastic behavior)}$$

- J_{IC} - Temperature relationships:

$$J_{IC}(T) = J_{IC}(0) + C_e T^2 \quad \text{(Low Temperatures)}$$

$$J_{IC}(T) = C_{ep} T \quad \text{(High Temperatures)}$$

- J_{IC} - strain rate relationships:

$$J_{IC}(\dot{\varepsilon}) = K_{ep} \log (\dot{\varepsilon}/10^{-3}) \quad \text{(low strain rates)}$$

$$J_{IC}(\dot{\varepsilon}) = K_o + K_e \left|\log(\dot{\varepsilon}/10^{-3})\right| \quad \text{(high strain rates)}$$

where C_1, C_2, C_p, $J_{IC}(0)$, C_e, C_{ep}, K_{ep}, K_o and K_e are constants which are functions of mechanical properties and microstructure of the material.

In the next chapter the applicability of the models shown through chapters 5 and 6 to a tempered martensitic structure will be demonstrated.

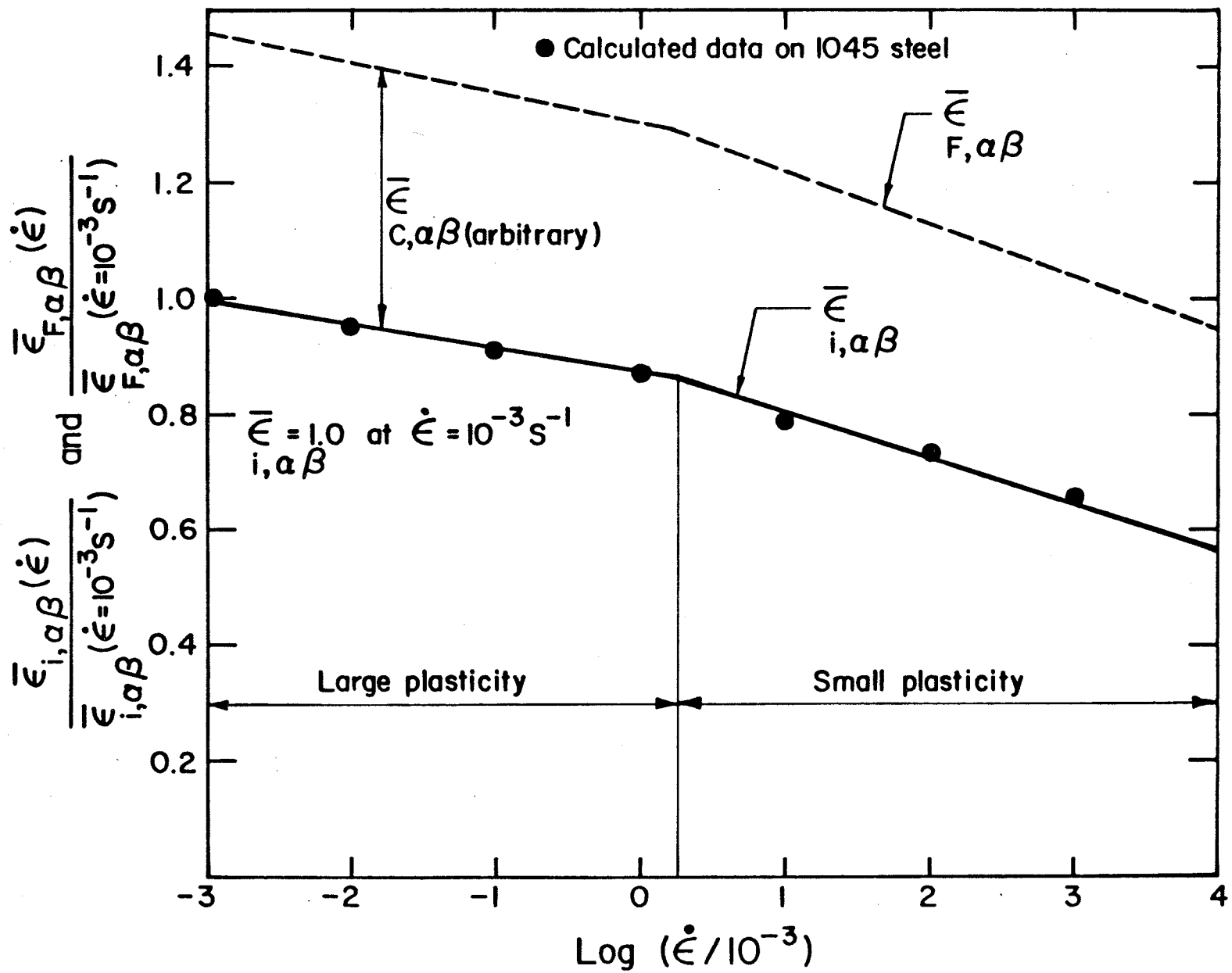

Figure 7.1 Strain rate dependence of $\bar{\varepsilon}_{i,\alpha,\beta}$ expressed as $\bar{\varepsilon}_{i,\alpha,\beta}(\dot{\varepsilon})/\bar{\varepsilon}_{i,\alpha,\beta}(\dot{\varepsilon} = 10^{-3})$ and $\bar{\varepsilon}_{F,\alpha,\beta}$ expressed as $\bar{\varepsilon}_{F,\alpha,\beta}(\dot{\varepsilon})/\bar{\varepsilon}_{F,\alpha,\beta}(\dot{\varepsilon} = 10^{-3})$, $\bar{\varepsilon}_{C,\alpha,\beta}$ denotes an arbitrary value for $\varepsilon_{F,\alpha,\beta}$.

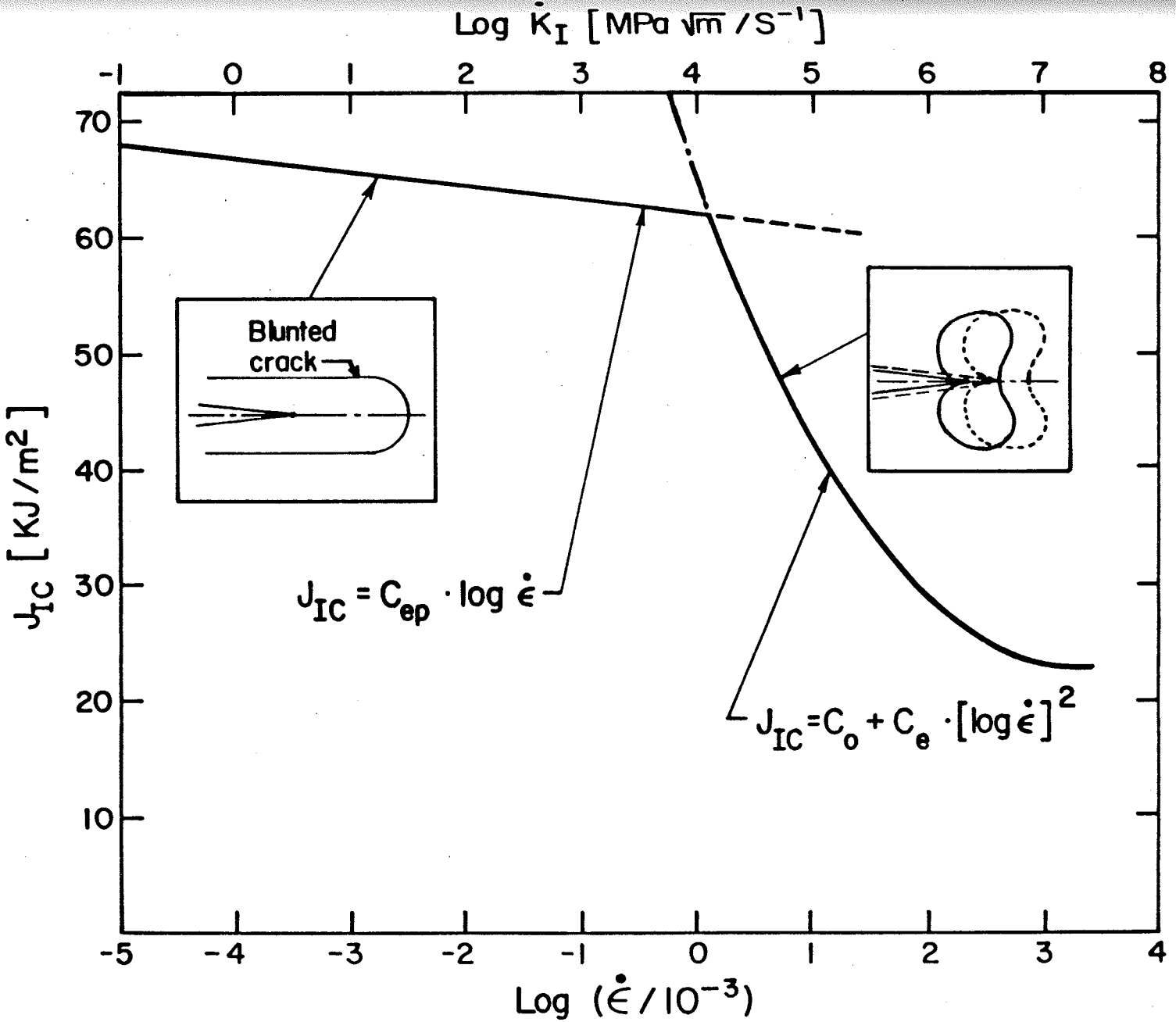

Figure 7.2 Relationship between J_{IC} and strain rate.

CHAPTER 8

FRACTURE TOUGHNESS AND DUCTILITY STUDIES OF TEMPERED MARTENSITIC AISI 1045 STEEL

The effect of metallurgical factors, such as microstructure, impurities and grain size on the value of fracture toughness is of great importance. The mechanisms leading to the nucleation and propagation of a crack are closely related to the presence of secondary phase particles, as well as to the parent metal matrix itself. The metal matrix, within the dimensions of a single grain, determines whether deformation will take place by slip, twinning or cleavage and what the direction of propagation of that deformation will be [105]. The phenomenon of fracture at the grain size level is determined by the stress state, the crystallography of the matrix and the presence of precipitates. Precipitates along grain boundary will tend to cause intergranular embrittlement while precipitates within a given grain are responsible for fracture by cleavage [106]. Tempered martensite embrittlement has an important role on plane strain fracture toughness K_{IC} [107-110].

In the present chapter, fracture toughness J_{IC} and ductility studies in the transition temperature range for tempered martensitic AISI 1045 steel will be described.

8.1 Experimental Results

The same experimental procedures described previously in Chapter 3 were adopted to obtain the experimental results for tempered martensitic AISI 1045 steel. The corresponding

sequence of the experimental results, similar to that reported in Chapter 4, is shown in Figs. 8.1 to 8.11.

Fig. 8.1 shows the variation of Charpy v-notch toughness with temperature. A ductility transition temperature corresponding to a Charpy energy of 15 ft. lb occurs at about 8°C compared with a transition temperature of 0°C for the annealed condition. Upper shelf was obtained at temperatures above 60°C while lower shelf was obtained at temperatures below -30°C. These temperature ranges are almost the same for 1045 steel in the annealed condition.

Figs. 8.2 and 8.3 show the tensile properties of the tempered martensitic AISI 1045 steel as a function of temperature. Fig. 8.2 shows the variation of σ_y, σ_u and σ_{flow} as a function of temperature, while Fig. 8.3 shows the temperature dependence of tensile ductility in percent elongation and percent reduction in area. It is observed that there is a noticeable temperature dependence of σ_y, σ_u and consequently σ_{flow}. The trend of variation of these properties with temperature is similar to that obtained for 1045 steel in the annealed condition but shifted up to higher values of σ_y, σ_u and σ_{flow}. Tensile ductility shows also a temperature dependence similar to that obtained for 1045 steel in the annealed condition, but with lower values in both percent elongation and percent reduction in area.

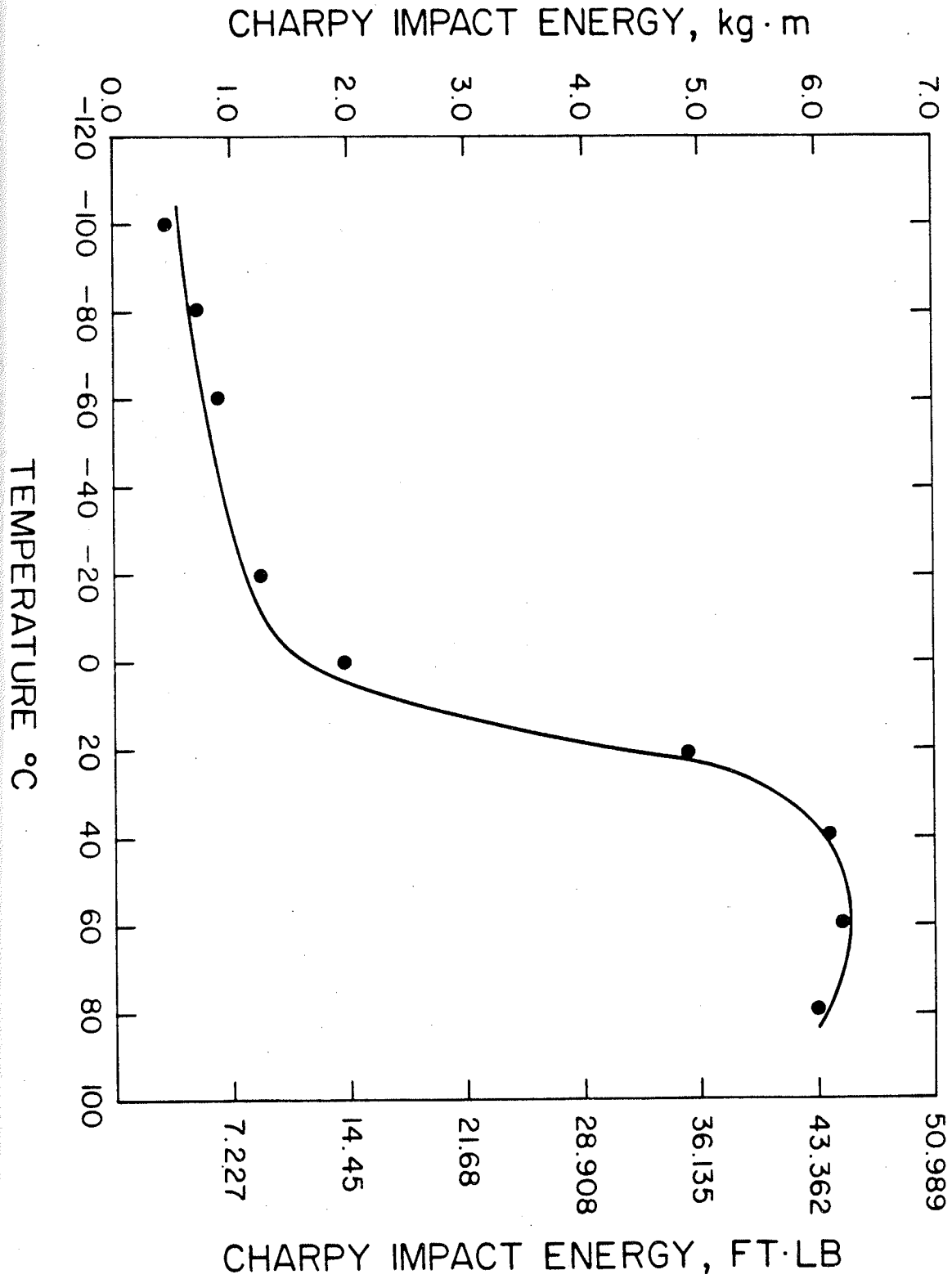

Figure 8.1 Variation of Charpy V-notch toughness with temperature for tempered martensitic AISI 1045 steel.

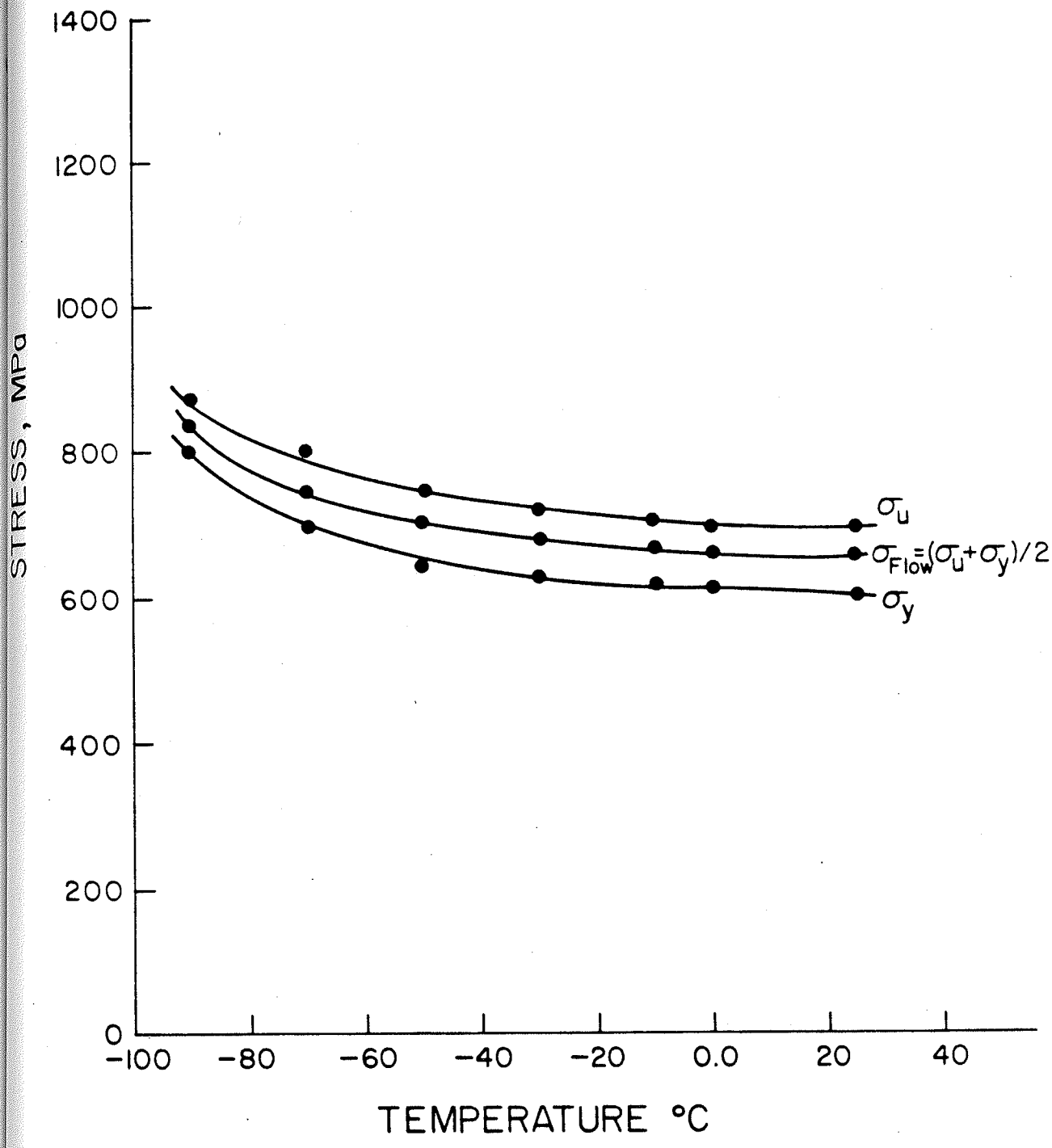

Figure 8.2 Variation of tensile properties with temperature for tempered martensitic AISI 1045 steel.

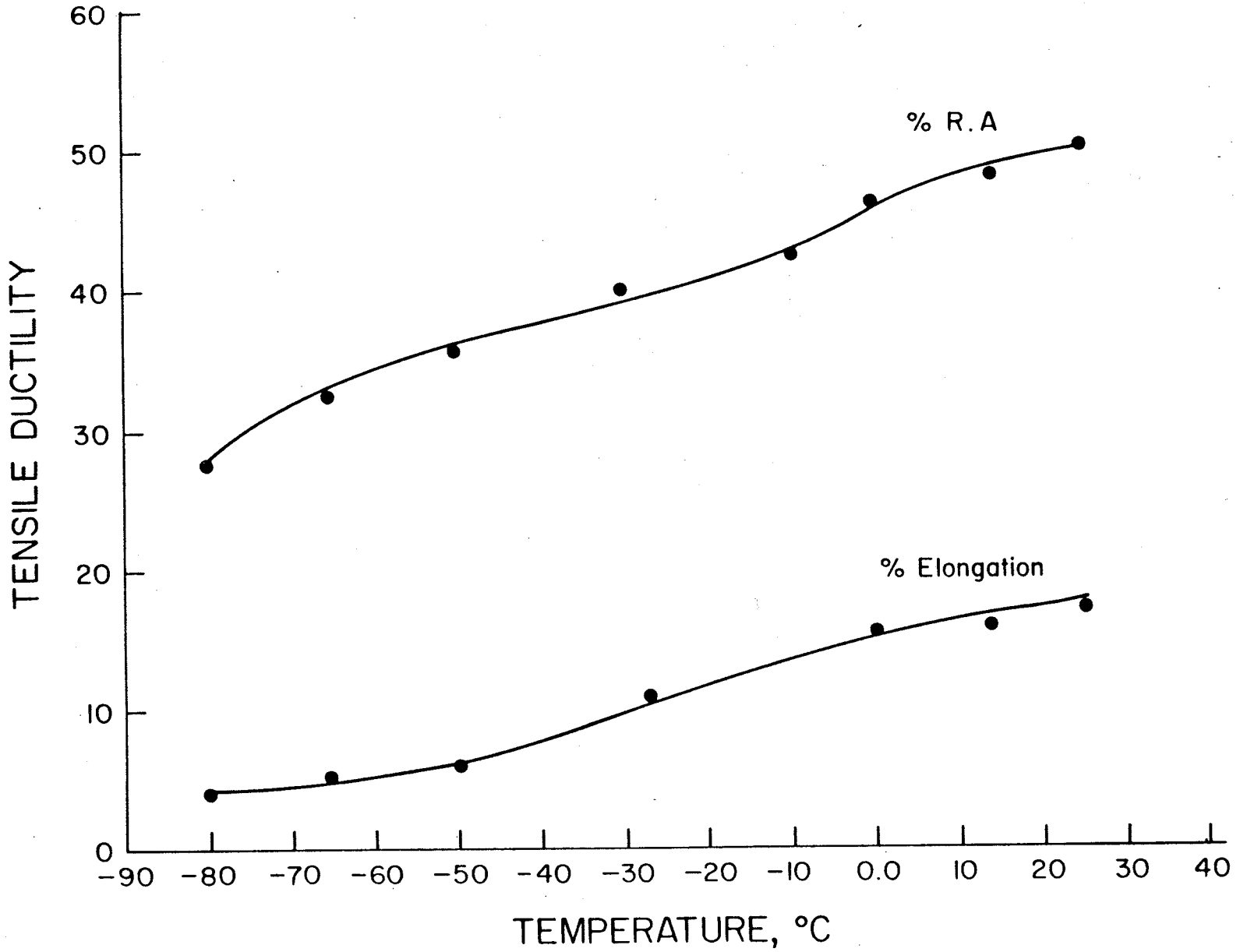

Figure 8.3 Variation of tensile ductility with temperature for tempered martensitic AISI 1045 steel.

Fig. 8.4 shows the variation of the bulge ductility with temperature for AISI 1045 steel in the tempered martensitic condition. It is shown that a marked drop in bulge ductility seems to take place below -30°C. The values of bulge ductility for the tempered martensitic microstructure, are lower than those obtained for the pearlitic structure.

Figs. 8.5(a) to 8.5(g) show J-resistance curves, which are the plots of J versus Δa, for different testing temperatures of 25, 10, 0, -10, -20, -30 and -40°C respectively. The intersection of the blunting line and the crack advance line gives the J_{IC} values as shown. J_{IC} variation with temperature is presented in Fig. 8.6. J_{IC} decreases from a value of 60 kJ/m^2 at 20°C to a value of about 9 kJ/m^2 at -90°C. The relation between J_{IC} and temperature for the tempered martensitic structure appears to have the same trend of that obtained for pearlitic microstructure, but the values of J_{IC} are generally less than those obtained for AISI 1045 steel in the annealed condition. There are two regions characterizing the relationship between fracture toughness and temperature, namely from -100°C to about -15°C the slope of the curve of J_{IC} with temperature is much lower than in the region from -15°C to 25°C.

Fig. 8.7 and 8.8 show respectively the slope of crack advance line as well as the tearing modulus T_R as a function

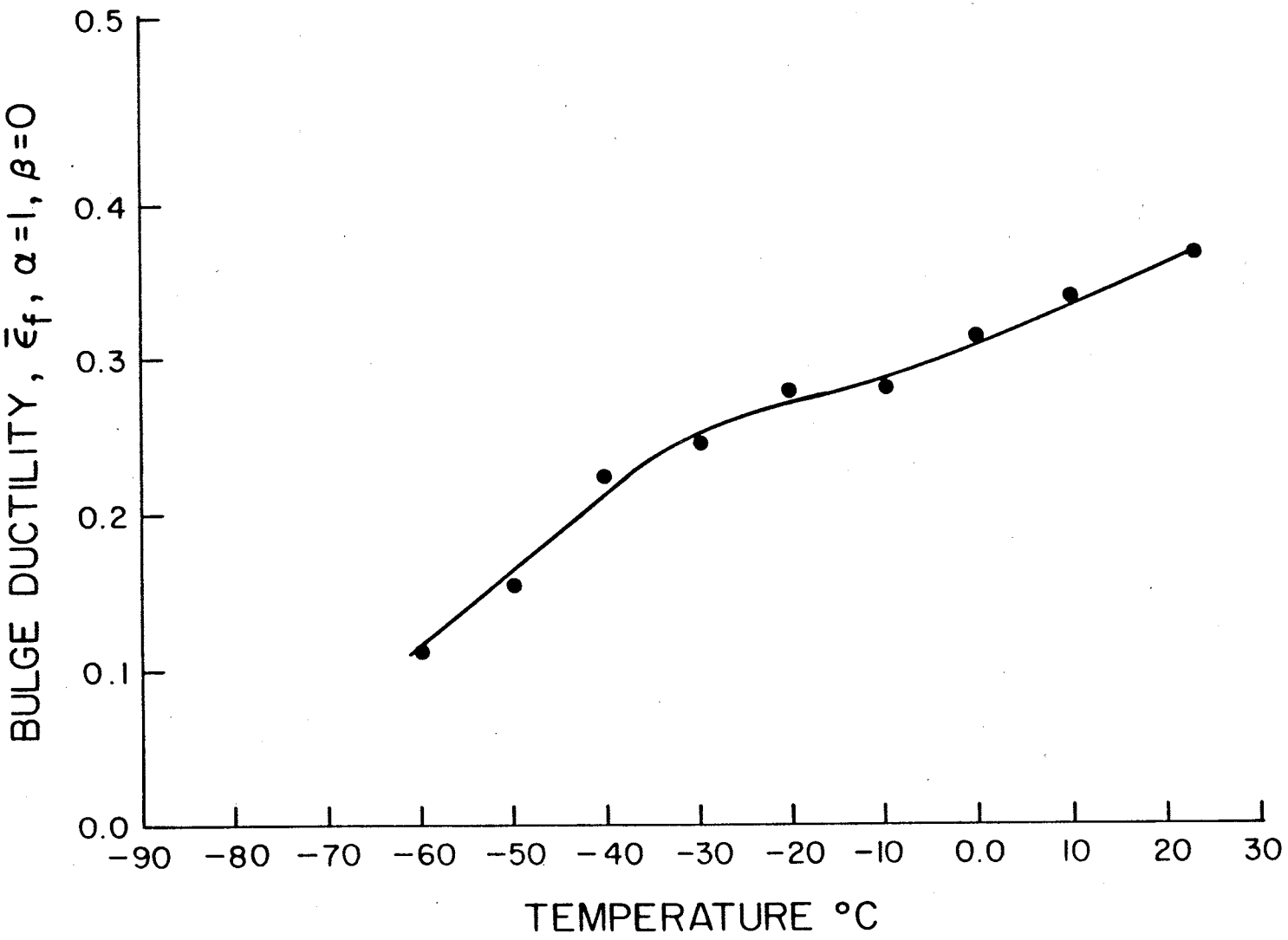

Figure 8.4 Variation of bulge ductility with temperature for tempered martensitic AISI 1045 steel.

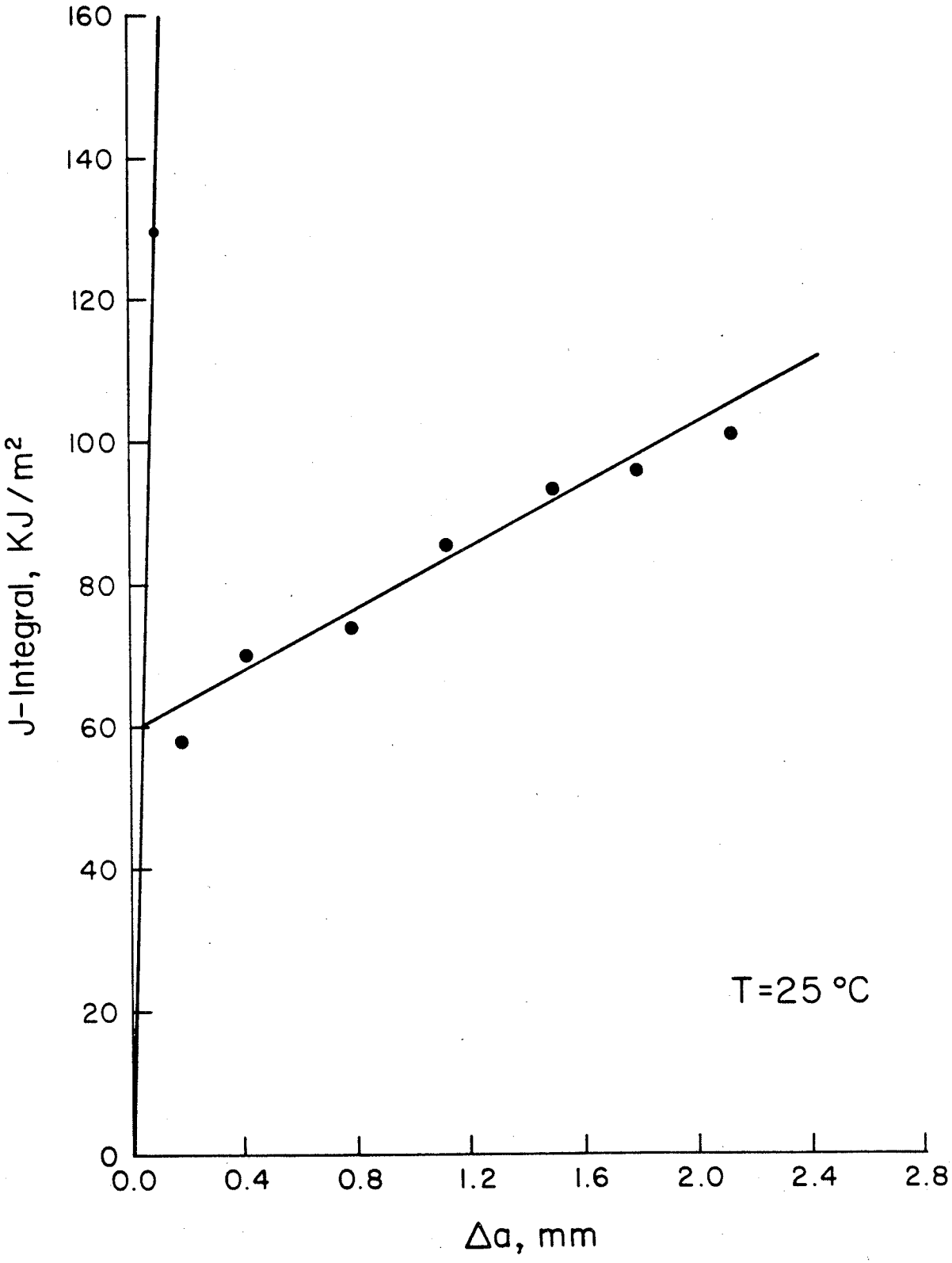

Figure 8.5(a) J-resistance curves for different testing temperature for tempered martensitic AISI 1045 steel.

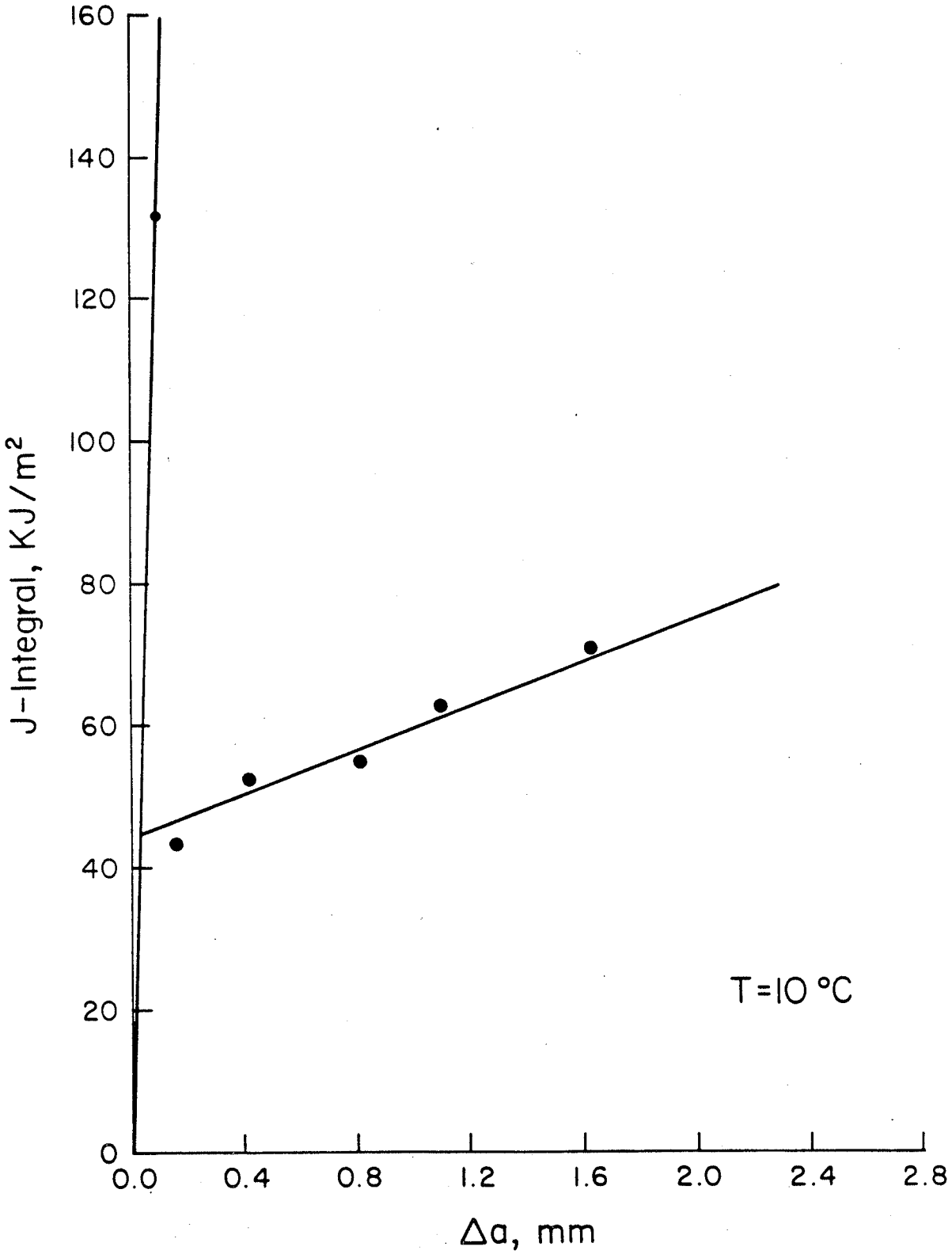

Figure 8.5(b) J-resistance curves for different testing temperature for tempered martensitic AISI 1045 steel.

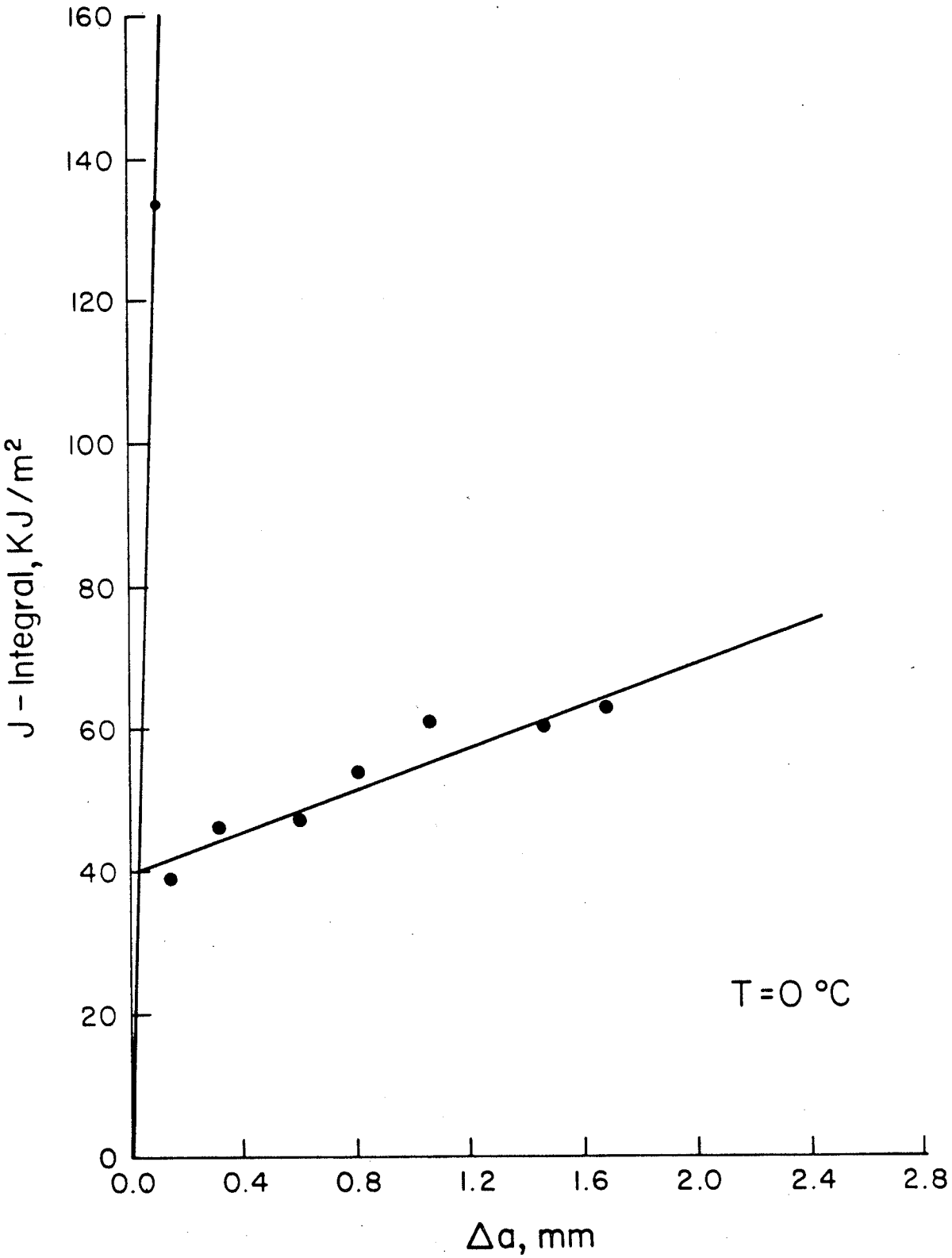

Figure 8.5(c) J-resistance curves for different testing temperature for tempered martensitic AISI 1045 steel.

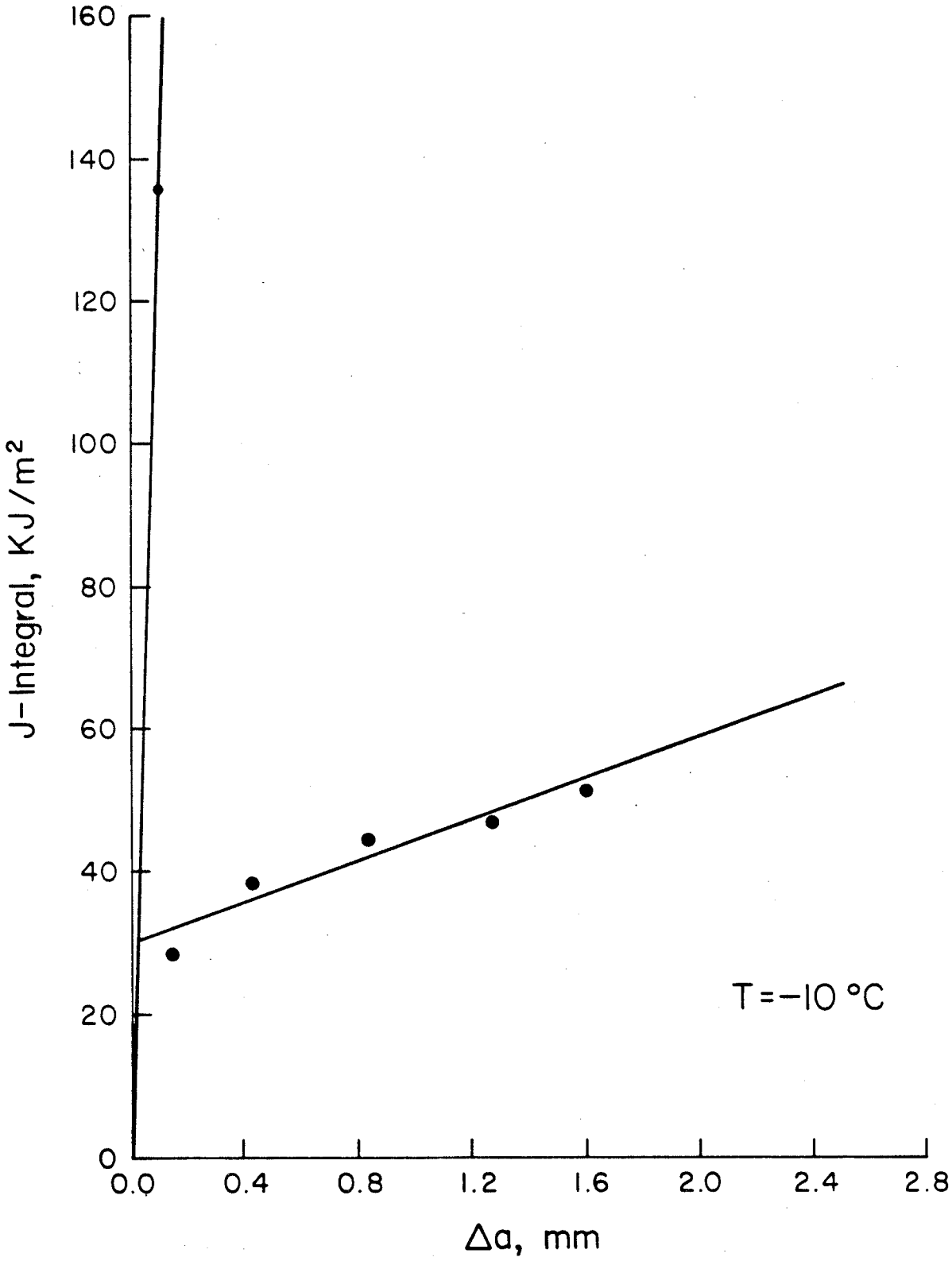

Figure 8.5(d) J-resistance curves for different testing temperature for tempered martensitic AISI 1045 steel.

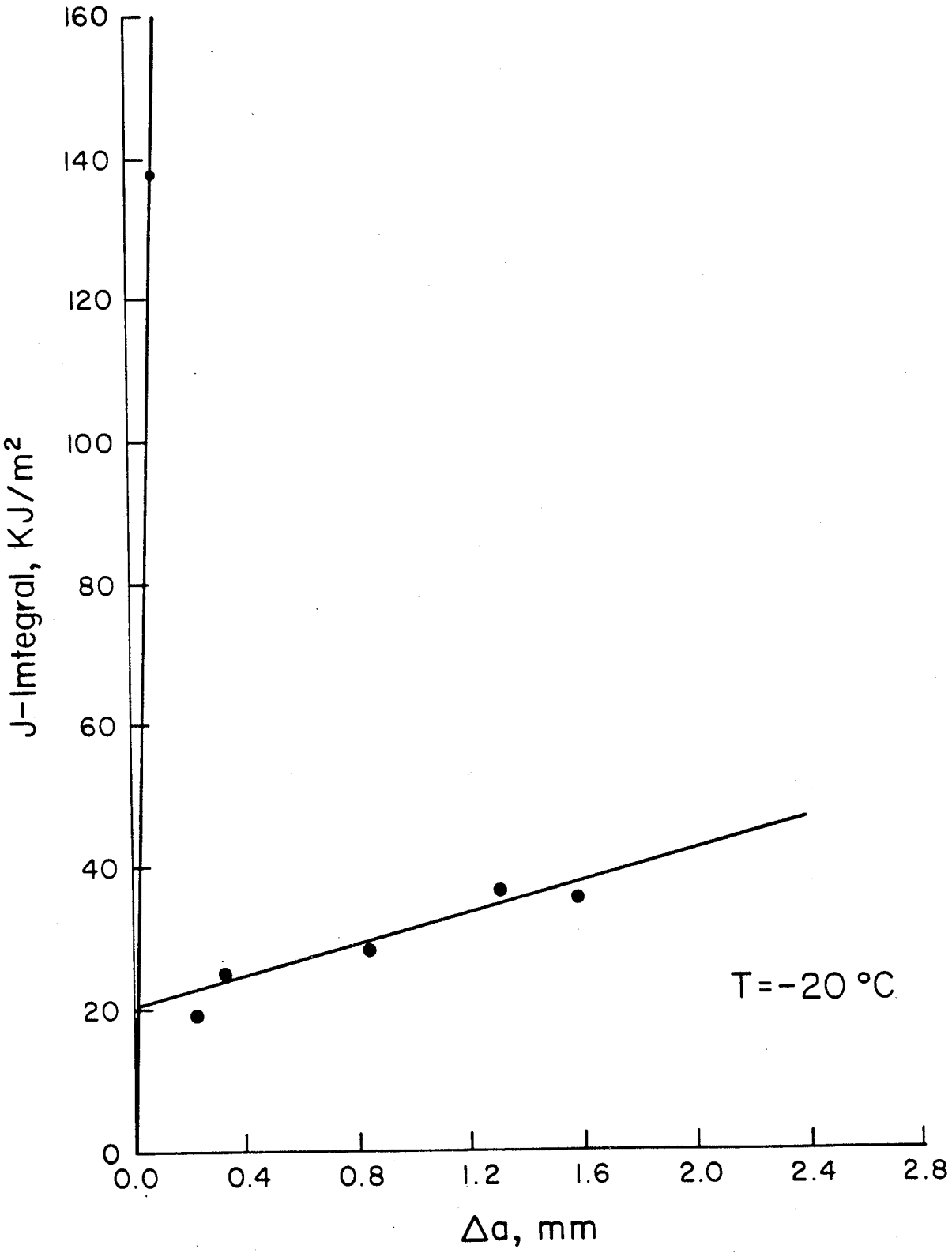

Figure 8.5(e) J-resistance curves for different testing temperature for tempered martensitic AISI 1045 steel.

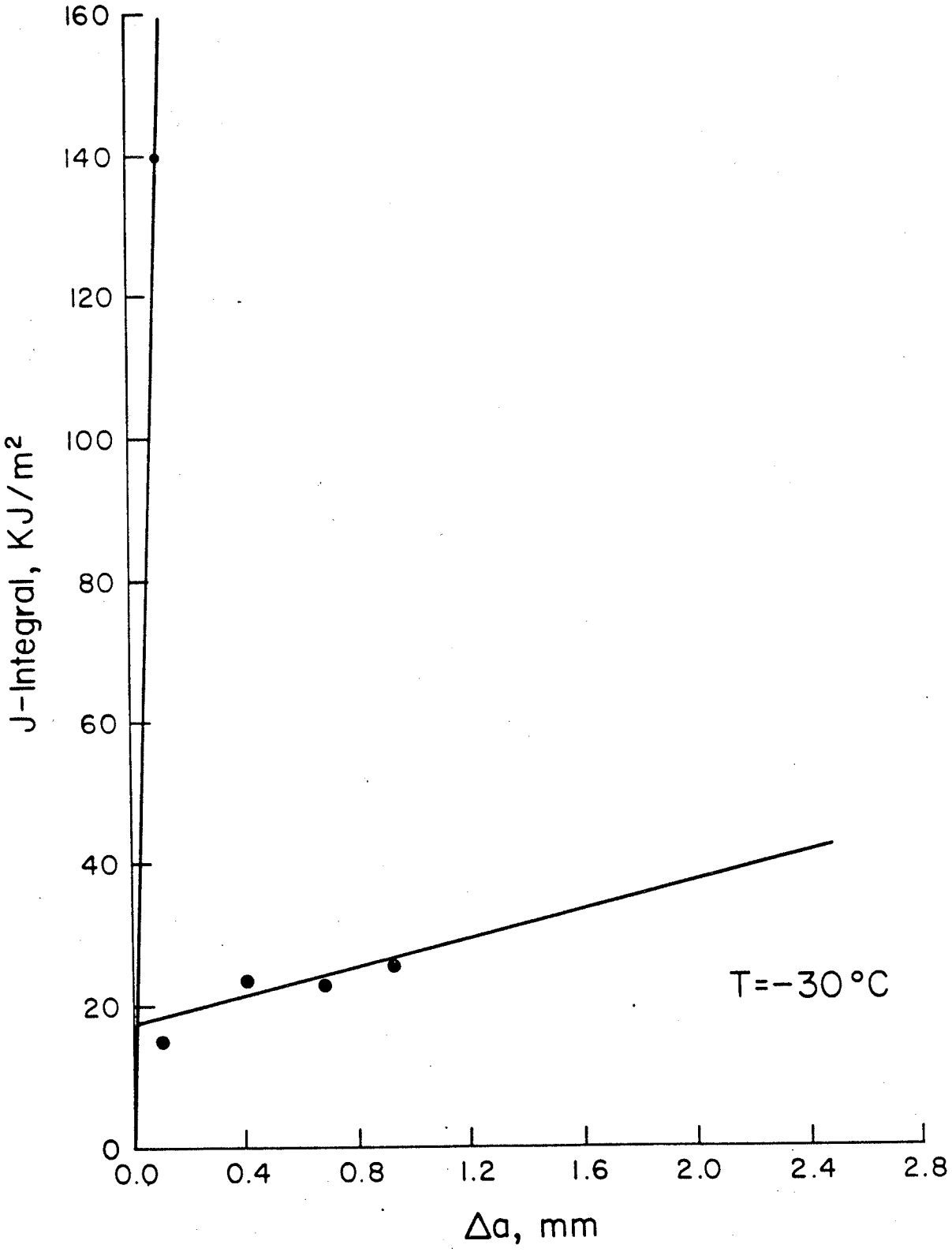

Figure 8.5(f) J-resistance curves for different testing temperature for tempered martensitic AISI 1045 steel.

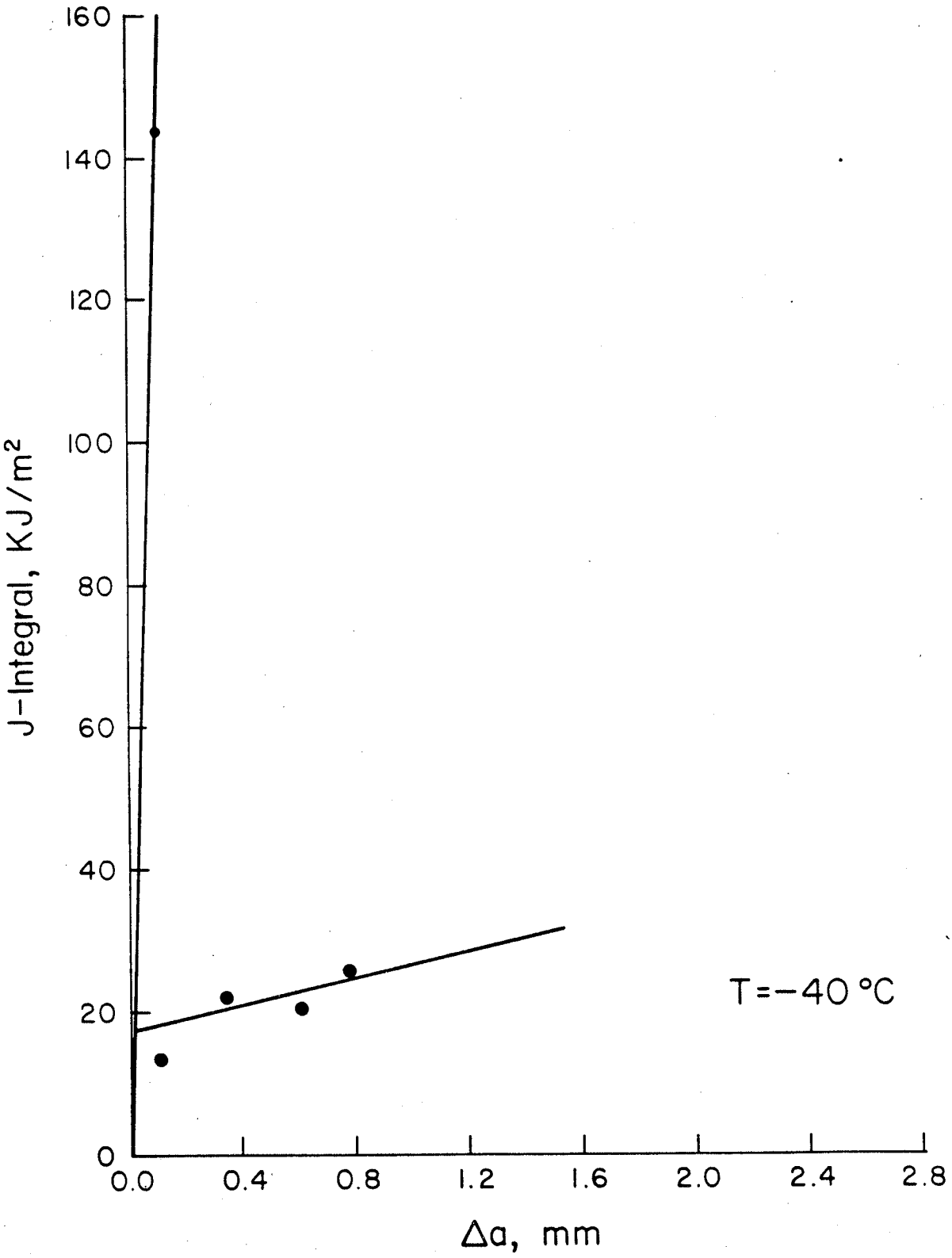

Figure 8.5(g) J-resistance curves for different testing temperature for tempered martensitic AISI 1045 steel.

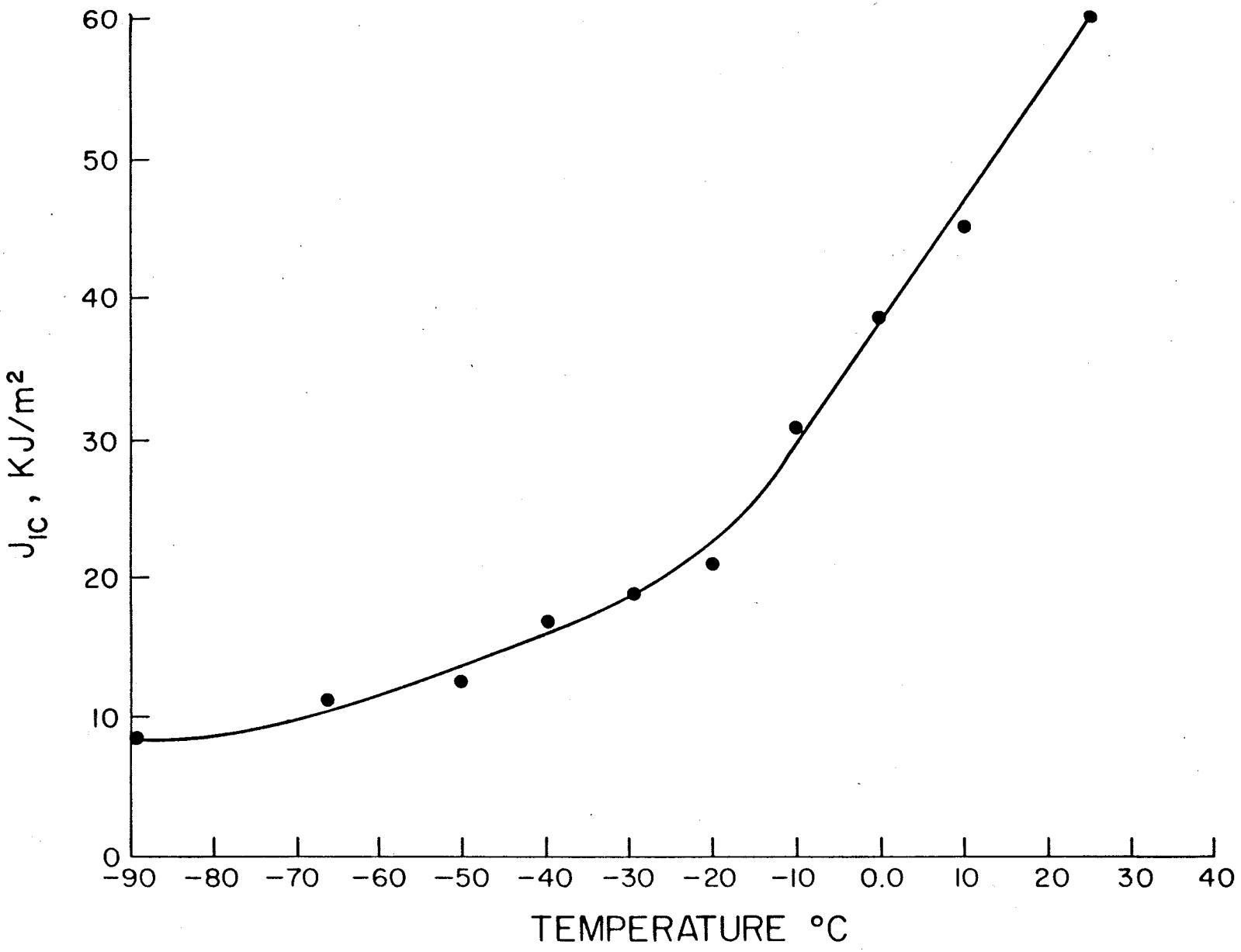

Figure 8.6 J_{IC} versus temperature for tempered martensitic AISI 1045 steel.

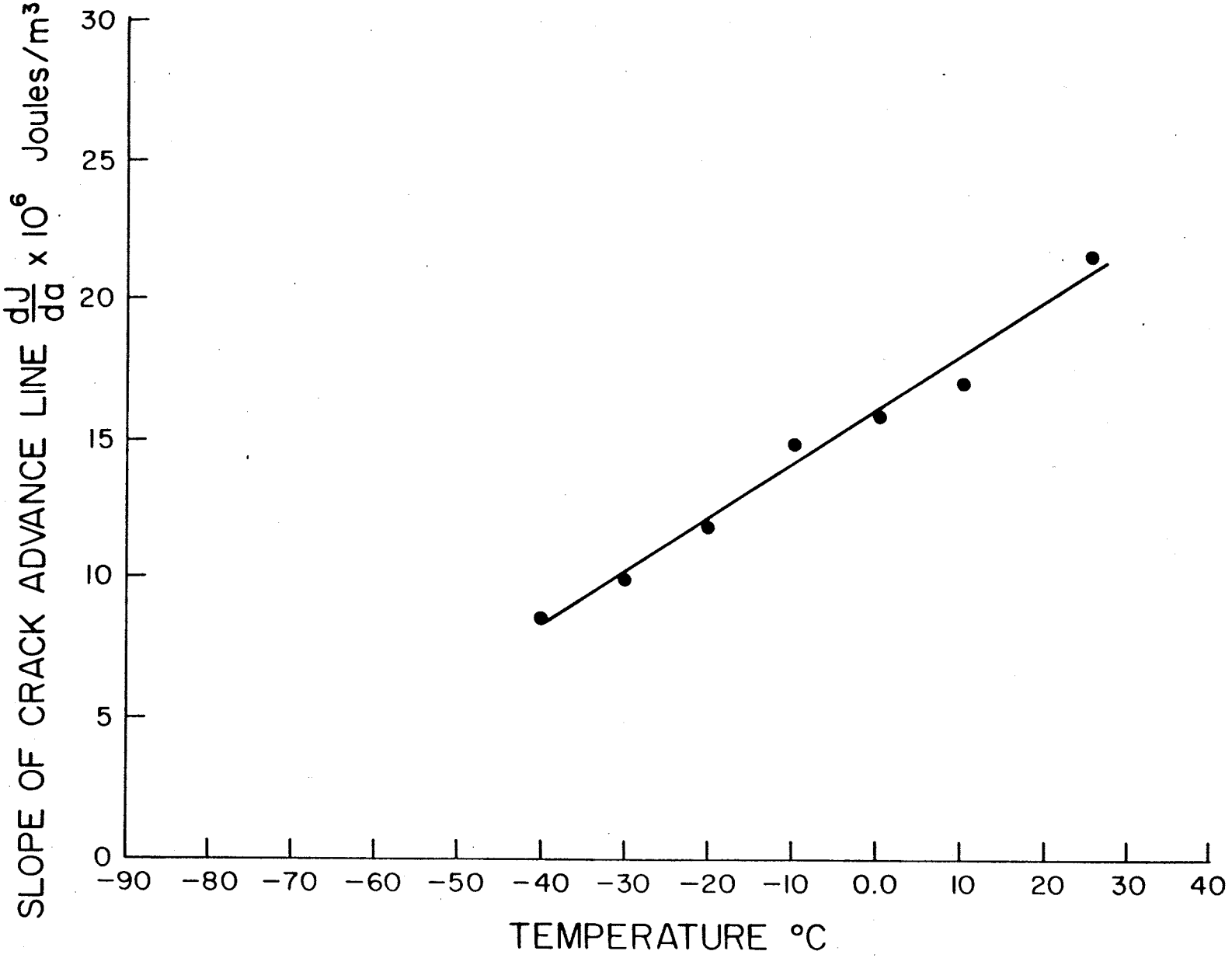

Figure 8.7 Variation of the slope of the crack advance line with temperature for tempered martensitic AISI 1045 steel.

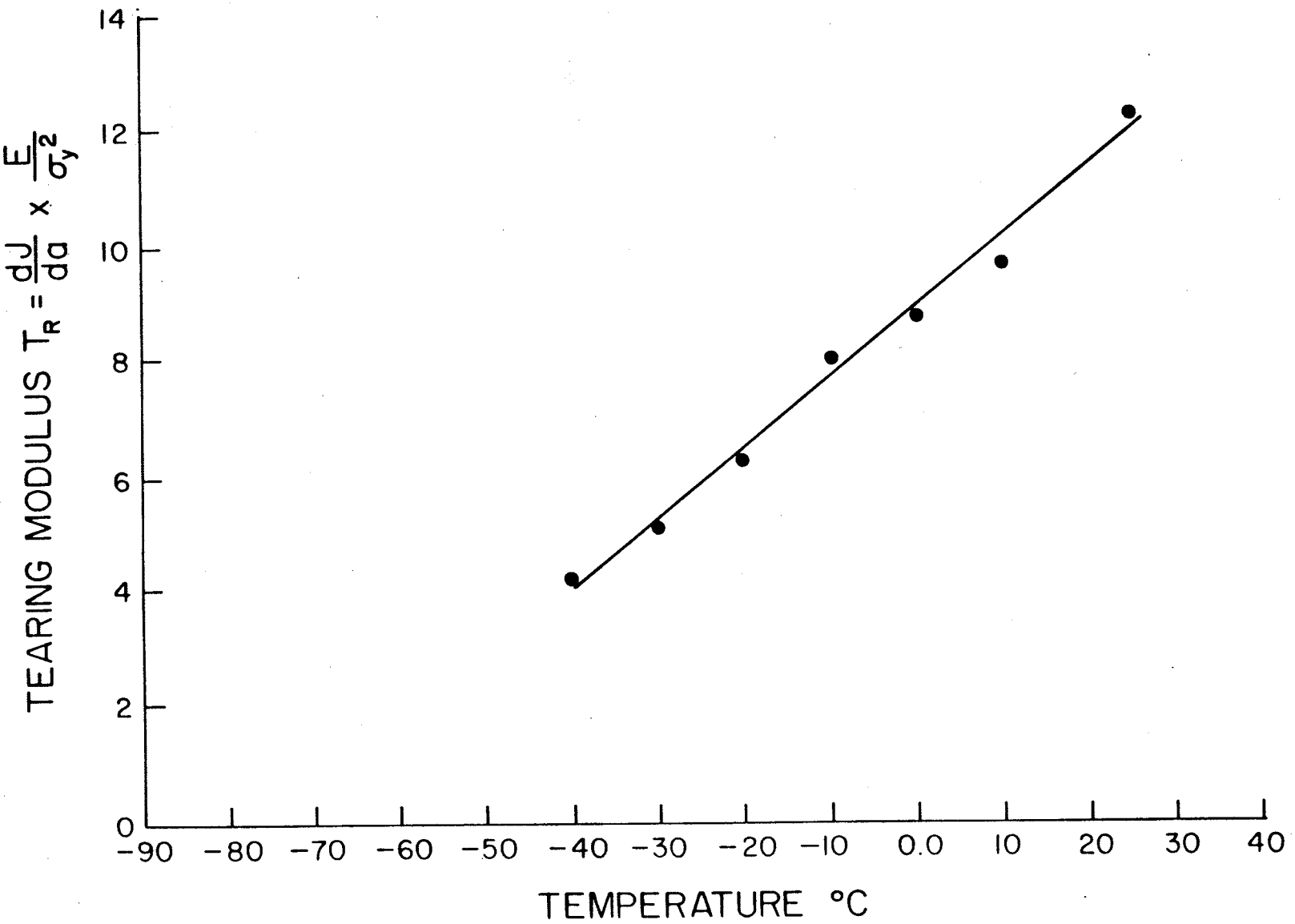

Figure 8.8 Variation of the tearing modulus (T_R) with temperature for temperature for tempered martensitic AISI 1045 steel.

of temperature. Both figures show the same trend as those obtained for AISI 1045 steel in the annealed condition. Specifically, an almost linear relation of these parameters with temperature, has been observed in the range from 25°C to -40°C. The values of the slope of crack advance line and the tearing modulus are less than those values for the same parameters, obtained for AISI 1045 in the annealed condition.

The variation of the critical crack extension Δa_{cr} and the critical load line displacement δ_{cr} with temperature are shown respectively in Figs. 8.9 and 8.10. Both of these parameters are less than those obtained for the pearlitic microstructure, but they have the same shape with a transition temperature of about -15°C.

The relationship between the fracture toughness J_{IC} and the bulge ductility for the tempered martensitic structure is presented in Fig. 8.11. A linear relationship is obtained in the range from -30°C to 25°C. The trend is similar to that obtained for AISI 1045 steel, but the slope of the line for the tempered martensitic 1045 steel is higher than the corresponding one obtained for the annealed 1045 steel.

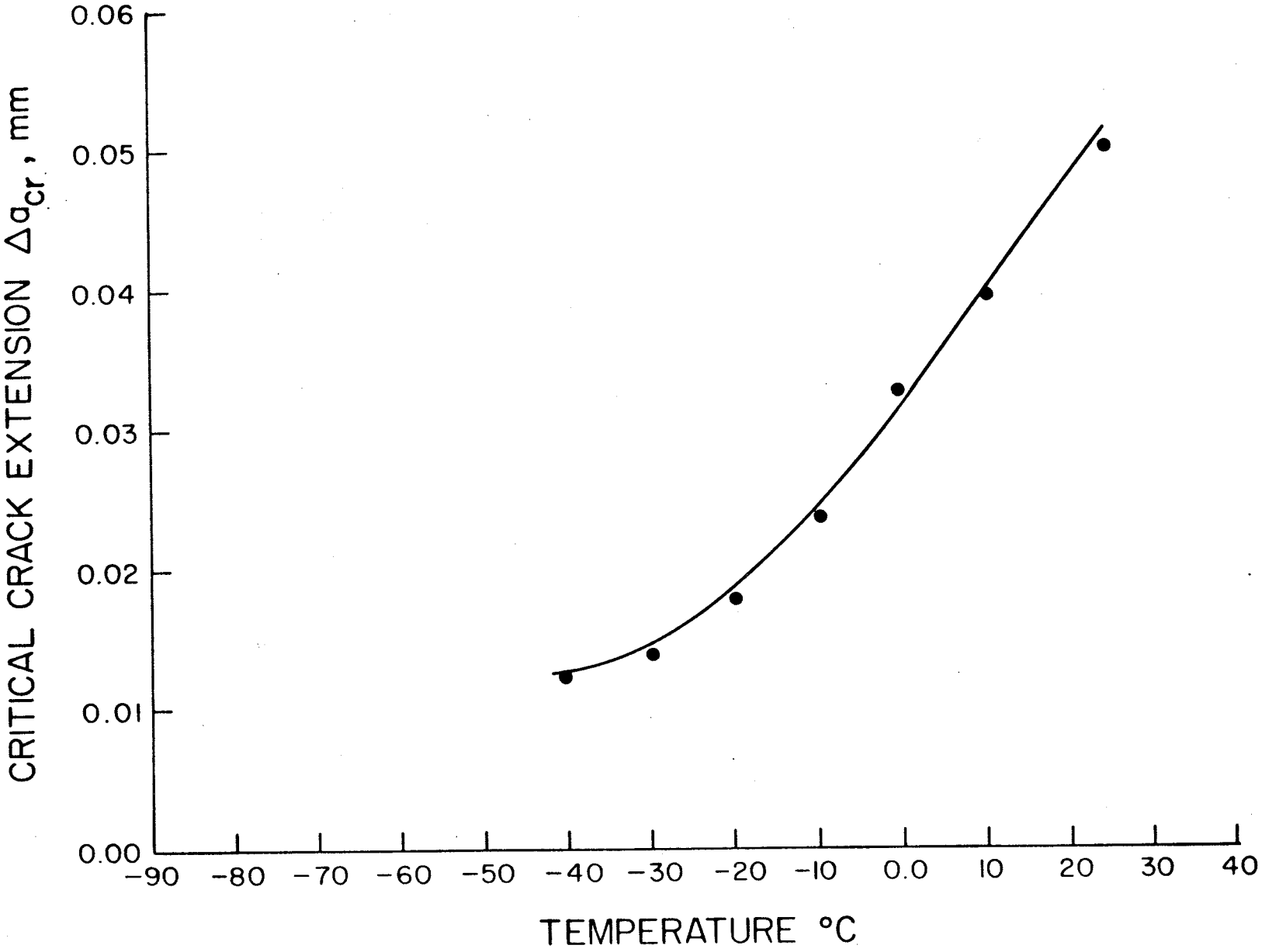

Figure 8.9 Variation of the critical crack extension (Δa_{cr}) with temperature for tempered martensitic AISI 1045 steel.

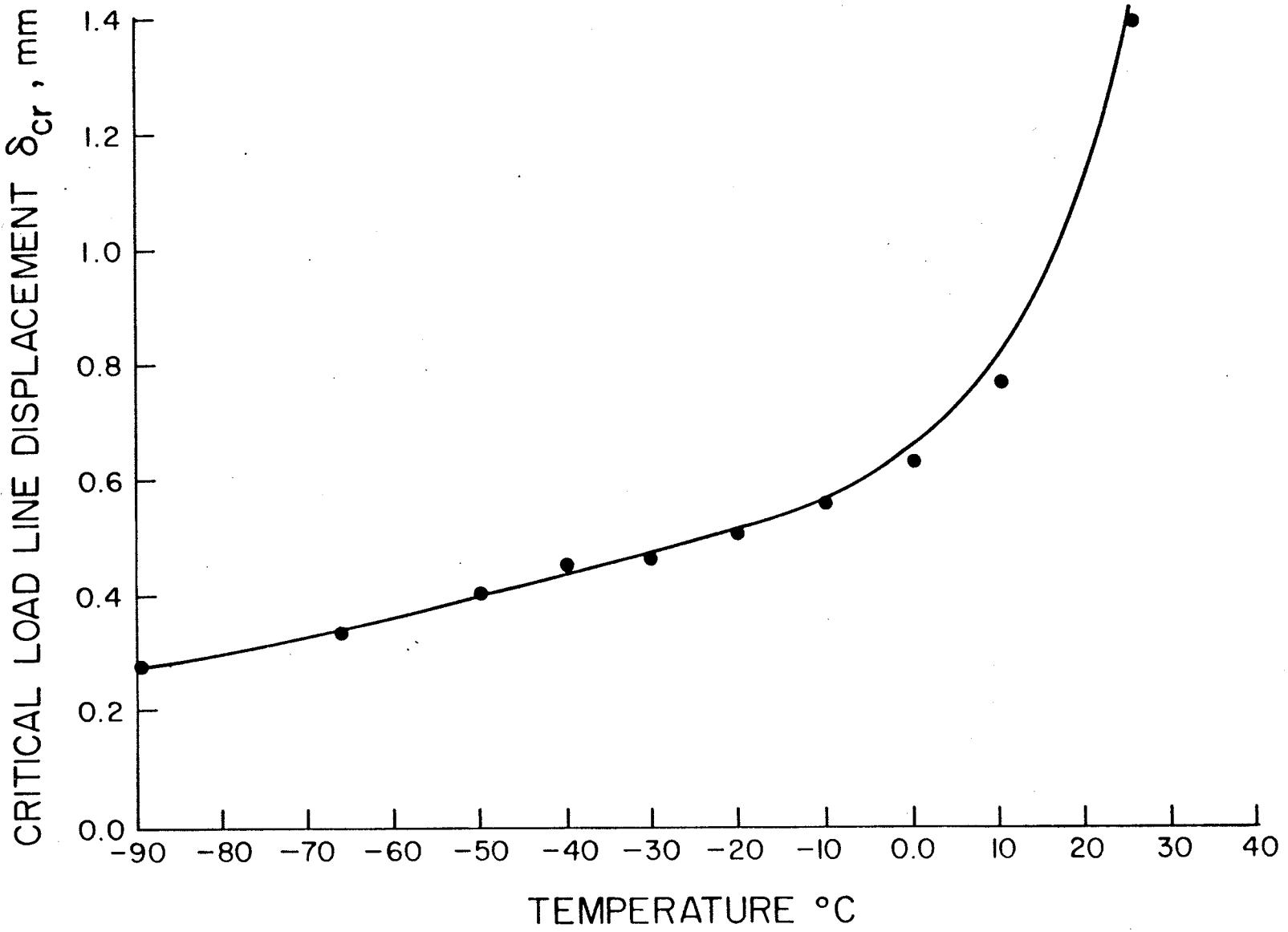

Figure 8.10 Variation of the critical load line displacement (δ_{cr}) with temperature for tempered martensitic AISI 1045 steel.

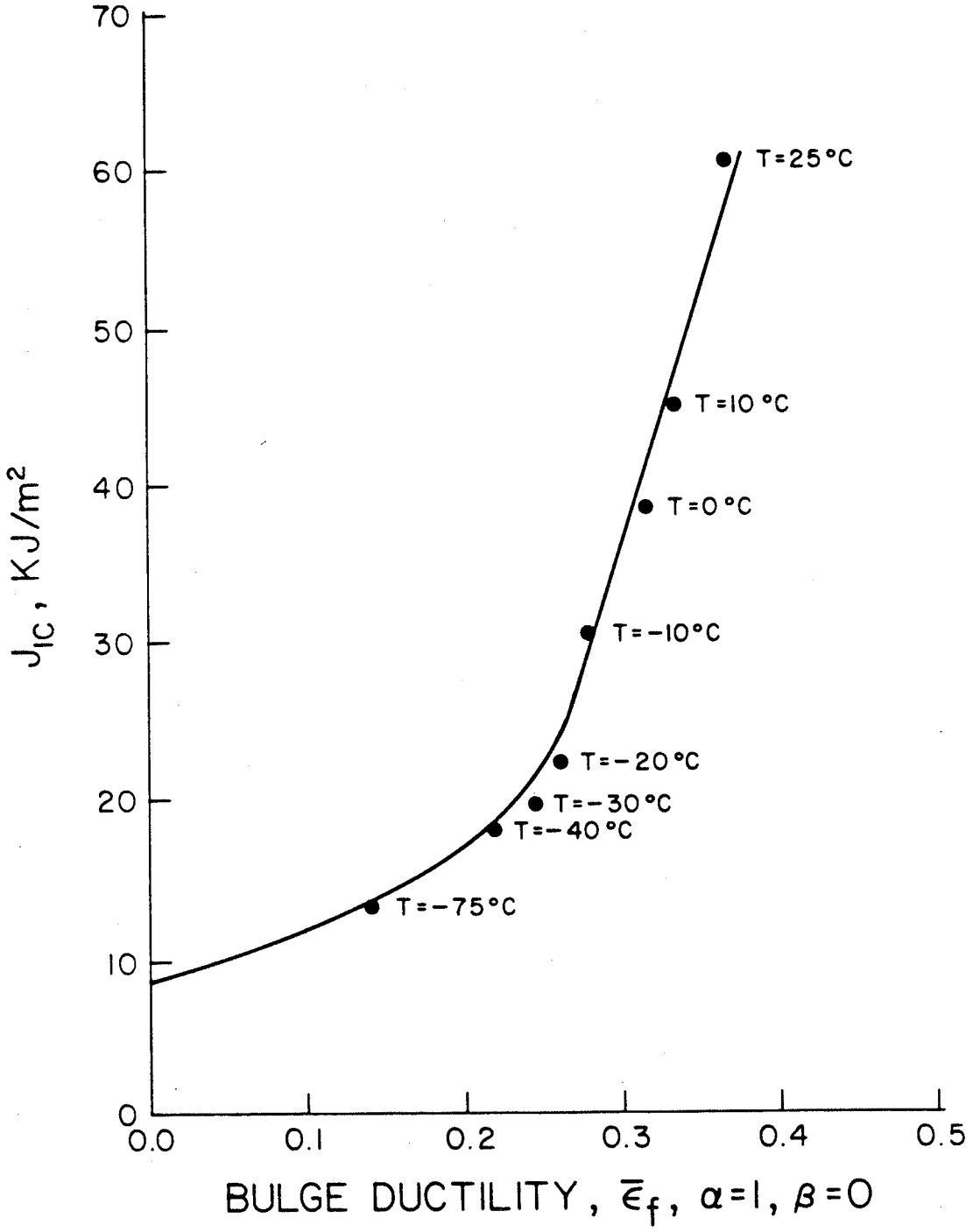

Figure 8.11 The relationship between J_{IC} and bulge ductility for tempered martensitic AISI 1045 steel.

8.2 Discussion

The experimental results for the tempered martensitic AISI 1045 steel show the same trend of behavior obtained with AISI 1045 steel in the annealed condition. Generally, the fracture toughness J_{IC} and ductility have decreased, while the strength has increased in comparison with the values obtained for the annealed 1045 steel. More specifically, there is a transition temperature of about -15°C in the relationship between fracture toughness and temperature. This transition temperature is similar to that obtained for the annealed 1045 steel. This variation of J_{IC} with temperature is attributed to the variation of the flow stress with temperature for both tempered and annealed 1045 steel (see Figs. 8.2 and 8.4). Therefore, the model described in Chapter 6 can be applied for the tempered 1045 steel. The values of the constants in equations (6.15) and (6.17) for the tempered AISI 1045 steel are shown in Table 8.1.

As indicated in Fig. 8.11, the variation of fracture toughness J_{IC} with bulge ductility $\varepsilon_{f,\alpha=1,\beta=0}$ was obtained for tempered martensitic AISI 1045 steel as a function of temperature. The range of temperature is -75 to 25°C and includes both the linear elastic and the elastic-plastic regions. These experimental results were used to evaluate

the constants C_1 and C_2 in equation (5.27) and C_p in equation (5.33). The values of these constants are given in Table 8.2.

In conclusion, the transition in behavior from linear elastic to elastic-plastic, in the relation between fracture toughness J_{IC} and temperature from one hand and in the relation between J_{IC} and bulge ductility from the other hand, for the tempered martensitic 1045 steel was shown to be similar to that obtained for 1045 steel in the annealed condition, since the flow stress as a function of temperature for both microstructures appears to exhibit the same behavior. However, the values of fracture toughness J_{IC} for tempered martensitic structure, are less than those values of fracture toughness obtained for pearlitic structure, since the ductility values, which control the size of the process zone ahead of the crack, are less than those ductility values of pearlitic structure.

8.3 Summary

In this chapter fracture toughness J_{IC} and ductility studies in the transition region of tempered martensitic AISI 1045 steel have been presented. The same trend as that obtained for annealed 1045 steel has been observed. This is mainly because both microstructures show similar trends of the variation of the flow stress as a function of temperature.

Table 8.1: Values of the constants in Eqns. (6.15) and (6.17) for tempered martensitic AISI 1045 steel

Constant	Value	
$J_{IC}(o)$ in Eq. (6.15)	8.2	KJ/m^2
C_e in Eq. (6.15)	0.0002	$KJ/m^2/°K^2$
$C_{ep} = \frac{\Delta J_{IC}}{\Delta T}$ in Eq. (6.17)	0.8	$KJ/m^2/°K$

Table 8.2: Values of the constants in Eqns. (5.27) and (5.33) for tempered martensitic AISI 1045 steel

Constant	Value	
C_1 in Eq. (5.27)	176	KJ/m^2
C_2 in Eq. (5.27)	9	KJ/m^2
$C_p = \frac{\Delta J_{IC}}{\Delta \varepsilon_{f,\alpha=1,\beta=0}}$ in Eq. (5.33)	292	KJ/m^2

The models described earlier in Chapters 5 and 6 have been applied, and the corresponding experimental constants have been calculated. It has been confirmed that the fracture toughness and ductility relationships in the transition region for both pearlitic microstructure and tempered martensitic microstructure can be described reasonably well by these models.

In the next chapter a general discussion and a main conclusions of the entire study is presented.

CHAPTER 9

DISCUSSION AND CONCLUSIONS

9.1 General Discussion

The experimental results described earlier indicate two different trends: (a) There is a transition temperature (about -20°C for the annealed 1045 steel, and about -15°C for the tempered martensitic 1045 steel) in the relationship between J_{IC} and temperature and (b) The variation of tensile ductility and bulge ductility with temperature indicates a transition only taking place at about -40°C for the annealed 1045 steel and about -30°C for the tempered martensitic 1045 steel. To further explain these findings, it is necessary to examine the effect of temperature on the different mechanisms contributing to the value of J_{IC}. J_{IC} is determined by the intersection of the blunting line and the crack advance line. The coordinates of this point of interesection are of course J_{IC} and Δa_{cr}. The slope of the blunting line is defined as 2 σ_{flow}. Referring to Figs. 4.2 and 8.2, it is clear that down to a temperature of about -20°C, there is no significant variation in σ_{flow}. Below -20°C, the variation between σ_{flow} and temperature T is nonlinear and σ_{flow} increases sharply as T is further decreased. It is thus assumed that the blunting line will remain with almost the same slope as temperature varies between about -20°C to 25°C but will increase in slope as temperature is below -20°C. The variation of σ_{flow} with temperature is typical of iron and steels and was reported elsewhere in the literature [111].

The intersection of the blunting line and crack advance line is also controlled by the position and slope of the crack advance line. The variation of the slope of the crack advance line, as well as the tearing modulus T_R with temperature (shown in Figs. 4.8 and 4.9 for the annealed 1045 steel and Figs. 8.7 and 8.8 for the tempered martensitic 1045 steel) show an almost linear relation of these two parameters as a function of temperature in the region from 25 to about -40°C. Because the slope of the crack advance line and T_R vary linearly with temperature down to -40°C, it can be deduced that the same mechanisms of stable crack growth are present as long as stable crack propagation takes place.

It was also found that the stretch zone width shows the same type of transition as J_{IC} varies with temperature. Thus, it is confirmed that the observed change in slope of the J_{IC}-temperature curve is due to the crack blunting process which is affected by the inherent strength in the material as expressed by σ_{flow}.

A model relating J_{IC} and bulge ductility $\bar{\varepsilon}_{F,\alpha=1,\beta=0}$ was proposed. This model shows that, in the linear elastic region,, J_{IC} varies with $\bar{\varepsilon}^2_{F,\alpha=1,\beta=0}$ while in the elastic-plastic region, J_{IC} varies linearly with $\bar{\varepsilon}_{F,\alpha=1,\beta=0}$. The two equations developed for the linear elastic and elastic-plastic regions contain constants which are evaluated experimentally for a given material, specimen geometry and

testing conditions. For these constants, it is possible to evaluate a characteristic length (L_e^* or kL_p^*) which is related to the microstructure of the material and which describe the fracture process at the crack tip. These microstructural parameters has been previously investigated in the linear elastic case. Ritchie et al [112] found that they may correspond to twice the ferrite grain diameter in mild steel while in A533B pressure vessel steel it was related to the prior austinite grain size [113]. Also Costin and Duffy [75] have stated that it corresponds to the presence of carbide particles at the ferrite grain boundaries. In the elastic-plastic case, the critical fracture strain will occur at some distance ahead of the crack tip where void nucleation takes place. It was reported that the critical strain will be reached over the mean spacing of pearlite colonies that nucleate voids in 1018 and 1020 steel [75]. In A533B, this microstructural parameter is of the order of between one and six or seven times the planar inter-inclusion distance [113].

The experimental results obtained in this present study seem to indicate that, for 1045 steel in the annealed condition at low temperature, the microstructural parameter is of the order of the size of a pearlite colony, while in the elastic-plastic region, the region of intense strain extends over 3 or 4 of these colonies (at room temperature).

The results indicate that, as stable crack growth takes place, the parameter J_{IC} becomes linearly proportional to the bulge ductility, thus indicating that bulge ductility measurements correspond to both crack blunting together with stable crack growth.

A model for the temperature dependence of J_{IC} in the transition region of BCC materials is proposed. The model suggests that the temperature dependence of ductility and fracture toughness arises in the void nucleation phase of ductile fracture. The void nucleation strain is strongly affected by the variation of the flow and yield stress of the materials with temperature. Thus a coherent relationship between fracture toughness, ductility and strength is established in both the linear elastic and the elastic-plastic regime. Knowledge of the temperature dependence of the mechanical properties (strength and ductility) is hence sufficient to determine J_{IC} as a function of temperature in both regimes.

The results of the dynamic fracture testing have shown that the WLCT specimen is a viable alternative for fracture toughness determination of materials which exhibit elastic-plastic behavior under loading rates varying from quasi-static to impact. With this specimen geometry it is possible to determine the load-displacement curves obtained in dynamic testing. The use of a strain gage as a method for determina-

tion of the onset of crack propagation in this particular geometry yields a reasonably accurate value of J_{IC} provided an appropriate value of the constant k in equation (4.3) is taken.

It has been thus demonstrated, both theoretically and experimentally, that for BCC materials, which exhibit a variation of flow stress with temperature as well as strain rate, that a quantitative analysis of the transition region can be formulated. The use of AISI 1045 steel as a typical material for the experiments which were carried out in this study provides a case study for the general behavior of BCC metals. The derived models, with the appropriate experimental constants are able to characterize the relationship between fracture toughness and ductility, temperature and strain (loading) rate.

9.2 Conclusions

(1) A study of the variation of fracture toughness J_{IC} and ductility measured under both tensile loading and biaxial plane strain (bulge) loading, in the transition temperature range for a typical BCC material, delineates the changes in behavior from linear elastic to elastic-plastic behavior. These trends in behavior are mainly affected by the flow stress of the material.

(2) A quantitative correlation relating fracture toughness expressed as J_{IC} and bulge ductility $\bar{\varepsilon}_{F,\alpha=1,\beta=0}$ for a material exhibiting linear elastic behavior and elastic-

plastic behavior was developed. This correlation shows a variation of J_{IC} with $\bar{\varepsilon}^{-2}_{F,\alpha=1,\beta=0}$ for linear elastic behavior and J_{IC} with $\bar{\varepsilon}_{F,\alpha=1,\beta=0}$ for elastic-plastic behavior. The correlations contain three constants to be determined experimentally for a given material, specimen geometry and testing conditions. The experimental results help in determining the size of the fracture zone ahead of the crack as well as the mechanisms for crack blunting and crack growth.

(3) The temperature dependence of ductility, strength and fracture toughness for a BCC material undergoing predominantly linear elastic behavior at low temperatures and elastic-plastic behavior at higher temperature was examined. A model, based on ductile fracture mechanisms involving void nucleation followed by cavity growth and void coalescence, was developed to relate the fracture toughness parameter J_{IC} with temperature. Two general equations for linear elastic and elastic plastic regimes of J_{IC} versus T were obtained. Application of this model to experimental data obtained on a carbon steel show that J_{IC} varies with T^2 at low temperatures and with T at higher temperatures, thus defining a transition temperature.

(4) The correlation between fracture toughness, bulge ductility and stretch zone width of fractured specimens has been investigated as a function of temperature in the

transition region. The results show the existence of a transition in the variation of fracture toughness and stretch zone width with temperature. Such a transition is indicative of the blunting process at the crack tip. However, the bulge ductility appears to be related to the process of stable crack growth process during fracture.

(5) A study of the variation of fracture toughness J_{IC} in materials which exhibit elastic-plastic behavior at the crack tip, with loading rates ranging from quasi-static to dynamic conditions was investigated. A wedge loaded compact tension (WLCT) specimen geometry was found to be suitable for fracture toughness J_{IC} determination under loading rates varying from quasi-static to impact. The experimental results indicate that a significant decrease in fracture toughness occurs under high loading rates for 1045 steel in the annealed condition.

(6) The strain rate dependence of ductility, strength and fracture toughness for materials with high strain rate sensitivity such as steels and aluminum alloys was examined. A model, based on ductile fracture mechanisms, was developed to relate the fracture toughness parameter J_{IC} with strain rate $\dot{\varepsilon}$. Application of this model to experimental data obtained on a carbon steel show that J_{IC} varies with log $(\dot{\varepsilon}/10^{-3})$ at low strain rates and with $[\log(\dot{\varepsilon}/10^{-3})]^2$ at higher strain rates.

(7) It was evident from the observations of the fractured surface using scanning electron microscopy and measurement of the stretch zone width, that there is a transition in fracture behavior with strain rate, namely fracture is predominantly ductile at low strain rates with significant plasticity at the crack tip resulting in excessive macroscopic blunting, while the fracture behavior is mostly elastic at high strain rates and the corresponding stretch zone ahead of the crack tip is very limited.

(8) The transition in behavior from linear elastic to elastic-plastic, in the relation between fracture toughness J_{IC} and temperature from one hand and in the relation between J_{IC} and bulge ductility from the other hand, for the tempered martensitic microstructure was shown to be similar to that obtained for pearlitic microstructure, as long as the flow stress as a function of temperature for both microstructures exhibits the same behavior.

References

[1] J.F. Knott, Fundamentals of Fracture Mechanics, Wiley, New York (1973).

[2] D. Broeck, Elementary Engineering Fracture Mechanics, Noordhoff International Publishing, Leyden (1974).

[3] A.A. Griffith, Transactions, Royal Society of London (1920) A-221.

[4] G.R. Irwin, Transactions of the American Society of Mechanical Eng., Journal of Applied Mechanics, Vol. 24 (1957) 361-364.

[5] G.R. Irwin, J.A. Kies and H.L. Smith, Proceeding of American Society for Testing and Materials, Vol. 58 (1958) 640-660.

[6] A.S. Kobayashi, D.E. Maiden, B.J. Simon and S. Ilda, American Society of Mechanical Eng., Paper No. 69-WA/PVP-12.

[7] S.K. Chan, I.S. Tuba and W.K. Wilson, Engineering Fracture Mechanics, Vl. 2 (1970) 1-17.

[8] V.B. Watwood, Nuclear Engineering and Design, Vol. 11 (1969) 323-332.

[9] W.K. Wilson, ASTM STP 513, American Society for Testing and Materials (1972) 90-105.

[10] E. Byskov, International Journal of Fracture, Vol. 6 (1970) 159-167.

[11] P.D. Hilton and G.C. Sih, Methods of Analysis and Solutions of Crack Problems, G.C. Sih, Ed., Noordhoff International Publishing, Leyden (1973) 426-483.

[12] D.M. Tracey, Engineering Fracture Mechanics, Vol. 3 (1971) 255-265.

[13] R.D. Henshell, International Journal for Numerical Methods in Engineering, Vol. 9 (1975) 495-507.

[14] R.S. Barsoum, International Journal for Numerical Methods in Engineering, Vol. 10 (1976) 25-37.

[15] R.S. Barsoum, International Journal for Numerical Methods in Engineering, Vol. 11 (1977) 85-98.

[16] D.S. Dugdale, Journal of Mechanics and Physics of Solids, Vol. 8 (1960) 100-104.

[17] A.A. Wells, British Welding Research Association Report M13/63 (1963).

[18] R.H. Heyer, ASTM STP 527, American Society for Testing and Materials (1973) 1-16.

[19] A. Frediani, Engineering Fracture Mechanics, Vol. 14 (1981) 289-322.

[20] A.M. Sullivan, C.N. Freed and J. Stoop, Ibid., 85-104.

[21] J.R. Rice, Transactions of the American Society of Mechanical Eng., Journal of Applied Mechanics, Vol. 35 (1968) 379-386.

[22] J.A. Begley and J.D. Landes, ASTM STP 514, American Society for Testing and Materials (1972) 1-20.

[23] J.R. Rice, P.C. Paris and J.G. Merkle, ASTM STP 536, American Society for Testing and Materials (1973) 231-245.

[24] J.G. Merkle and H.T. Corten, J. Pressure Vessel Tech., Trans. ASME Vol. 96 (1974) 286-292.

[25] J. Lanteigne, M.N. Bassim and D.R. Hay, ASTM STP 631, American Society for Testing and Materials (1977) 202-216.

[26] B. Marandet and G. Sanz, ASTM STP 631, American Society for Testing and Materials (1977) 302-316.

[27] P. Nguyen-Duy and G. Philippeau, Journal of Testing Evaluation, Vol. 7 (1979) 310-316.

[28] G.A. Clarke, W.R. Andrews, P.C. Paris and D.W. Smidt, ASTM STP 590, American Society for Testing and Materials (1976) 27-42.

[29] D. Munz and H.P. Keller, ASTM STP 631, American Society for Testing and Materials (1977) 217-231.

[30] A. Penelon, M.N. Bassim and J.M. Dorlot, ASTM STP 677, American Society for Testing and Materials (1979) 449-462.

[31] K.F. Amouzouvi and M.N. Bassim, in Fracture Problems & Solutions in the Energy Industry, L.A. Simpson, Ed., Pergamon Press (1981) 179-189.

[32] S.J. Goods and L.M. Brown, Acta Metallurgica, Vol. 27 (1979) 1-15.

[33] J.D. Eshelby, in Progress in Mechanics, I.N. Sneddon and R. Hill (Eds), North-Holland Publishing Company, Amsterdam (1961).

[34] R. Tanaka, T. Mori and T. Nakaruma, Transactions ISIJ, Vol. 11 (1971) 383-392.

[35] A.S. Argon, J. Im., and R. Safoglu, Metallurgical Transactions, Vol. 6A (1975) 825-837.

[36] A.S. Argon, J. Im., Metallurgical Transactions, Vol. 6A (1975) 839-851.

[37] J.R. Fisher and J. Gurland, Metal Science, Vol. 15 (1981) 185-192.

[38] J.R. Fisher and J. Gurland, Metal Science, Vol. 15 (1981) 193-200.

[39] G. LeRoy, I.D. Embury, G. Edwards and M.F. Ashby, Acta Metallurgica, Vol. 29 (1981) 1509-1517.

[40] P. Neumann, Material Science Engineering, Vol. 25 (1976) 217-225.

[41] F.M. Bermin, in Three-Dimensional Constitutive Relations and Ductile Fracture, S. Nemat-Nasser, Editor, North-Holland Publishing Company (1981) 185-205.

[42] A.R. Rosenfield, Metal Review, Vol. 13 (1968) 29-34.

[43] F.A. McClintock, Journal of Applied Mechanics, Vol. 35 (1968) 363-368.

[44] J.R. Rice and D.M. Tracey, Journal of Mechanics and Physics of Solids, Vol. 17 (1969) 201-211.

[45] P.F. Thomason, Journal of Institute of Metals, Vol. 96 (1968) 360-370.

[46] C.A. Berg, Proceedings of 4th U.S. National Congress on Applied Mechanics, Vol. 2, American Society of Mechanical Engineers, New York (1962) 885-892.

[47] F.A. McClintock, S.M. Kaplan and C.A. Berg, International Journal of Fracture, Vol. 2 (1966) 614-622.

[48] D.M. Tracey, Engineering Fracture Mechanics, Vol. 3 (1971) 301-311.

[49] J.R. Rice and G.F. Rosengren, Journal of Mechanics and Physics of Solids, Vol. 16 (1968) 1-13.

[50] F.A. McClintock, Transactions of the American Society of Mechanical Engineers, Journal of Applied Mechanics, series E, Vol. 35 (1968) 368-371.

[51] V. Weiss, Y. Kasai and K. Sieradzki, ASTM STP 615, American Society for Testing and Materials (1976) 16-33.

[52] S. Mikhail, M.Sc. Thesis, Ecole Polytechnique, Montreal, Canada (1978).

[53] T. Iwadati, Y. Tanaka, S. Ono and J. Watanabe, 2nd International Symposium on Elastic-Plastic Fracture Mechanics, Philadelphia (1981) in press.

[54] H. Kotilainen, ASTM STP 700, American Society for Testing and Materials (1980) 352-367.

[55] V.D. Yaroshevich and D.G. Ryvkina, Soviet Physics - Solid State, Vol. 12, No. 2 (1970) 71-85.

[56] C.E. Turner, In Proceedings of the 5th International Conference on Fracture, Vol. 3 (1981) 1167-1175.

[57] M.N. Bassim and S. Mikhail, Canadian Metallurgical Quarterly (1977) 210-213.

[58] J.M. Kraft and A.M. Sullivan, Transactions of the American Society for Metals, Vol. 56 (1963) 160-175.

[59] J.M. Krafft, Applied Materials Research, Vol. 3 (1964) 88-101.

[60] G.R. Irwin, J.M. Krafft, P.C. Paris and A.A. Wells, in Technology of Steel Pressure Vessels for Water-Cooled Nuclear Reactors, G.D. Whitman, G.C. Robinson Jr., amd A.W. Savolainen, Eds, U.S. Atomic Energy Commission, Report ORNL-NSIC-21 (1967) 430-538.

[61] G.T. Hahn and A.R. Rosenfield, ASTM STP 432, American Society for Testing and Materials (1968) 5-32.

[62] G.T. Hahn, R.G. Hoagland and A.R. Rosenfield, Metallurgical Transactions, Vol. 2 (1971) 537-541.

[63] J. Malkin and A.S. Tetelman, Engineering Fracture Mechanics, Vol. 3, No. 2 (1971) 151-167.

[64] R.H. Sailors and H.T. Corten, ASTM STP 514, American Society for Testing and Materials (1972) 164-175.

[65] K. Schwable, in Proceedings of the Third International Conference on Fracture, 4 Verin Deutscher Eisenhuttenleute, Dusseldorf, Vol. III (1973) 515-524.

[66] V. Weiss and M. Sengupta, in Proceedings of the Third International Conference on Fracture, 4 Verein Deutscher Eisenhuttenleute, Dusseldorf, Vol. III (1973) 341-348.

[67] G.T. Hahn and A.R. Rosenfield, Metallurgical Transactions, Vol. 6A (1975) 653-659.

[68] T.L. Tobler, R.P. Mikesell and R.P. Reed, ASTM STP 677, American Society for Testing and Materials (1979) 85-97.

[69] Committee on Rapid Inexpensive Tests for Determining Fracture Toughness, International Journal of Fracture, Vol. 13 (1977) RCR 227-230.

[70] J. Hopkinson, Original Papers, Cambridge University Press (1901) 316-320.

[71] B. Hopkinson, Scientific Papers (1912) 461-467.

[72] H. Liebowitz, Ed., Fracture: An Advanced Treatise, Academic Press, Vol. 1-7 (1968).

[73] ASTM Standard Specification E399-74, American Society for Testing and Materials (1981).

[74] C.E. Turner, ASTM STP 466, American Society for Testing and Materials (1970) 93-103.

[75] L.S. Costin and J. Duffy, Transactions of the American Society of Mechanical Engineers, Journal of Engineering Materials and Technology, Vol. 101 (1979) 258-264.

[76] L.S. Costin, J. Duffy and L.B. Freund, ASTM STP 627, American Society for Testing and Materials (1977) 307-320.

[77] M.L. Wilson, R.H. Hawley and J. Duffy, Engineering Fracture Mechanics, Vol. 13 (1980) 371-385.

[78] H. Kolsky, Proc. Phys. Soc., Vol. 62 (1949) 676-686.

[79] J. Klepaczko, Proc. Inst. Phys. Conf., Ser. No. 47, Bristol (1979) 201-214.

[80] A. Andrzejewski, J. Klepaczko and G. Pluvinage, Proc. Inst. Conf. on analytical and Experimental Fracture Mechanics, Rose, Italy (1980).

[81] S.T. Rolfe and J.M. Barsom, "Fracture and Fatigue Control in Structures: Applications of Fracture Mechanics", Prentice-Hall, Inc., Englewood Cliffs, New Jersey (1977).

[82] P.W. Bridgeman, Studies in Large Plastic Flow and Fracture, Harvard University Press, Cambridge, Mass. (1964).

[83] F.C. Allen, ASTM STP 486, American Society for Testing and Materials (1971) 16-38.

[84] D.P. Clausing, International Journal of Fracture, Vol. 6 (1970) 71-85.

[85] J.M. Barsoum and J.V. Pellegrino, Engineering Fracture Mechanics, Vol. 5 (1973) 209-221.

[86] R.H. Sailors, T & AM Report, No. 367, Illinois University, Urbana, Ill., (1973).

[87] V. Weiss, in Proceedings of the 1971 International Conference on Mechanical Behavior of Materials, The Society of Materials Science, Japan, Vol. 1 (1972) 458-474.

[88] M. Azrin and W.A. Backofen, Metallurgical Transactions, Vol. 1 (1970) 2857-2865.

[89] P. Albrecht, W.R. Andrews, J.P. Gudas, J.A. Joyce, F.I. Loss, D.E. McCabe, D.W. Smidt and P. Vander Sluys, Private Communication.

[90] J.A. Joyce, D.F. Hasson and C.R. Crowe, Journal of Testing Evaluation, ASTM, Vol. 6 (1980) 293-300.

[91] J.R. Klepaczko, M.N. Bassim and T.R. Hsu, Engineering Fracture Mechanics, (1983), in press.

[92] J.R. Klepaczko, Transactions of the American Society of Mechanical Engineers, Journal of Engineering Materials and Technology, Vol. 104 (1982) 29-35.

[93] J.R. Klepaczko and Z. Malinowski, in Proceedings of IUTAM Symposium, K. Kawata, Ed., Spring Verlag (1977) 403-411.

[94] J.N. Robinson and A.S. Tetelman, Engineering Fracture Mechanics, Vol. 8 (1976) 301-313.

[95] P. Nguyen-Duy and S. Bayard, Transactions of the American Society of Mechanical Engineers, Journal of Engineering Materials and Technology, Vol 103 (1981) 55-61.

[96] A. J. Krasowsky and V.A. Vainshtok, International Journal of Fracture, Vol. 17, No. 6 (1981) 579-592.

[97] K.F. Amouzouvi and M.N. Bassim, Material Science Engineering, Vol. 55 (1982) 257-262.

[98] J.D. Hayes and C.E. Turner, International Journal of Fracture, Vol. 10 (1974) 17-26.

[99] M.G. Dawes, ASTM STP 668, American Society for Testing and Materials (1979) 307-321.

[100] P.C. Paris, H. Tada, A. Zahoor and H. Ernst, ASTM STP 668, American Society for Testing and Materials (1979) 5-36.

[101] G.E. Dieter, Mechanical Metallurgy, McGraw-Hill Inc., Second Edition (1976).

[102] J.R. Rice, in Treatise on Fracture, H.A. Liebowitz, Ed., Vol. 2, Academic Press (1968) 191-311.

[103] M. Singupta, Ph.D. dissertation, Syracuse University, N.Y. (1974).

[104] J.R. Rice and M.A. Johnson, in Inelastic Behavior of Solids, M.F. Kanninen, W.F. Adler, A.R. Rosenfield and R.I. Jafee, Ed., McGraw-Hill, New York (1970) 641-672.

[105] N. Tsangarakis, Material Science and Engineering, No. 58 (1983) 269-276.

[106] K.H. Schwalbe, Engineering Fracture Mechanics, Vol. 9, No. 4 (1977) 795-832.

[107] J.P. Materkowski and G. Krauss, Metallurgical Transactions A, No. 10 (1979) 1643-1651.

[108] R.M. Horn and R.O. Ritchie, Metallurgical Transactions A, No. 9 (1978) 1039-1053.

[109] K.H. Khan and W.E. Wood, Metallurgical Transactions A, No. 9 (1978) 899-907.

[110] S.K. Chaudhuri and R. Brook, International Journal of Fracture, Vol. 12, No. 1 (1976) 101-106.

[111] F.A. McClintock and A.S. Argon, Mechanical Behavior of Materials, Addison-Wesley, Reading, Mass. (1966).

[112] R.O. Ritchie, J.F. Knott and J.R. Rice, Journal of Mechanics and physics of solids 21 (1973) 395-410.

[113] R.O. Richie, W.L. Server and R.A. Wullaert, Metallurgical Transactions 10A (1979) 1557-1570.